

# Automation of One-Loop Computations for Scattering Amplitudes and Applications to Collider Phenomenology

THÈSE N° 5736 (2013)

PRÉSENTÉE LE 17 MAI 2013

À LA FACULTÉ DES SCIENCES DE BASE  
LABORATOIRE DE PHYSIQUE DES PARTICULES ET DE COSMOLOGIE  
PROGRAMME DOCTORAL EN PHYSIQUE

ÉCOLE POLYTECHNIQUE FÉDÉRALE DE LAUSANNE

POUR L'OBTENTION DU GRADE DE DOCTEUR ÈS SCIENCES

PAR

Valentin HIRSCHI

acceptée sur proposition du jury:

Prof. O. Schneider, président du jury  
Dr S. Frixione, directeur de thèse  
Dr C. G. Papadopoulos, rapporteur  
Prof. R. Rattazzi, rapporteur  
Dr P. Z. Skands, rapporteur



ÉCOLE POLYTECHNIQUE  
FÉDÉRALE DE LAUSANNE

Suisse  
2013



Ideas are no less, no more, than what  
contains them.

— *Solmeng-Jonas Hirschi*



# Acknowledgements

I wish to thank my supervisor Stefano Frixione who continuously supported me throughout my thesis. I am indebted to Rikkert Frederix and Johan Alwall for their patience and great help during my first steps in MADFKS and MADGRAPH5. I also thank Pierre Artoisenet for his help in validating MADSPIN for the tri-boson production process and Olivier Mattelaer for his precious collaboration in the implementation of the open loop technique. Finally, I am grateful to Fabio Maltoni and Roberto Pittau for the many useful discussions we had together.

*Lausanne, 3 March 2013*

V. H.



# Abstract

This thesis presents the automation of loop computations for the calculation of Next-to-Leading Order contributions to theoretical predictions for particle colliders. We start with the general techniques for performing such predictions and how they can be expressed as perturbative expansions in the coupling constants controlling the strength of particle interactions. This leads to the discussion of the subtleties arising when considering higher order corrections, in particular the methods employed for isolating and canceling the infrared divergences occurring at intermediate steps of the computation. We then introduce the Passarino-Veltman and Ossola-Papadopolous-Pittau loop reduction algorithms. The latter is used by the computer code MADLOOP that we wrote specifically for the automation of loop computations. The main part of the thesis focuses on the description of this program, starting with its original loop diagram generation algorithm and how it is embedded within the MADGRAPH5 environment. An initiation to the usage of the code is given, followed by a discussion of its optimizations where particular attention is paid to the implementation of the *open-loop* technique. Great details about the validation of MADLOOP results against those of other codes are given in appendix B for specific kinematic configurations. We also list in the main text the total rates obtained for various processes. Quantitative information on the runtime speed and numerical stability performances are presented for many processes, each representative of a certain class of complexity. This serves as a comparison benchmark, and shows that realistic studies can be performed for any  $2 \rightarrow 3$  and most  $2 \rightarrow 4$  processes in the Standard Model. We finish by providing two examples of phenomenology study at the Large Hadron Collider using the tools we developed. The first treats the production of a scalar or pseudo-scalar in association with a top quark pair while the second addresses the tri-boson production channel  $Z W^+ W^-$  with MADSPIN simulating the subsequent decay to leptons. We conclude with some insights on MADLOOP prospects.

**Keywords:** QCD, NLO, loop corrections





# Résumé

Cette thèse présente l'automatisation des calculs de diagrammes de Feynman à boucle, ceci dans le but d'évaluer les contributions sous-dominantes des prédictions théoriques pour les collisionneurs de particules. Je commence par les techniques générales utilisées pour effectuer de telles prédictions et comment elles peuvent s'écrire comme une expansion perturbative avec comme paramètres les constantes de couplages définissant l'intensité des interactions de particules. Ceci m'amène à discuter des subtilités qui apparaissent dans le cadre des corrections d'ordre supérieur, en particulier les méthodes employées pour isoler et annuler les divergences infrarouges qui surviennent aux étapes de calcul intermédiaires. J'introduis ensuite les algorithmes de réduction de boucle de Passarino-Veltman et Ossola-Papadopolous-Pittau. Ce dernier est utilisé par le programme informatique MADLOOP qui j'ai créé spécifiquement pour l'automatisation des calculs de boucles. La partie principale de la thèse se concentre sur la description de cet outil, avec tout d'abord son algorithme original pour la génération de diagrammes à boucle et comment ce dernier est implémenté dans l'environnement de MADGRAPH5. Une initiation à l'utilisation du code est donnée, suivie d'une discussion de ses optimisations où une attention particulière est portée à l'implémentation de la technique dite *open loop*. Les détails précis de la validation de MADLOOP par confrontation aux résultats d'autres codes sont donnés dans l'appendice B pour des configurations cinématiques prédéfinies. Je liste aussi dans le texte principal les sections efficaces intégrées obtenues pour un grand panel de processus. Des informations quantitatives sur les performances en termes de vitesse d'exécution et stabilité numérique sont présentés pour un grand nombre de processus, chacun représentatif d'une certaine classe de complexité. Cela sert d'étalon de comparaison et montre que des études réalistes peuvent être effectuées pour n'importe quel processus  $2 \rightarrow 3$  dans le modèle standard (et la plupart des  $2 \rightarrow 4$ ). Je termine par donner deux exemples d'étude phénoménologique au *Large Hadron Collider* qui utilisent les outils développés dans cette thèse. Le premier traite de la production d'un scalaire ou pseudo-scalaire en association avec une paire de quarks top, tandis que le second concerne le canal de production tri-bosonique  $Z W^+ W^-$  avec MADSPIN simulant la désintégration en leptons. Je conclus avec quelques perspectives d'évolution de MADLOOP.

**Mots clés :** QCD, NLO, corrections de boucle



# Contents

<b>Acknowledgements</b>	<b>v</b>
<b>Abstract (English/Français)</b>	<b>vii</b>
<b>1 Introduction</b>	<b>1</b>
1.1 High energy physics today . . . . .	1
1.1.1 Theoretical predictions at hadron colliders . . . . .	2
1.1.2 The prediction chain . . . . .	4
1.1.3 Anatomy of a Next-to-Leading Order calculation . . . . .	5
1.2 MADFKS . . . . .	7
1.2.1 Subtraction formalism . . . . .	7
1.2.2 Infrared collinear divergences in QCD . . . . .	11
1.2.3 MADFKS strategy: divide and conquer . . . . .	12
<b>2 Loop computation techniques</b>	<b>17</b>
2.1 Notation . . . . .	17
2.2 The Passarino-Veltman reduction . . . . .	20
2.3 The Ossola-Papadopolous-Pittau reduction . . . . .	23
<b>3 MadLoop</b>	<b>27</b>
3.1 Organization of the calculation . . . . .	27
3.1.1 Generation of one-loop amplitudes from tree amplitudes . . . . .	29
3.1.2 $R_2$ contribution and UV renormalization . . . . .	32
3.1.3 Summary of MADLOOP features . . . . .	34
3.1.4 Checks . . . . .	36
3.2 Limitations of MADLOOP . . . . .	40
3.3 Results from the MADGRAPH4 original framework . . . . .	42
3.4 The MADLOOP5 successor . . . . .	47
3.4.1 AMC@NLO5 and MADLOOP5 usage . . . . .	47
3.4.2 Model independence: the UFO format . . . . .	57
3.4.3 Code optimizations . . . . .	59
3.4.4 Robustness against numerical instabilities . . . . .	65
3.4.5 Performance benchmarks . . . . .	71

<b>4</b>	<b>LHC phenomenology with AMC@NLO</b>	<b>75</b>
4.1	AMC@NLO4 applied to $pp \rightarrow H/A t \bar{t}$	75
4.1.1	Results	77
4.2	AMC@NLO5 applied to $pp \rightarrow Z W^+ W^-$	83
4.2.1	Results at the LHC, 8 TeV	83
<b>5</b>	<b>Conclusion</b>	<b>91</b>
5.1	Prospects	91
5.1.1	Computation of electro-weak corrections	91
5.1.2	BSM model support	92
5.1.3	Interface to tensor integral reduction codes	95
5.1.4	Further code optimizations	95
5.2	Closing remarks	97
<b>A</b>	<b>MadLoop technical details</b>	<b>99</b>
A.1	MADGRAPH5 testing suite	99
A.2	UFO format for loop models	100
A.2.1	CouplingOrder	100
A.2.2	Particle	101
A.2.3	CTVertex	101
A.3	UV renormalization counterterms	102
A.4	Restoring precision on input kinematic configurations	103
A.5	MADLOOP runtime parameters	104
A.6	Example of filtering of loop diagrams	105
<b>B</b>	<b>Comparisons with existing results</b>	<b>111</b>
B.1	QCD processes	113
B.1.1	The process $u\bar{u} \rightarrow d\bar{d}$	113
B.1.2	The process $dg \rightarrow dg$	114
B.1.3	The processes $d\bar{d} \rightarrow t\bar{t}$ and $gg \rightarrow t\bar{t}$	115
B.1.4	The process $ug \rightarrow t\bar{t}u$	116
B.1.5	The process $u\bar{u} \rightarrow b\bar{b}b\bar{b}$ with massless $b$	116
B.1.6	The process $u\bar{u} \rightarrow t\bar{t}b\bar{b}$ with massless $b$	117
B.2	Processes with a single vector boson	118
B.2.1	The process $u\bar{d} \rightarrow e^- \bar{\nu}_e$	118
B.2.2	The processes $u\bar{d} \rightarrow \nu_e e^+ g$ and $ug \rightarrow \nu_e e^+ d$	119
B.2.3	The processes $d\bar{d}(\rightarrow \gamma^*/Z) \rightarrow e^- e^+ g$ and $dg(\rightarrow \gamma^*/Z) \rightarrow e^- e^+ d$	120
B.2.4	The processes $dc(\rightarrow W^-) \rightarrow e^- \bar{\nu}_e uc$ and $dg(\rightarrow W^-) \rightarrow e^- \bar{\nu}_e ug$	122
B.2.5	The process $ug(\rightarrow Z/\gamma^*) \rightarrow e^- e^+ ug$	124
B.2.6	Closed fermion loops contributing to $e^+ e^- \rightarrow d\bar{d}gg$	126
B.2.7	The $gg \rightarrow Zg$ one-loop amplitude squared	127
B.2.8	The process $ug \rightarrow t\bar{b}d$ (four-flavor $t$ -chan. single-top production)	130
B.2.9	The process $u\bar{d}(\rightarrow W^+) \rightarrow \nu_e e^+ b\bar{b}$ with massive $b$	132

B.3	Processes with two vector bosons . . . . .	133
B.3.1	The process $d\bar{d} \rightarrow W^+W^- \rightarrow \nu_e e^+ e^- \bar{\nu}_e$ . . . . .	133
B.3.2	The processes $u\bar{u} \rightarrow W^+W^- b\bar{b}$ and $gg \rightarrow W^+W^- b\bar{b}$ with massless $b$ 134	
B.4	Processes with a single Higgs boson . . . . .	136
B.4.1	The process $bg \rightarrow Hb$ . . . . .	136
B.4.2	The process $gb \rightarrow H^- t$ . . . . .	137
B.4.3	The processes $u\bar{u} \rightarrow t\bar{t}H$ and $gg \rightarrow t\bar{t}H$ . . . . .	138
B.5	Checks of MADLOOP5 . . . . .	139
B.5.1	The process $gg \rightarrow ng, n=2,3,4$ . . . . .	139
B.5.2	The channels of the process $pp \rightarrow 4j$ . . . . .	141
B.5.3	Pushing MADLOOP to the edge: a result for $d\bar{d} \rightarrow t\bar{t}t\bar{t}b\bar{b}$ . . . . .	142
<b>Bibliography</b>		<b>145</b>
<b>Curriculum Vitae</b>		<b>157</b>



# 1 Introduction

## 1.1 High energy physics today

Particle physics always had as a driving principle the construction of mathematical models for explaining and predicting fundamental natural phenomena. Until the middle of the 20<sup>th</sup> century, guessing or deducing this underlying model was more of a challenge than confronting its actual predictions to observational data. However, in the last 40 years, the validity of the Standard Model (SM) of elementary particles has been established in a vast variety of experiments and to a very high accuracy so that new physics searches now very often rely on indirect detection through *precise* comparison of experimental observations with theoretical predictions.

In high energy physics, there is the possibility of systematically improving the prediction for most observables by means of perturbative techniques, writing it as an expansion in the coupling constants of the particle interactions. The computation of contributions of increasingly higher orders in this expansion is analogous to the accumulation of data in real experiments such as ATLAS, CMS, LHCb and ALICE at CERN. While the latter results in the decrease of the statistical error associated with the measurement, the former implies the reduction of the theoretical uncertainty affecting the prediction. Precise determinations on both the theoretical and experimental sides have been essential in the success of physics programmes at particle colliders, and continue playing a very important role in pinning down potential discrepancies between predictions and observations. It should be further stressed that some discovery strategies pursued by collider experiments (a prime example being the single-top analysis of the CDF and D0 collaborations at FermiLab) make extensive use of theoretical predictions, whose accuracy is crucial to reduce as much as possible any theoretical bias on evidence of new physics.

The reduction of the uncertainties that affect theoretical predictions is only one of the consequences of computing higher orders in the perturbative series. In general, one expects to find corrections that are non-trivial, in the sense that they cannot possibly be obtained by simply rescaling the Leading-Order (LO) results by a constant. One reason for this is that processes occurring in hadron collisions have a rich structure where new partonic channels can open up only at higher orders.

Some processes, referred to as *loop-induced*, only occur via loops of virtual particles so that the computation of the LO contributions to the related observables already has the

same complexity as that of the evaluation of the Next-to-Leading Order (NLO) terms in processes with tree diagrams contributing at LO. For these loop-induced processes, the technology developed in this thesis is simply unavoidable for providing any exact LO prediction at all. A very relevant example in the SM is the Higgs boson production through gluon fusion<sup>1</sup> which is by far its main production channel at the Large Hadron Collider (LHC).

In 2005, the creation of the Les Houches priority list [8] further emphasized that computing higher order contributions to the perturbative series of theoretical predictions is desirable for most processes and studies. Unfortunately few analysis include them because they are computationally extremely cumbersome and very often impossible to carry out by hand. There is therefore a clear need for an automated, flexible and user-friendly framework to tackle them. The work presented in this thesis aimed at the development of such a tool and its use for high precision phenomenology at collider experiments.

### 1.1.1 Theoretical predictions at hadron colliders

The LHC collides proton beams at a center of mass energy of 8 TeV (eventually at 14 TeV) and with luminosities two orders of magnitude larger than those of the second largest collider ever built, namely Tevatron. Its main goal is to explore potential new physics beyond the electroweak scale. However, most of what governs the proton collisions at these high energies is hard Quantum ChromoDynamics (QCD), i.e processes driven by strong interactions occurring at large energy scales. Processes in QCD therefore constitute the dominant backgrounds to most new physics searches and it is essential that they are well modeled and predicted to an accuracy matching the experimental resolution. Also, because of the large accessible energy at the LHC, multi-jet observables originating either from pure QCD or from the decay of new massive particles will play a key role. The theoretical simulation of these processes with large number of final states is computationally very challenging and automated methods such as that developed in this thesis are at present the only viable approaches.

A remarkable feature of QCD is the dependence of its coupling parameter  $\alpha_s$  on the typical energy of the interaction. This *running* of the strong coupling is such that QCD becomes non perturbative at an energy  $\Lambda_{QCD}$  of around 1 GeV, with the consequence that colored asymptotic states (quarks and gluons) are not directly observable by experiments. This also implies that perturbative methods on their own can predict scattering of these unobservable states only. To study realistic hadronic collisions, extra information needs to be input to model how they are bound together in the colliding protons. The collinear factorization theorem [57] states that this modelization can be given as Parton Density Functions (PDF) which enter the generic expression of the cross section for the

---

<sup>1</sup>One can however use the approximate *Higgs effective theory* (the dependance on the virtual quark masses is then lost) in which tree-diagrams describe this Higgs production channel at LO.



hadroproduction of a set of final states  $\{F\}$ :

$$d\sigma_{pp \rightarrow \{F\}} = \sum_{ab} \int dx_1 dx_2 f_a^{(p)}(x_1, \mu) f_b^{(p)}(x_2, \mu) d\hat{\sigma}_{ab \rightarrow \{F\}}(\mu, M_{\{F\}}) \quad (1.1.1)$$

with  $f_{a/b}^{(p)}$  the PDFs,  $d\hat{\sigma}_{ab \rightarrow \{F\}}$  the hard cross section and the sums run over all partonic configurations, i.e. components of the proton. The essence of the factorization theorem is to state the universality of the PDFs, in the sense that they can be measured for one set of observables and then inserted in eq. (1.1.1) to predict another process.

Contrary to the PDFs,  $d\hat{\sigma}_{ab \rightarrow \{F\}}$  describes the physics at the large energy scale  $M_{\{F\}}$ , where QCD is in a perturbative regime. It can therefore be expressed as an expansion in a parameter  $\lambda$ . We shall call *Born* the first order in  $\lambda$  at which the short distance cross section receives a contribution. Terms of order  $\lambda^{\text{Born}+1}$  and  $\lambda^{\text{Born}+2}$  are referred to as Next-to-Leading Order (NLO) and Next-to-Next-to-Leading Order (NNLO) respectively. In general, the expansion is performed in terms of the coupling constant of the relevant interactions for the process, so that in QCD for example  $\lambda_1 = \alpha_s/2\pi$ . However, in specific cases where two widely separated scales  $\mu$  and  $M$  appear in the computation, the logarithm of their ratio can be large and compete with the smallness of the coupling constant. In these situations,  $\lambda$  can be set proportional to these logarithms,  $\lambda_2 = \alpha_s \log(\frac{M}{\mu})^k$  with  $k$  typically equal to one or two depending on the target accuracy and observable considered. The prediction can then be rewritten via an exponential of a serie in  $\lambda_2$  which<sup>2</sup> *resums* the contribution of all powers of  $\lambda_2$ . These resummation techniques are a vast domain by themselves and we shall not comment further on them as they are outside the scope of this thesis.

It should be noted that the final state partons in the  $pp \rightarrow \{F\}$  process of eq. (1.1.1) are not yet the observed states in detectors. Similarly to what was presented for the PDF of initial state partons, it is possible to devise distributions characterizing the probability of a final state parton to turn into a given hadron. These distributions called fragmentation functions cannot be computed via perturbative techniques but are universal within a certain defining class of processes and can be measured at collider experiments.

However, the most common way (especially at hadron colliders) of accounting for the low energy QCD effects in the propagation of final state partons is the *Parton Shower Monte-Carlo* (PSMC) technique. The idea is that each parton in  $\{F\}$  can split into a pair of new partons according to a probabilistic distribution obtained from an approximate<sup>3</sup> QCD description of the branching. The procedure is iterated, with at each step the resulting partons carrying less energy than their mother. The algorithm stops when reaching the non-perturbative regime, around  $\Lambda_{QCD}$ . At this stage the parton multiplicity is much

<sup>2</sup>The logarithms in the exponent are most often not exactly those of  $\lambda_2$ , but a conjugate variable obtained via some integral transformation.

<sup>3</sup>Exact in the collinear/soft limit

greater than the one of the starting configuration  $\{F\}$  and an empirical hadronization model is used to turn these partons into hadrons which can be compared with those observed in real experiments. Since the probability of the successive splittings of a parton is independent of its history, quantum coherence is partially lost (depending on the choice of the evolution variables, some of it is kept). It turns out however that this pseudo classical description describes the data very well and hence efficiently models the soft QCD effects affecting the partons in  $\{F\}$  before their hadronization. This is less of a surprise when considering that parton showers effectively perform a resummation of large logarithms originating from the soft/colinear radiation.

The problem addressed by this work is that of automatically computing  $d\hat{\sigma}_{ab \rightarrow \{F\}}$  at NLO accuracy for any process and within general theories. In the next section, we discuss the state of the art in this domain and describe the computational framework for high energy physics predictions.

### 1.1.2 The prediction chain

It is a long and tedious task to provide a theoretical prediction for an observable at collider experiments when starting from the Lagrangian of the theory of choice, arguably its highest level of representation. Fig.1.1.1 depicts the various steps to be taken successively and for each of them the specific tool used for this task in our computational framework.

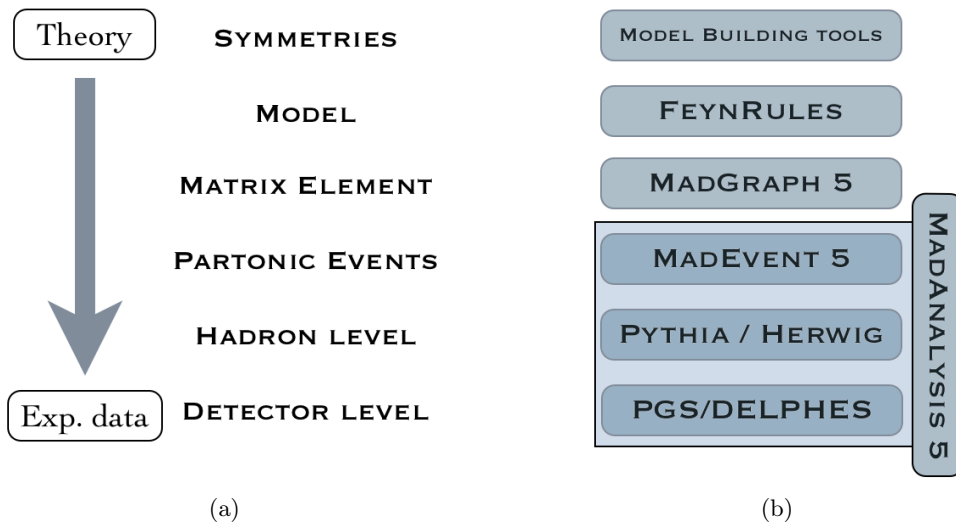


Figure 1.1.1: Fig. a) shows the long path from the Lagrangian of a specific model to theoretical predictions which can directly be compared with experimental data. Fig. b) shows the specific tools used in our framework for each step of the computation.

First, the operators present in the Lagrangian must be turned into analytical build-

ing blocks suited for computations using Feynman diagrammatical methods<sup>4</sup>. These are called Feynman rules and are deduced from the Lagrangian by the MATHEMATICA package FEYNRULES [56] which then outputs them to a general purpose model file [67] (see sect. 3.4.2). This model can then be loaded into a matrix-element generator like MADGRAPH [152, 7] so as to generate a numerical code computing the hard scattering amplitudes<sup>5</sup> corresponding to the user-defined processes. To obtain inclusive quantities like cross-sections, the output of this code is integrated over the kinematic phase-space of the final states  $\{F\}$  of the process. The number of dimensions of this integral grows with the particle multiplicity of the process so that we rely on Monte-Carlo techniques such as embedded in MADEVENT [129] for the integration of LO quantities. When considering NLO computations, MADFKS [105] (see sect. 1.2) instead is used as it is equipped for dealing with the singularities occurring in this class of contributions.

In order to generate a set of unweighted *events* similar to the collision products observed in real detectors, the parton-level Monte-Carlo must be *matched* to showering programs like discussed in sect. 1.1.1. The most common ones are SHERPA [114], the FORTRAN versions of HERWIG [60] and PYTHIA6 [150] as well as their C++ successors HERWIG++ [13] and PYTHIA8 [151]. Eventually, detector simulation takes place to account for their (in)efficiencies and defects.

### 1.1.3 Anatomy of a Next-to-Leading Order calculation

This whole procedure is now completely automated for LO predictions and tools such as those mentioned have enjoyed tremendous success in all high energy experimental collaborations where they constitute the backbone of their analysis. As mentioned in the introduction, it is however highly desirable to have the same technology including the NLO contributions in the perturbative expansion of the prediction. To achieve this, several of the steps depicted in fig. 1.1.1 must be modified, in particular the matrix element generator and the Monte-Carlo computational setup. This is because the higher order amplitude contributions  $\mathcal{A}_{loop}^{(1)}$  and  $\mathcal{A}_{real}^{(1)}$  shown<sup>6</sup> in fig. 1.1.2 for the example of  $e^+e^- \rightarrow t\bar{t}$  production are much more problematic to compute. They exhibit a non-trivial cancellation of singularities, typically achieved by a technique called *dimensional regularization*.

---

<sup>4</sup>These methods are the canonical approach to computations in quantum field theory, see [142] for an introduction.

<sup>5</sup>Scattering amplitudes are the main ingredients building  $d\hat{\sigma}_{ab \rightarrow \{F\}}$  of Eq. (1.1.1)

<sup>6</sup>The figure depicts only one representative Feynman diagram for each of the three classes of contributions.

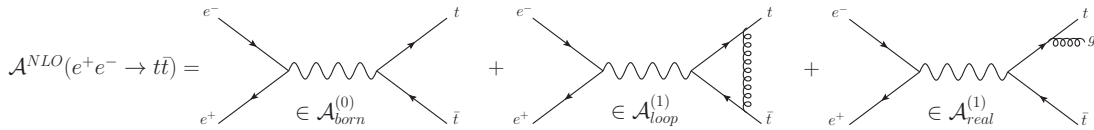


Figure 1.1.2: The three classes of contributions to an NLO amplitude.

In order to be treated on an equal footing with the other contributions,  $\mathcal{A}_{real}^{(1)}$  must be integrated over the phase-space of its extra parton in the final state. The integrand becomes divergent when this parton becomes soft and/or collinear to the particle it is emitted from, thus yielding singularities which need to be systematically treated by the Monte-Carlo. Several techniques exist to tackle this problem; our framework uses the FKS [107, 110] method as implemented in MADFKS [105] (see sect. 1.2).

The contribution  $\mathcal{A}_{loop}^{(1)}$  features a novel topology corresponding to the pictorial representation of an integral over an unconstrained loop-momentum  $\ell^\mu$ . The general form of this integral is presented in the next chapter in fig. 2.1.1.

The computation of this class of integrals stood for long as the bottleneck of theoretical predictions including NLO terms but the last 15 years showed great progress in this field, as summarized for example in review [90]. Even with these new techniques for calculating the loop integrals, one still needs to be able to automatically generate for any process a numerical code exploiting them to calculate  $\mathcal{A}_{loop}^{(1)}$ . The code MADLOOP [123, 122] developed over the course of this thesis achieves this by exploiting the Ossola-Papadopoulos-Pittau (OPP) [139, 136] loop reduction method (see sect. 2.3) as implemented in CUTTOOLS [138]. Other groups have provided similar solutions to the same problem: HELAC-1LOOP [28] proposes a numerical method also based on the OPP algorithm and with a recursive approach to the construction of loop amplitudes, GoSAM [61] employs a fully analytical approach and MCFM [46] features a large collection of dedicated handwritten codes brought together in a common framework. The BLACKHAT [20] collaboration exploits generalized unitarity techniques to compute NLO QCD corrections to specific very complicated SM processes, such as  $pp \rightarrow W + 4j$  [22]. MADLOOP on the other hand puts a special emphasis on being very flexible towards the physics models and processes considered.

The matching to PSMC is more subtle at NLO because, in this case, the first soft/collinear emission off final partons is already accounted for in  $\mathcal{A}_{real}^{(1)}$ . The MC@NLO [112] method is employed to avoid this double counting.

These tools together form the AMC@NLO framework (the prepended 'A' stands for *automatic*) which is the first fully automated event generator for Standard Model processes at NLO in the strong coupling constant  $\alpha_s$ . Equipped with this technology, we were able to study the phenomenology of many high energy processes in a short time and at NLO accuracy. In particular, the collaboration published on four important processes

at the LHC;  $pp > Ht\bar{t}$  [103],  $pp > Zb\bar{b}$  [104], four-leptons production [102] and finally  $pp > Wjj$  [101]. This last one came as a response to a published measurement [3] by the CDF collaboration at Tevatron presenting unexpected excess in the tail of the dijet invariant mass distribution in  $pp > Wjj$ . Applications of the AMC@NLO framework for NLO phenomenology is the object of chapter 4, with in particular the presentation of unpublished results on triple vector boson production at the LHC.

The so far published analysis were performed with codes based on MADGRAPH4, an old fortran code started in 1992. Its successor MADGRAPH5 is entirely rewritten in PYTHON, hence offering a flexible and powerful developing environment. This is why MADLOOP was re-implemented from scratch in this framework and dubbed MADLOOP5, described in sect. 3.4, which is already faster and more comprehensive than MADLOOP4 (the old version). As fig. 1.1.3 shows, the whole AMC@NLO framework is now completely embedded in the version 2.0 of MADGRAPH5, whose beta version is already publicly available at [amcatnlo.cern.ch](http://amcatnlo.cern.ch) or directly at [launchpad.net/madgraph5](http://launchpad.net/madgraph5) since November 8<sup>th</sup>, 2012.

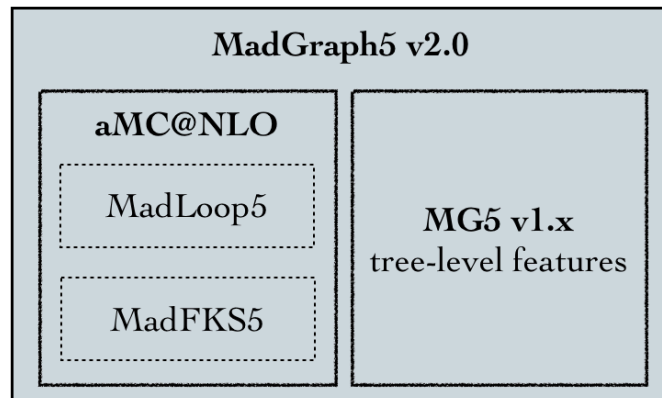


Figure 1.1.3: How AMC@NLO is incorporated into MADGRAPH5.

## 1.2 MADFKS

The computation of predictions for high energy physics observables at NLO accuracy necessitates to improve LO generators to include all three pieces of fig. 1.1.2. It is an especially difficult task because of the non-trivial cancellation of the divergences intrinsic to  $\mathcal{A}_{loop}^{(1)}$  with those occurring upon the integration of  $\mathcal{A}_{real}^{(1)}$ .

### 1.2.1 Subtraction formalism

To illustrate the possible solutions to this problem, it is simpler to start from the unphysical simplified model proposed in ref. [86] with all the key properties of QCD. In this one-dimensional model, a system can radiate a massless particle, called photon in this example,

## Chapter 1. Introduction

---

and with energy  $x$  comprised between 0 and 1. After an emission, the energy of the remaining system is  $1 - x$ . In analogy with fig. 1.1.2, the leading contribution corresponds to the case of no-emission,  $\mathcal{A}_{Born}^{(0)}$ , while the contributions to the NLO corrections come from the single emission of a virtual or real photon,  $\mathcal{A}_{loop}^{(1)}$  or  $\mathcal{A}_{real}^{(1)}$  respectively.

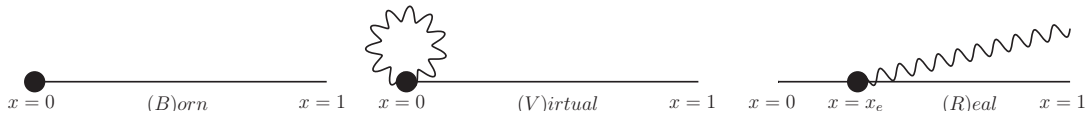


Figure 1.2.1: The Born, Virtual and Real contribution illustrated for the toy model described in the text. The dark blob is the system and the wiggly line the massless particle it emits.

The contribution to the differential cross-section  $\frac{d\sigma}{dx}$  of each of the three terms of fig. 1.2.1 can be written

$$\begin{aligned}\frac{d\sigma_B}{dx} &= B\delta(x) \\ \frac{d\sigma_V}{dx} &= \alpha\left(\frac{B}{2\epsilon} + V\right)\delta(x) \\ \frac{d\sigma_R}{dx} &= \alpha\frac{R(x)}{x}\end{aligned}\tag{1.2.1}$$

for the Born, Virtual and Real terms respectively, with  $\epsilon$  the parameter entering dimensional regularization in  $d = 4 - 2\epsilon$  dimensions. The parameter  $\alpha$  is the coupling constant defining the expansion parameter and controlling the strength of the photon emission.  $B$  and  $V$  do not depend on  $x$  as they both exhibit the Born kinematic configuration. The function  $R(x)$  has the key property:

$$\lim_{x \rightarrow 0} R(x) = B\tag{1.2.2}$$

The appearance of the same quantity  $B$  in eq. (1.2.2) and in  $d\sigma_R$  of eq. (1.2.1) originates from the expectation that the residue of the leading singularity of  $d\sigma_R$  and  $d\sigma_V$  factorizes the Born term. This result is assumed in this toy model but it can be derived from the Lagrangian in the QCD case where the  $B$  term turns out not to be exactly the Born but specific constituents of it altered by color algebra kernels, set to one in the toy model for simplicity. The prediction of an observable  $\mathcal{O}$  to NLO accuracy amounts to computing the following integral

$$\langle \mathcal{O} \rangle = \lim_{\epsilon \rightarrow 0^+} \int_0^1 dx x^{-2\epsilon} \mathcal{O}(x) \left[ \frac{d\sigma_B}{dx} + \frac{d\sigma_V}{dx} + \frac{d\sigma_R}{dx} \right]\tag{1.2.3}$$

The folding over parton distribution functions presented in eq. (1.1.1) is omitted here as it plays no role at this stage of the discussion and has no meaning in the context of the toy model considered. In a realistic model, the Born phase-space (corresponding to  $x = 0$  here) is denoted  $d\phi_n$  with  $n$  the number of particles in the process definition. Because  $d\phi_n$  is

common to the three integrands of eq. (1.2.3) and does not bring in divergences<sup>7</sup>, it greatly simplifies the expression to have it zero-dimensional like in this toy-model. The one-dimensional integration variable  $x$  is the only one affected by dimensional regularization bringing the  $x^{-2\epsilon}$  term and is associated to the phase-space of the emitted photon. It symbolically corresponds to  $\frac{d\phi_{n+1}}{d\phi_n}$  in the physical case.

The function  $\mathcal{O}(x)$  defines the observable as a function of  $x$  (and  $\phi_n$  if it were not zero-dimensional) and typically includes a set of Heaviside  $\Theta$  functions defining histogram bins. In order to have the cancellation of infrared divergences, the analogue of eq. (1.2.2) must also hold for the function  $\mathcal{O}(x)$

$$\lim_{x \rightarrow 0} \mathcal{O}(x) = \mathcal{O}(0) \quad (1.2.4)$$

This continuity constraint is referred to as the *infrared safety* condition of an observable. In the context of QCD, this condition translates into the fact that the observable  $\mathcal{O}$  must remain invariant if the kinematic configuration at which it is evaluated is modified by the addition of an exactly soft and/or collinear parton.

The computation of the integral of eq. (1.2.3) must be performed numerically because of its high dimensionality and complexity of the functions  $\mathcal{O}(x)$  and  $R(x)$  in realistic models. The presence of the regulator  $\epsilon$  necessitates to employ a semi-numerical method which first isolates the pole in  $\epsilon$  arising from the integration of  $d\sigma_R$  so as to analytically cancel it against the intrinsic one of  $d\sigma_V$ . The remaining piece of the integral is then  $\epsilon$ -finite and conventional numerical integration techniques can be employed.

We present here the two classes of methods that have been proposed to perform this isolation. The *slicing method* introduces a small parameter  $\delta$  into the integral of  $d\sigma_R$  as follows

$$\langle \mathcal{O} \rangle_R = \int_0^\delta dx x^{-2\epsilon} \mathcal{O}(x) \frac{d\sigma_R}{dx} + \int_\delta^1 dx x^{-2\epsilon} \mathcal{O}(x) \frac{d\sigma_R}{dx} \quad (1.2.5)$$

This achieves the separation between the divergent and finite region in the most direct way. In the first term of the r.h.s of eq. (1.2.5), one can expand  $\mathcal{O}(x)$  and  $R(x)$  in a Taylor series around  $x = 0$  (the Born kinematic configuration) and only keep the first term. This approximation is best for small values of  $\delta$  and the higher order contributions left out are denoted  $\Delta(\delta)$ . Thanks to this splitting, or *slicing*, of the integration domain, the second term on the r.h.s is now finite and the regulator  $\epsilon$  can be set to zero in this part. Substituting  $d\sigma_R$  with its expression in eq. (1.2.1) and the limits of eq. (1.2.2) and

---

<sup>7</sup>As long as the observable  $\mathcal{O}$  is finite for any Born kinematic configuration.

eq. (1.2.4), one obtains

$$\begin{aligned}\langle \mathcal{O} \rangle_R &= \alpha B \mathcal{O}(0) \int_0^\delta dx \frac{x^{-2\epsilon}}{x} + \Delta(\delta) + \int_\delta^1 dx \mathcal{O}(x) \frac{d\sigma_R}{dx} \\ &= \alpha B \mathcal{O}(0) \left( -\frac{1}{2\epsilon} + \log(\delta) \right) + \Delta(\delta, \epsilon) + \alpha \int_\delta^1 dx \frac{\mathcal{O}(x)R(x)}{x}\end{aligned}\quad (1.2.6)$$

When this expression for  $\langle \mathcal{O} \rangle_R$  is plugged into eq. (1.2.3), the cancellation of the pole in  $\epsilon$  is explicit and all remnants are finite

$$\langle \mathcal{O} \rangle_{slice} = B \mathcal{O}(0) + \alpha \left[ (B \log(\delta) + V) \mathcal{O}(0) + \int_\delta^1 dx \frac{\mathcal{O}(x)R(x)}{x} \right] + \Delta(\delta) \quad (1.2.7)$$

where the limit  $\epsilon \rightarrow 0$  has already been taken. The smaller the parameter  $\delta$ , the smaller the missing terms  $\Delta(\delta)$  and the better the approximation of the slicing method. Unfortunately, for smaller values of  $\delta$ , the computation features a cancellation between two increasingly larger numbers: the integral  $\int_\delta^1 dx \frac{\mathcal{O}(x)R(x)}{x}$  and the quantity  $B \mathcal{O}(0) \log(\delta)$ . At some point, the accuracy of the numerical integration reaches the magnitude of this large number cancellation and their difference (*i.e.* the final result) becomes numerically unstable. There is therefore a trade-off between small  $\delta$  values minimizing the impact of the slicing approximation and larger ones insuring numerical stability. The optimal choice for setting  $\delta$  is then process and observable dependent so that it is in principle necessary to always assess that physical results are invariant upon a continuous change of  $\delta$  over a suitable range of small values. This test should be performed for each observable  $\mathcal{O}$  but in practice, only a finite set of sufficiently inclusive ones are considered.

The approach of the *subtraction method* is similar except for the crucial difference that it implies no approximation. In this case, the real contribution is decomposed as follows:

$$\langle \mathcal{O} \rangle_R = \alpha B \mathcal{O}(0) \int_0^1 dx \frac{\Theta(\xi - x)}{x^{1+2\epsilon}} + \alpha \int_0^1 dx \frac{\mathcal{O}(x)R(x) - B \mathcal{O}(0)\Theta(\xi - x)}{x^{1+2\epsilon}} \quad (1.2.8)$$

with  $\xi$  an *arbitrary* parameter in the range  $0 < \xi \leq 1$ . The second term on the r.h.s of this equation is finite thanks to the limiting behavior<sup>8</sup> of  $R(x)$  and  $\mathcal{O}(x)$  imposed by eq. (1.2.2) and eq. (1.2.4) so that the regulator  $\epsilon$  can directly be set to zero in the integrand. The subtraction method provides this final expression for the NLO prediction

$$\langle \mathcal{O} \rangle_{subtr} = B \mathcal{O}(0) + \alpha \left[ (B \log(\xi) + V) \mathcal{O}(0) + \int_0^1 dx \frac{\mathcal{O}(x)R(x) - B \mathcal{O}(0)\Theta(\xi - x)}{x} \right] \quad (1.2.9)$$

Despite being very similar to eq. (1.2.9), it differs by the fact that the new parameter  $\xi$  introduced does not need to be small as the subtraction method involve no approximation. In turn, this implies that there is no need for a check on the invariance of the physics result with respect to  $\xi$ . Moreover, the subtraction prescription handles the cancellation of

---

<sup>8</sup>Because the integral is logarithmically divergent, the subtraction term renders it finite irrespectively of the pace at which  $R(x)$  and  $\mathcal{O}(x)$  converge towards their finite limit at  $x = 0$ .



the divergences occurring at the intermediate steps of the computation by exploiting only the limiting behavior of the observable  $\mathcal{O}$  and of the integrand of the real contribution  $R(x)$ . In particular, no further information on the matrix element and the process in general is necessary, making this formalism well suited for automation. It is therefore the method of choice in AMC@NLO.

### 1.2.2 Infrared collinear divergences in QCD

It is interesting to see how the divergence of the integrand  $\frac{d\sigma_R}{dx}$  really occurs in the QCD case. It turns out that the only Feynman diagrams sourcing divergences of the matrix element for the real-emission processes are those for which a massless parton is emitted from an external leg of the underlying Born process. The case of the emission of a gluon from a quark can be depicted very generally as in fig. 1.2.2.

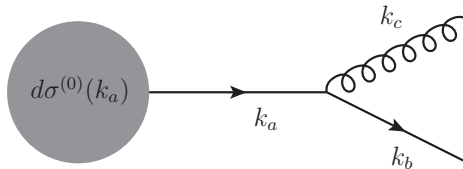


Figure 1.2.2: Formal representation of a final state quark leg emitting a gluon. This is one of the possible contributions to the real emission part of cross-section denoted  $d\sigma^{(1,R)}$ .

The case of a gluon emission by a gluon and of a quark splitting into two gluons is completely analogous. The gray blob indicates the underlying Born diagram whose square builds the LO contribution denoted by  $d\sigma^{(0,B)}$ . To compute this diagram in a way that the collinearity of the emitted parton is made explicit, one typically parametrizes the momenta  $k_b$  and  $k_c$  as follows:

$$k_b = zk_a + k_T + \beta_b \hat{n}, \quad k_c = (1-z)k_a - k_T + \beta_c \hat{n} \quad (1.2.10)$$

where  $k_a$  and  $\hat{n}$  are two non collinear massless four-momenta orthogonal to  $k_T$ . The coefficients  $\beta_b$  and  $\beta_c$  are determined by the onshell conditions<sup>9</sup>  $k_c^2 = 0$  and  $k_b^2 = 0$

$$\beta_b = -\frac{k_T^2}{2z\hat{n} \cdot k_a}, \quad \beta_c = -\frac{k_T^2}{2(1-z)\hat{n} \cdot k_a} \quad (1.2.11)$$

This diagram leads to a divergence in the in the matrix element squared only when interfered against itself and an explicit computation of its contribution shows that the

---

<sup>9</sup>The energy-momentum conservation violation of  $k_a = k_b + k_c$  vanishes when approaching the soft and/or collinear region of the emission.

divergent contribution factorizes the underlying Born expression and can be written

$$d\sigma^{(1,R)} = \frac{\alpha_s}{2\pi} \int dk_T^2 \int_0^1 dz C_F \frac{1+z^2}{1-z} \frac{1}{k_T^2} d\sigma^{(0)}(k_a) + \mathcal{R} \quad (1.2.12)$$

with the color factor  $C_F = 4/3$ . The second term on the r.h.s of eq. (1.2.12) is a finite remnant whose integrand corresponds to  $\frac{R(x)-B}{x}$  in the toy model. The first term is the divergent piece and needs to be regularized consistently with the scheme used for the computation of the virtual contribution  $d\sigma^{(0,V)}$ . This insures not only the explicit single pole cancellation but also the respective consistency of the finite remainders  $\mathcal{R}$  and  $\mathcal{V}$  which drive the physics result. The conventional choice of dimensional regularization modifies the integration measure of eq. (1.2.12) by a factor  $k_T^{-2\epsilon}(1-z)^{-2\epsilon}$ . The expression of the multiplicative term  $\frac{1+z^2}{1-z}$  is characteristic of a class of functions called the *Altarelli-Parisi* splitting kernels. The study of soft emissions proceeds analogously except that it necessitates a different parametrization of the kinematics and that also the interference of diagrams featuring a soft emission from different final state partons are divergent. The counterpart of the Altarelli-Parisi kernel in this case is called the *Eikonal* kernel.

This development shows that the divergences occurring in QCD are more complex than the simple  $1/x$  integrand of the toy model. Indeed, eq. (1.2.12) features a divergence at both  $z = 1$  and  $k_T^2 = 0$  which corresponds to an emission of a collinear and soft parton<sup>10</sup> respectively. The case of the emitted parton being both soft and collinear is responsible for the double pole  $1/\epsilon^2$  in dimension regularization whose residue is the same as the one of the virtual contribution, with opposite sign. Notice that all these divergences are of infrared origin. The cancellation of the divergences of UV origin, present in the loop contribution only, is not discussed here and is typically handled by the Lagrangian renormalization through the addition of suitably defined set of counterterms (see ref. [142] for a general introduction on that topic). The treatment of collinear singularities in the real emission of initial state partons is similar to what is presented above, to the minor difference that it involves the folding of the partonic cross-section over the parton distributions function. Exploiting the factorization theorem, this allows to move a non-perturbative left-over contribution into the PDF definition at the cost of introducing the factorization scale  $\mu_f$ . The universality of the PDF along with the collinear factorization theorem of eq. (1.1.1) saves the predictivity of perturbative computations in QCD.

### 1.2.3 MADFKS strategy: divide and conquer

The situation of eq. (1.2.12) treats the emission of a parton from one particular external leg denoted  $a$  but the complete treatment of realistic QCD processes is more complicated since one must consider all possible real emission configurations. For each of them, the subtraction formalism applies, with a specific kinematic parametrization and underlying

---

<sup>10</sup>This divergence of soft origin is however incomplete as it arises from collinear parametrization of the emission.

Born configuration  $d\sigma^{(0)}(k_a)$ . It is therefore necessary to isolate each of these real emission configurations and correctly define, for each of them, the corresponding local subtraction counterterm.

Several solutions for achieving this separation exist, and AMC@NLO chooses the FKS universal subtraction formalism [110, 107] as implemented in the Monte-Carlo Integrator (MCI) MADFKS [105]. In this formalism, the singularities are isolated through the following manipulation of the real-emission integrand  $d\sigma_R$

$$d\sigma_R = \sum_{ij} d\sigma_{ij}^{(R)}, \quad d\sigma_{ij}^{(R)} = \mathcal{S}_{ij} d\sigma_R \quad (1.2.13)$$

where the definition of the function  $\mathcal{S}$  is based on the identification of the parton pairs  $(i, j)$  that can give collinear and soft singularities

$$\begin{aligned} \text{a) } & \sum_{ij} \mathcal{S}_{ij} = 1 \\ \text{b) } & \lim_{\vec{k}_i \parallel \vec{k}_j} \mathcal{S}_{ij} = 1 \\ \text{c) } & \sum_j \lim_{k_i^0 \rightarrow 0} \mathcal{S}_{ij} = 1 \\ \text{d) } & \mathcal{S}_{ij} \rightarrow 0 \quad \forall \text{ other singularities not corresponding to b) and c).} \end{aligned} \quad (1.2.14)$$

The constraint a) insures a correct normalization for the rewriting of eq. (1.2.13) while c) and d) make sure that the limiting cases of collinearity of the parton pair  $(i, j)$  and of soft parton  $i$  are unaffected by the phase-space splitting function  $\mathcal{S}$ . The power of the FKS formalism lies in its ability to handle soft divergences through the definition of phase-space regions solely based on the identification of the collinear divergences. This makes the FKS method very effective at limiting the total number of counterterms, which scales at most as  $n^2$ , with  $n$  the number of strongly-interacting particles that enter the process. Furthermore, the method renders it particularly easy to further reduce the subtractions to perform by efficiently exploiting the symmetries of the matrix elements in the case of identical final-state particles:

$$\mathcal{O}(d\sigma_{ij}^{(R)}) = \mathcal{O}(d\sigma_{kl}^{(R)}) \quad \text{if } \mathcal{I}(i) = \mathcal{I}(k) \text{ and } \mathcal{I}(j) = \mathcal{I}(l) \quad (1.2.15)$$

where  $\mathcal{O}$  is any observable and the operator  $\mathcal{I}(x)$  is the identity (flavored quark or gluon) of parton  $x$ . This means for example that  $n$ -gluon processes have exactly three subtraction terms, independently of  $n$ .

In the FKS formalism one introduces three arbitrary parameters<sup>11</sup> that control the subtractions, and of which any physical observable is independent by construction. While

<sup>11</sup> $\xi_{cut}$ ,  $\delta_I$ , and  $\delta_O$ , the analogue of  $\xi$  in the toy model, for soft, initial-state collinear, and final-state collinear singularities respectively

the explicit numerical verification of this property is not necessary (contrary to the case of the slicing method), it still provides a powerful check of the implementation of the subtraction method.

To compute the quantity  $\langle \mathcal{O} \rangle_{subtr}$  of eq. (1.2.9), traditional LO Monte-Carlo approaches can be employed as such for the Born contribution  $B\mathcal{O}(0)$  as well as for the virtual plus integrated counterterm  $\alpha\mathcal{O}(0)(B \log(\xi) + V)$ . The numerical integration of the last term, performed independently of the others, is a bit different and can be superficially described by the following recipe:

1. Pick at random  $0 \leq x \leq 1$ . This correspond to a given real emission configuration.
2. Compute  $w_{EV} = \alpha \frac{R(x)}{x}$ , the *event weight*.
3. Compute  $w_{CT} = -\alpha \frac{B}{x}$ , the *counter-event weight*.
4. Fill the histograms of the analysis by adding the event weight  $w_{EV}$  to the bin specified by the observable evaluated at the *real-emission* kinematic,  $\mathcal{O}(x)$ . The counter-event weight  $w_{CT}$  is added to the bin corresponding to the *Born* kinematic, given by  $\mathcal{O}(0)$ .
5. Iterate  $N$  times steps 1 to 4, with  $N$  depending on the accuracy sought for and normalize by  $1/N$ .

The details of the real-emission kinematic configuration (schematically embodied by  $x$  in the above) as well as the associated weight  $w_{EV}$  is referred to as an *event* because it is at this stage independent of the definition of the observable  $\mathcal{O}$ . The name *event* comes from the analogy with a complete description of one specific outcome of a high energy particle collision.

There are additional subtleties in the context of the integration of the real-emission contribution  $d\sigma_R$  related to the fact that *two* events (one being the counter-event) are output for *one* single random pick of a real kinematic configuration. These contribute to the observable  $\mathcal{O}(k)$  evaluated at the two different kinematic configurations  $k = 0$  and  $k = x$ , possibly giving rise to the so-called *misbinning* effects. This happens when the real emission kinematic configuration is very close to the underlying Born one (i.e.  $x$  very small in the toy model) so that both  $w_{EV}$  and  $w_{CT}$  are large and almost equal up to a sign. Most of the time  $\mathcal{O}(x)$  and  $\mathcal{O}(0)$  turn out to be the same bin and the two contribution cancel each other, but occasionally they may fall in two contiguous bins and the final histogram presents a kink. The smaller the bin size, the more likely misbinning is to occur but this effect is not problematic for reasonable common binning choices. It is fundamentally related to the fact that QCD does not have infinite resolution power.

Also, the conventional *hit-or-miss* unweighting procedure fails because  $w_{EV}$  and  $w_{CT}$  are not bounded from above and diverge for  $x \rightarrow 0$  (corresponding to a soft and/or collinear emission). The matching of the FKS fixed-order predictions to parton shower

Monte-Carlo tools comes to the rescue with the introduction of yet another set of local counterterms called *MC-counterterms* which capture the  $\mathcal{O}(\alpha_s)$  contribution of the PSMC. The MC-counterterms therefore depend on the characteristics of the PSMC considered but they can be written in terms of process independent kernels so that the automation of NLO computation is preserved. Loosely speaking, the first role of the MC-counterterms is to prevent the double counting of the first real emission originating from the parton shower and from the matrix element. Secondly, they insure that the one-loop contribution does not account for what is already covered by the parton shower via the Sudakov definition. Thanks to these properties, the MC-counterterms weights  $w_{MC}$  damp the growth of  $w_{EV}$  and  $w_{CT}$  when approaching the diverging regions, hence rendering the unweighting procedure meaningful. Even then, it is clear that since  $w_{EV} - w_{MC}$  or  $w_{MC} - w_{CT}$  can turn negative, it is possible that a fraction of the unweighted events has a negative unit weight. This poses no problem since one is guaranteed never to have negative differential cross-sections, provided that large enough statistics is considered. Also, the unweighted parton level events are not physical until they are processed by the PSMC which restores what is taken out by the MC-counterterms.

In light of the above, it is clear why MADFKS provides two running modes:

- *Fixed order analysis* — This running mode corresponds to the kind of analysis performed by MCFM for example, and inherits its name from the fact that no PSMC is considered. No unweighting procedure is carried out and the analysis is performed on-the-fly since writing out the weighted events to the disk is memory consuming and rather inconvenient<sup>12</sup>. This is the analysis mode of choice for computing inclusive cross-sections (and the related K-factor) or for performing shower-independent studies.
- *Event generation* — MADFKS needs the PSMC-specific MC-counterterms to function as an unweighted event generator. The user is compelled to pass the generated events to the chosen PSMC and to perform the analysis at the hadronic level only. Except for this, the unweighted events generated can be used exactly as for a LO run<sup>13</sup> after the parton shower. In particular, the rest of the detector simulation and analysis goes through unchanged.

The above shows how fixed order analysis and event generation runs complement each other. In the public code AMC@NLO5, both are available; see sect. 3.4.1 for more details.

---

<sup>12</sup>Depending on the needs, this is however a possibility which has been exploited by other groups, such as the BLACKHAT collaboration.

<sup>13</sup>The presence of events with negative unit weights is never an issue (except maybe technical).



## 2 Loop computation techniques

Before proceeding, it is worth stressing that the very idea of automating virtual corrections would have been unthinkable without the introduction of procedures for the computations of loop tensor integrals that are alternative to the traditional ones based on analytic techniques. Although the latter, by a clever use of tensor-reduction methods [141, 70, 35], have helped obtain remarkable results (see e.g. refs. [79, 74] for some recent ones), they do not constitute an effective starting point for automation, the main drawbacks being the need of heavy symbolic manipulations, and that of special treatments of unstable decompositions (in particular, the analytic approach obliges one to guess *a priori* where numerical instabilities could occur, before taking actions such as Taylor-expanding small Gram determinants). With some degree of arbitrariness, one can classify the modern procedures for loop evaluations into two classes, that we call Generalized Unitarity (GU) [25, 91, 92] and Integrand Reduction (IR) [137, 68, 131]. Both have obtained very significant results: so far, GU- and IR-based efforts have focused primarily on studies of large-multiplicity final states [106, 22] and of massive final states [29, 31] respectively. As shown in sect. 2.3, Integrand Reduction is a procedure independent of the identities of the particles entering in the process (i.e. if they are fermions or bosons, or if they are massless or massive). It is thus perfectly suited to our goal of performing computations in the most flexible way, which is the reason why it has first been adopted in MADLOOP.

### 2.1 Notation

I shall first describe here the framework embedding the different loop reduction approaches and setup the notation. Let us consider a UV-unrenormalized,  $n$ -point one-loop amplitude  $\mathcal{A}_U^{(n,1)}$ . We have:

$$\mathcal{A}_U^{(n,1)} = \sum_{\alpha} \mathcal{C}_{\alpha}, \quad (2.1.1)$$

where the sum runs over all Feynman diagrams relevant to  $\mathcal{A}_U^{(n,1)}$ , and  $\mathcal{C}_{\alpha}$  is the contribution of a given Feynman diagram after loop integration. The loop evaluation procedure can be viewed as a linear operator, and therefore in what follows we shall consider only a given  $\mathcal{C}_{\alpha}$  – hence, the index  $\alpha$  will be dropped in order to simplify the notation. The quantity  $\mathcal{C}$  is in general a tensor in the Lorentz and color spaces formed by the group indices carried by the external legs. What follows is however independent of these dependences of  $\mathcal{C}$ ,

## Chapter 2. Loop computation techniques

which will therefore be understood and omitted; this is equivalent to fixing the external Lorentz and color indices in  $\mathcal{C}$ , and manipulate the resulting scalar quantity. It simplifies the present discussion to consider all external momenta as outgoing:

$$0 = k_1 + k_2 + \cdots k_n. \quad (2.1.2)$$

We consider a diagram with  $m$  propagators in the loop; the value of  $m$  does not need to be specified here, and it suffices to say that it satisfies the constraint  $1 \leq m \leq n$ . It is not restrictive to assume that the external momenta are in the same order as in fig. 2.1.1 (since such a configuration can always be obtained through a relabeling). We denote the loop momentum in  $d = 4 - 2\epsilon$  dimensions by  $\bar{\ell}$ , and decompose it into the sum of a 4-dimensional and of a  $(-2\epsilon)$ -dimensional components, which we denote by  $\ell$  and  $\tilde{\ell}$  respectively. Hence:

$$\bar{\ell} = \ell + \tilde{\ell} \quad \text{with} \quad \ell \cdot \tilde{\ell} = 0. \quad (2.1.3)$$

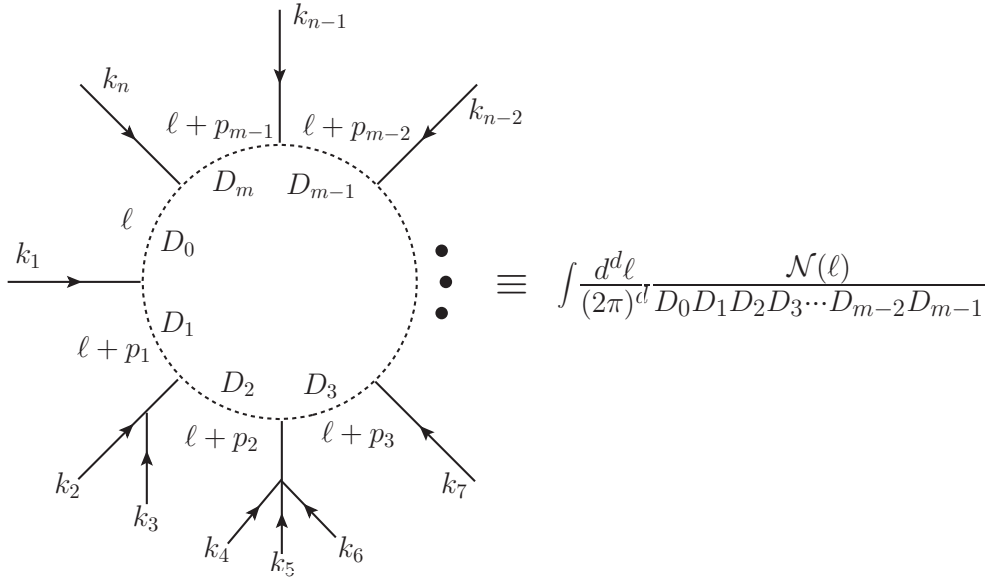


Figure 2.1.1: A generic  $m$ -point loop diagram, with  $n$  external momenta  $k_i$ . The internal momenta are denoted  $p_i = \sum_{j=1}^{M_i} k_j$ , the denominators  $D_i = (\ell - p_i)^2 - m_i^2$  and the regularized dimension  $d = 4 - 2\epsilon$ . The numerator  $\mathcal{N}(\ell)$  depends on the spin of the loop particles as well as the vertices structures. It is worth noting that in Feynman gauge,  $\mathcal{N}(\ell)$  is a polynomial in  $\ell^\mu$ .

We introduce the partial sums that enter the propagators that form the loop:

$$p_i = \sum_{j=1}^{M_i} k_j, \quad 1 \leq i \leq m; \quad p_0 = p_m. \quad (2.1.4)$$

The values of the integers  $M_i$  depend on the particular diagram considered (e.g. in fig. 2.1.1



we have  $M_1 = 1$ ,  $M_2 = 3$ ,  $M_3 = 6$ ), but they must always fulfill the following conditions:

$$1 \leq M_i < M_{i+1}, \quad M_m = n \quad \implies \quad p_0 = 0, \quad (2.1.5)$$

where the last equality follows from eq. (2.1.2).

The denominators of the loop propagators in  $d$  and four dimensions is denoted by  $\bar{D}$  and  $D$  respectively. Hence:

$$\bar{D}_i = (\bar{\ell} + p_i)^2 - m_i^2 = D_i + \bar{\ell}^2 \equiv (\ell + p_i)^2 - m_i^2 + \tilde{\ell}^2, \quad 0 \leq i \leq m - 1, \quad (2.1.6)$$

which follows from eq. (2.1.3), and from the fact that the  $(-2\epsilon)$ -dimensional parts of the external four-vectors are equal to zero, since the 't Hooft-Veltman scheme is adopted. Note that  $m_i$  is the mass of the particle flowing in the  $i^{\text{th}}$  propagator, and therefore in general  $p_i^2 \neq m_i^2$ . With these definition, we can write a concise generic expression for any loop diagram as

$$\mathcal{C} = \int d^d \bar{\ell} \bar{C}(\bar{\ell}), \quad \bar{C}(\bar{\ell}) = \frac{\bar{N}(\bar{\ell})}{\prod_{i=0}^{m-1} \bar{D}_i}, \quad (2.1.7)$$

which follows from fig. 2.1.1 and eq. (2.1.6), and implicitly defines  $\bar{N}(\bar{\ell})$ . In Feynman gauge,  $\bar{N}(\bar{\ell})$  is generically a polynomial in  $\bar{\ell}$ . Moreover, for renormalizable theories, one can show that the maximal rank  $r_{max}$  of this polynomial is at most equal to twice the number of loop propagators (*i.e.* the rank of the denominator). The class of integrals with  $\bar{N}(\bar{\ell}) = 1$  is referred to as *scalar integrals* as opposed to *tensor integrals*. This abuse of language originates from the fact that any integral with  $\bar{N}(\bar{\ell})$  of rank  $r > 1$  can easily be recast in terms of integrals with  $\bar{N}(\bar{\ell}) = \prod_{i=0}^r \bar{\ell}^{\mu_i}$  which form the tensor integral basis. A trivial example of this is

$$\bar{N}(\bar{\ell}) = \frac{1}{4} \text{Tr}[\bar{\ell}(\bar{\ell} + \not{p})] = g^{\mu\nu} \bar{\ell}_\mu \bar{\ell}_\nu + p^\mu \bar{\ell}_\mu \quad (2.1.8)$$

A crucial result, originally stated in [141], is that in the limit  $d \rightarrow 4$  any one-loop integral  $\mathcal{C}$  can be expressed as a cut-constructible (CC) part, *i.e.* a linear combination of scalar boxes, triangles, bubbles, and tadpoles, plus a (non cut-constructible) remainder term  $R$ ,

called rational part:

$$\begin{aligned}
 \mathcal{C} = & \sum_{0 \leq i_0 < i_1 < i_2 < i_3}^{m-1} d(i_0 i_1 i_2 i_3) \int d^d \bar{\ell} \frac{1}{\bar{D}_{i_0} \bar{D}_{i_1} \bar{D}_{i_2} \bar{D}_{i_3}} \\
 & + \sum_{0 \leq i_0 < i_1 < i_2}^{m-1} c(i_0 i_1 i_2) \int d^d \bar{\ell} \frac{1}{\bar{D}_{i_0} \bar{D}_{i_1} \bar{D}_{i_2}} \\
 & + \sum_{0 \leq i_0 < i_1}^{m-1} b(i_0 i_1) \int d^d \bar{\ell} \frac{1}{\bar{D}_{i_0} \bar{D}_{i_1}} \\
 & + \sum_{i_0=0}^{m-1} a(i_0) \int d^d \bar{\ell} \frac{1}{\bar{D}_{i_0}} \\
 & + R.
 \end{aligned} \tag{2.1.9}$$

The essence of *most* loop evaluation techniques is that of computing  $\mathcal{C}$  by determining (in a numerical manner) the set of coefficients and the rational part

$$d(i_0 i_1 i_2 i_3), \quad c(i_0 i_1 i_2), \quad b(i_0 i_1), \quad a(i_0), \quad R, \tag{2.1.10}$$

and by using the well-known expressions for scalar loop integrals [153, 94, 154]. The same notation but with capital letters will be used for the scalar integrals corresponding to each one of these coefficients. For example,

$$C_{i_0 i_1 i_2} = \int d^d \bar{\ell} \frac{1}{\bar{D}_{i_0} \bar{D}_{i_1} \bar{D}_{i_2}} \tag{2.1.11}$$

The functional dependence of these scalar integral is unambiguously specified by the actual values  $i_j$ . For example,  $C_{269}$  is a function of  $(p_2, p_6, m_2, m_6, m_9)$ , as  $p_9$  is automatically retrieved via  $p_2$  and  $p_6$  using energy momentum conservation.

We are now equipped to proceed with the description of two of the most important loop reduction techniques.

## 2.2 The Passarino-Veltman reduction

Before digging into the details of the OPP procedure used by MADLOOP, we wish here to first present the traditional Passarino-Veltman (PV) reduction technique. This algebraic procedure for evaluating loop integrals is the grandfather of modern tensor integral reduction techniques and was first introduced in the avant-garde work of [141]. As we will see, this method lacks efficiency but provides a very direct approach giving a good understanding of the challenges of the loop reduction problem.

Rather than attempting a complete description of the method, we will illustrate it here

## 2.2. The Passarino-Veltman reduction

---

when applied to the rank-one triangle tensor integral. Also, the fact that the loop momentum lives in  $4 - 2\epsilon$  dimensions is not crucial here and we will drop the bar notation for this section. The triangle scalar integral is:

$$C^\mu(p_1, p_2, m_0, m_1, m_2) = \int d^d \ell \frac{\ell^\mu}{D_0 D_1 D_2} \quad (2.2.1)$$

Exploiting Lorentz invariance of  $C^\mu$  we can write, without loss of generality:

$$C^\mu = p_1^\mu C_1 + p_2^\mu C_2 \quad (2.2.2)$$

where  $C_1$  and  $C_2$  are *form factors* to be computed. The existence of such Lorentz decomposition for any tensor integral is at the origin of the universal expression of eq. (2.1.9). Now contracting eq. (2.2.2) on both sides with  $p_1^\mu$  and  $p_2^\mu$ , one obtains the following set of equations for the determination of form factors.

$$\begin{aligned} \int d^d \ell \frac{\ell \cdot p_1}{D_0 D_1 D_2} &= p_1^2 C_1 + p_1 \cdot p_2 C_2 \\ \int d^d \ell \frac{\ell \cdot p_2}{D_0 D_1 D_2} &= p_2 \cdot p_1 C_1 + p_2^2 C_2 \end{aligned} \quad (2.2.3)$$

It is easy to rewrite the scalar products  $\ell \cdot p_1$  and  $\ell \cdot p_2$  in terms of the denominators  $D_0, D_1$  and  $D_2$ .

$$\begin{aligned} \ell \cdot p_1 &= \frac{1}{2}(\alpha + D_1 - D_0), & \alpha &= m_1^2 - m_0^2 - p_1^2 \\ \ell \cdot p_2 &= \frac{1}{2}(\beta + D_2 - D_0), & \beta &= m_2^2 - m_0^2 - p_2^2 \end{aligned} \quad (2.2.4)$$

When inserting eq. (2.2.4) in eq. (2.2.3) and using the notation introduced in eq. (2.1.11), one arrives at the following matrix representation of the system of eq. (2.2.3).

$$\frac{1}{2} \begin{pmatrix} \alpha C_{012} + B_{02} - B_{12} \\ \beta C_{012} + B_{01} - B_{12} \end{pmatrix} = \underbrace{\begin{pmatrix} p_1^2 & p_1 \cdot p_2 \\ p_2 \cdot p_1 & p_2^2 \end{pmatrix}}_{G_2} \begin{pmatrix} C_1 \\ C_2 \end{pmatrix} \quad (2.2.5)$$

The matrix  $G_2$  is a particular realization of a more general structure called the *Gram matrix* and its inversion solves eq. (2.2.5) for  $C_1$  and  $C_2$ , yielding the expressions for the coefficients  $c(i_0 i_1 i_2)$ ,  $b(i_0 i_1)$  and  $a(i_0)$  of the decomposition of eq. (2.1.9). This procedure can be generalized for tensor integrals of arbitrarily more loop propagators and higher ranks, each time identifying the form factors of the most general Lorentz decomposition of the tensor integrals and then computing them using the set of equations built from the several Lorentz contractions of this decomposition. Notice that the PV algorithm allows one to cast a rank  $R$   $n$ -point tensor integral into a basis of  $m$ -point tensor integrals of rank  $r < R$  with  $m \leq n$ , but not directly into the scalar integral basis (2.1.9). This

reduction procedure must therefore be iterated on all the remaining tensor integrals of lower rank to eventually arrive at a decomposition involving only scalar integrals. For example, if we had started this example with a rank-two tensor triangle, the Lorentz decomposition of eq. (2.2.2) would read

$$C^{\mu\nu} = g^{\mu\nu} C_{00} + \sum_{i,j=1}^2 p_i^\mu p_j^\nu \quad (2.2.6)$$

and the expression of the form factors  $C_{ij}$  would involve rank-one tensor triangles and bubbles which must be further reduced.

Notice that when starting with a  $n$ -point tensor integral with  $n > 4$ , the decomposition obtained will also include scalar integrals larger than boxes that the PV algorithm can in principle not reduce further. However, owing to the dimensionality of space-time and the use of the 't Hooft-Veltman scheme which keeps the external momenta in four dimensions, any  $n$ -point scalar integral with  $n > 4$  can be rewritten as a sum of boxes, as shown in [26]. This is a key result for the existence of the finite basis of eq. (2.1.9).

There are essentially three reasons why this algorithm is not suited for numerical automation of one-loop computations.

Firstly, inversions of Gram matrices such as  $G_2$  in our example arise at each step of the reduction. Its determinant, the *Gram determinant*, can vanish for specific kinematical configurations, referred to as *exceptional* phase-space points, rendering the algorithm numerically unstable. In the example above,  $\det[G_2] = p_1^2 p_2^2 - (p_1 \cdot p_2)^2$  vanishes for  $p_1 \parallel p_2$ . Such singularities are artificial in the sense that the original loop integral exhibits a smooth behavior around these points and they are introduced by the reduction mechanism which picks specific arbitrary reference vectors for the Lorentz contractions (like in eq. (2.2.3)). Secondly, the iterative nature of the PV reduction ineluctably yields a rapid growth of the number of terms generated, eventually spoiling its efficiency for tensor integrals of larger rank and number of external particles. Thirdly, the method necessitates extensive analytical information about the loop integrand which is not readily available in purely numerical methods.

The first two points are addressed by modern tensor integral techniques [98, 37, 113, 70] in various ways and they can now be considered solved for loops of small enough<sup>1</sup> ranks (i.e. typically  $\leq 6$ ). An original (partial) solution to the last issue was recently found as a by-product of the development of the *open-loop* technique which will be discussed in sect. 3.4.3.

---

<sup>1</sup>We are considering here the isolated problem of the reduction of a given loop Feynman diagram, within a purely diagrammatical approach. The possibility of increasing the efficiency of tensor integral reduction exploiting a recursive approach is not discussed.

## 2.3 The Ossola-Papadopolous-Pittau reduction

We are now ready for describing the OPP method which belongs to the more modern class of reduction mechanisms at the integrand level and was first proposed in [137].

The key point of the OPP method is the fact that the determination of the quantities in eq. (2.1.10) is achieved by working at the *integrand level*. We start by decomposing the numerator  $\bar{N}$  of eq. (2.1.7) into the sum of a term sourced by only the four-dimensional part of the phase-space and an extra piece. Notice that by definition this extra piece contains all the dependence on  $\tilde{\ell}$  and on  $\epsilon$ ; also there is no dependence on the  $(-2\epsilon)$ -dimensional parts of the external four-vectors  $k_i$  in the 't Hooft-Veltman scheme (and the dependance on the 4-dimensional part is left implicit):

$$\bar{N}(\bar{\ell}) = N(\ell) + \tilde{N}(\ell, \tilde{\ell}^2, \epsilon). \quad (2.3.1)$$

This decomposition is not straightforward, because  $\bar{N}(\bar{\ell})$  is a scalar quantity and the *tilde* notation does not refer to the projection of  $\bar{N}(\bar{\ell})$  onto any kind of subspace but really characterizes its functional dependences. More formally, it corresponds to splitting the Lorentz objects of the numerator function into a four-dimensional component and an extra term originating from the  $(-2\epsilon)$  part of the integration dimension.

$$\begin{aligned} \bar{\ell} &= \ell + \tilde{\ell} \\ \bar{\gamma}_\mu &= \gamma_\mu + \tilde{\gamma}_\mu \\ \bar{g}_{\mu\nu} &= g_{\mu\nu} + \tilde{g}_{\mu\nu} \end{aligned} \quad (2.3.2)$$

To illustrate this, we can work it out for the simple numerator below

$$\bar{N}(\bar{\ell}) = Tr(\bar{\gamma}^\alpha \bar{\ell} \bar{\gamma}_\alpha \bar{\ell}) = \underbrace{-8\ell^2}_{N(\ell)} + \underbrace{8(\epsilon - 1)\tilde{\ell}^2 + 8\epsilon\ell^2}_{\tilde{N}(\ell, \tilde{\ell}, \epsilon)} \quad (2.3.3)$$

And the term  $8(\epsilon\ell^2 - \tilde{\ell}^2)$  in  $\tilde{N}(\ell, \tilde{\ell}, \epsilon)$ , once integrated with the two denominators of a bubble loop diagram, will yield a finite contribution because of the  $1/\epsilon$  UV pole. This rational contribution is called  $R_2$  and the OPP procedure cannot compute it because only numerical evaluations of  $N(\ell)$  only are provided in input. Fortunately, the UV nature of the rational terms guarantees that only loops up to boxes can have an  $R_2$  contribution (see ref. [36] for a formal proof). This crucial point implies that  $R_2$  contributions can be reconstructed via tree-level computations involving a *finite* set of dedicated counterterm vertices whose relatively simple Feynman rules can be computed once and for all for any given renormalizable theory. In the perspective of the OPP algorithm, the problem of computing the  $R_2$  contribution is then considered solved.

Now, when inserting the decomposition of eq. (2.3.1) in the integrand definition of

## Chapter 2. Loop computation techniques

---

eq. (2.1.7), one obtains

$$\bar{C}(\bar{\ell}) = \frac{N(\ell)}{\prod_{i=0}^{m-1} \bar{D}_i} + \frac{\tilde{N}(\ell, \bar{\ell}^2, \epsilon)}{\prod_{i=0}^{m-1} \bar{D}_i}, \quad (2.3.4)$$

The two contributions above are treated rather differently and are defined as separate quantities

$$\mathcal{C} = \mathcal{C}_{cc+R_1} + R_2, \quad (2.3.5)$$

$$\mathcal{C}_{cc+R_1} = \int d^d \bar{\ell} \frac{N(\ell)}{\prod_{i=0}^{m-1} \bar{D}_i}, \quad (2.3.6)$$

$$R_2 = \int d^d \bar{\ell} \frac{\tilde{N}(\ell, \bar{\ell}^2, \epsilon)}{\prod_{i=0}^{m-1} \bar{D}_i}. \quad (2.3.7)$$

Here,  $R_2$  contributes only to the rational part  $R$ , while  $\mathcal{C}_{cc+R_1}$  is the sum of a cut-constructible and of a rational term (called  $R_1$ ); we discuss how to disentangle the latter two in what follows. One starts by showing [137] that the numerator function  $N(\ell)$  can always be cast in the following form:

$$\begin{aligned} N(\ell) &= \sum_{0 \leq i_0 < i_1 < i_2 < i_3}^{m-1} \left[ d(i_0 i_1 i_2 i_3) + \hat{d}(\ell; i_0 i_1 i_2 i_3) \right] \prod_{\substack{i=0 \\ i \notin \{i_0, i_1, i_2, i_3\}}}^{m-1} D_i \\ &+ \sum_{0 \leq i_0 < i_1 < i_2}^{m-1} \left[ c(i_0 i_1 i_2) + \hat{c}(\ell; i_0 i_1 i_2) \right] \prod_{\substack{i=0 \\ i \notin \{i_0, i_1, i_2\}}}^{m-1} D_i \\ &+ \sum_{0 \leq i_0 < i_1}^{m-1} \left[ b(i_0 i_1) + \hat{b}(\ell; i_0 i_1) \right] \prod_{\substack{i=0 \\ i \notin \{i_0, i_1\}}}^{m-1} D_i \\ &+ \sum_{0 \leq i_0}^{m-1} \left[ a(i_0) + \hat{a}(\ell; i_0) \right] \prod_{\substack{i=0 \\ i \neq i_0}}^{m-1} D_i \\ &+ \hat{P}(\ell) \prod_{i=0}^{m-1} D_i, \end{aligned} \quad (2.3.8)$$

where the terms proportional to  $\hat{d}$ ,  $\hat{c}$ ,  $\hat{b}$ ,  $\hat{a}$  and  $\hat{P}$  (called spurious terms) vanish upon integration. By exploiting the fact that  $D_i = \bar{D}_i - \bar{\ell}^2$  (see eq. (2.1.6)) in eq. (2.3.8), one obtains the identity:

$$N(\ell) = N_{cc}(\ell, \bar{\ell}^2) + N_{R_1}(\ell, \bar{\ell}^2), \quad (2.3.9)$$

### 2.3. The Ossola-Papadopolous-Pittau reduction

where we have defined

$$N_{cc}(\ell, \tilde{\ell}^2) = N(\ell) \Big|_{D_i \rightarrow \bar{D}_i}. \quad (2.3.10)$$

As the notation suggests,  $N_{cc}$  is identical to eq. (2.3.8), except for the formal replacements of all  $D_i$ 's with the corresponding  $\bar{D}_i$ 's (i.e., the four-dimensional denominators by their  $d$ -dimensional counterparts). Eq. (2.3.9) implicitly defines  $N_{R_1}$ . From eq. (2.1.6) we see that:

$$N_{R_1}(\ell, 0) = 0. \quad (2.3.11)$$

We can now define the cut-constructible and  $R_1$  contributions separately:

$$\mathcal{C}_{cc+R_1} = \mathcal{C}_{cc} + R_1 \quad (2.3.12)$$

$$\mathcal{C}_{cc} = \int d^d \bar{\ell} \frac{N_{cc}(\ell, \tilde{\ell}^2)}{\prod_{i=0}^{m-1} \bar{D}_i}, \quad (2.3.13)$$

$$R_1 = \int d^d \bar{\ell} \frac{N_{R_1}(\ell, \tilde{\ell}^2)}{\prod_{i=0}^{m-1} \bar{D}_i}. \quad (2.3.14)$$

The rational part  $R$  introduced in eq. (2.1.9) is the sum of  $R_1$  and  $R_2$ , defined in eqs. (2.3.14) and (2.3.7) respectively.

The key point is that the coefficients  $d$ ,  $c$ ,  $b$ , and  $a$  which appear in eq. (2.3.8) are the *same* as those which appear in eq. (2.1.9), as can be easily seen by inserting eq. (2.3.8) into eq. (2.3.10), and by using the result so obtained in eq. (2.3.13). This is ultimately the reason why the OPP procedure is carried out at the integrand level, where the loop momentum  $(\ell, \tilde{\ell})$  is just an external and fixed quantity. Thus, eq. (2.3.8) is the master equation used in the OPP method for the determination of the coefficients  $d$ ,  $c$ ,  $b$ , and  $a$ , which is achieved by solving numerically a system of linear equations. The idea is that of computing  $N(\ell)$  for suitable values of  $\ell$ , which render the just-mentioned linear system easy to solve. A pre-condition for this to happen is the fact that the spurious terms can be determined fully as functions of the external momenta; this has been proved in ref. [68, 136]. At this point, the easiest way to proceed is that of computing the cut-constructible and  $R_1$  contributions separately. One starts with the former, by setting  $\tilde{\ell}^2 = 0$  and using eq. (2.3.11). Then, one determines the two solutions<sup>2</sup>  $\ell^\pm$  to the equations:

$$D_{i_0}(\ell^\pm) = D_{i_1}(\ell^\pm) = D_{i_2}(\ell^\pm) = D_{i_3}(\ell^\pm) = 0, \quad (2.3.15)$$

---

<sup>2</sup>There are two (complex) momenta owing to the quadratic nature of the propagators.

## Chapter 2. Loop computation techniques

---

for given  $i_0, i_1, i_2$  and  $i_3$ . Eq. (2.3.8) then becomes

$$N(\ell^\pm) = \left[ d(i_0 i_1 i_2 i_3) + \hat{d}(\ell^\pm; i_0 i_1 i_2 i_3) \right] \prod_{\substack{i=0 \\ i \notin \{i_0, i_1, i_2, i_3\}}}^{m-1} D_i(\ell^\pm), \quad (2.3.16)$$

and using the explicit expression of  $\hat{d}$ , one can prove [137] that the coefficients of the box diagrams are simply given by

$$d(i_0 i_1 i_2 i_3) = \frac{1}{2} \left[ \frac{N(\ell^+)}{\prod_{i \neq i_0, i_1, i_2, i_3} D_i(\ell^+)} + \frac{N(\ell^-)}{\prod_{i \neq i_0, i_1, i_2, i_3} D_i(\ell^-)} \right]. \quad (2.3.17)$$

We point out that eq. (2.3.15) is nothing but the application of quadruple unitarity cuts. Once the solutions for the  $d$  coefficients are known thanks to eq. (2.3.17), the corresponding terms in eq. (2.3.8) are moved to the l.h.s. there. The procedure is then iterated by considering triple, double, and single unitarity cuts in succession, i.e. values of  $\ell$  such that three, two, and one denominators vanish respectively. In exactly the same way one deals with the computation of  $R_1$  [140]. The only difference w.r.t. the case of the cut-constructible part is that the basis of the scalar loop integrals used in the two cases is not the same (with that relevant to  $R_1$  being almost trivial). Alternative methods for the derivation of  $R_1$  are presented in [140].

The procedure described above is implemented in the computer program `CUTTOOLS` [138] which, being given in input the *function*  $N(\ell)$ , the momenta defined in the partial sums of eq. (2.1.4) and the masses  $m_i$  of the corresponding propagators, returns the numerical values of the cut-constructible part and of  $R_1$ . Note that by giving to `CUTTOOLS` the momenta and the masses entering the loop propagators, rather than the numerical values of the propagators themselves, one is allowed to bypass the problem of introducing  $d$ -dimensional quantities in `MADLOOP` – these are completely dealt with internally by `CUTTOOLS`. As far as  $R_2$  is concerned, this quantity is not returned by `CUTTOOLS`. As already mentioned, its computation can be performed by considering tree-level Feynman diagrams which get contributions both from the usual rules of the theory under consideration, and from special  $R_2$  vertices with up to four external lines (in any renormalizable theory), as we discuss in sect. 3.1.2. The Feynman rules of these vertices can be worked out once and for all from the Lagrangian of the theory (see ref. [87, 88] for the resulting expressions in the Standard Model). Both the use of `CUTTOOLS` and the calculation of the  $R_2$  contribution for a given one-loop amplitude are controlled by `MADLOOP`, in a way which is presented in chapter 3.



# 3 MadLoop

In this section, we describe the techniques employed in order to obtain the one-loop contributions to any generic process. As discussed in the introduction, the automation of the computation of one-loop amplitudes has been achieved by means of a computer program called MADLOOP, written entirely by the author of the present thesis and constituting the core of the work presented. The reduction procedure followed by MADLOOP is the Ossola-Papadopolous-Pittau (OPP) technique described in sect. 2.3. We devote the next section to summarizing MADLOOP workflow in more details.

## 3.1 Organization of the calculation

The input of MADLOOP is a  $2 \rightarrow n$  Standard Model partonic process<sup>1</sup>

$$r = (\mathcal{I}_1, \mathcal{I}_2, \mathcal{I}_3, \dots, \mathcal{I}_{n+2}) , \quad (3.1.1)$$

which can be either user-defined, or generated by a third-party code such as MADFKS; examples of the two uses are given in appendix B and in sect. 3.3 respectively. The main output of MADLOOP is the finite part<sup>2</sup> of the quantity:

$$V(r) = \overline{\sum_{\substack{\text{colour} \\ \text{spin}}} 2\Re \left\{ \mathcal{A}^{(n,0)}(r) \mathcal{A}^{(n,1)}(r)^* \right\}} , \quad (3.1.2)$$

with  $\mathcal{A}^{(n,0)}$  and  $\mathcal{A}^{(n,1)}$  being the tree-level and one-loop amplitudes of the process  $r$ , after the latter has been UV-renormalized. Note that  $\mathcal{A}^{(n,1)}$  is the same quantity as that in eq. (2.1.1), except for the fact that in this section the amplitude is UV-renormalized, and that  $n$  denotes here the number of particles in the final states only. The bar over the sum symbol on the r.h.s of eq. (3.1.2) understands the averaging factors relevant to the color and spin degrees of freedom of initial-state particles. The finite part of  $V$  is convention dependent and, unless otherwise specified, MADLOOP works in the 't Hooft Veltman (HV) scheme where the particle fields belonging to the loop are treated in D-dimension (unlike Dimensional Reduction (DR)) and the other fields are 4-dimensional (unlike Conventional

---

<sup>1</sup>Here and in what follows, we adopt the notation of ref. [105]:  $\mathcal{I}_i$  denotes the identity of the  $i^{\text{th}}$  particle that enters the process. Furthermore, the momenta of the first two particles in eq. (3.1.1) are incoming, and all the others are outgoing.

<sup>2</sup>Up to a standard pre-factor, see eq. (B.0.1).

Dimensional Regularization (CDR)). See appendix B and ref [149] for further discussion on scheme choices.

As a byproduct, MADLOOP also returns the residues of the double and single infrared poles. The complete information on  $\mathcal{A}^{(n,1)}$  is available internally in MADLOOP and may be given as an additional output if so desired – this is useful e.g. for computing the LO cross section of a loop-induced process, which is proportional to  $|\mathcal{A}^{(n,1)}|^2$  (see app. B.2.7 for an example of such a case).

Schematically, for a given input process  $r$ , MADLOOP goes through the following steps.

1. Generates the diagrams relevant to  $\mathcal{A}^{(n,1)}(r)$ . There are two classes of them, one for the cut-constructible plus  $R_1$  contribution, and one for the  $R_2$  contribution and UV renormalization.
2. Constructs the two integrands associated with the diagrams determined in item 1. The one relevant to the cut-constructible plus  $R_1$  contribution is the linear combination of eq. (2.1.1) at the integrand level, whose components are in the form of the term  $N(\ell)$  as defined <sup>3</sup> in eq. (2.3.1).
3. For a given kinematic configuration (user-defined or generated by MADFKS), applies the OPP reduction to each of the terms, or group of terms<sup>4</sup>, of the linear combination determined in item 2. This is achieved by passing to CUTTOOLS the function  $N(\ell)$  and any other inputs it needs (see sect. 2.3). After summing over all diagrams and helicities, one thus obtains the cut-constructible plus  $R_1$  contribution  $\mathcal{C}_{cc+R_1}$ .
4. For the same kinematic configuration as in item 3, computes the rational part  $R_2$  (which is not returned by CUTTOOLS), and includes UV renormalization counterterms if necessary. These calculations are also carried out at fixed helicities, which are summed over as the final step. Notice that this step is computationally marginally time-consuming compared to step 3.
5. Performs sanity checks.

Items 1 and 2 are referred to as the *process generation* stage and only involve symbolic manipulations. They construct the computer code for the function  $N(\ell)$  whose numerical evaluations will be performed in items 3–5. In the case of the computation of a physical

---

<sup>3</sup>This, in particular, means that the loop momentum is 4-dimensional and therefore suited for a numerical evaluation by MADLOOP. Also, the the denominators  $\bar{D}_i$  of the the loop propagators are not included as they are constructed directly within CUTTOOLS, so as to properly account for their  $(-2\epsilon)$ -dimensional component sourcing the  $R_1$  contribution.

<sup>4</sup>As it will be discussed in 3.4, one major optimization brought in the version 5 of MADLOOP is to group together integrand contributions (corresponding to possibly different diagrams and helicity configurations) sharing the same loop denominators structure and apply the OPP reduction on it only once.

cross section (when MADLOOP is called by MADFKS or by an analogous event generator), steps 3 to 5 are iterated, with each iteration using a different kinematic configuration. The efficiency of the method at run-time is dictated by how long takes the code to perform these three steps once, i.e. per phase-space point.

The original private version of MADLOOP (and of MADFKS [105]) was based on MADGRAPH v4 [152]. This implied a few limitations on the possible structure and use of this code that we dub MADLOOP4 [123]. Most of the physics results (including table 3.2 and the process of sect. 4.1) presented in this thesis have been obtained with this older version.

The newer version of MADGRAPH (v5 [7]) is mature, and our whole NLO computational framework has now been ported on it. In particular, MADLOOP was completely rewritten in PYTHON and is now embedded within MADGRAPH5. The resulting program MADLOOP5 is now publicly distributed at *amcatnlo.cern.ch* as part of MADGRAPH5 v2.0, and sect. 3.4 presents its specific features making it more flexible, faster and more user-friendly. As for MADFKS, the core FORTRAN files implementing the various counterterms and the Monte-Carlo integration are recycled from the original version<sup>5</sup>, but the generation of the real-emission trees as well as the event-generation is now steered by MADGRAPH5.

A brief description of the least trivial aspects (common to both MADLOOP4 and MADLOOP5) of the procedure 1–5 is given in sect. 3.1.1 and 3.1.2, while sect. 3.1.3 summarizes the various techniques specifically developed for MADLOOP. Some further details can be found in appendix A. For a discussion on the checks performed by MADLOOP, of which those of item 5 above are only a part, see sect. 3.1.4.

#### 3.1.1 Generation of one-loop amplitudes from tree amplitudes

Given the fact that MADLOOP is based on the MADGRAPH framework, it is clear that the most economic way of generating one-loop amplitudes is that of exploiting as much as possible the capabilities of the latter code. These are however limited to constructing tree-level quantities, and therefore MADLOOP must be able to perform some non-trivial operations on top on those available with MADGRAPH in order for us to achieve our goal. We start by observing that any one-loop diagram can be turned into a tree-level diagram by simply cutting *one* (and only one) of the propagators entering the loop. It must be clear that this cut has nothing to do with the cuts performed when computing one-loop integrals with unitarity methods. Thus, in order to avoid any confusion, we shall call L-cut this specific type of cut. The tree-level diagram obtained by L-cutting a one-loop diagram will be called an L-cut diagram. In such a diagram, there will be two particles (that we consider as being in the final state by definition) which arise from L-cutting the chosen propagator in the loop: their identities will be denoted by  $q^*$  and  $\bar{q}^*$ , and they will

---

<sup>5</sup>Not exactly, as some optimizations have been brought in the process. This is however not the focus of this thesis.

be called L-cut particles. If we consider one-loop corrections to the process  $r$  as defined in eq. (3.1.1), the L-cut diagrams we obtain with the L-cut operation will be a *subset* of those relevant to the process:

$$r_{L-cut} = (\mathcal{I}_1, \mathcal{I}_2, q^*, \bar{q}^*, \mathcal{I}_3, \dots, \mathcal{I}_{n+2}) . \quad (3.1.3)$$

This discussion suggests to define a procedure which is the inverse of L-cutting. Namely, for a given  $2 \rightarrow n$  process such as that in eq. (3.1.1), we consider all possible L-cut processes of the kind of that in eq. (3.1.3), use MADGRAPH to construct the corresponding amplitudes, and sew together the two L-cut particles. In this way, we achieve the construction of one-loop diagrams without actually having to start from one-loop topologies, contrary to what is done by FeynArts [117] for example. This idea is also at the basis of the one-loop computations performed by HELAC-1Loop (see ref. [155]).

This construction of one-loop amplitudes by sewing tree-level ones poses several problems. Firstly, we have to define a minimal set of L-cut processes so as not to miss any contributions to the one-loop amplitude we are seeking to construct. Secondly, for a given L-cut process, when sewing together the L-cut particles we shall obtain one-loop diagrams with an incorrect multiplicity: one particular diagram may appear more times than prescribed by perturbation theory. We have therefore to discard the one-loop diagrams in excess after sewing. We call this operation *diagram filtering*. Finally, after filtering, the amplitudes for the L-cut diagrams we are left with are constructed. However, these amplitudes will not coincide with the corresponding one-loop amplitudes, because of the special roles played by the L-cut particles. These are associated with external wave functions in L-cut diagrams, and with an internal propagator in one-loop diagrams (therefore, technically the sewing operation corresponds to removing the wave functions of the L-cut particles, and to replacing them with a suitable propagator). MADGRAPH must therefore be instructed to treat L-cut particles in a special way – this includes the fact that such particles are off-shell and carry complex momenta.

It is easy to convince oneself that when computing QCD corrections, the L-cut processes one needs to consider correspond to the following choices of the L-cut particles:

$$\begin{aligned} (q^*, \bar{q}^*) &= (g, g) && \text{gluons ,} \\ &= (u, \bar{u}); (d, \bar{d}); \dots (Q, \bar{Q}) && \text{quarks ,} \\ &= (\eta, \bar{\eta}) && \text{ghosts .} \end{aligned} \quad (3.1.4)$$

Here,  $Q$  denotes the heaviest flavor one wants to have circulating in the loop (in physical applications,  $Q$  is typically either a bottom or a top quark). In general, one needs to consider as L-cut particles all particles which can possibly run in the loop according to the type of loop corrections specified by the user in the process.

Diagram filtering is performed in the following way. We start by observing that any

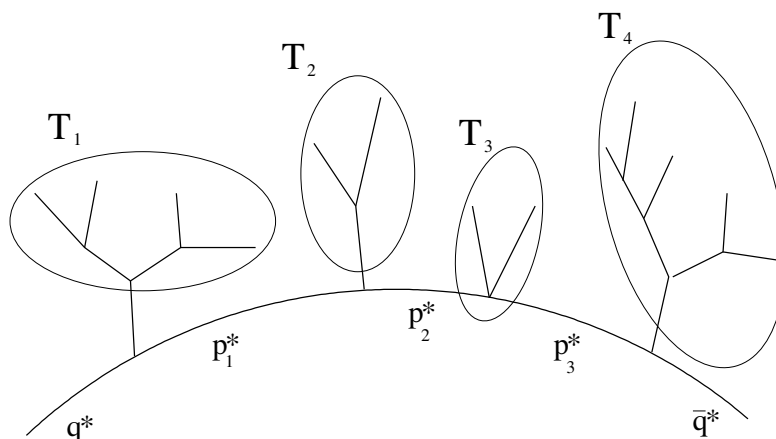


Figure 3.1.1: Example of an L-cut diagram that corresponds to a box one-loop diagram.

L-cut diagram can be depicted as in fig. 3.1.1. There,  $T_i$  denotes a tree-level structure<sup>6</sup>. The particles whose propagators enter in the loop have been denoted by  $p_j^*$ , to make the distinction clear from those that contribute to the tree-level structures  $T_i$ ; the notation is also consistent with that used for the L-cut particles. MADLOOP first records the necessary information on  $T_i$  and  $p_j^*$  (such as particle identities and four momenta); this is done for each L-cut diagram. In this way, each diagram has an unambiguous representation (its “identity”), internal to MADLOOP, that we can for example identify with the string

$$q^* T_1 p_1^* T_2 p_2^* T_3 p_3^* T_4 q^* \quad (3.1.5)$$

for the case of fig. 3.1.1.

At the end of the day, MADLOOP will loop over all L-cut diagrams, checking their identities. If a diagram identity has not been previously found, the diagram is kept, otherwise it is discarded (i.e., it is filtered out). It must be stressed that two diagram identities must be considered equivalent if they are identical up to a cyclic permutation, or to mirror symmetry, or to a cyclic permutation plus mirror symmetry. This is because two L-cut diagrams that differ by a cyclic permutation correspond to the same one-loop diagram which was L-cut in two different propagators (see appendix A.6 for more details). For example, a cyclic permutation equivalent to the identity of eq. (3.1.5) would read:

$$p_1^* T_2 p_2^* T_3 p_3^* T_4 q^* T_1 p_1^* . \quad (3.1.6)$$

Likewise, two L-cut diagrams that differ by mirror symmetry correspond to the same one-loop diagram with the loop momentum flowing in opposite direction. The identity of the L-cut diagram obtained by mirror symmetry acting on eq. (3.1.5) reads:

$$q^* T_4 p_3^* T_3 p_2^* T_2 p_1^* T_1 q^* . \quad (3.1.7)$$

<sup>6</sup>Note that for an  $n$ -point one-loop amplitude,  $1 \leq \#\{T_i\} \leq n$ , with  $\#\{T_i\}$  the number of  $T_i$ 's.

Equivalence under cyclic permutations and mirror symmetry can be used by MADLOOP as a powerful self-consistency check – see sect. 3.1.4.

As we shall explain in appendix A.6, when writing diagram identities MADLOOP4 decides not to distinguish between fermions and antifermions for the particles circulating in the loop, and hence no overlines appear in eq. (3.1.5) or its analogues (despite the fact that one of the two L-cut particles has been correctly denoted by  $\bar{q}^*$  on the l.h.s. of eq. (3.1.4)). This behavior does not spoil any result in the SM provided that, in such a case, mirror symmetry is not considered when loops contain only fermions or only ghosts so that only equivalence under cyclic permutations is checked for in these cases. In general however (for theories with multi-fermions interactions for example) it is better to have a universal filtering rule and account for the fermion flow properly, as it is done in MADLOOP5.

### 3.1.2 $R_2$ contribution and UV renormalization

As it was discussed in sect. 2.3, MADLOOP, by calling CUTTOOLS, computes the cut-constructible part of, and the  $R_1$  contribution to, the one-loop amplitude  $\mathcal{A}^{(n,1)}(r)$  that appears in eq. (3.1.2) (item 3 of the list in sect. 3.1). Therefore, in order to obtain the full  $V(r)$  quantity, we still need to include the  $R_2$  contribution, and the UV renormalization (item 4 of the list in sect. 3.1). The key observation here is that, thanks to the fact that the  $R_2$  part can be seen as arising from a set of finite counterterms, its automated computation proceeds through the same steps as UV renormalization.

In essence, both the  $R_2$  and UV-renormalization contributions to  $V(r)$  can be cast in the following form:

$$\sum_{\substack{\text{colour} \\ \text{spin}}} 2\Re \left\{ \mathcal{A}^{(n,0)}(r) \mathcal{A}^{(n,X)}(r)^* \right\}, \quad X = R_2, \text{ UV}, \quad (3.1.8)$$

that is, an interference between the Born amplitude,  $\mathcal{A}^{(n,0)}(r)$ , and another tree-level amplitude,  $\mathcal{A}^{(n,R_2)}(r)$  or  $\mathcal{A}^{(n,\text{UV})}(r)$ . The latter are the amplitudes of the  $2 \rightarrow n$  process  $r$ , constructed with the standard Feynman rules, *plus* the rules relevant to either the  $R_2$  or the UV-renormalization contributions, with the condition that the amplitude be exactly one perturbation order ( $\alpha_S$  for QCD) higher than the Born-level one. The  $R_2$  Feynman rules are obtained by explicit loop calculations, and can be cast in the form of  $n$ -point functions, with  $2 \leq n \leq 4$  (see ref. [88]). As far as UV renormalization is concerned, the additional rules are simply read off the one-loop UV counterterms of the theory considered. The consequence of these facts, together with the condition on the power of  $\alpha_S$  that must appear in the amplitudes, is that  $\mathcal{A}^{(n,R_2)}(r)$  and  $\mathcal{A}^{(n,\text{UV})}(r)$  are constructed using the standard vertices and propagators, plus *one and only one*  $R_2$  or UV-renormalization  $n$ -point function.

It is clear, therefore, that in order to compute the quantities in eq. (3.1.8) we can exploit the ability of MADGRAPH to construct tree amplitudes, and the functionalities of MADLOOP to calculate interference terms, which is already at play when computing the cut-constructible and  $R_1$  contributions to eq. (3.1.2). Note that the above procedure to compute eq. (3.1.8) should be applied to truncated one-loop amplitudes. When generating tree-level diagrams with MADGRAPH, we also get the contributions due to two-point functions on external legs, which are discarded. As is known, wave-function renormalization is commonly carried out through the multiplication of the  $Z$  factors, which is effectively done according to eqs. (A.3.4) and (A.3.5). The  $R_2$  contributions to the  $Z$  factors are already included in eqs. (A.3.4) and (A.3.5), and hence their explicit computations are not necessary in this case.

The procedure outlined above is fully general. Details about its implementation in MADLOOP4 can be found in [123]. The drawback of generating the  $R_2$  and UV counterterm amplitudes independently of the loops (i.e. by exploiting the regular tree-diagram generation algorithm with specific coupling order constraints) is that nothing insures that there is the corresponding counterterm amplitude for each of the loop considered. This becomes especially problematic when user-defined constraints are applied to the loops which must be considered (such as forbidding particles, requiring specific s-channels, etc...), because the corresponding selection must also apply to the tree-diagram generation for the  $R_2$  and UV counterterm amplitudes. MADLOOP5 therefore offers the possibility to choose to construct some or all the  $R_2$  and UV counterterm directly from the loops generated; for each loop, MADLOOP5 checks in the definitions of the counterterms if any matches the loop considered. If so, it constructs the corresponding counterterm tree-amplitude directly from the tree-structures attached to this loop. Unfortunately, the UV-counterterms are conventionally expressed in terms of the renormalization of the coupling constant,  $\delta\alpha_s$  for QCD, and not of the vertices,  $\delta V_{d\bar{d}g}$  for example. The two are related by the wavefunction renormalization constants. In our QCD example, we would have

$$\alpha_s \rightarrow \delta\alpha_s = \delta V_{d\bar{d}g}^2 Z_d^{-1} Z_{\bar{d}}^{-1} Z_g^{-1} \alpha_s \quad (3.1.9)$$

This UV-renormalization scheme has the advantage of including the wavefunction renormalization constants only on the external particles and not on the internal ones but it loses the one-to-one correspondence between a UV counterterm and a loop. This is why MADLOOP5 allows one to specify for each counterterm whether it must be accounted for via its mapping to a specific loop generated or via the traditional tree-diagram generation method used by MADLOOP4. A fully automatic approach allowing for arbitrary loop selections would necessitate to define counterterms so as to be sourced by one loop exactly. This is quite simple to obtain in view of the recent development in the automatic generation of loop model files by FEYNRULES, see sec. 3.4.2 for more details on that subject.

For QCD perturbations, the  $R_2$  counterterms considered are those listed in [88]. The UV counterterms definitions are given in sec. A.3, where their factorization of the full born cross-section is assumed. This assumption is only present in MADLOOP4 and it has been relaxed in MADLOOP5 in order to apply the UV renormalization procedure independantly for each Born amplitude. These are therefore no longer required to factorize the same coupling factors, hence opening the way to mixed coupling expansions (*e.g.* QCD and electroweak).

Finally, the counterterms feature some Lorentz structures which are not present in the original model for tree-level computations. In MADLOOP4, the new corresponding building blocks for the amplitudes computation, called HELAS routines, were hardcoded. In MADLOOP5, ALOHA [65] (already used for tree-level computations) can automatically write out these new routines on the fly from the counterterm vertices information provided in the model file. This replacement of HELAS with ALOHA removes the last model dependent ingredient of MADGRAPH code generation.

### 3.1.3 Summary of MADLOOP features

We list here the features that required substantial writing of computer code, either in MADLOOP proper, or in one of the modules that MADLOOP uses.

- The generation of loop diagrams in a way that exploits as much as possible the tree-level capabilities of MADGRAPH (through L-cut-diagram construction and subsequent filtering). Thanks to significantly greater efficiency of the tree-diagram generation algorithm of MADGRAPH5, the loop diagram generation time is much faster in MADLOOP5 than it is in MADLOOP4.
- The computation of the resulting one-loop amplitude, in a form suited to being given as input to CUTTOOLS. This implies, in particular, the removal of the denominators of the propagators of loop particles, and the reconstruction of the propagator of the sewed L-cut particles.
- The numerical code structure that allows MADGRAPH to compute the interference only of two different kinds of amplitudes (the L-cut and Born ones), including the relevant color algebra.
- The possibility of using complex four-momenta (that circulate in the loops).
- The implementation of ghosts.
- The implementation of dedicated structures for the generic  $R_2$  and UV counterterms, and the handling of the corresponding amplitudes.

The second item in particular deserves further attention and we will illustrate here the related numerical techniques of MADLOOP with this gluon bubble:



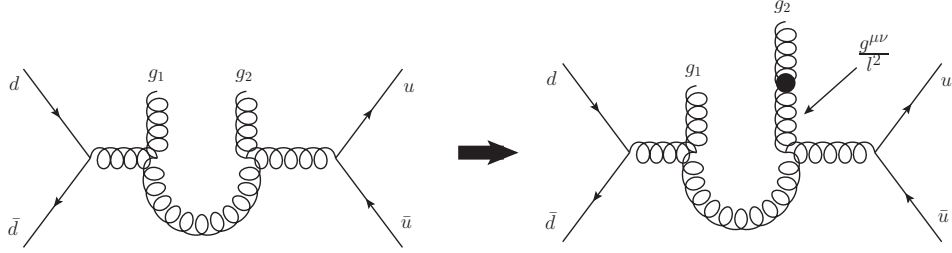


Figure 3.1.2: An example of a gluon bubble (cut at  $g_1-g_2$ ) where a gluon two-point interaction is added to restore the missing propagator of the L-cut particle.

The fig. 3.1.2 above shows how MADLOOP5 adds back the missing propagator of the L-cut particles by systematically adding a two-point vertex to one external L-cut particle. The denominators of the loop propagators are stripped off in the corresponding HELAS-like subroutines and they support complex momenta. The loop color trace simply necessitates to add the appropriate color delta to the diagram color string used for color factors computation. In this case, the color string obtained is :

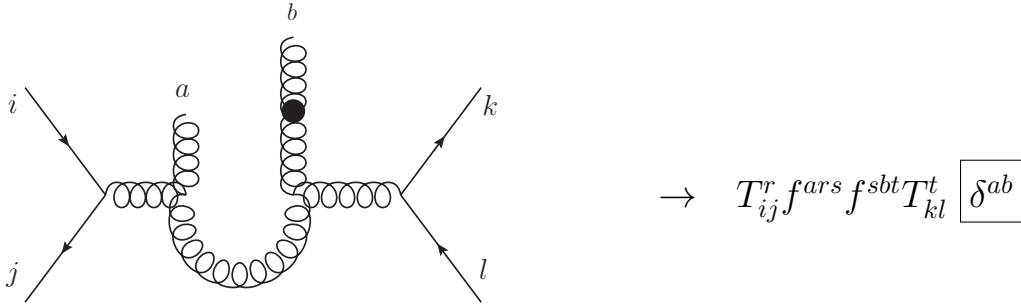


Figure 3.1.3: Closing the loop color trace of a gluon bubble (cut at  $g_1-g_2$ ) by simply adding an  $SU(3)_c$  delta in the right representation.

The additional subtlety is that the resulting color string for loop diagrams must be squared against the Born ones only, so that the color basis built for the loop diagrams is no longer identical to the one built from the Born ones. MADLOOP5 readily offers such a flexibility and no major modification was needed to achieve this. The closing of the loop Lorentz trace is more involved than the color one and involves the structure  $\delta^{xy}$  with  $x$  and  $y$  the indices belonging to the Lorentz representation of the L-cut particles<sup>7</sup>. In our example, we have

<sup>7</sup> $x=1, y=1$  for spin-0 particles,  $x=i, y=j$  for the fermionic indices of spin-1/2 particles,  $x=\mu, y=\nu$  for spin-1 particles, and finally  $x=\mu\nu, y=\rho\sigma$  for spin-2 particles.

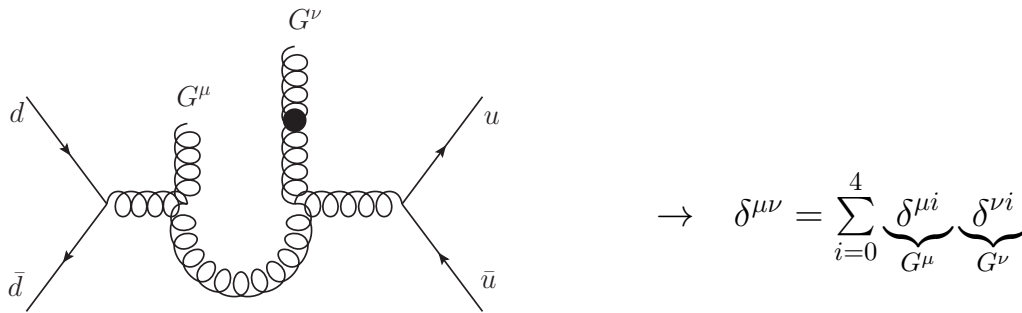


Figure 3.1.4: Closing the loop Lorentz trace of a gluon bubble (cut at  $g_1$ – $g_2$ ) by using the polarization vectors  $G^\mu$  and  $G^\nu$  of the L-cut particles to reconstruct  $\delta^{\mu\nu}$ .

The L-cut particles are not physical and their polarization vectors  $G^\mu$  and  $G^\nu$  must be chosen such that one recovers the result of the loop Lorentz trace. The relation of fig. 3.1.4 suggests to compute the L-cut tree diagram with  $G^\mu = \delta^{\mu i}$ ,  $G^\nu = \delta^{\nu i}$  for  $i = 1, \dots, 4$  and sum the four contributions to obtain a numerical evaluation of the Lorentz trace. The same formalism holds for fermionic L-cut particles while for scalar particles, such as the  $SU(3)_c$  ghost, it suffices to consider only one evaluation with  $\phi_{Lcut} = 1$ . When considering particles of higher spin running in the loop, the sum would contain more terms (i.e. 16 for a rank-2 tensor particle) and even though it is not useful for the Standard Model, MADLOOP5 structure will easily support this in the future.

With these modifications, MADLOOP can return numerical evaluations of the quantity  $N(\ell)$  of eq. (2.3.8) which are used by CUTTOOLS to evaluate the loop integral. In general however, CUTTOOLS is a black box to MADLOOP so that any future upgrade of the OPP implementation (with the condition that its inputs be those introduced in sect. 2.3) will be compatible with the current implementation. Also, MADLOOP can easily be linked with a different implementation of OPP, such as SAMURAI [131] for example, as well as to tensor integral reduction tools too, as is shown in sec. 3.4.3.

Likewise, MADLOOP can be considered a black box for MADFKS (or any equivalent calling event generator) – the only cross-talk is in the form dictated by the Binot-Houches accord [33]<sup>8</sup>.

### 3.1.4 Checks

One of the main advantages of the automation of computations as performed by MADLOOP is that the sanity of the results for individual processes (irrespective of their complication)

<sup>8</sup>This is definitely true in MADLOOP4. MADLOOP5 is still completely standalone but it does not support the actual Binot-Houches accord input as it is too restrictive in its actual implementation. When the upgrade of the format will appear, and that there will be direct interest in linking the code to another event-generator, this will be straight-forwardly implemented.

### 3.1. Organization of the calculation

---

is basically guaranteed to be correct. The key point is that the computer code which returns the relevant one-loop amplitude is written by (in other words, is an output of) MADLOOP. This code uses a fixed number of pre-defined building blocks, essentially (but not only) the HELAS routines,<sup>9</sup> without the user being involved.

Therefore, the correctness of any one-loop amplitude follows from establishing the correctness of MADLOOP. In turn, this entails two kinds of checks:

- a) The building blocks used by MADLOOP must be proven correct.
- b) The way in which the building blocks are combined must be proven correct.

We point out that this structure of checks is fully analogous to that of MADGRAPH, although of course the technical aspects are not identical.

It is easy to realize that the checks of item *a)* are process-independent, while those of item *b)* do depend on the particular one-loop amplitude one wants to compute. In spite of this, the most straightforward way to carry out the checks of item *a)* is that of comparing the results of MADLOOP with those available in the literature, for a suitable list of processes. Since the number of building blocks used by MADLOOP is finite, so is such a list. Clearly, when following this procedure one also performs the checks of item *b)* for the processes of the list. However, this does not guarantee that the same checks will be successful for processes which do not belong to the list (although it is a powerful hint that this is indeed the case). Hence, in order to carry out fully the program of item *b)*, we have implemented several *self-consistency* checks, that MADLOOP will perform for any generated process and for any desired  $2 \rightarrow n$  kinematic configurations among those chosen by the user or by the calling program. We shall describe these checks later in this section.

The list of processes that we have used in order to compare MADLOOP4 results with their analogues available in the literature, and in computer codes other than MADLOOP, is reported in appendix B. We stress that this list is actually redundant as far as the goal of item *a)* is concerned (*i.e.* each HELAS loop-related routine is checked at least once, but typically more than once). For each process, we compare the finite part and the residues of the infrared poles of the quantity  $V$  defined in eq. (3.1.2) with those of other computations. It should be pointed out that, although in some cases codes other than MADLOOP will not return the residues of the infrared poles, these can in any case be checked against their analytically-known expressions, which we get from the implementation in MADFKS of eq. (B.2) of ref. [105]. As can be seen from appendix B, the agreement between MADLOOP and previously-known results is excellent and MADLOOP even helped correct bugs in some other codes dedicated to the computation of the loops of specific processes.

---

<sup>9</sup>Hardcoded for the SM in the case of MADLOOP4 and generated on the fly by ALOHA in the case of MADLOOP5.

We now turn to the discussion of the self-consistency checks we have mentioned previously. Some of them are not applicable to specific processes; the general strategy we have followed is that of testing each process generated by MADLOOP in the largest possible number of ways. The checks we have set up are listed in what follows.

1. *Alternative diagram filtering.* L-cut diagrams whose identities differ by cyclic permutations or mirror symmetry correspond to codes which are not written by MADLOOP in the same way, in spite of the fact that they will eventually give exactly the same loop-integrated results<sup>10</sup>. In MADLOOP4, an easy way to do this is that of choosing the L-cut particles in an order different from that of eq. (3.1.4). This is because L-cut-diagram identities not filtered out when looping over all diagrams will not be the same as those kept with the “canonical order” of eq. (3.1.4), but rather their equivalents under cyclic permutations and/or mirror symmetry (for example, this corresponds to keeping eq. (3.1.5) and discarding eq. (3.1.6), versus keeping eq. (3.1.6) and discarding eq. (3.1.5)). In MADLOOP5, the choice of the L-cutting rule can be done independently of the order of the L-cut diagrams generation.
2. *Crossing* – We consider the two processes

$$r_1 = (\mathcal{I}_1, \mathcal{I}_2, \dots, \mathcal{I}_i, \dots, \mathcal{I}_{n+2}), \quad r_2 = (\mathcal{I}_1, \bar{\mathcal{I}}_i, \dots, \bar{\mathcal{I}}_2, \dots, \mathcal{I}_{n+2}). \quad (3.1.10)$$

For a given  $2 \rightarrow n$  kinematic configuration

$$k_1 + k_2 \longrightarrow k_3 + \dots + k_i + \dots + k_{n+2} \quad (3.1.11)$$

one checks that the corresponding one-loop amplitudes fulfill the following equation:

$$\mathcal{A}^{(n,1)}(r_1; k_1, k_2, \dots, k_i, \dots, k_{n+2}) = \omega \mathcal{A}^{(n,1)}(r_2; k_1, -k_i, \dots, -k_2, \dots, k_{n+2}), \quad (3.1.12)$$

with  $\omega$  a constant that only depends on the identities of the particles that are crossed. This is non trivial, given that MADLOOP constructs  $\mathcal{A}^{(n,1)}(r_1)$  and  $\mathcal{A}^{(n,1)}(r_2)$  in two different ways (which includes the fact that the HELAS routines used in the constructions of the two amplitudes may not even be the same). Crossing is a very powerful method during the debugging phase, since eq. (3.1.12) holds diagram by diagram.

3. *Dependence on the mass of a heavy quark  $Q$*  – When the one-loop amplitude for a given process includes diagrams that feature a closed fermion loop, we can study the dependence of the result on  $m_Q$  (by default, such a dependence is included exactly by MADLOOP). We typically identify the heavy quark with the top, but this is not mandatory. In particular, we may check the following two regimes.

---

<sup>10</sup>This is what MADGRAPH usually does, and is not specific to L-cut diagrams. One can see it by comparing the codes written by MADGRAPH that correspond to the same physical process at the LO, but differ e.g. in the ordering of final-state particles in the user-specified process.

- (a) Decoupling limit:  $m_Q \rightarrow \infty$ . We compute the amplitude with the full  $m_Q$  dependence for increasingly large values of  $m_Q$ , and compare it to the one we obtain by excluding altogether the heavy quark from contributing to the loops (in the case  $Q = t$ , this corresponds to a five light flavors amplitude).
- (b) Zero-mass limit:  $m_Q \rightarrow 0$ . We compute the amplitude with the full  $m_Q$  dependence for increasingly small values of  $m_Q$ , and compare it to the one we obtain by replacing the heavy quark with an additional massless quark in the loops.

We stress that the comparisons between these two limits of the amplitude and the  $n_{lf}$ - and  $(n_{lf} + 1)$ -light-flavours results are not straightforward, owing to the possible presence of anomalies and to the UV-renormalization scheme adopted here respectively. Each process is to be studied as a case on its own, which is what we do in appendix B.

4. *Ward identities* – If the process  $r$  under study involves at least a massless gauge vector (gluon or photon in the SM), we check that the corresponding one-loop amplitude satisfies the gauge-invariance condition:

$$\mathcal{A}_{\mu_i}^{(n,1)}(r; k_1, k_2, \dots, k_i, \dots, k_{n+2}) k_i^{\mu_i} = 0, \quad (3.1.13)$$

where  $\mathcal{A}_{\mu_i}^{(n,1)}$  is the loop amplitude contracted with the polarization vectors of all the external particles except for the  $i^{\text{th}}$  one which is replaced in the equation above by the four-momentum  $k_i^{\mu}$  carried by it. When this check applies to a gluon for example, it explicitly checks the  $SU(3)$  gauge invariance.

5. *Infrared pole residues* – The form of the double and single infrared poles is analytically known for any process  $r$  (see e.g. eq. (B.2) of ref. [105]). We compare the residues returned by MADLOOP with those computed with the analytic formulae, implemented in MADFKS. We point out that by checking the single pole result we also indirectly test the correctness of the UV renormalization procedure.
6. *Lorentz invariance*. The amplitudes must be Lorentz invariant and this can be checked by comparing MADLOOP output  $V(r)$  of eq. (3.1.2) for a kinematic configuration  $\{k_i\}$  with the same evaluation for the kinematic configuration  $\{\Lambda_\mu k_i^{\mu}\}$  where  $\Lambda_\mu$  is a Lorentz boost and/or rotation. These two evaluations will match only when summed over all helicity configurations because the Lorentz transformation effectively modifies the chosen reference vector for the helicity projection of external states. For this reason, the invariance of the loop matrix element under Lorentz boosts is also sensitive to gauge invariance.
7. *Gauge invariance* – MADLOOP can so far perform computations only in the Feynman gauge. This limitation comes from the fact that most reduction methods, including OPP, requires the loop numerator  $N(\ell)$  of the integrand to be a polynomial in  $\ell$  and,

equivalently, that the denominators  $D_i$  be all distinct. However, when performing computations with only QCD charged particles running in the loop, it is then possible to switch from Feynman to unitary gauge for the electroweak sector of the theory, without affecting the loop reduction algorithm mechanisms. This check necessitates a proper implementation of the electroweak ghosts and, when those contribute, it is typically more sensitive than the Ward identities applied to the photon<sup>11</sup>. Typically, not only the widths of the electroweak unstable particles must be set to zero (when not working within the complex mass scheme), but also the Yukawa couplings must be set equal to the pole masses of the corresponding massive particles.

We stress that all these seven checks are local in phase space, i.e. they are performed for a given  $2 \rightarrow n$  kinematic configuration. In principle, they can therefore be carried out for each kinematic configuration when integrating over the phase space; in practice however, this would significantly increase the load on CPU. Therefore, MADLOOP5 provides an automatic way of performing some of the checks above on a user-defined process. They can be run by the user for a couple of PS-points before proceeding with the actual integration so as to assess the sanity of the loop evaluations. See sect. 3.4.1 for more information on these automatic checks.

Given the nature of these checks, it is basically impossible for a one-loop amplitude to pass them for some kinematic configurations, and to fail them for others. An exception to this is a failure due to some numerical instability occurring during the calculation. For this reason, the Lorentz rotational invariance and infrared poles cancellation tests are used by MADLOOP, among other methods outlined in sec. 3.4.4, as a numerical stability check performed at runtime for all phase-space points.

### 3.2 Limitations of MADLOOP

Sect. 3.3 presents a non exhaustive set of results obtained using MADLOOP4 for the virtual contribution. It shows that this first version was already able to cope with a large variety of process, even though it suffered from mainly four physics limitations, now all lifted in the MADLOOP5 version.

1. A process could not be generated if it contained a four-gluon vertex in its Born tree diagrams.
2. MADLOOP4 could not handle automatically any loop featuring electroweak massive vector bosons.

---

<sup>11</sup>Moreover, it can be applied irrespectively of the final states of the process considered (*i.e.* also in the case where no photons are present in the final state).

3. A process could not be generated if all contributions to the Born amplitude squared did not factorize the same powers of coupling factors.
4. Finite-width effects, due to intermediate massive unstable (*i.e.* that can decay) particles that could also enter in the loops, were not implemented.

The restriction in item 1 is removed in MADLOOP5 thanks to the fact that the internal model representation allows for particles interactions to be written in terms of several color and Lorentz structures. The four-gluons  $R_2$  Feynman rule implementation is then immediate.

The condition of item 2 is relieved because MADLOOP5 can now work in the Feynman gauge in which the problematic<sup>12</sup> longitudinal part  $k^\mu k^\nu / m^2$  of the numerator of the massive vector propagator is absent.

The case of item 3 originated from MADLOOP4 assumption that the UV counterterms factorize the whole Born cross-section. MADLOOP5 constructs the quantity  $\mathcal{A}^{(n,x)}$  of eq. (3.1.8) by picking the right counterterm contributions individually for each of the contributing diagrams. The Born diagrams are then no longer required to share any property. This is important for mixed coupling expansions and in cases where different Yukawa couplings, each with its specific QCD renormalization, enter in the Born diagrams (for example in the process  $pp \rightarrow ht\bar{b}$ ).

Finally, SM cases relevant to item 4 are those of the top quark and of the massive EW vector bosons. When considering diagrams which include one or more propagators of one or more of these particles, there may be configurations of external momenta which end up putting some of them on their mass shells. This thus results in a divergence, which can be avoided by giving finite widths to the unstable particles. In the case in which the relevant particles also enter in the loops, the use of non-zero widths is non trivial, and consistency dictates the use of a scheme like the *complex-mass* one [71, 75]. MADLOOP5 supports the use of such a scheme and can handle finite-width effects of loop particles in a gauge invariant way.

The physics model in MADLOOP5 is specified by an independent module in the UFO format [67] (sect. 3.4.2) setting all model properties, including those only relevant to loop computations such as the UV and  $R_2$  counterterms. MADLOOP5 is therefore completely agnostic of the particular physics studied and there is no intrinsic limitation to the capabilities of MADLOOP5. It can for example potentially handle models with higher spin representations, Majorana fermions, larger SU(3) representations and in general whatever feature is already supported by MADGRAPH5. However, as of today, only the UFO model for QCD perturbative expansion within the SM has been validated and work is ongoing for the simplest extensions of the SM as well as for computing electroweak corrections. This

---

<sup>12</sup>Most reduction procedure, like OPP, need  $N(\ell)$  of eq.( 2.1.7) to be a polynomial in  $\ell$ .

already allows MADLOOP5 to handle QCD-loop contributions to processes of arbitrary complexity with the sole limitation of its computational load. Sect. 3.4.5 provides a timing benchmark showing that any processes with up to five color charged particles in the external states can be both generated with MADLOOP5 and integrated<sup>13</sup> with AMC@NLO. Processes with up to six color charged external particles can easily be generated and evaluated for a couple of phase-space point but the resulting code is in general too slow for phenomenological applications.

As a general and concluding remark on CPU-driven issues, it is clear that, regardless of the amount of optimization done on the code, the use made of Feynman diagrams in the current version introduces a factorially-growing complexity in the calculation. However, it is easy to realize that the FKS subtraction method is completely independent of Feynman-diagram techniques, and that to a large extent this is also the case for the OPP reduction procedure.

### 3.3 Results from the MADGRAPH4 original framework

This section presents a sample of the results obtained with MADFKS and MADLOOP in their former implementation exploiting MADGRAPH4. It is however important to stress already that this whole list could have been obtained using the AMC@NLO5 framework as well. It has been checked, for given kinematic configurations, that MADLOOP4 and MADLOOP5 return the same results for these processes<sup>14</sup>.

The great variety of processes displayed in this table and the fact that it can be obtained automatically, without any ad-hoc procedure, leaves no doubt that NLO QCD corrections to Standard Model processes of that complexity are now as trivial to calculate as LO results, and must thus be treated on equal footing with the latter. This fact has two main implications. Firstly, *technicalities are independent of the process*, and can be understood once and for all. Secondly, the range of accessible processes is limited only by CPU-time considerations.

Given that the goal here is not that of performing any phenomenological studies, we have considered processes that feature a fair diversity (pure QCD, with EW vector bosons, with SM Higgs, with massive/massless  $b$  quarks, and at different jet multiplicities) in order to fully test and prove the flexibility of our setup. We therefore limit ourself here to presenting results for total rates, even though differential distributions can be studied equally well within this framework (see chapter 4 for examples of such a usage). A few standard distributions (such as transverse momenta, rapidities, and pair invariant masses) have been monitored and we reckon that the statistics used to obtain fairly accurate

---

<sup>13</sup>The virtual contributions are in all cases the most time consuming part of the integration within the AMC@NLO framework.

<sup>14</sup>In appendix A.1, we show that these checks belong to the class of MADLOOP5 *parrallel tests* which can be automatically run to insure the stability of the code upon development.



### 3.3. Results from the MADGRAPH4 original framework

Parameter	value	Parameter	value
$m_Z$	91.188	$\alpha^{-1}$	132.50698
$m_W$	80.419	$G_F$	$1.16639 \cdot 10^{-5}$
$m_b$	4.75	$\text{CKM}_{ij}$	$\delta_{ij}$
$m_{top}$	172.5	$\Gamma_Z$	2.4414
$m_H$	120	$\Gamma_W$	2.0476
		$\Gamma_t$	0.0
$\alpha_S^{(\text{NLO},5)}(m_Z)$	0.120179	$\alpha_S^{(\text{NLO},4)}(m_Z)$	0.114904
$\alpha_S^{(\text{LO},5)}(m_Z)$	0.139387	$\alpha_S^{(\text{LO},4)}(m_Z)$	0.133551

Table 3.1: General settings of physical parameters used for the computations of the cross sections in table 3.2, with dimensionful quantities given in GeV. The upper indices on  $\alpha_S$  indicate whether the coupling has been used to obtain an NLO or an LO result, with five or four light flavors, and the corresponding values are dictated by the choice of PDFs. Some processes may adopt specific parameter values, different from those reported in this table; in particular, the  $b$  quark can be treated as massless. See the text for details.

results for total rates is also sufficient to get reasonably smooth distributions. This is consistent with past experience with FKS subtraction, and is ultimately due to the fact that in this formalism, for any given integration channel, there is always exactly one kinematic configuration associated with a subtraction counterterm, thereby reducing to a minimum the probability of mis-binning (see ref. [105]).

Section 3.4.1 explains in details how these results can easily be reproduced from the public version of AMC@NLO, the only minimal input required by the user being the identity of the initial and final state particles. Code-writing is only necessary if ones wants to consider specific observables, cuts or dynamical scales not among the default available ones. The processes simulated all belong to the class of  $pp$  collisions at 7 TeV. Masses, couplings, and widths are chosen as reported in table 3.1, with some process-specific exceptions, to be described below. For NLO (LO) results with five light flavors, the PDF set [130] MSTW2008nlo (MSTW2008lo) was used, while in the case of four light flavors, MSTW2008nlo\_nf4 (MSTW2008lo\_nf4) was adopted. Each of these sets is associated with a different value of  $\alpha_S$ , which is reported in table 3.1. Jets are defined using the  $k_T$ -clustering algorithm [53] (as implemented in FastJet [44]), with  $p_T^{(jet)} > 25$  GeV and pseudo-cone size  $\Delta R = 0.7$ . Renormalization and factorization scales are set equal to a common value,

$$\mu \equiv \mu_R = \mu_F. \quad (3.3.1)$$

Since we present results for total cross sections, it is appropriate to assign a fixed (*i.e.* that does not depend on the kinematics) value to  $\mu$ , which is process-dependent as reported in

table 3.2. The results are therefore easily reproducible and can be used as a standard reference. In table 3.2, by  $n_{lf}$  we have denoted the number of quarks whose masses are equal to zero. Thus  $n_{lf}$  is equal to five or to four when the  $b$  quark is considered to be massless or massive, respectively. In all cases, all six quark flavors have been included in the loops. As discussed in ref. [105], AMC@NLO allows one to integrate all contributions to the NLO cross section in one single computation, regardless of whether they have a real-emission or a Born-type kinematics. For the results presented here, however, a different strategy was adopted and the one-loop contributions have been integrated separately from the other ones (i.e., the Born and real-emission matrix elements, and the subtraction counterterms). This is because for a given phase-space point the evaluation of virtual corrections performed by MADLOOP takes much longer than all the other operations carried out by MADFKS. On the other hand, no phase-space subtraction is done on virtual corrections, and therefore the numerical computations are inherently more stable than those relevant to the subtracted real-emission contributions. Hence, it turns out to be more efficient to integrate the one-loop contributions separately from all the others, using a reduced statistics (on average, about one-tenth<sup>15</sup> of that employed for real corrections). The integration in MADFKS as implemented in MADGRAPH5 automatically organizes the computation in this optimal way. Even so, for processes with the highest multiplicities, the virtual corrections require more computing time than the rest of the calculation, in order to attain similar integration uncertainties. This was certainly true when using MADLOOP4 but still holds now with MADLOOP5, despite the many optimizations implemented (see sect. 3.4.3). Given that MADLOOP5 runtime speed is now competitive (see sect. 3.4.5), this shows the efficiency of the MADFKS integration. This is actually good news, as it means that any given runtime speed increase obtained for the virtuals evaluation code, i.e. MADLOOP output, directly translates into the same speedup for the integration of the whole process.

I finally mention a few technical points relevant to phase-space integration. All contributions to the cross sections are integrated using multi-channel techniques, following the procedure outlined in ref. [105]. The sums over colors and helicities are performed explicitly (event though both MADFKS and MADLOOP are equipped to carry out helicity sums with Monte Carlo methods, but this was simply not necessary for the processes considered here). The virtual contributions are integrated in a direct manner, i.e. no reweighting by the Born matrix elements has been performed.

---

<sup>15</sup>A more precise figure is difficult to give, since the total number of integration points per channel is determined dynamically, in order for the various channels to contribute to the total rate with similar absolute accuracies.

### 3.3. Results from the MADGRAPH4 original framework

Process	$\mu$	$n_{lf}$	Cross section (pb)	
			LO	NLO
a.1 $pp \rightarrow t\bar{t}$	$m_{top}$	5	$123.76 \pm 0.05$	$162.08 \pm 0.12$
a.2 $pp \rightarrow tj$	$m_{top}$	5	$34.78 \pm 0.03$	$41.03 \pm 0.07$
a.3 $pp \rightarrow tjj$	$m_{top}$	5	$11.851 \pm 0.006$	$13.71 \pm 0.02$
a.4 $pp \rightarrow t\bar{b}j$	$m_{top}/4$	4	$31.37 \pm 0.03$	$32.86 \pm 0.04$
a.5 $pp \rightarrow t\bar{b}jj$	$m_{top}/4$	4	$11.91 \pm 0.006$	$7.299 \pm 0.05$
b.1 $pp \rightarrow (W^+ \rightarrow)e^+\nu_e$	$m_W$	5	$5072.5 \pm 2.9$	$6146.2 \pm 9.8$
b.2 $pp \rightarrow (W^+ \rightarrow)e^+\nu_e j$	$m_W$	5	$828.4 \pm 0.8$	$1065.3 \pm 1.8$
b.3 $pp \rightarrow (W^+ \rightarrow)e^+\nu_e jj$	$m_W$	5	$298.8 \pm 0.4$	$289.7 \pm 0.3$
b.4 $pp \rightarrow (\gamma^*/Z \rightarrow)e^+e^-$	$m_Z$	5	$1007.0 \pm 0.1$	$1170.0 \pm 2.4$
b.5 $pp \rightarrow (\gamma^*/Z \rightarrow)e^+e^- j$	$m_Z$	5	$156.11 \pm 0.03$	$203.0 \pm 0.2$
b.6 $pp \rightarrow (\gamma^*/Z \rightarrow)e^+e^- jj$	$m_Z$	5	$54.24 \pm 0.02$	$54.1 \pm 0.6$
c.1 $pp \rightarrow (W^+ \rightarrow)e^+\nu_e b\bar{b}$	$m_W + 2m_b$	4	$11.557 \pm 0.005$	$22.95 \pm 0.07$
c.2 $pp \rightarrow (W^+ \rightarrow)e^+\nu_e t\bar{t}$	$m_W + 2m_{top}$	5	$0.009415 \pm 0.000003$	$0.01159 \pm 0.00001$
c.3 $pp \rightarrow (\gamma^*/Z \rightarrow)e^+e^- b\bar{b}$	$m_Z + 2m_b$	4	$9.459 \pm 0.004$	$15.31 \pm 0.03$
c.4 $pp \rightarrow (\gamma^*/Z \rightarrow)e^+e^- t\bar{t}$	$m_Z + 2m_{top}$	5	$0.0035131 \pm 0.0000004$	$0.004876 \pm 0.000002$
c.5 $pp \rightarrow \gamma t\bar{t}$	$2m_{top}$	5	$0.2906 \pm 0.0001$	$0.4169 \pm 0.0003$
d.1 $pp \rightarrow W^+W^-$	$2m_W$	4	$29.976 \pm 0.004$	$43.92 \pm 0.03$
d.2 $pp \rightarrow W^+W^- j$	$2m_W$	4	$11.613 \pm 0.002$	$15.174 \pm 0.008$
d.3 $pp \rightarrow W^+W^- jj$	$2m_W$	4	$0.07048 \pm 0.00004$	$0.08241 \pm 0.0004$
e.1 $pp \rightarrow HW^+$	$m_W + m_H$	5	$0.3428 \pm 0.0003$	$0.4455 \pm 0.0003$
e.2 $pp \rightarrow HW^+ j$	$m_W + m_H$	5	$0.1223 \pm 0.0001$	$0.1501 \pm 0.0002$
e.3 $pp \rightarrow HZ$	$m_Z + m_H$	5	$0.2781 \pm 0.0001$	$0.3659 \pm 0.0002$
e.4 $pp \rightarrow HZ j$	$m_Z + m_H$	5	$0.0988 \pm 0.0001$	$0.1237 \pm 0.0001$
e.5 $pp \rightarrow Ht\bar{t}$	$m_{top} + m_H$	5	$0.08896 \pm 0.00001$	$0.09869 \pm 0.00003$
e.6 $pp \rightarrow Hb\bar{b}$	$m_b + m_H$	4	$0.16510 \pm 0.00009$	$0.2099 \pm 0.0006$
e.7 $pp \rightarrow Hjj$	$m_H$	5	$1.104 \pm 0.002$	$1.333 \pm 0.002$

Table 3.2: Results for total rates, possibly within cuts, at the 7 TeV LHC, obtained within the AMC@NLO framework based on the fortran version 4 of MADGRAPH. The errors are due to the statistical uncertainty of Monte Carlo integration. See the text for details.

Further process-specific comments are given in what follows.

- A cut

$$m_{e^+e^-} > 30 \text{ GeV} \quad (3.3.2)$$

has been applied to processes b.4, b.5, b.6, c.3, and c.4.

- In the case of process c.5, the photon has been isolated with the prescription of ref. [108], with parameters

$$\delta_0 = 0.4, \quad n = 1, \quad \epsilon_\gamma = 1, \quad (3.3.3)$$

and parton-parton or parton-photon distances defined in the  $\langle \eta, \varphi \rangle$  plane. The photon is also required to be hard and central:

$$p_T^{(\gamma)} \geq 20 \text{ GeV}, \quad \left| \eta^{(\gamma)} \right| \leq 2.5. \quad (3.3.4)$$

- In the case of processes a.3, a.4, a.5, and e.7, diagrams with EW vector bosons in the loops have been removed, because MADLOOP4 could not perform computations in the Feynman gauge, nor could it exploit the complex-mass scheme. This removal is justified by the fact that these contributions are color-suppressed.
- In the case of processes a.3, a.4, and a.5, diagrams with s-channel  $W$ 's have been removed, in order to avoid  $t\bar{t}$ -type resonances. In the narrow width approximation this is a well-defined procedure, and for consistency we thus set  $\Gamma_W = 0$  for these processes.
- In the case of processes a.4, a.5, c.1, c.3, and e.6, we do *not* apply any cuts on  $b$  quarks, which is possible since  $m_b \neq 0$  implies the possibility of integrating down to zero transverse momenta. This is important, firstly because it allows us to test the robustness of phase-space integration in a very demanding situation (the  $b$  quark being very light), and secondly in view of the matching of these results with parton shower Monte Carlos, where this gives the possibility of studying  $b$ -flavoured hadrons also at small transverse momenta.

All the results reported in table 3.2 could be computed with MADLOOP4 by employing up to two hundreds machines running simultaneously for two weeks. This running time does not include that required for actually generating the codes to be run. This latter operation is not parallelized and one must use one machine per process. This is however not a limitation as the running time of the generation phase is marginal, even for the most complicated among the processes considered in table 3.2. Both these timings have been significantly improved within MADLOOP5, see sect. 3.4.5 for the quantitative details.

The uncertainties reported in table 3.2 are of statistical origin. In a fully-numerical approach as the one adopted here, another source of uncertainty is that associated with potential numerical instabilities. MADLOOP4 and MADLOOP5 procedures to handle this issue are very different and the latter is discussed in details in sect. 3.4.4. As of MADLOOP4 case and the processes of table 3.2, it is enough to say that unstable kinematic configurations occurred very rarely (less than a percent) and that the corresponding uncertainties are completely negligible w.r.t. the statistical errors, being *at least* two orders of magnitude smaller.

### 3.4 The MADLOOP5 successor

MADLOOP4 was based on the old fortran version 4 of MADGRAPH and MADEVENT which lacked flexibility and whose designs prohibited the implementation of new functionalities within it, let alone advanced NLO features. As a consequence, MADLOOP4 and MADFKS4 were developed as independent plugins, the former in C++ and the latter in FORTRAN77, treating MADGRAPH4 as a blackbox. The whole set of tools, reunited under the denomination AMC@NLO4, was coordinated by ad-hoc scripts for specific usages of the code.

The net result is indeed automation of QCD corrections computations for SM processes, as advocated in [123], but only in the sense that no process-related information or operation was required from the user but not that anyone could achieve this without prior extensive knowledge of the code. This last point is not essential from a physics point of view but definitely crucial for the method and tool to be used by a large fraction of the high energy physics community.

The version 4 of AMC@NLO had reached its limit and achieved its primary goal: a feasibility proof. It was then obvious that making the framework user-friendly and stable upon further development as well as extending its reach (BSM applications, mixed coupling expansions, etc...) would necessitate a complete re-implementation from scratch. The modern PYTHON version of MadGraph5 [7] appeared to be a perfect host for such a work.

This section presents the outcome of this rewriting, getting us yet closer to the ultimate goal of automated computation at the push-of-a-button of one-loop contributions to scattering amplitudes within general physics models.

#### 3.4.1 AMC@NLO5 and MADLOOP5 usage

MADGRAPH5 v2.0.0 $\beta$  featuring AMC@NLO with MADLOOP5 and MADFKS5 was made public on November 8<sup>th</sup> 2012 and can be obtained at the website [amcatnlo.cern.ch](http://amcatnlo.cern.ch) or directly at the download section of [launchpad.net/madgraph5](http://launchpad.net/madgraph5). The downloaded archive

has to be decompressed and, in what follows, the path of the resulting folder will be referred to as 'MGPath'.

As the name suggests, AMC@NLO is completely embedded within MADGRAPH5 which means that all its powerful tree-level LO capabilities are accessible at the same time as the NLO ones. In particular, these are all controlled via an intuitive *user-interface* which can be launched by executing the following:

```
| cd MGPath  
| ./bin/mg5
```

This will start the MG5 interface inviting one to type commands in front of the `mg5>` prompt. This works very similarly to a terminal, and one has access to auto-completion, command history with the up and down arrow keys and the mighty `help commandName` functionality. Also, one can simply type in `tutorial` followed by the tab completion to choose among several inline tutorials.

The dependencies of the code are minimal: PYTHON v2.6 or above (but not 3.x) and the compiler GFORTTRAN v4.6 or above. Also, AMC@NLO (not MADLOOP5 standalone) requires FASTJET v3.x or above. If the executable named `fastjet-config`<sup>16</sup> is not in the system environment path, its absolute path must be specified, once only, in the file `MGPath/input/mg5_configuration.txt` which is created the first time the user interface is launched. Finally, if the user wishes to have AMC@NLO steering the showering of the parton-level events, customized version of the common showering programs (such as HERWIG++ and PYTHIA6) need to be installed. This can be done automatically by typing `install MCatNLO-utilities` in the user-interface.

There are many options controlling the general behavior of MADGRAPH5. These are not only the running environment settings above but also the parameters affecting the physics schemes considered by MADGRAPH5, such as the gauge choice for example. Before running anything on the MG5 user interface, it is preferable that the user starts by displaying all options and their current values with `display options`. They can then be individually modified by the user via the `set` command:

```
| MG5> set {Option} {Value}  
| Ex: MG5> set complex_mass_scheme True
```

Listing 3.1: Syntax of the set command.

The goal of this section is not that of providing an exhaustive manual of AMC@NLO, but we still wish to list here part of the various commands available, with their syntax and some of their options. Before this, as a teaser, we give a short example of a quick run of MADLOOP5 for evaluating  $gg > d\bar{d}g$  for a random kinematic configuration.

---

<sup>16</sup>This executable is created at the time of FASTJET installation in the folder `<FastJetInstall-Path>/bin/`.

```

MG5> generate g g > d d~ g [virt=QCD]
[...]
ML5> output
[...]
ML5> launch -f
Initializing process gg > ddxg.
=====
|| Results for process gg > ddxg
=====
|| Phase-Space point specification (E,px,py,pz)
[...]
|| Born contribution (GeV^-2):
|   Born           = 4.1971282651714599e-04
|| Virtual contribution normalized with born*alpha_S/(2*pi):
|   Finite         = -8.2085331293627704e+00
|   Single pole    = -3.3204822515046402e+01
|   Double pole    = -1.1666666666666700e+01
=====

```

Listing 3.2: Example of a simple run of MADLOOP5 standalone for the process  $gg > d\bar{d}g$ .

This whole run takes less than a minute and the parts in *italic* are the only user inputs required after having started the interface. The notation [...] refers to additional information provided by MADLOOP5 and omitted here.

As the example above already suggests, the analysis of a given process necessitates three consecutive steps: the diagram generation, the write-out of the numerical code to the disk (*i.e. output*) and finally its compilation and running for a specific purpose.

### Generation of a process

When *generating* a process, MADLOOP5 constructs all Born, loop and counterterm Feynman diagrams contributing to it and stores an internal representation of these. The general syntax for the generation of a process is (arguments are denoted with curly brackets):

```

MG5> generate {Process} {AmpOrders} [ {Mode} {PertOrder} ] {AmpSquaredOrders}
Ex: MG5> generate d d~ > z > u u~ / t b QED=2 QCD=0 [virt=QCD] QED=4 QCD=2

```

Listing 3.3: Syntax of the generate command.

The *{Process}* argument is the only mandatory one and follows the exact same syntax as for MADGRAPH5 at Leading Order (see `help generate`) with the restriction that decay chains<sup>17</sup> are not supported. The initial and final states are separated by the `>` symbol

<sup>17</sup>The concept of decay chains is dangerous when considering loop contributions, because including corrections to only the core process might lead to gauge dependent results, when considering the top decay for example. For this reason, the tool of choice for handling decay chains on top of an NLO core process, is MADSPIN [10] (see the `launch` command). It performs the decay after AMC@NLO event

and with a space between particles. The list of active particles in the loaded model can be consulted at any time with `'display particles'`. In the example provided, the process  $u\bar{u} \rightarrow d\bar{d}$  is specified, with the requirement of having a  $Z$ -boson in the s-channel and excluding the top and bottom massive quarks contributions (also for the loops). Notice that both for LO and NLO processes, only *physical* restrictions can be specified and, in particular, there is no possibility for a general user-defined diagram filtering routine. This is to prevent the average user to ever produce unphysical results when employing MADGRAPH5, but of course the expert user can still access such a feature via a trivial modification of the python source code.

The `{AmpOrders}` specifies upper bounds on the coupling orders appearing in all the diagrams  $\mathcal{C}_\alpha$  of eq. (2.1.1) building the *amplitudes*, similarly as for the Leading Order generation. For example, if the process includes QCD corrections and the user specifies `'QCD=3'`, all Born amplitudes will be constrained to include at most three powers of  $g_s$ , so that the Born matrix element squared is of order  $\alpha_s^3$  at most, and the loop amplitudes limited to factorize at most five (3+2) powers of  $g_s$  so that its interferences with the Born ones are at most of order  $\alpha_s^4$ .

The `{AmpSquaredOrders}` is specific to the NLO<sup>18</sup> and sets similar upper bounds but applying to the coupling orders of the *squared amplitudes*. This option does not have sensible applications for pure QCD corrections and really makes sense only in the context of mixed coupling expansions. For `{AmpSquaredOrders}` exclusively, negative value can be used to select what sub-leading terms to keep. For instance, setting `'QCD=-N'`, with  $N$  a positive non-zero integer, is equivalent to setting `'QCD= BornOrder + 2(N-1)'`, with *BornOrder* the lowest QCD order (equivalent to the power of the coupling constant  $g_s$ ) contribution to the squared Born amplitudes. These coupling orders specifications are optional and, if absent, MADLOOP5 considers only the corrections which are numerically leading based on the coupling orders weights (see sect. 3.4.2 for information on coupling orders weights). In the example provided, they are equivalent to what MADLOOP5 would have employed if they had been omitted. In general, one can type `'display coupling_order'` to print those defined within the current active physics model.

The `{Mode}` option selects what NLO type of contribution should be considered and can take any of the three values `'all='`, `'real='` and `'virt='`. The first option implies using the whole AMC@NLO framework to construct both the real emission and loop contributions in view of their numerical integration with MADFKS. The `'real='` mode differs only by the fact that the code for the virtual contributions is not generated (MADLOOP5 is not called) and it is assumed that they will be linked and provided externally by the user. The `'virt='` mode corresponds to MADLOOP5 standalone mode, and real emission diagrams

---

generation while retaining most of the spin-correlation and some off-shell effects.

<sup>18</sup>This restriction is relevant mostly for mixed coupling expansions and is correctly implemented up to the generation stage only. It will become fully supported only at the time Electro-Weak (EW) loops will be properly handled.



are not considered. The subsequent 'output' and 'launch' commands apply differently in this standalone mode and limit themselves to the evaluation of the quantity  $V(r)$  of eq. (3.1.2) for user-defined kinematic configurations.

Notice that the loop-induced processes<sup>19</sup> can only be studied in MADLOOP5 standalone mode as they are not yet supported for event generation. Process definitions in standalone mode must correspond to a single production channel and cannot include multiparticle labels such as `p` (proton) or `j` (jet content). The default value of `{Mode}` is 'all'.

The `{PertOrder}` argument is mandatory for loop processes and specifies what *type* of loops must be considered. Loops in MADLOOP5 are assigned to certain types corresponding to the coupling orders of the physics model. The assignment of a loop to a given coupling order, being 'QCD' to be definite here, are two:

1. The loop must contain at least one loop QCD vertex<sup>20</sup>.
2. Each particle running in this loop has to appear as an external state of at least one QCD vertex of the model.

The more physical description of the second rule is that all loop particles must be charged under the corresponding group (color SU(3) in this example). This is however not strictly equivalent, because the coupling orders of an interaction are not directly related to the quantum numbers of the particles involved. In fact, coupling orders are formally arbitrary but nonetheless intended to be related with the appearance of certain coupling constants in the interaction. In the SM, the QCD order corresponds to the power of  $g_s$  in the interaction coupling while QED is mapped to the electric charge  $e$  and the Yukawas. The three loops below all belong to the SM process  $d\bar{d} \rightarrow u\bar{u}$  but are not of the same *type*.

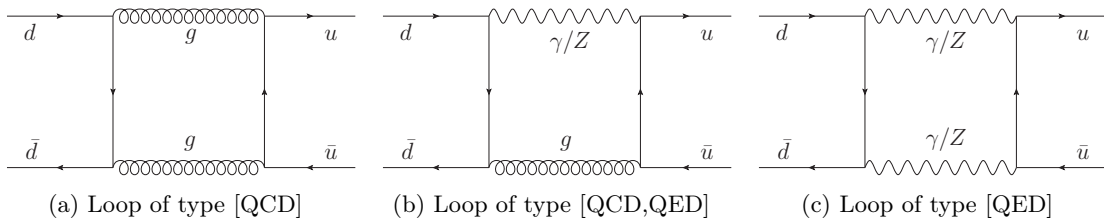


Figure 3.4.1: Illustration of three different loop types for the process  $d\bar{d} \rightarrow u\bar{u}$ .

The loop 3.4.1b, despite being responsible for an  $\alpha_s$  correction to the Born diagram with a photon or Z-boson in the s-channel, is *not* of type [QCD] only. As a consequence,

<sup>19</sup>Loop-induced processes receive their LO contribution by loop-diagrams because no tree-level diagrams contributes to the corresponding scattering amplitude. A typical example of loop-induced process is  $gg \rightarrow H$  when not working in the Higgs effective theory.

<sup>20</sup>A QCD vertex or interaction is defined as any vertex defined with a coupling constant featuring QCD in its 'order' attribute (see appendix A.2.). In the loop UFO model of MADLOOP5, this is equivalent to saying that the analytical expression of the coupling constant includes  $\alpha_s$ .

the example of process definition given in listing 3.3 excludes this type of diagrams and MADLOOP5 will warn the user that it did so. For this process, the correct syntax to insure having MADLOOP5 include all  $\alpha_s$  NLO corrections would be

```
| MG5> generate d d~ > z > u u~ [virt= QCD QED] QCD=-2
```

Where the 'QCD QED' type includes all possible contributing loops in the SM while 'QCD=-2' forces MADLOOP5 to cut the matrix element expansion at exactly  $\alpha_s^{BornOrder+1}$ . Notice that the class of loop diagrams defined by a given type is not necessarily a gauge invariant subset, so that the  $\{PertOrder\}$  option can potentially yield unphysical results. The reason for this option is therefore purely technical but nonetheless necessary because loops such as 3.4.1b feature all the difficulties of generic electroweak corrections computations and AMC@NLO cannot handle them as of today. The main obstacle is that MADFKS5 does not yet include photon real emissions, necessary for canceling the infrared singularities induced by the photon in the loop.

In future versions, AMC@NLO will support all types of corrections and the  $\{AmpSquare-dOrders\}$  argument will allow to unambiguously specify what terms must be kept in the coupling constants expansion.

### Output stage

After having generated a process, the 'output' command writes out to the disk a numerical code for its analysis. The syntax is simply

```
| ML5> output {ProcFolder}
| Example: ML5> output TestProc
```

with  $\{ProcFolder\}$  an optional argument for specifying the name or path of the output location. By default, it is placed under 'MGPath' with a self-explanatory folder name. Notice that the prompt MG5> switched to ML5> and indicates that the user is now in the MADLOOP5 standalone environment.

The output for a process defined in MADLOOP5 standalone mode (*i.e.* with  $\{Mode\} \rightarrow$  'virt=') is limited to the source code for the evaluation of the quantity  $V(r)$  of Eq. (3.1.2) and no analysis or cross-section integration routines are provided. This mode is suited for producing libraries for the computation of the virtual contributions to be called within external Monte-Carlo tools. It can also be used solely for the purpose of cross-checking one's private code for the loop computations against MADLOOP5 automatically generated one.

The running of the code is best steered from the user interface directly, but one can also directly execute the scripts placed in the 'bin' directory<sup>21</sup>. For AMC@NLO runs, the

---

<sup>21</sup>Placed under the folder  $\{ProcFolder\}$ . The same comment applies to all other directories mentioned further in this section.

cross-section computed as well as the plots and event files generated are all stored in the 'Events' directory. The fortran source code common to the whole process is placed both in 'Source' and directly under 'SubProcesses'. Finally, the code specific to each production channel is located in the corresponding subdirectories of 'SubProcesses'.

#### Running the code: launch

Once the code is output, it can be compiled and run directly from the user interface via the command

```
ML5> launch {ProcFolder} {Mode} {Options}
Example: ML5> launch TestProc aMC@NLO -p -f
```

where  $\{ProcFolder\}$  is the optional name/path of a process folder the user wants to run and which has been previously generated with the 'output' command. The default value for this option is the latest process output in the active session. A key remark here is that one can exit the interface at any time after having output a process and decide to run it later with the 'launch' command. This does not need to be done within the same session because the necessary process information has already been exported to the disk at the output stage.

The launch command for MADLOOP5 standalone processes and AMC@NLO are different. In the first case, it simply provides a single evaluation of the quantity  $V(r)$  of eq. (3.1.2). We shall first describe such a usage for which an example of output is shown in listing 3.2. No  $\{Mode\}$  option can be specified in this case and the only available  $\{Options\}$  is  $-f$  for bypassing the specification of the kinematic configuration (then randomly chosen) and of the various parameters stored in ' $\langle ProcFolder \rangle/Cards$ '. The card 'MadLoopParams.dat' specifies MADLOOP5 parameters at runtime and the description of the most relevant ones can be found in appendix A.5. The model parameters (such as particles masses, widths and interaction couplings) are set in 'param\_card.dat'.

The AMC@NLO runs (for processes generated with 'all=' or 'real=') are initiated with the same 'launch' command. The  $\{Mode\}$  option can be omitted (recommended for the typical user) in which case AMC@NLO will prompt the following to facilitate the user's choice.

```

Which programs do you want to run?
 0 / auto      : All for which cards exist.
 1 / NLO       : Fixed order NLO calculation (no event generation).
 2 / aMC@NLO   : Event generation (include running the shower).
 3 / noshower  : Event generation (without running the shower).
+10 / +madspin : Add decays with MadSpin (before the shower).
[0, auto, 1, NLO, 2, aMC@NLO, 12, aMC@NLO+madspin, 3, ... ][60s to answer]
> UserEntry

```

This prompt will be followed by another one for editing the parameter cards. On top of the two cards already discussed, AMC@NLO also reads in `'run_card.dat'` specifying a number of properties of the simulation. In particular, the beam type and energy, PDF set, renormalization scale and generation level cuts can be set in this card. If the renormalization scale is set dynamical, its functional form is by default the sum of transverse masses of final state particles but this can be modified by directly editing for example the function `'scale_global_reference'` of the source file `'<ProcFolder>/SubProcesses/setscales.f'`. The run card already proposes standard cuts, but user-defined ones can be added directly in `'<ProcFolder>/SubProcesses/cuts.f'`. These optional source code modifications can be cumbersome and, in future versions, it is possible that MADANALYSIS5 [58] takes over this task if so wished by the user.

AMC@NLO running modes either belong to the class of *fixed-order* analysis, with `{ 'Mode' }` = `'NLO'` or `'LO'`<sup>22</sup>, or *event generation*, with `{ 'Mode' }` = `'aMC@NLO'` or `'aMC@LO'`.

In fixed-order analysis, no Monte-Carlo counterterm is considered so that unweighted events cannot be generated at NLO (the raw matrix element weights are not bounded from above in this case). Instead, the histograms of the analysis are filled on the fly with the weighted events generated (and not stored in this case). Some default standard observables are recorded automatically and the resulting histograms are stored in `'<ProcFolder>/Events/run_XX/'` in the *topdrawer* format. Additional user-defined observables can be coded directly in the source file `'<ProcFolder>/SubProcesses/madfks_plot.f'`. This running mode is equivalent to what programs like MCFM [46] do and as the name fixed-order suggests, matching to parton showers is not possible in this case. Fixed-order is therefore the method of choice for shower independent analysis and NLO inclusive cross-section computations.

For event generations, the Monte-Carlo (MC) counterterm allows for the unweighting of events at the price that they are not *physical*<sup>23</sup> until showered. Because the MC counterterms have a functional form depending on the shower program, it is crucial to specify it *before* event generation in `'run_card.dat'`. This means that a given sample of parton-level events can only be showered with the shower program it has been designed

---

<sup>22</sup>The Leading Order ('LO') modes are formally equivalent to what MADEVENT does. It is however convenient to have AMC@NLO being able to perform leading order predictions as well so as to make comparisons easier (all with the same framework and process output).

<sup>23</sup>In the sense that they are missing the NLO contribution accounted for by the parton shower

for<sup>24</sup>. Event generation with AMC@NLO is organized in three steps

- *step 0* – The total cross-section for each integration channel<sup>25</sup> is computed to an accuracy matching the parameter `'req_acc'` of the run card. MADFKS being based on adaptative Monte-Carlo integration, this step also serves to initialize the integration grids which shall remain fixed from this point on.
- *step 1* – Discrete importance sampling is employed to improve the unweighting efficiency and for each integration channel, the phase space is divided into a few *unweighting cells*. For each cell, its contribution to the total cross-section is computed<sup>26</sup> and the maximum weight occurring in it is stored for the unweighting of step 2.
- *step 2* – This step generates a number of events as specified by `'nevents'` in the run card. Once step 0 and 1 are performed, this step can be run alone several times (assuming the model and run parameters are left untouched) to generate more events, provided the `'req_acc'` parameter employed in step 0 and 1 was sufficiently<sup>27</sup> high.

The sample of unweighted parton-level events generated after step 2 is stored in `'<ProcFolder>/Events/events.lhe.gz'`. Unless the option `'-p'` (for parton-level) has been specified, AMC@NLO will automatically shower it with the program specified in the run card.

Due to the number of options and possibilities of the `'launch'` command, an alternative way is proposed to steer AMC@NLO: the user can start a dedicated *running console* directly from the main user interface by adding `'-i'` to `{Options}` of `'launch'`, for instance:

```
aMC@NLO> launch TestProc -i
[... ]
aMC@NLO_run>
```

Notice that `'_run'` is appended to the prompt to clearly indicate to the user that the interface environment has changed. It is now bound to the output process `'TestProc'` in the sense that any command executed here applies to this exported process. Also, the original set of commands for process generation, output and checks is no longer available<sup>28</sup> and replaced by dedicated ones for controlling AMC@NLO runs. Some functionalities are

<sup>24</sup>This might change in the future as it is possible in principle to reweight an already generated event sample by the weight of the MC counterterm suited for the shower program chosen by the user.

<sup>25</sup>As already mentioned, AMC@NLO exploits a multi-channel technique based on the diagrammatical information of the process. See ref. [105].

<sup>26</sup>To an accuracy which this time depends on both `'req_acc'` and the relative contribution of the particular channel to which the cell belongs.

<sup>27</sup>A rule of thumb is that one wants to perform step 0 and 1 with a relative accuracy of roughly the square root of the number of events generated.

<sup>28</sup>You can return to the standard user-interface at any point with the hotkey `'ctrl+d'` or the command `'EOF'`.

only available in this run interface, such as showering an already existing parton level event sample (the `'shower'` command), and the contextual help is more precise, so that for involved simulations, the use of this run interface is preferred.

Running AMC@NLO on a computer cluster is simply achieved by specifying `'--cluster'` in the `{Options}`. Several cluster types are supported and the details of the user's cluster architecture must be specified in `'MGPath/input/mg5_configuration.txt'`.

Finally, MADGRAPH5 supports scripting and it is possible to write a sequence of commands in a given file, `'mg5.cmd'` for example, and run `'MGPath/bin/mg5 mg5.cmd'` to automatically execute them all.

### Automatic testing of user-defined processes

MADGRAPH5 already includes extensive testing routines (see appendix A.1) helping the developers to make sure that the generic behavior of the implemented algorithms is correct and to insure a stable evolution of the code.

Unfortunately, process-dependent issues might escape those self-consistency tests as they are not able to cover the infinite set of possible inputs and models. It is therefore up to the user to investigate the sanity of MADGRAPH5 output and to this aim the command `'check'` provides a powerful automation of process-specific consistency checks.

```
MG5> check {Type} {Process}
Ex: MG5> check g g > t t~ g [virt=QCD]
```

The `{Type}` argument can be `'crossing'`, `'brs'`, `'lorentz'` and `'gauge'` for the checks 2, 4, 6 and 7 respectively, of those presented in sect. 3.1.4. If omitted, the default value is `'full'` and these four checks are run sequentially. The `{Process}` attribute is mandatory and the process specification follows the same rule as for the `'generate'` command, to the exception that only tree-level processes or MADLOOP5 standalone ones (i.e. with mode `'virt='`) are supported.

For loop processes only, the `'check'` command can also automatically profile the numerical code generated by MADLOOP5 and provide key statistics on it. With `{Type}='timing'`, the command returns timing measurements for the process generation and running in various scenarios and a memory usage report. With `{Type}='stability nPoints'`, the command runs the code for `nPoints` random kinematic configurations and returns the outcome of the different runtime numerical stability tests (see sect. 3.4.4).

The `'check'` command therefore offers an efficient way for the user to assess the validity of MADLOOP5 code for the virtuals while also providing the necessary information for him to decide if it is fast and stable enough for its purpose.

This concludes the description of the basic usage of AMC@NLO5 and MADLOOP5. For more information, visit the [amcatnlo.cern.ch](http://amcatnlo.cern.ch) webpage and [launchpad.net/madgraph5](http://launchpad.net/madgraph5) where questions and bugs can be reported.

### 3.4.2 Model independence: the UFO format

Great progress towards complete model independence was achieved when integrating MADLOOP5 within MADGRAPH5, thanks to the UFO format [67] for specifying the physics model properties. This format proposes an organization of the model information as a PYTHON module. The MATHEMATICA package FEYNRULES automatically generated a vast variety of BSM model files in the UFO format which can be loaded in MADGRAPH5 and used for phenomenology studies at tree-level. The general idea of this format is that of introducing a collection of objects mapping to the concepts that define a high energy particle physics model, these being `Particle`, `Vertex`, `Coupling`, `Parameter`, `CouplingOrder` and `Lorentz`. Each of these objects are essentially containers for the attributes defining them and conceived as general as possible to embody almost all (B)SM physics. This model module is loaded by PYTHON and translated into an internal representation specific to the computer code reading in the model. This two steps mechanism allows one to have a unique model file suited for a variety of physics tools which will extract from it the pieces of information of their interest. This greatly facilitates the interface between physics tools and reduces the possibility of inconsistencies in their inputs.

The nature of loop-computations necessitates from the model builder more information than required for LO studies. A crucial consequence of this is that a model file for a given BSM model in the UFO format cannot be used by MADLOOP as it stands. The missing information are the set of UV and  $R_2$  counter-terms which cannot be obtained directly by MADLOOP as they require a global analytic understanding of the Lagrangian so that they must be specified by the model. To this aim, we have extended the UFO format so as to include this lacking information while retaining the original flexibility.

A counterterm is represented by an instance of a new class `CTVertex` inheriting from the original one, `Vertex`, for tree-level applications. This new object features an additional attribute `loop_particles` characterizing the identity of the particles entering the loop this counterterm originates from. The color and Lorentz structure is specified in the same way as for regular vertices (see ref. [67]). However, the couplings of the `CTVertex` are specific to the particle content of the loop sourcing the counterterm (*i.e.* to each choice of `loop_particles`) and their `value` attribute is given as a dictionary identifying their expression as a Laurent expansion in the loop regularizing parameter  $\epsilon$  setting the number of dimensions  $d = 4 - 2\epsilon$ . With this syntax, one can independently specify the contribution of certain UV-counterterms to both the finite part and the residue of the single pole of the loop matrix element evaluation.

To cope with this, the parameters can be instances of either of two very similar classes, `Parameter` or `CTParameter`; the first having its `value` attribute as string and the second as a dictionary with helper functions to access it. The `Coupling` class remains the same, but the `value` attribute can now either be a simple string or a dictionary to directly define the terms of the Laurent expansion. To access this `value` attribute irrespectively of its nature, the `Coupling` class provides a dedicated function to access the  $n^{\text{th}}$  pole of the definition of the value independently of its type. In particular, if the coupling value is a string defining an expression including a `CTParameter`, this function will recognize it<sup>29</sup> and substitute the corresponding Laurent serie in the coupling value definition. The example below efficiently illustrates this seemingly complicated behavior:

```
MyCoup = Coupling(name = 'MyCoup',
                  value = '4.0 * g_s ** 2 * MyCTParam',
                  order = {'QCD' : 2})

MyCTParam = CTParameter(name = 'MyCTParam',
                        type = 'real',
                        value = {-1 : 'A', 0 : 'B'},
                        texname = 'MadRules')
```

In this case, `MyCoup.value(-1)` would return the single pole contribution `'4.0*g_s**2*A'` and `MyCoup.value(0)` the finite one `'4.0*g_s**2*B'`. The kind of loops supported by the model are specified via the new attribute `perturbative_expansion` of the `CouplingOrder` class. More details and examples about the UFO format for models allowing loop computations can be found in appendix A.2.

All the  $R_2$  and UV counterterms for QCD corrections have been coded by hand in the UFO model `'loop_sm'` available with the public distribution of AMC@NLO. This model, being able to perform both LO and NLO phenomenology, will eventually supersede the `'sm'` model suited for LO only. For now the switch from one model to another is performed automatically in a transparent manner depending on the user inputs. The FEYNRULES authors are actively working so as to be able to automatically produce UFO model suited for loop computations as easily as the BSM models are generated now for LO studies. Also within the Standard Model, a UFO model including QED corrections is being set up.

This shows that the original goal of identifying all sources of model dependance and isolating them within a flexible model module is now attained for loop computations with MADLOOP5.

---

<sup>29</sup>Notice that for more than one loop, it might be convenient to have the coupling value being defined in terms of more than one `CTparameter`, which renders cumbersome the substitution of their Laurent series in the coupling definition. This is why for now the `value(n)` function handles the presence of at most one `CTparameter` in the coupling definition.



### 3.4.3 Code optimizations

The flexibility of the MADGRAPH5 framework permits the implementation of optimizations structurally very involved. There are two class of optimizations, those affecting the process generation time and those improving the runtime speed. With MADLOOP, the generation time is faster than for any competitor and typically not a limiting factor, so that most of the effort was focused on optimizing runtime speed, critical for Monte-Carlo applications.

#### Process generation improvements

The MADGRAPH5 algorithm for tree diagram generation, described in ref. [7], is much more performant than its MADGRAPH4 counterpart, essentially because it already exploits the model vertices definitions when building the tree topologies.

MADLOOP5 fully benefits from this improvement and takes even further advantage of it. Let  $\{q_i^*\}$  be the set of identities of particles which have to be considered as L-cut particles when considering a certain kind of loops. The loop diagram generation algorithm outlined in 3.1.1 shows that when MADLOOP considers the L-cut particle  $q_1^*$ , it generates **all** loop diagrams which can possibly be cut at a loop line of this identity. In other terms, this means that the only loop diagrams missing are those without  $q_1^*$  circulating anywhere in the loop. It is therefore possible to significantly speed-up the L-cut diagram generation for the subsequent choices of L-cut particles  $q_i^*$  by explicitly forbidding any particle  $q_j^*$  already considered as a L-cut particle to appear in the loop. For QCD corrections for example, one starts with the gluon as the L-cut particle and the subsequent runs for the L-cut quarks are very fast as they only yield the closed fermion loops.

The original tree diagram generation algorithm was also modified so as to discard wavefunction renormalization diagrams and tadpoles already at the generation stage and as soon as the loop is formed, possibly even before the whole loop diagram is constructed.

For the rest of the generation steps, MADLOOP5 inherits from the existing optimizations brought by MADGRAPH5 to tree processes, but further specific optimizations for loop processes were implemented.

#### Efficient helicity summation

This is the first simple but crucial optimization of runtime speed. The naive approach for computing the quantity  $V(r)$  of eq. (3.1.2) is to evaluate each loop amplitude individually, interfere it with the Born amplitudes, and repeat this procedure over all contributing

helicity configurations<sup>30</sup>. This amounts to computing  $V(r)$  as follows:

$$V(r) \propto \sum_{h=hel} \sum_{l=loop} 2\Re \left( \underbrace{CT \left[ \int \frac{d^D q \mathcal{N}_{l,h}}{D_0 D_1 \cdots D_{n-1}} \right]}_{\mathcal{A}_{l,h}} \sum_{b=Born} C_{l,b} \mathcal{A}_{b,h}^* \right) \quad (3.4.1)$$

where for simplicity all indices carried by the amplitudes are understood and  $\mathcal{N}_{l,h}$  is the numerator of a certain loop diagram  $l$  for a given helicity configuration  $h$ . When the loop amplitudes color indices are contracted with those of the Born amplitudes, they yield the color factor  $C_{l,b}$  which depend on the identity of both the loop and Born diagrams  $l$  and  $b$ . The operator  $CT[\dots]$  corresponds to calling CUTTOOLS for a given numerator and denominator configurations so as to obtain a numerical evaluation of the resulting integral. As explained in sect. 2.3, this operation is time consuming and the implementation of eq. (3.4.1), corresponding to the MADLOOP4 structure, had the great disadvantage that it necessitated a total of  $N_{HelConfigs} \times N_{loop}$  calls to CUTTOOLS for each evaluation of  $V(r)$  for a given phase-space point.

Profiling MADLOOP4 showed that half of the evaluation time was spent in CUTTOOLS so that speeding up the code necessarily implied reducing the number of call to CUTTOOLS<sup>31</sup>. This can in fact easily be achieved by realizing that the interference with the Born amplitudes can be computed before evaluating the loops with CUTTOOLS. Namely, this corresponds to reordering the computation of eq. (3.4.1) in this way<sup>32</sup>:

$$V(r) \propto \sum_{l=loop} 2\Re \left( CT \left[ \int d^D q \frac{\overbrace{\sum_{h=hel} \sum_{b=Born} \mathcal{N}_{l,h} C_{l,b} \mathcal{A}_{b,h}^*}^{\mathcal{N}'_{l,h}}}{D_0 D_1 \cdots D_{n-1}} \right] \right) \quad (3.4.2)$$

This yields exactly the same result but has the great advantage of calling CUTTOOLS with a modified numerator  $\mathcal{N}'_{l,h}$  which already accounts for the Born interference and helicity sum. This formulation only necessitates  $N_{loop}$  calls to CUTTOOLS which effectively means that the time spent in it for one evaluation of  $V(r)$  is divided by  $N_{HelConfigs}$  (a number typically larger than one hundred for complicated process). Another great advantage of this is that because the color factors  $C_{l,b}$  are now part of the numerator  $\mathcal{N}'_{l,h}$ , it is possible to add loops together *before* calling CUTTOOLS. The only constraint being the loop grouped together must have the same *topology*, namely the same denominator configuration  $D_0 D_1 \cdots D_{n-1}$ . Typically, for a given box loop contribution to the process  $gg \rightarrow gg$ , the cases where gluons, SU(3) ghosts or massless fermions circulate in the loop

<sup>30</sup>Of course, MADLOOP employs an helicity filter to discard helicity configurations which are identically zero. This helicity filter is setup by registering the numerical importance of each helicity configuration relative to the their sum.

<sup>31</sup>The code CUTTOOLS being already close from being fully optimized (the independent implementation of the OPP method in the code SAMURAI [131] shows similar timings).

<sup>32</sup>The optimizations discussed here are not an option for loop-induced processes for which one has no other option but to reduce each loop individually.

all share the same denominator configuration, so that they are identical from the point of view of the OPP algorithm and can therefore be processed together. In view of this, the formulation of eq. (3.4.2) is further refined in MADLOOP5 to take the final form:

$$V(r) \propto \sum_{t=\text{topologies}} 2\Re\left(\text{CT}\left[\int d^D q \frac{\overbrace{\sum_{l=\text{loop}\in t} \sum_{h=hel} \sum_{b=\text{Born}} \mathcal{N}'_{l,h} C_{l,b} \mathcal{A}_{b,h}^*}^{\mathcal{N}'_{t,h}}}{D_0 D_1 \cdots D_{n-1}}\right]\right) \quad (3.4.3)$$

where the number of calls to CUTTOOLS is further reduced to being equal to the number of loop topologies. Unfortunately, this optimization only improves the total evaluation time by a factor two as it is now completely dominated by the time spent in the several necessary evaluations of  $\mathcal{N}'_{l,h}$  which remained the same throughout these reformulations of the computation. The *open-loop* technique discussed in the next subsection is the modern method of choice for reducing the computational load of these many numerator evaluations.

### Open loop technique

In 2011, S. Pozzorini and his collaborators published in ref. [52] an original method for greatly speeding up the evaluations of the numerator  $\mathcal{N}'_{l,h}$ . The backbone of this formalism is the fact that the successive evaluations of the numerator  $\mathcal{N}'_{l,h}(q, \{p_i\})$  required by the OPP algorithm only differ by the value of the loop four-momentum  $q$  while the rest of kinematic configuration  $\{p_i\}$  remains identical. It is therefore convenient to cast  $\mathcal{N}'_{l,h}(q, \{p_i\})$  into a polynomial of the loop momentum  $q^\mu$ :

$$\mathcal{N}'_{l,h}(q, \{p_i\}) = \sum_{r=0}^{r_{max}} C_{\mu_0 \mu_1 \cdots \mu_r}^{(r)}(\{p_i\}) q^{\mu_0} q^{\mu_1} \cdots q^{\mu_r} \quad (3.4.4)$$

with  $r_{max}$  the maximal rank in  $q^\mu$  of the numerator  $\mathcal{N}'_{l,h}(q, \{p_i\})$ . The existence of such a decomposition of the loop numerator is guaranteed by the locality of the Lagrangian and the form of the massive vector boson propagator in Feynman gauge. The adage "Compute numerically when you can and analytically where you should" suggests to numerically evaluate the *open loop* coefficients  $C_{\mu_0 \mu_1 \cdots \mu_r}^{(r)}$ , because they depend only on the external kinematic configuration  $\{p_i\}$ , and to simply substitute in eq. (3.4.4) the numerical values of  $q^\mu$  the OPP algorithm requires. The key to the success of this formulation of  $\mathcal{N}'_{l,h}$  is to realize that  $C_{\mu_0 \mu_1 \cdots \mu_r}^{(r)}$  is a fully symmetric tensor of rank  $r$  with only  $\binom{3+r}{r}$  independent coefficients. In renormalizable theories, the maximal rank in  $q^\mu$  of an  $n$ -point loop is  $n$ , so that the total number of coefficients necessary to express the numerator of any loop of a  $2 \rightarrow 6$  process for example is at most  $N_{coef}(r_{max} = 8) = \sum_{r=0}^{r_{max}=8} \binom{3+r}{r} = 495$  which remains very manageable given the complexity of such a process. It is now clear that once the open loop coefficients evaluation are known, subsequent evaluations of the loop numerator for different values of the loop momentum are basically for free from a CPU

load point of view. The challenge is therefore to compute the open loop coefficients faster than several repeated direct evaluations of  $\mathcal{N}'_{l,h}$ .

Before detailing the MADLOOP5 approach to open loop, It is convenient to rewrite eq. (3.4.4), and more generally any polynomial  $P^{(r_{max})}(q^\mu)$  of maximal rank  $r_{max}$  in  $q^\mu$ , with the shorthand

$$P^{(r_{max})}(q^\mu) = C_{\dot{k}}^{(r_{max})} q^{\dot{k}} \quad (3.4.5)$$

where  $\dot{k}$  runs from 1 to  $N_{coeff}(r_{max})$ . The dotted index recalls that the Einstein summation rule is modified to match the expression of eq. (3.4.4). This abusive notation also implies that one picked a canonical ordering to concatenate into a one-dimensional array the set of independent coefficients  $C_{\mu_0\mu_1\dots\mu_r}^{(r)}$ . The choice of this ordering is arbitrary, but a convenient one is given by

$$C_{\mu_0\dots\mu_r}^{(r)}, \mu_0 \leq \dots \leq \mu_r \rightarrow C_{\dot{k}}^{(r_{max})}, \dot{k} = N_{coeff}(r-1) + \sum_{i=0}^r \frac{(\mu_i + i)!}{(i+1)!(\mu_i - 1)!} \quad (3.4.6)$$

with  $N_{coeff}(-1) = 0$ . To make things more explicit, we show below the completely expanded version of the r.h.s of eq. (3.4.5) with  $r_{max} = 2$

$$\begin{aligned} C_{\dot{k}}^{(2)} q^{\dot{k}} &= C_0^{(2)} + C_1^{(2)} q^0 + C_2^{(2)} q^1 + C_3^{(2)} q^2 + C_1^{(4)} q^3 \\ &+ C_5^{(2)} q^0 q^0 + C_6^{(2)} q^0 q^1 + C_7^{(2)} q^1 q^1 + C_8^{(2)} q^0 q^2 + C_9^{(2)} q^1 q^2 \\ &+ C_{10}^{(2)} q^2 q^2 + C_{11}^{(2)} q^0 q^3 + C_{12}^{(2)} q^1 q^3 + C_{13}^{(2)} q^2 q^3 + C_{14}^{(2)} q^3 q^3 \end{aligned} \quad (3.4.7)$$

To compute the open-loop coefficients, MADLOOP5 adopts a structure very similar to the one outlined in sect. 3.1.3. In the traditional approach, wavefunctions are denoted  $w_j^{(\#)}$  where the integer ' $\#$ ' numbers them and the index  $j$  lives in the Lorentz representation of the particle this wavefunction describes. In the open-loop approach, the *loop* wavefunctions are promoted to more general objects representing polynomials in  $q^\mu$  and denoted  $W_{i,r,\dot{k},j}^{(\#)}$  with the additional index  $i$  specifying the choice of polarization vector for the first L-cut particle ( $G^\mu = \delta^{\mu i}$  in fig. 3.1.4) and  $\dot{k}$  labels the coefficients of the polynomial of rank  $r$  according to the convention of eq. (3.4.6).

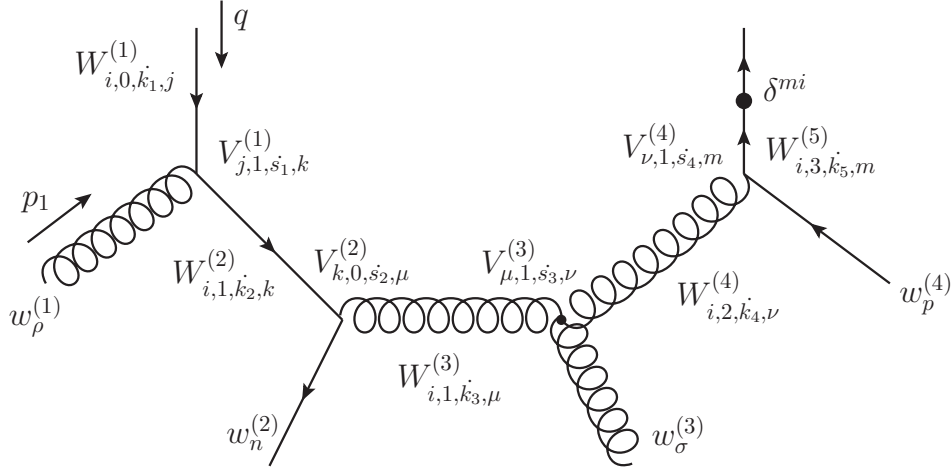


Figure 3.4.2: An example of MADLOOP5 construction of open loop coefficients.  $W$  denotes the loop wavefunctions and  $V$  the vertex polynomials. The figure depicts an L-cut diagram corresponding to a box loop when the two fermion lines at the top are sewed back together.

The fig. 3.4.2 shows a complete example of the different numerical objects manipulated by MADLOOP5 to construct the open loop coefficients of a standard box diagram. Notice that because the wavefunctions  $w^{(\#)}$  attached to the loop are independent of the loop momentum  $q^\mu$ , it is irrelevant to know whether they are directly external wavefunctions or originating from large subtrees. The starting loop wavefunction  $W_{i,0,k_1,j}^{(1)}$  correspond to the "polarization vector" of the first L-cut particle. It is a polynomial of rank 0 as it does not have any loop momentum dependence yet, so that the loop wavefunction can be non-zero for  $k_1 = 0$  only. Then, from fig. 3.1.4, we must set  $W_{i,0,k_1,j}^{(1)} = \delta_{ij}\delta_{k_1 0}$ .

The objects  $V_{a,r,s,b}^{(\#)}$  are the vertex polynomials of rank  $r$ . They correspond to the vertex plus propagator structures, with the loop momentum unspecified and the incoming and outgoing loop leg wavefunction indices ( $a$  and  $b$  respectively) left free. For example, the explicit expression of  $V_{j,1,s_1,k}^{(1)}$  in fig. 3.4.2 is

$$V_{j,1,s_1,k}^{(1)} q^{s_1} = \underbrace{ig_s \gamma_{ji}^\rho w_\rho^{(1)}}_{\text{vertex}} \underbrace{\gamma_{ik}^\mu (q_\mu + p_{1\mu})}_{\text{propagator}} \quad (3.4.8)$$

where the denominator of the propagator is already removed according to the need of the OPP algorithm. To be more definite, eq. (3.4.8) can be rewritten as to explicitly give the expression of the vertex polynomial for each value of  $s_1$

$$V_{j,1,0,k}^{(1)} = ig_s (\psi^{(1)} p_1)_{jk} \text{ and } V_{j,1,s_1,k}^{(1)} = ig_s (\psi^{(1)} \gamma^{(s_1-1)})_{jk} \text{ for } s_1 = 1, \dots, 4 \quad (3.4.9)$$

In renormalizable theories, the rank of the vertex polynomials is maximally equal to

one as only one power of the loop momentum can arise from either the propagator or the vertex itself (but not both). The structure of MADLOOP5 does not enforce such a limitation so that loop computations within effective theories<sup>33</sup> is straightforward for that matter.

The loop wavefunction  $W^{(n+1)}$  is obtained from the previous one  $W^{(n)}$  and the vertex polynomial  $V^{(n)}$  placed in between via the defining implicit relation

$$W_{i,r_1+r_2,k_1,j}^{(n+1)} q^{k_1} = (W_{i,r_1,k_2,m}^{(n)} q^{k_2})(V_{m,r_2,s,j}^{(n)} q^s) \quad (3.4.10)$$

The r.h.s. of eq. (3.4.10) is a multiplication of two polynomials in the loop momentum and each coefficient of  $W^{(n+1)}$  is obtained by summing the corresponding terms in the expanded product. This implies that a symmetrization of the coefficients is performed after each loop vertex and this step is crucial in order to limit their proliferation and the resulting computing time. To illustrate this, eq. (3.4.10) is rewritten here for the case  $r_1 = r_2 = 1$  with  $k_1 = 9$ , corresponding to the term in  $q^1 q^2$  which can come either from  $k_2 = 2, s = 3$  or  $k_2 = 3, s = 2$

$$W_{i,2,9,j}^{(n+1)} = W_{i,1,2,m}^{(n)} V_{m,1,3,j}^{(n)} + W_{i,1,3,m}^{(n)} V_{m,1,2,j}^{(n)} \quad (3.4.11)$$

Notice again the implicit summation on the index  $m$  which lives in the Lorentz representation of the loop particle preceding the vertex  $V^{(n)}$ . The notation of fig. 3.4.2 differentiates spin 1 indices from the spin 1/2 ones by switching from the greek to the latin alphabet. In MADLOOP5 code however, this difference is irrelevant as they both range over four integer values. Scalar indices (like for the  $SU(3)_c$  ghost) can be replaced by a dummy 1 and all related implicit sums simplify to a single term. MADLOOP5 structure is flexible enough to easily accommodate for indices of higher spin representations (such as spin-2 indices ranging over 16 integer values) so that it can in principle handle loops involving particles of higher spin.

MADLOOP5 iterates the use of eq. (3.4.10) to progressively compute all loop wavefunctions until it reaches the one of the second L-cut leg which includes the last vertex and the L-cut propagator. The open loop coefficients  $C_k$  of an  $n$ -point loop diagram are then in general simply obtained by "closing" the Lorentz trace

$$C_k = W_{i,r,k,i}^{(n+1)} \quad (3.4.12)$$

In the example of fig. 3.4.2, this translates into

$$C_k = W_{i,3,k,m}^{(5)} \delta^{mi} = \sum_{i=1}^4 W_{i,3,k,i}^{(5)} \quad (3.4.13)$$

with the sum made explicit for clarity.

---

<sup>33</sup>In this context, a relevant case is the Higgs effective theory

In addition to providing practically instantaneous evaluations of the numerator  $\mathcal{N}'_{l,h}$ , the open-loop technique offers, as byproducts, the following advantages.

- The operations performed on  $\mathcal{N}'_{l,h}$  to define  $\mathcal{N}_{t,h}$  in eq. (3.4.3) can be applied to the open-loop coefficients directly. In essence, this means that the loop amplitudes can be multiplied against the Born ones, summed over helicities and even added together (if they share the same denominator structure) *before* calling the OPP program to reduce them.
- The loop wavefunctions no longer depend on the loop momentum and they can therefore be recycled across the computations of different loop diagrams. For example, after having computed the box diagram of fig. 3.4.2, the computation of the triangle loop obtained by moving the branching point of  $w_\sigma^{(3)}$  to the line  $w_p^{(4)}$  can directly start from  $W_{i,1,k_3,\mu}^{(3)}$  which is the identical in both diagrams, hence saving significant amount of computational time. It is clear that the possibilities of loop wavefunction recycling depend on the choice of loop cut placements. MADLOOP5 implements the algorithm proposed in ref. [52] to optimize<sup>34</sup> this choice and this significantly improved the number of recycled loop wavefunctions.
- Once the open-loop coefficients are known, MADLOOP5 can be linked with tensor integral reduction tools to reduce each tensor loop appearing instead of using the OPP method to reduce the original physical loop at once. This option, not yet available, is very promising as an alternative to quadruple precision for stability detection and curing methods.

MADLOOP5 uses the open-loop technology by default, but it can be turned off via the option 'loop\_optimized\_output' of the interface in which case the structure of the resulting code is completely different. Despite being slower, the non optimized output mode provides a powerful self-consistency check and is still useful for loop-induced processes<sup>35</sup> and debugging purposes.

#### 3.4.4 Robustness against numerical instabilities

Once a process has been generated and the checks described in sect. 3.1.4 have been performed, the process is deemed correct by MADLOOP, and phase-space integration can be carried out. While doing so, kinematic configurations may be encountered that render it particularly difficult to execute the necessary numerical manipulations. Numerical instabilities are typically related either to inaccuracies in the solution of the system of linear equations built by CUTTOOLS (which determines the quantities in eq. (2.1.10)),

---

<sup>34</sup>The algorithm does not guarantee the choice to be maximally optimal and there is still room for improvement.

<sup>35</sup>In principle the open-loop technology can be applied to loop-induced processes as well, but not in the actual implementation of MADLOOP5 because the optimization of eq. (3.4.2) is not possible in this case.

or to the occasional occurrence of almost linearly-dependent subsets of external four momenta. The latter case is also problematic in naive implementations of tensor integral reduction algorithms because some Gram matrices, such as  $G_2$  in eq. (2.2.5), can become singular.

MADLOOP5 strategy for handling numerical instabilities is very different than that of MADLOOP4 (see [123]). The stability diagnostics of individual loop diagrams and based on CUTTOOLS internal stability checks are given up in favor of inclusive checks. For each kinematic configuration given in input to MADLOOP5, the code first produces a numerical evaluation of the quantity  $V(r)$  of eq. (3.1.2) using double precision arithmetics. The finite part of this first evaluation is denoted  $E_1^{DP}$ . Then, MADLOOP5 performs several new independent evaluations  $E_i^{DP}, 1 < i < n_{test} + 1$  of the same quantity but with some modifications in the computational setup. Each of these subsequent evaluations is referred to as a *stability test* in what follows. Finally, MADLOOP5 computes an estimation of the relative inaccuracy  $\chi^{DP}$  of the double precision result and decides that the kinematic configuration is unstable if

$$\frac{(n_{test} + 1)(\max\{E_i^{DP}\} - \min\{E_i^{DP}\})}{|\sum_{i=1}^{n_{test}} E_i^{DP}|} = \chi^{DP} > \epsilon \quad (3.4.14)$$

with  $\epsilon$  a user-defined threshold setting the maximal relative inaccuracy of the result. The quantity  $\chi^{DP}$  directly translates into the estimated number of accurate digits  $\kappa^{DP}$  via the relation

$$\kappa^{DP} = -\log_{10}(\chi^{DP}) \quad (3.4.15)$$

There are two kinds of stability tests available in MADLOOP5:

1. *Direction test* — Re-computing the loops with a different loop cut placement modifies the order of the propagators given in input to the OPP algorithm and it reshuffles the iterative solution for the scalar integral coefficients of eq. (2.3.8), yielding a very different result in case of numerically unstable reduction. Arbitrary loop cut modifications can be difficult to implement, except for the simplest one which consist in keeping the loop cut placement identical and *reading* the loop in the opposite direction. Effectively this corresponds to specifying to the OPP algorithm the denominators  $D_0 D_1 \dots D_n$  in the reversed order and to flip the sign of the loop momentum at which the integrand numerator  $\mathcal{N}(\ell)$  is evaluated<sup>36</sup>. MADLOOP5 implements this specific change of loop cut configuration as a stability test. When used together with the open-loop technology, this test has the great advantage of doubling only the time spent in CUTTOOLS as the open-loop coefficients computed for the first evaluation  $E_1^{DP}$  can be recycled for this test and need not

---

<sup>36</sup>In the terminology of sect. 3.1.1, this is the equivalent of a mirror operation on the L-cut diagram identity.



be recomputed.

2. *Lorentz test* — The quantity  $V(r)$  is normally Lorentz invariant and re-computing the loops with the input kinematic configuration Lorentz-transformed should yield identical results. MADLOOP5 considers a particular Lorentz rotation for this test. In principle, Lorentz boosts could be used too but only for helicity summed evaluations because they modify the reference vectors for helicity projection. Also, it is clear that if a given kinematic configuration is stable, so is its Lorentz rotated equivalent. This is not necessarily the case for the Lorentz boost transformation. The drawback of this test is that it doubles MADLOOP5 computation time.

In practice, MADLOOP5 default runtime parameters set  $n_{test}$  to 2, hence performing one test of each of the two kinds above. When these stability tests fail, the kinematic configuration is classified as an Unstable Phase-Space point (UPS) and MADLOOP attempts a stability recovery procedure. In MADLOOP4, this procedure was unsatisfactory because it failed quite often and implied slight modifications to the input kinematic configuration. The recovery method in MADLOOP5 is more direct and simply consists in re-performing the whole computation with quadruple precision arithmetics which is unfortunately hundred times slower. In order to systematically cure all UPS, it was observed to be important to upgrade the numerical precision of *both* the internal algebra of CUTTOOLS and of the computation of the numerator  $\mathcal{N}(\ell)$ . This implies that all quantities previously defined with 17 significant digits must be redefined in a format with 34 digits. This extension must be performed with care for the input kinematic configuration as it is crucial in this case that energy-momentum conservation and onshell relations be respected to quadruple precision accuracy (see appendix A.4). The same stability tests are performed on the quadruple precision results. These multiple evaluations are in this case denoted  $E_i^{QP}$  and they are compared as in eq. (3.4.14) to decide if the quadruple precision computation is stable enough. If it is not, the kinematic configuration is called an Exceptional Phase-Space point (EPS) and MADLOOP5 does not proceed with further rescuing attempts. Fortunately, this situation never occurs in practice as no EPS has ever been registered to this day, even for the most complicated processes<sup>37</sup>. Finally, the different parameters controlling the detection and handling of numerical instabilities can all be set in the MADLOOP param card (see app. A.5).

It is worth stressing here that irrespectively of how MADLOOP5 treats the input phase-space point (*i.e.* wether it is considered stable or unstable and computed in double or quadruple precision), MADFKS5 always checks the cancellation of the residues of the single pole of the loop matrix element with that of the real-emission contributions<sup>38</sup>. In the event that MADLOOP5 shall leave some unstable double precision computations undetected, this additional check would reveal this by recording a significant number of

---

<sup>37</sup>The smallest relative accuracy ever observed on quadruple precision evaluation is  $\epsilon = 10^{-9}$ .

<sup>38</sup>This single pole residue is computed by MADFKS directly from its analytic expression given in eq. (B.2) of ref. [105]).

kinematic configurations featuring imprecise single pole cancellation. This behavior has never been observed to this day, hence further assessing the sensitivity of the direction and Lorentz stability tests.

The fraction of UPS configurations is an important figure because their computation in quadruple precision is a factor 100 slower than for stable configurations. This means that a Monte-Carlo integration is already twice slower if as little as 1% of the phase-space points considered are unstable. Sec. 3.4.1 already mentioned the MADLOOP5 command 'check stability' which performs the direction and Lorentz stability test for a large number of random kinematic configurations<sup>39</sup>. We present here the stability results obtained via this command for four processes evaluated at 10'000 random kinematic configurations. The processes are

- $gg \rightarrow t\bar{t} + ng$  with  $n=0,1,2$  — These processes can be used as standard candles as they feature almost all of the most interesting loop topologies with massive and massless internal lines. Monitoring each  $n$  from 0 to 2 shows how the fraction of unstable points scales when pentagons and hexagons start contributing.
- $gg \rightarrow e^+\nu_e\mu^-\bar{\nu}_\mu b\bar{b}$  — This is the signature of the full leptonic decays of a top-quark pair, but it also includes all other singly-resonant diagrams. For this process, the complex mass scheme is turned on so that it is sensitive to possible numerical instabilities related to the use of complex arguments for the scalar loop master integrals. Also, some loops of this process involve two mass scales which is a complication not present in the precedent class of processes.

The following statistics are given on the quantities  $E_i^{DP}$  computed for each of the 10'000 kinematic configurations (the quadruple precision evaluations  $E_i^{QP}$  are computed only for the UPS, defined by a relative accuracy threshold  $\epsilon$  set to 0.1 for these runs.)

- $\beta(\Delta)$  — This is the most important figure; it specifies the fraction of points for which the estimated inaccuracy  $\chi^{DP}$  is larger than  $\Delta$ . The user can thus infer from the plot of  $\beta(\Delta)$  what is the fraction of UPS he would obtain at runtime from setting their defining threshold  $\epsilon$  to a different value than the default  $10^{-3}$ .
- $-\log_{10}(\text{med}\{\chi\})$  — The median for the set of computed inaccuracies  $\chi^{DP}$  and  $\chi^{QP}$ . The logarithm in base 10 is there in order to directly translate the result into the estimated number of correct digits.
- *Direction test Power*  $P = \log_{10}(\text{med}\{\eta\})$  — With the quantity  $\eta$  defined as

$$\eta = \frac{\chi_{\text{dir.test}}}{\chi_{\text{Lor.test}}} \quad (3.4.16)$$

---

<sup>39</sup>Except for a cut of  $P_t > 50\text{GeV}$  and  $\Delta R_{ij} > 0.5$  applied to massless final state particles (if any in the process chosen by the user for the stability check) in order to screen possible soft/collinear divergences.

with  $\chi_T$  defined like in eq. (3.4.14) but with only the evaluations  $E_i$  belonging to the test T. It is positive if the instability resolving power of the direction test is greater than the Lorentz one and negative otherwise.

- *Stability tests Consistency*  $C = \log_{10}(\text{med}\{\tau\})$  — With the quantity  $\tau$  defined as

$$\tau = \frac{\chi^{DP}}{|\langle E_i^{DP} \rangle - \langle E_i^{QP} \rangle|} \quad (3.4.17)$$

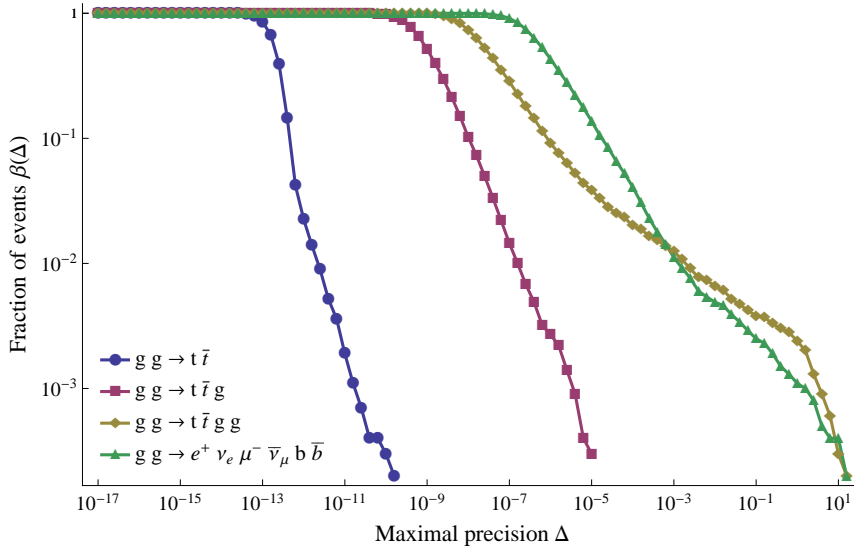
Notice that  $\tau$  can be computed only when quadruple precision computations have been performed. Ideally one would like to design stability tests on double precision results which produce an estimation of the inaccuracy as close as possible to the discrepancy with respect to the exact result (assumed to be the quadruple precision one here); this is the case if  $C$  is close to zero. If  $C$  is positive, the stability tests underestimate the accuracy of the double precision result (very unlikely) and they overestimate it otherwise.

The plot of fig. 3.4.3a shows a clear change of stability regime as the process multiplicity increases. This is reflected by the progressive breakdown of numerical precision from a median of 13 correct digits for the  $2 \rightarrow 2$  case down to 7 digits for the  $2 \rightarrow 4$  topologies. For all processes, the equivalent statistical measure  $-\log_{10}(\text{med}\{\chi^{QP}\})$  for quadruple precision evaluations shows that 17 digits at least are numerically stable<sup>40</sup> so that no EPS was ever registered during these stability checks. For the last two complicated processes, the fraction of UPS is  $\mathcal{O}(1\%)$ , so not a showstopper even if it is already enough to double the integration time. The power P of the direction stability test is very similar to the common Lorentz one and this suggests that for Monte-Carlo applications, one can afford to rely only on the direction stability test which only marginally increase the computation time. This can easily be done so by editing the value of the parameter 'NRotations\_DP' in the MADLOOP parameter card. The figure of consistency  $C$  shows that the stability tests employed tend to overestimate the real accuracy of the result in double precision by about one digit. This gives some confidence in the stability test efficiency, but the real figure of failure  $F(\epsilon)$  is, for a given UPS defining threshold  $\epsilon$ , the fraction of kinematic configurations for which  $\chi^{DP} < \epsilon$  but  $|\langle E_i^{DP} \rangle - \langle E_i^{QP} \rangle| > \epsilon$ . The recorded results of  $C$  however lead to anticipate<sup>41</sup> very small values for  $F(10^{-3})$ . Further analysis can confirm this if need be.

Process multiplicities higher than six are not presented here and the trend observed bodes ill for their numerical stability. The origin of numerical instabilities in the OPP reduction algorithm is not always well understood and a systematic cure is not yet possible in this context. The situation is better for tensor integral reduction algorithms

<sup>40</sup>The precise number cannot be established because the stability tests are performed on double precision arithmetics, even for the evaluations originating from computations in quadruple precision.

<sup>41</sup>There are nonetheless some configurations with  $C$  as negative as -8.



(a)

Process	$\beta(10^{-3})$	$-\log_{10}(\text{med}\{\chi^{DP}\})$	$P$	$C$
$gg \rightarrow t\bar{t}$	0%	12.7	-0.2	-0.6
$gg \rightarrow t\bar{t} g$	0%	9.0	-0.1	-0.9
$gg \rightarrow t\bar{t} g g$	1.25%	7.5	0.0	-1.1
$gg \rightarrow e^+ \nu_e \mu^- \bar{\nu}_\mu b \bar{b}$	1.11%	6.1	0.2	-1.7

(b)

Figure 3.4.3: Statistics on the stability tests performed by MADLOOP for characteristic processes, using 10'000 random kinematic configurations with  $P_t > 50\text{GeV}$  and  $\Delta R_{ij} > 0.5$  cuts on massless final state particles. For all these processes and the points considered, MADLOOP5 evaluations using quadruple precision arithmetics provided at least 9 stable digits.

where the numerically unstable regions can be identified and the reduction procedure accordingly stabilized around these points<sup>42</sup>. The computer codes for tensor integral reduction PJFRY++ [98, 99] and COLLIER [70] successfully<sup>43</sup> implement such solutions. MADLOOP5 will be able to benefit from these codes upon completion of its interface to these tools.

<sup>42</sup>In the example of sec. 2.2, one sees that the procedure fails around kinematic configurations of linearly dependent momenta which render the Gram matrix  $G_2$  singular. Around these configurations, it is possible to stabilize the numerical solution by means of Taylor expansions of Gram determinants which lift the artificial singularity introduced by the reduction procedure [69].

<sup>43</sup>The loop reduction in ref. [52] is performed with the computer code COLLIER and it shows a plot similar to fig. 3.4.3 but featuring a better scaling of the numerical accuracy.

As sect. 3.4.5 shows, processes of this larger multiplicity are already too slow in double precision for Monte-Carlo applications, so that their numerical instabilities is not the limiting factor. As of running MADLOOP5 output for these more involved processes on only a couple of kinematic configurations to use as a cross-check of an independent faster code, this is still possible thanks to quadruple precision whose speed is not an issue in this case.

### 3.4.5 Performance benchmarks

Sect. 3.2 shows that all old intrinsic limitations of MADLOOP4 are relaxed in MADLOOP5, sect. 3.4.2 presents the UFO format paving the way ahead of the most imaginative model builders and sect. 3.4.4 assessed that numerical instabilities are nothing to worry about until heptagons are considered. It is then clear that the sole limitation of MADLOOP5 is its computational load and this section presents in details the repartition and amount of computing time for characteristic high energy physics processes. These processes are not chosen for their scientific relevance but in order to illustrate a class of complexity so that any process of the reader's interest can find its counterpart in table 3.4.4b.

Fig. 3.4.4a shows the pace at which the evaluation time for a given helicity configuration (polarized case) increases with the number of contributing Feynman diagrams. This seemingly linear behavior is in part due to the loop wavefunction recycling made possible by the open loop technology and which compensates for the fact that the loops of higher multiplicity processes are of higher rank and hence take longer to evaluate. For the  $n$ -gluon amplitude case, the open loop coefficients of the closed massless quark loops are each computed independently. The optimization consisting of computing such contribution once and multiplying it by the number of massless flavors considered in the model is quite trivial to implement as an ad-hoc fix and its effect is emulated here by forbidding the down, charm and strange flavors in the process definition. The same could have been done for  $gg \rightarrow t\bar{t}gg$  and it would have reduced the time  $t_{unpol}$  from 16.9 seconds to 11.4 seconds.

The number of independent helicity configurations explicitly computed by MADLOOP5 is indicated in the second column of table 3.4.4b. With the first kinematic configurations given in input to MADLOOP5, it sets up numerically a filter which discards the helicity configurations which are identically zero and attempts to put together helicity configurations whose contributions are consistently identical.

When not using the open loop technology, MADLOOP5 must recompute all the loop wavefunctions building the numerator  $\mathcal{N}(q)$  for each new value of  $q^\mu$ : this is typically much slower, by up to a factor 8 for the process  $gg \rightarrow t\bar{t}gg$ .

MADLOOP5 computation time with open loops splits into the time  $t_{CT}$  spent within CUTTOOLS to work out the numerical solutions to OPP constitutive equations and the

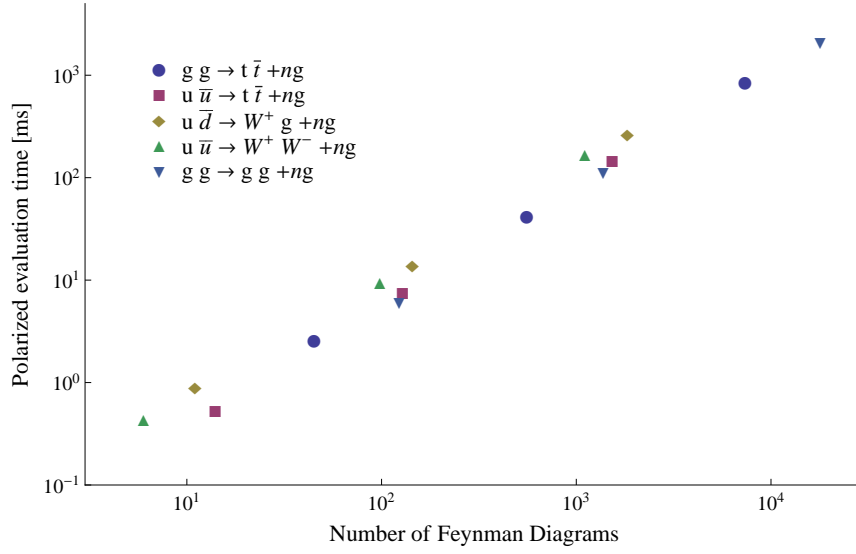
time  $t_{coeff}$  spent for the computation of the open loop coefficients. Thanks to eq. (3.4.2),  $t_{CT}$  is independent of the number  $N_{hel.conf}$  of helicity configuration computed while  $t_{coeff}$  is exactly linear in it. This means that for complicated enough processes with many helicity configurations, the computing time is dominated by  $t_{coeff}$ .

The processes chosen for this benchmark are identical to those of ref. [52] but we refrain the reader from directly comparing the timing  $t_{unpol}$  of the two codes, because the total number of helicity configurations computed are not the same as in ref. [52] since they assume the top-quark and W-boson to decay to massless particles so that only one helicity of these final state unstable particle is considered. When correcting for this and considering the most complicated  $2 \rightarrow 4$  processes, MADLOOP5 is at most 3 times slower than the program OPENLOOPS interfaced with OPP reduction tools. The reasons for this difference in speed are not yet understood.

The generation time and size of numerical code output for these processes is very moderate in regard of their complexity and therefore not the limiting factor. The *RAM* usage at runtime is  $\mathcal{O}(100Mb)$  for the  $2 \rightarrow 4$  processes which is no obstacle for modern clusters. The real limitation for Monte-Carlo applications lies in  $t_{unpol}$  which is typically 2ms for  $2 \rightarrow 2$ , 50ms for  $2 \rightarrow 3$  and 2s for  $2 \rightarrow 4$  processes. It is difficult to translate these timings directly into an estimation of the related computing time for phenomenology studies as this depends on many factors. Most importantly, the number of integration channels must remain under control and ideally be smaller than the number of cluster cores at disposal. Also, the nominal time  $t_{unpol}$  must be increased by  $t_{CT}$  to account for the direction stability test and the result yet multiplied by  $(1 + 100 \cdot \beta(\epsilon))$  for the time spent in the re-computation of UPS points in quadruple precision. With MADFKS and its current computational organization of the integration, it is challenging<sup>44</sup> to study any process at NLO for which the virtuals evaluation time for one phase-space point exceeds a couple of seconds. This table shows that AMC@NLO5 is for now limited, when using MADLOOP5 for loop computations, to the study of  $2 \rightarrow 4$  processes at most, simply because of CPU power. In the future and if proven necessary, the integration structure can easily be made fully parallel so as to be able to exploit arbitrarily large computing resources, hence opening the way to the study of NLO corrections to even more complicated processes. A more detailed list of all the processes already attempted with the current architecture and validated by the AMC@NLO collaboration can be consulted at [amcatnlo.cern.ch](http://amcatnlo.cern.ch).

---

<sup>44</sup>Even with clusters of arbitrarily large size because at this stage step 0 and 1 of the computation (see 3.4.1) are not fully parallelized, so that one is still forced to run the slowest integration channel of virtual origin on a single node.



(a)

Process	$N_{diags}$	$N_{hel.conf}$	$t_{unpol}$ [ms]	$t_{pol}$ [ms]	$t_{gen}$ [s]	$C_{size}$ [Mb]
$gg \rightarrow gg / dcs$	123	3/16	10.3 (62%)	5.9 (38%)	18.2	0.7
$gg \rightarrow t\bar{t}$	45	6/16	5.4 (66%)	2.5 (25%)	12.8	0.6
$u\bar{u} \rightarrow t\bar{t}$	14	3/16	0.72 (42%)	0.52 (20%)	9.1	0.4
$u\bar{d} \rightarrow W^+g$	11	6/24	1.51 (52%)	0.87 (16%)	13.9	0.4
$u\bar{u} \rightarrow W^+W^-$	6	10/36	1.0 (69%)	0.4 (21%)	12.4	0.5
$gg \rightarrow ggg / dcs$	1373	20/32	940 (93%)	110 (44%)	208	4.0
$gg \rightarrow t\bar{t}g$	556	32/32	381 (92%)	41 (29%)	62	1.5
$u\bar{u} \rightarrow t\bar{t}g$	128	16/32	28 (78%)	7.4 (18%)	18.3	0.7
$u\bar{d} \rightarrow W^+gg$	144	12/48	37 (69%)	13 (17%)	24.3	0.8
$u\bar{u} \rightarrow W^+W^-g$	98	36/72	82 (91%)	9.3 (24%)	35.3	0.8
$gg \rightarrow gggg / dcs$	17900	50/64	51500 (96%)	2020 (65%)	38300	231.0
$gg \rightarrow t\bar{t}gg$	7356	64/64	16900 (97%)	826 (35%)	12300	25.5
$u\bar{u} \rightarrow t\bar{t}gg$	1530	32/64	1010 (88%)	142 (22%)	180	3.1
$u\bar{d} \rightarrow W^+ggg$	1827	24/96	1300 (84%)	260 (20%)	254	4.0
$u\bar{u} \rightarrow W^+W^-gg$	1108	72/144	2820 (95%)	166 (25%)	204	2.3

(b)

Figure 3.4.4: Benchmark of MADLOOP timing performances, using open-loop technology and the OPP loop reduction algorithm, for characteristic processes on an APPLE laptop of the macbook pro series, single core usage of an i7, 2.8 GHz CPU with the gfortran v4.6.2 compiler, and optimizations turned off. Similar timings have been obtained with different compilers and compiler options. The percentage in parenthesis correspond to the fraction of time spent in the computation of the open-loop coefficients. The quantity  $C_{size}$  indicates the size of the source code, including the helicity and color factors data. The notation ‘/ dcs’ indicates that the corresponding massless quark contributions have been removed to emulate the fact that one could very easily group them together for any serious application of that process.





# 4 LHC phenomenology with AMC@NLO

The high level automation achieved with AMC@NLO allows one to quickly produce NLO predictions matched to parton showers for the processes relevant to experimental analysis or prospective theoretical work. The long list of NLO cross-sections for the processes of table 3.2 could not have been obtained in such a short time via ad-hoc computations by hand and it thereby attests the efficiency and flexibility of the framework. AMC@NLO can however do much more and produce fully differential analysis for all kind of observables and the four publications [104, 103, 102, 101] provide examples of such an application. In the first section of this chapter, I wish to recap the results obtained in [103] for the production of a scalar or pseudo-scalar in association with a top pair obtained using the AMC@NLO4 framework. In the second section, I present an unpublished calculation to NLO in QCD of triple vector boson production at the LHC using AMC@NLO5 which, among other things, illustrates the use of MADSPIN for simulating the vector boson decays.

## 4.1 AMC@NLO4 applied to $pp \rightarrow H/A t \bar{t}$

A new bosonic resonance has recently been observed at the LHC [2, 55] and is highly expected to be the long-sought Higgs boson, the scalar remnant(s) of the Englert-Brout-Higgs mechanism [96, 121, 120] in the standard model. At the end of 2011, both the ATLAS [1] and CMS [54] experiments at the LHC have recorded some excess of events in four-leptons analysis consistent with the decay of a Higgs boson of about 125 GeV into weak vector bosons. A corresponding excess<sup>1</sup> was also seen in the two-photons analysis, receiving contribution from the Higgs boson via its loop-induced decay<sup>2</sup>. Finally, some evidence is also seen at the Tevatron [4] in the  $b\bar{b}$  Higgs decay channel, although the analysis suffers from large uncertainties and features a poor mass resolution. It is by now clear that these excesses are not experimental flukes but all consistent with the SM Higgs.

The days of the Higgs discovery now give way to the era of more precise measurements for the determination of its properties and couplings. A coordinated theoretical/experimental effort in the last years has led to a number of remarkable achievements in the accuracy and usefulness of the available theoretical predictions, and in the role these play in current analysis techniques [77, 78]. The parity of this new resonance is a crucial one to determine

---

<sup>1</sup>Although marginally larger than expected.

<sup>2</sup>This observation rules out the possibility of a vector-like Higgs boson, since an onshell spin-1 particle cannot decay into two massless spin-1 bosons as proved by the Landau-Yang theorem [157, 126].

and several strategies have been proposed already (see ref. [133] for a list of references on that topic). We wish in this section to relate the main results of our publication [103] showing an alternative way to probe the parity of a scalar Higgs-like particle. This is Higgs production mode in association with a top quark pair, which is directly sensitive to the top Yukawa coupling, so that its study can potentially also provide constraints on its value.

Given the branching ratios of a Standard Model Higgs with mass around 125 GeV, its study at the LHC is very promising since many decay modes are accessible. Its dominant decay mode, into a  $b\bar{b}$  pair, is challenging to observe, being completely overwhelmed by the irreducible QCD background. A possible solution is that of considering the Higgs in association with other easier-to-tag particles<sup>3</sup>. An interesting case is that of a top-antitop pair, since the large Yukawa coupling  $t\bar{t}H$ , and the presence of top quarks, can be exploited to extract the signal from its QCD multi-jet backgrounds. Unfortunately, this production mechanism is also plagued by large backgrounds that involve a  $t\bar{t}$  pair, and hampered by its rather small rates, and thus turns out to be difficult to single out. Several search strategies have been proposed, based on different decay modes: from  $b\bar{b}$  which leads to the largest number of expected events, to the more rare but potentially cleaner  $\tau\tau$  [18],  $WW^{(*)}$  [128] and  $\gamma\gamma$  [42] final states. All of them are in fact very challenging, and dedicated efforts need be made. For example, recently it has been argued that in the kinematical regions where the Higgs is at quite high transverse momentum, the  $b\bar{b}$  pair would be merged into one “fat” jet, whose typical structure could help in discriminating it from QCD backgrounds [43, 144] (boosted Higgs scenario).

It is then clear that accurate and flexible simulations, for both signals and backgrounds, can give a significant contribution to the success of any given analysis. Predictions accurate to NLO in QCD and at the parton level for  $t\bar{t}H$  hadroproduction have been known for some time [15, 16, 63, 62, 80], and recently confirmed by other groups [8, 123]. As for the most relevant background processes to the Higgs decay mode into  $b\bar{b}$ , NLO calculations for  $t\bar{t}b\bar{b}$  [41, 29] and  $t\bar{t}jj$  [30] are available in the literature. In this section, we extend the results for the signal to computing the associated production  $t\bar{t}A$  of a pseudo-scalar Higgs boson.

The work presented in this section has been performed in the AMC@NLO4 framework. All its calculational aspects, including the matching to shower with the MC@NLO method, are therefore fully automated. This is even more true now that such an analysis can also be performed with AMC@NLO5 and our results were, at the time of their publications, the first example of NLO computations matched to showers in which *all* ingredients of the calculation were automated, and integrated in a unique software framework. For the sake of this specific application, a dedicated comparison with the results of ref. [78] has been performed for the total  $t\bar{t}H$  cross section, and an agreement at the permil level was

---

<sup>3</sup>This is indeed the strategy pursued by the CDF and D0 collaboration at the Tevatron where the Higgs production was studied in association with an electroweak vector boson.

found.

### 4.1.1 Results

We present selected results for total cross sections and distributions relevant to  $t\bar{t}H/t\bar{t}A$  production at the LHC in three scenarios:

- I. Scalar  $H$ , with  $m_H = 120$  GeV;
- II. Pseudoscalar  $A$ , with  $m_A = 120$  GeV;
- III. Pseudoscalar  $A$ , with  $m_A = 40$  GeV;

where the Yukawa coupling to the top is always assumed SM-like,  $y_t/\sqrt{2} = m_t/v$ .

The three scenarios above allow one to compare the effects due the different parity of the Higgs couplings on total rates as well as on differential distributions. In this respect and even in light of the recent LHC findings, it is interesting to consider the situation in which the Higgs boson is light and pseudoscalar, as is predicted in several beyond-the-standard-model theories (see *e.g.* Refs. [76, 66, 95]).

The main purpose of this section is that of studying the impact of QCD NLO corrections at both the parton level and after shower and hadronization. For the numerical analysis we choose  $\mu_F = \mu_R = \left(m_t^t m_{\bar{t}}^{\bar{t}} m_T^{H/A}\right)^{\frac{1}{3}}$ , where  $m_T = \sqrt{m^2 + p_T^2}$  and  $m_t^{pole} = m_t^{\overline{MS}} = 172.5$  GeV. We have used LO and NLO MSTW2008 parton distribution functions for the corresponding cross sections. The parton shower in AMC@NLO has been performed with FORTRANHERWIG, version 6.520.

Scenario	Cross section (fb)					
	7 TeV			14 TeV		
	LO	NLO	$K$ -factor	LO	NLO	$K$ -factor
I	104.5	103.4	0.99	642	708	1.10
II	27.6	31.9	1.16	244	289	1.18
III	69.6	77.3	1.11	516	599	1.16

Table 4.1: Total cross sections for  $t\bar{t}H$  and  $t\bar{t}A$  production at the LHC ( $\sqrt{s} = 7, 14$  TeV), to LO and NLO accuracy. The integration uncertainty is always well below 1%. Scale choices and parameters are given in the text.

The predicted production rates at the LHC running at  $\sqrt{s} = 7$  and 14 TeV are given in Table 4.1 where, for ease of reading, we also show the fully inclusive  $K$ -factor. As far

as differential distributions are concerned, we restrict ourselves to the 7 TeV LHC, and begin by studying a few fully-inclusive ones (see figs. 4.1.1, 4.1.3, 4.1.2a and 4.1.2c). We then consider a “boosted” case, *i.e.* apply a hard cut on the transverse momentum of the Higgs (see figs. 4.1.2b and 4.1.2d). Finally, in figs. 4.1.4a to 4.1.4f we present our AMC@NLO predictions for correlations constructed with final-state  $B$  hadrons, which may or may not arise from the decays of the Higgs and/or of the tops (see a discussion on this point later).

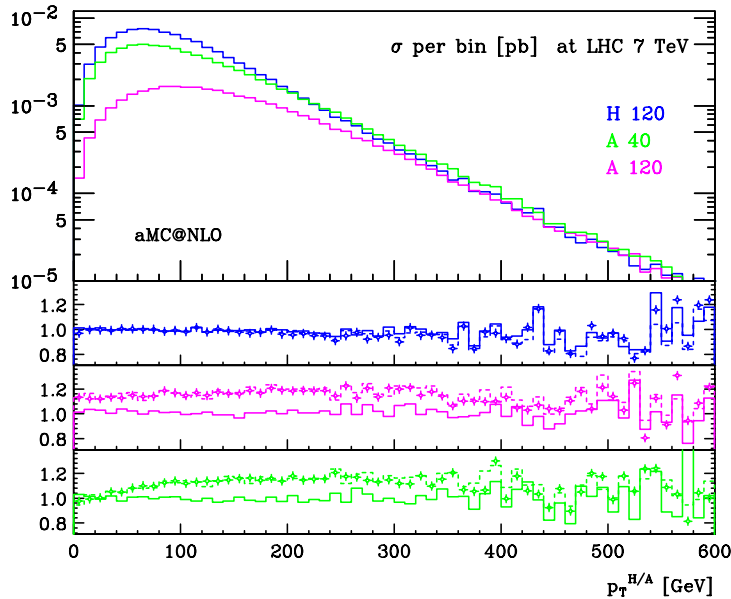


Figure 4.1.1: Higgs transverse momentum distributions in  $t\bar{t}H/t\bar{t}A$  events at the LHC ( $\sqrt{s}=7$  TeV), with AMC@NLO in the three scenarios described in the text: Scalar (blue) and pseudoscalar (magenta) Higgs with  $m_{H/A} = 120$  GeV and pseudoscalar (green) with  $m_A = 40$  GeV. In the lower panels, the ratios of AMC@NLO over LO (dashed), NLO (solid), and aMC@LO (crosses) are shown for each scenario.

We first note a very interesting feature of fig. 4.1.1: the  $p_T$  distributions corresponding to the three different scenarios, while significantly different at small transverse momenta, become quite close to each other at higher values. This is expected from the known pattern of the Higgs radiation off top quarks at high  $p_T$  in both the scalar and the pseudoscalar cases [64, 81, 15]. This difference is not affected by NLO corrections, and could therefore be exploited to identify the parity of the coupling at low  $p_T$ . On the other hand, the independence of the parity and masses of the  $p_T$  distributions at high values implies that the boosted analyses can equally well be used for pseudoscalar states.

#### 4.1. AMC@NLO4 applied to $pp \rightarrow H/A t \bar{t}$

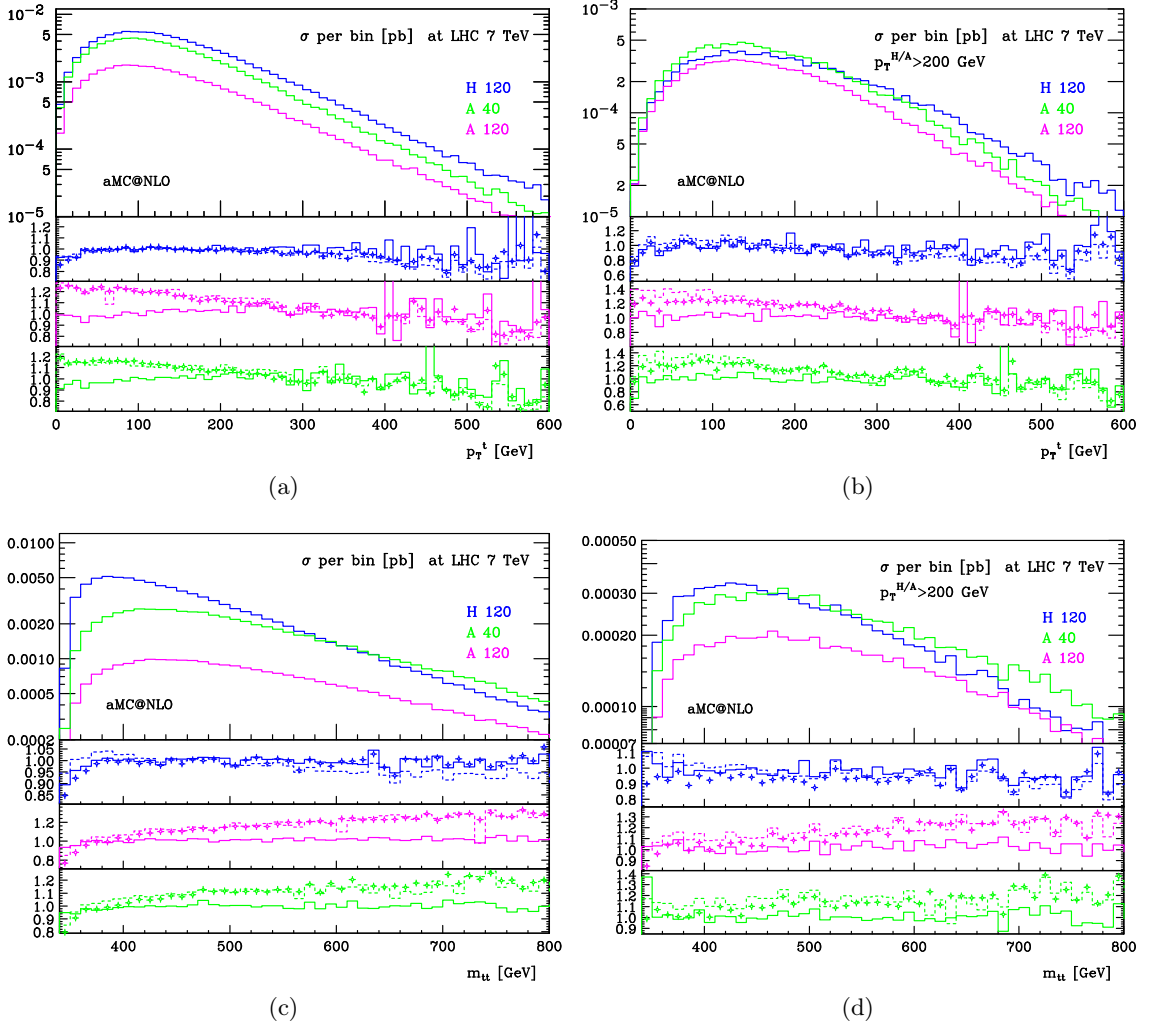


Figure 4.1.2: Transverse momentum and invariant mass distributions of the top quarks in  $t\bar{t}H/t\bar{t}A$  events at the LHC ( $\sqrt{s}=7$  TeV). The color scheme as described in caption of fig. 4.1.1 has been used. Figures 4.1.2b and 4.1.2d include only events selected with a cut on the Higgs transverse momentum  $p_T^{H/A} > 200$  GeV.

In general, we find that differences between LO and aMC@LO<sup>4</sup>, and between NLO and AMC@NLO, are quite small for observables involving single-inclusive distributions, see figs. 4.1.1, 4.1.2a and 4.1.2c. The same remark applies to the comparison between LO and NLO, and between aMC@LO and AMC@NLO. However, if the cut  $p_T^{H/A} > 200$  GeV is imposed (boosted Higgs analysis), differences between LO and NLO (with or without showers) are more significant, and cannot be approximated by a constant  $K$ -factor.

<sup>4</sup>We call aMC@LO the analogue of AMC@NLO, in which the short-distance cross sections are computed at the LO rather than at the NLO. Its results are therefore equivalent to those one would obtain by using, *e.g.* MADGRAPH/MADEVENT [6, 7] interfaced to showers.

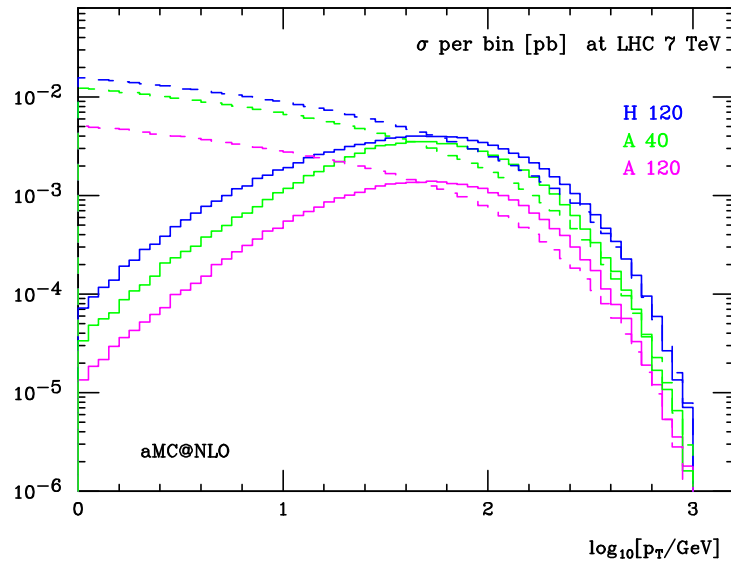


Figure 4.1.3: Transverse momentum of the  $t\bar{t}H$  or  $t\bar{t}A$  system. The same color scheme as in fig. 4.1.1 has been used. Solid histograms are  $\text{aMC@NLO}$ , dashed ones are NLO.

As is obvious, the impact of the shower is clearly visible in the three-particle  $p_T(t\bar{t}H/t\bar{t}A)$  distribution of fig. 4.1.3. This observable is infrared-sensitive at the pure-NLO level for  $p_T \rightarrow 0$ , where it diverges logarithmically. On the other hand, the predictions obtained after interfacing with shower do display the usual Sudakov suppression in the small- $p_T$  region. At large transverse momenta the  $\text{aMC@NLO}$  and NLO predictions coincide in shape and absolute normalization, as prescribed by the  $\text{MC@NLO}$  formalism.

## 4.1. AMC@NLO4 applied to $pp \rightarrow H/A t \bar{t}$

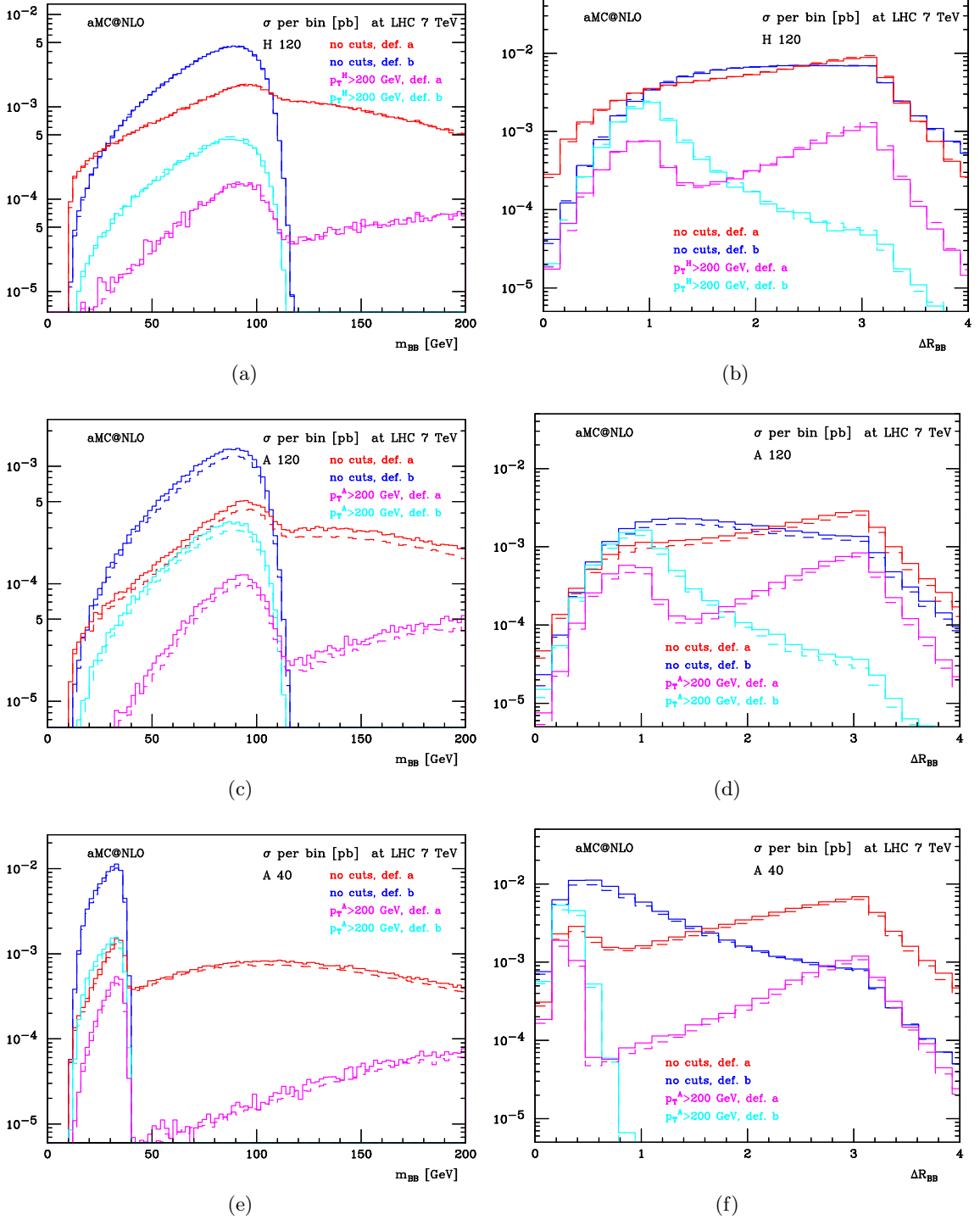


Figure 4.1.4: Distributions of the invariant mass and  $\Delta R_{BB}$  separation of the  $B$ -hadron pairs defined as  $a$ ) (red) and  $b$ ) (blue) in the text for the three scenarios considered. The results obtained by imposing  $p_T^{H/A} > 200$  GeV (magenta and cyan, respectively) are also displayed. Solid histograms are AMC@NLO, dashed ones are aMC@LO.

In our Monte Carlo simulations, we have included the  $t \rightarrow e^+ \nu b$ ,  $\bar{t} \rightarrow e^- \bar{\nu} \bar{b}$ , and  $H \rightarrow b\bar{b}$  decays at LO with their branching ratios set to one<sup>5</sup>. After showering, the  $b$  quarks emerging from the decays of the primary particles will result into  $b$ -flavored hadrons. As prescribed by the MC@NLO formalism, the showering and hadronization steps are performed by the event generator the NLO computation is matched to, *i.e.* HERWIG in this work. The parameters that control hadron formation through cluster decays are set to their default values in HERWIG [60]. Additional  $b$ -flavored hadrons may be produced as a consequence of  $g \rightarrow b\bar{b}$  branchings in the shower phase. For example, for scalar Higgs production at 7 TeV, about 2.7% and 0.5% of events have six and eight lowest-lying  $B$  hadrons respectively. In our analysis, we have searched the final state for all lowest-lying  $B$  hadrons, and defined two pairs out of them. *a)* The pair with the largest and next-to-largest transverse momenta; *b)* the pair with the largest and next-to-largest transverse momenta among those  $B$  hadrons whose parent parton was one of the  $b$  quarks emerging from the decay of the Higgs (there are about 0.2% of events with four or six  $B$  hadrons connected with the Higgs). The definition of *b)* relies on MC truth (and in all cases we assume 100% tagging efficiency), but this is sufficient to study the basic features of final-state  $B$  hadrons.

In figs. 4.1.4a to 4.1.4f we plot the pair invariant mass ( $m_{BB}$ ) and the  $\eta - \varphi$  distance ( $\Delta R_{BB}$ ) correlations between the  $B$ -hadron pairs defined as explained above. The effects of the NLO corrections to  $t\bar{t}H/t\bar{t}A$  are, in general, moderate. A cut of 200 GeV on the  $p_T$  of the Higgs is seen to help discriminate the  $B$  hadrons arising from the Higgs from those coming either from top decays, or from the shower. The shapes of the distributions are similar between scenarios I and II while, due to the lower Higgs mass, the  $m_{BB}$  and  $\Delta R_{BB}$  histograms peak at lower values in the case of a pseudoscalar  $A$  with  $m_A = 40$  GeV [118].

---

<sup>5</sup>We have neglected production angular correlations [111], as these are expected to have a minor impact for the kind of processes and observables we consider here. In case one would like to recover most of these effects, MADSPIN can be used to decay the events produced at parton level by AMC@NLO.



## 4.2 AMC@NLO5 applied to $pp \rightarrow Z W^+ W^-$

Triple vector boson production and their subsequent decays is an interesting process as it represents the most important background to an experimental analysis that requires many leptons. Such signatures are very clean and shared by many BSM processes, particularly the ones of Supersymmetry.

On top of this, it is also sensitive to the electroweak quartic couplings whose values could be further constrained at the LHC [116, 89]. This is of great importance since the only direct precise measurements of these couplings now come from the Large Electron Positron collider (LEP) [5] as the hadronic environment of Tevatron, combined with its comparatively low beam energy, proved to be challenging for such a measure [116, 89].

As expected from the computation of the QCD corrections to diboson production<sup>6</sup>, these lead to a large enhancement of total rates also in the case of triple vector boson production. In this latter case, K-factors as large as 2 have been computed by several groups for various combinations of final state electroweak vector bosons [9, 127, 119, 45, 38]. In this work, we choose to study the  $pp \rightarrow ZW^+W^-$  production which features the largest total rate and at variance with the work of ref. [119] which considers the decay of the vector bosons to leptons of three different families, we study the decay channels  $W^+ \rightarrow \mu^+\nu_\mu$ ,  $W^- \rightarrow \mu^-\bar{\nu}_\mu$  and  $Z \rightarrow e^+e^-$ . We use MADSPIN to implement these decays so as to retain most of the spin-correlation<sup>7</sup> and off-shell effects. This computation has been entirely performed within the now publicly available AMC@NLO5 framework (see sect. 3.4.1) and it stands as the first NLO computation of a triboson process matched to a parton shower. For the results presented in this section, the Higgs contribution was not considered but the same analysis including it as well as the vector boson decays at the matrix element level is readily possible<sup>8</sup> with AMC@NLO5.

### 4.2.1 Results at the LHC, 8 TeV

The goal of this study is to provide a full-fledged example of AMC@NLO5 use. In this spirit and because parton showers are anyway not supposed to have a major impact for this process, we only present the results matched to the parton shower HERWIG, version 6.520.

As aforementioned, the vector boson decays can be simulated either via MADSPIN (MS)

---

<sup>6</sup>Known for a long time, see [135] for a list of references to the pioneer works on that process. Also, a study of four leptons production at the LHC has been performed in ref. [102] with AMC@NLO4.

<sup>7</sup>This is especially true in this particular application because there are no non-factorizable contributions typical of loops involving the decay products so that all spin-correlations effects are retained, were it not for the singly and doubly resonant diagrams missing for lepton production.

<sup>8</sup>At the time of the writing of this thesis, a minor issue regarding how MADFKS handles competing resonances prevented us from doing so. This problem is now fixed and does not stand as an obstacle anymore. One can now even perform the computation within the complex mass scheme [71, 75].

or via a “flatly” distributed decay implemented by HERWIG. In order to investigate the magnitude of the off-shell and spin-correlation effects, the plots show the distributions obtained in both cases. However, notice that in none of these approaches one includes all the singly and doubly resonant diagrams.

We remind to the reader that the Higgs contribution is not accounted for and that the mass effects of the massive quarks in the loop are computed exactly and with zero width. The characteristic Born topologies contributing to this process are then the following

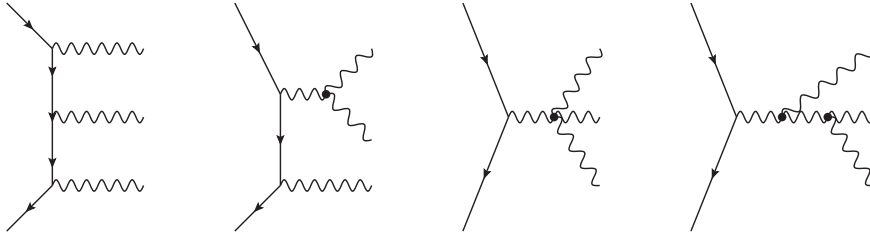


Figure 4.2.1: The four different Born topologies contributing to  $pp \rightarrow ZW^+W^-$  without the Higgs contribution. The intermediate virtual vector bosons can be  $Z$ ,  $W^\pm$  or the photon  $\gamma$ .

We use the LO and NLO MSTW2008 parton distribution functions with their corresponding values of  $\alpha_s(M_Z)$ . The center of mass energy is set to 8 TeV. The value of the other parameters used are:

Parameter	value	Parameter	value
$\alpha^{-1}$	132.507	$G_F$	$1.16639 \cdot 10^{-5}$
$m_W$	80.419	$\Gamma_W$	2.0476
$m_Z$	91.188	$\Gamma_Z$	2.441404
$m_t$	173.0	$m_b$	4.7
$n_{lf}$	4	$\mu_R = \mu_F$	$\sum_{V=\{W^+,W^-,Z\}} m_T(V)$

Table 4.2: Parameters used for this analysis with dimensionful quantities given in GeV and the transverse mass defined as  $m_T(V) = \sqrt{m_V^2 + p_T(V)^2}$ .

We adopt a fixed width scheme for the electroweak bosons. Notice that the default UFO standard model loaded by AMC@NLO5 for this analysis uses an electroweak input scheme with  $m_W$  and the Weinberg angle  $\theta_w$  as internal parameters.

We start by presenting in table 4.3 the total rates

LO	NLO	$K$ -factor
$35.33^{+1.48(4.2\%)}_{-1.41(4.0\%)}$	$59.91^{+3.41(5.7\%)}_{-2.82(4.7\%)}$	1.7

Table 4.3: Total cross sections in femtobarns for  $ZW^+W^-$  production at the LHC ( $\sqrt{s} = 8$  TeV), to LO and NLO accuracy. The integration uncertainty is always well below 1% and the variation in upper and lower indices correspond to the maximum deviations obtained by independently multiplying the renormalization and factorization scale by a factor 2 and 0.5.

The  $K$ -factor of 1.7 obtained together with the relatively large scale uncertainty, even at NLO, is consistent with the findings of ref. [119]. It is worth stressing here that the  $\mu_R$  and  $\mu_F$  scale variations were not obtained by iterating the whole computation but much more efficiently through the reweighting techniques presented in ref. [102].

We now turn to the results obtained for various observables selected for their sensitivity to either NLO corrections or spin-correlation and offshell effects. In all the plots presented in this section, the distributions have been normalized to the NLO cross-section including the branching ratios of the decays  $W^+ \rightarrow \mu^+\nu_\mu$ ,  $W^- \rightarrow \mu^-\bar{\nu}_\mu$  and  $Z \rightarrow e^+e^-$ .

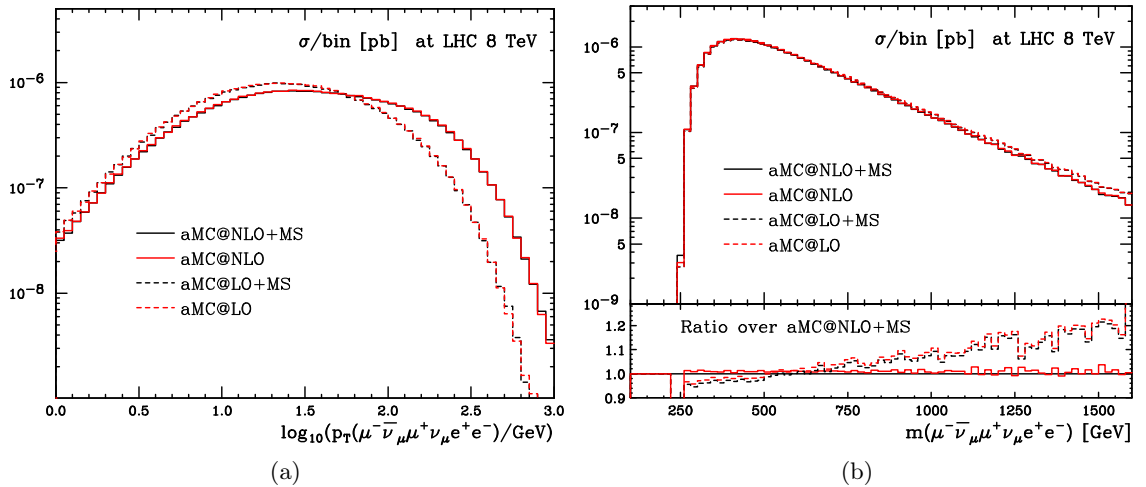


Figure 4.2.2: Transverse momentum and invariant mass distributions of the whole system in  $ZW^+W^-$  decayed events at the LHC ( $\sqrt{s}=8$  TeV). The red curves correspond to the vector boson “flatly” decayed by HERWIG and the black one by MADSPIN (MS). The dashed and solid curves are the LO and NLO predictions respectively. All curves are normalized to the one of AMC@NLO+MS.

Fig. 4.2.2a displays the same Sudakov suppression as observed in fig. 4.1.3 for the case of  $Ht\bar{t}$  production and results from the matching to the parton shower. At large values of the system  $p_T$ , the NLO distribution is larger than the LO one because the NLO matrix

element yields a first emission typically harder than the one from the parton shower of the LO sample.

The reconstruction of off-shell effects by MADSPIN is best observed with the invariant mass of the two electrons emerging<sup>9</sup> the Z-boson. For convenience, we also give here the same distribution for the  $W^+$  decay products.

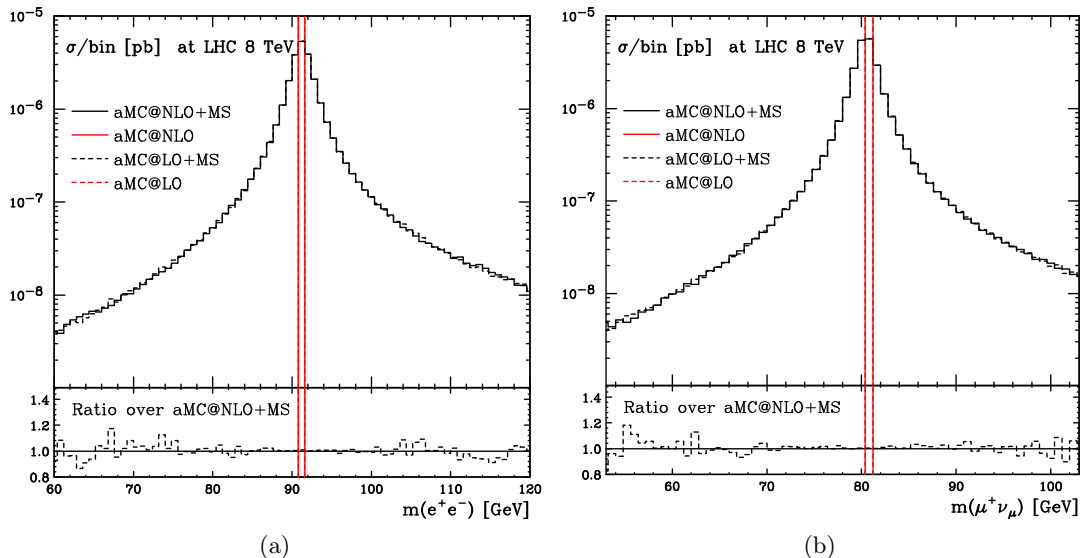


Figure 4.2.3: Invariant mass distributions of the decay products of the  $Z$  and  $W^+$  bosons.

When decayed with HERWIG, the invariant mass of the  $Z$  and  $W^+$  decay products fills a single bin placed at the corresponding pole masses and this is no surprise since the parton shower does not alter the parton level kinematics where the vector boson are produced exactly on-shell. This is unlike MADSPIN which thereby reproduces the Breit-Wigner shape characteristic of unstable particle propagators. One must however keep in mind that this is still an approximation which breaks down when far offshell because of the presence of some singly and doubly resonant diagrams not taken into account here (as well as the virtual photon decay to leptons).

We now turn to the investigation of the spin-correlation effects by considering the angular correlations between the decay products. We stress that we verified that LO results including all the contributions to the bosonic decays at matrix element level agree very well with MADSPIN predictions at LO. The angle between the directions of flight of leptons  $l_1$  and  $l_2$  measured in the laboratory frame is denoted by  $\theta(l_1, l_2)$  while  $\phi(l_1, l_2)$  is the same angle but with the direction of flights defined in the rest frame of the vector boson they decayed from.

<sup>9</sup>The electroweak shower is turned off by default in HERWIG so that the only electrons present at the hadron level are the two already present at parton level.

We show here distributions for  $\phi$  and  $\theta$  of the two lepton pairs  $(\mu^-, e^+)$  and  $(\mu^-, \mu^+)$

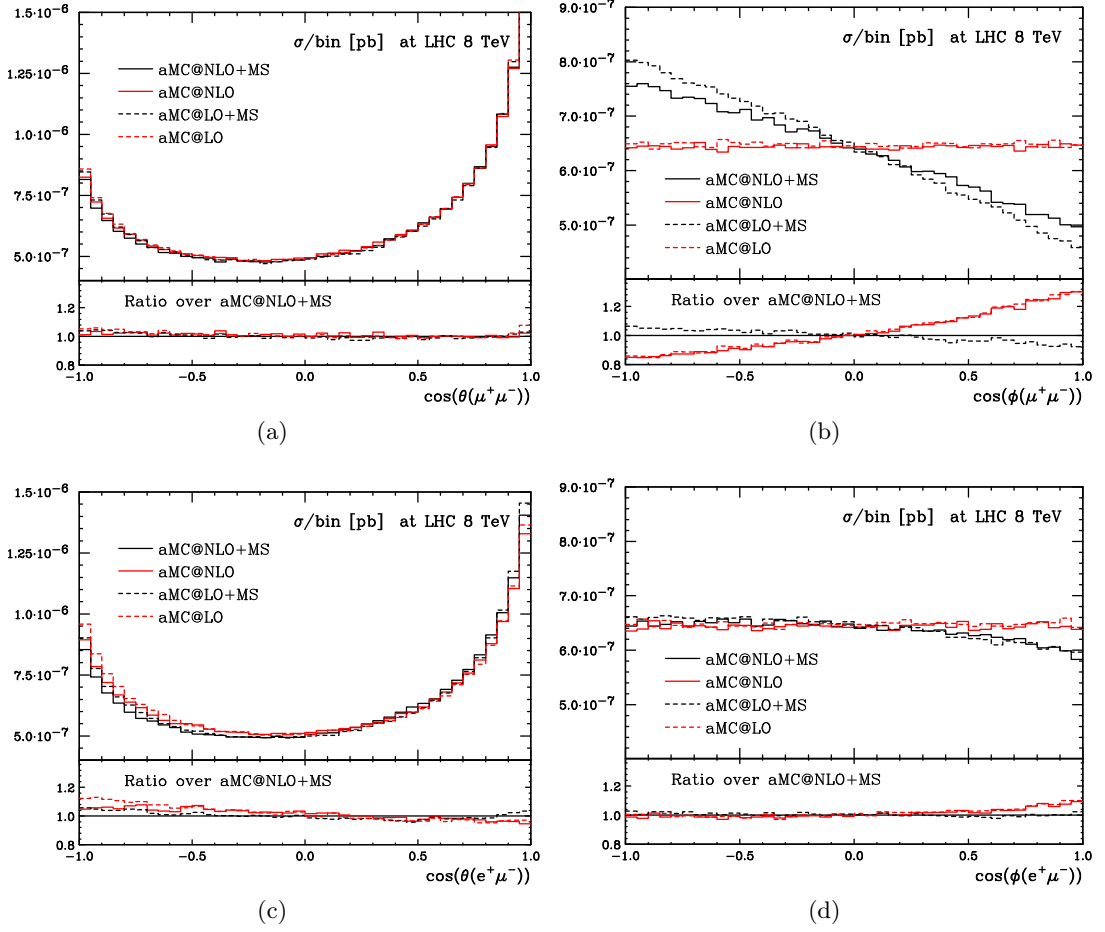


Figure 4.2.4: Distributions of the angles  $\theta(l_1, l_2)$  and  $\phi(l_1, l_2)$  as defined in the text.

The bowl shape of the  $\theta$  distributions is driven by the kinematic boosts of the decaying vector bosons and this washes out any spin-correlation effects. The  $\phi$  distributions are engineered not to be sensitive to this and we obtain in this case a flat curve for the sample decayed by HERWIG. This is expected since the PSMC gives no preference to a particular direction of flight in the rest frame of the mother particle. We see a significant departure from a flat distribution only in the case of the correlation between the decay products of the  $W$ 's, and it turns out that the  $Z$  decay products seem not to be spin-correlated with any of the other leptons. It is interesting to notice the small tilt of the  $\phi(\mu^+ \mu^-)$  slope when including NLO corrections. We should also mention here that a small MADSPIN impact can be observed in the  $\theta(e^+, e^-)$  distribution (not shown here) which is solely induced by the MADSPIN change of the  $Z$  kinematic (off-shell effect).

Another observable readily measurable at collider experiments and prone to be sensitive to spin-correlation effects is the pseudorapidity  $\eta$  of given leptons. We present here the

results for the charged leptons:

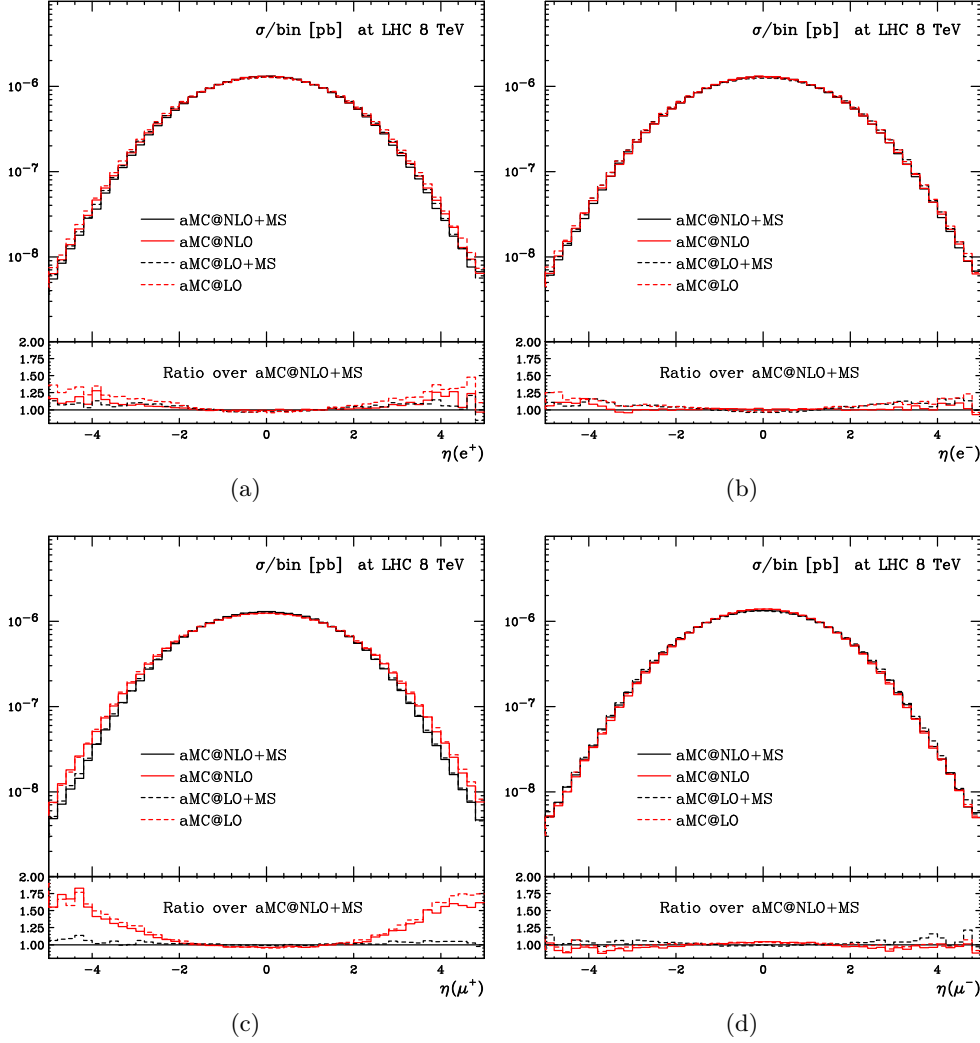
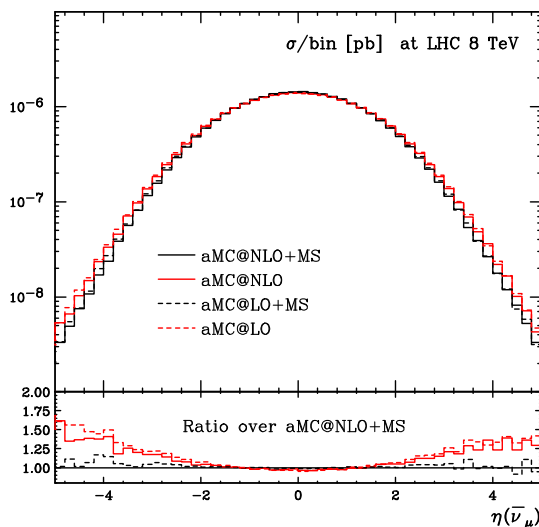
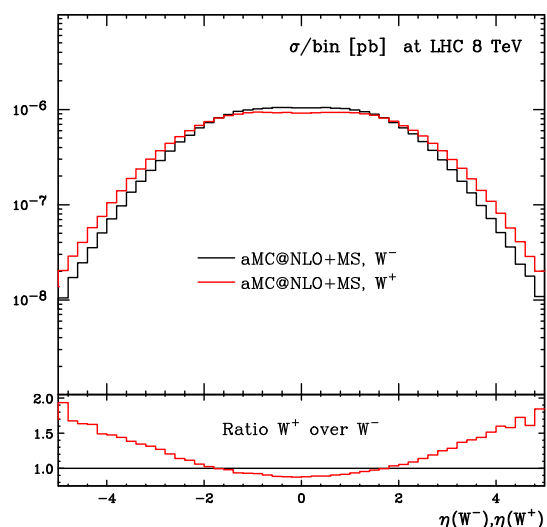


Figure 4.2.5: Pseudorapidity distributions of charged leptons.

Once again the  $Z$  decay products do not feature any striking change in the sample decayed by MADSPIN w.r.t. the one decayed by HERWIG, confirming the presumption that they are only mildly or not at all affected by spin-correlation effects. This is unlike the  $\mu^+$  case where the tail at large pseudo rapidity is almost twice larger in the MADSPIN sample. Interestingly, this is not observed in the case of  $\mu^-$ . We hypothesize that this originates from the different  $U(1)$  charge  $Y$  of left-handed leptons and anti-leptons because the antineutrino  $\bar{\nu}_\mu$  pseudorapidity (see fig. 4.2.6) exhibits the same behavior as  $\mu^+$  (the same holds true for  $\nu_\mu$  and  $\mu^-$ , although the former is not shown here). We also notice that with a cut of 20 GeV on the  $p_T$  of the mother of the lepton considered, the MADSPIN sample (unlike the HERWIG one) has even more forward antileptons and central leptons..


 Figure 4.2.6: Pseudorapidity of  $\bar{\nu}_\mu$ .

 Figure 4.2.7: Comparison of the  $W^+$  (red) and  $W^-$  (black) pseudorapidities.

The small difference in the shape of the  $\mu^+$  and  $\bar{\nu}_\mu$  pseudorapidities comes from the asymmetry between  $W^+$  and  $W^-$  induced by the PDF. Indeed, in the first and second topology of fig. 4.2.1, the  $W^+$  is always emitted by the parton and  $W^-$  by the corresponding *anti*-parton, leading to differences in  $W$  pseudorapidities since the valence  $u$  and  $d$  quarks are distributed at larger Bjorken  $x$ 's at a  $pp$  collider. This turns out to be of sizable effect, as shown in the fig. 4.2.7.

We conclude here by stressing once again that a computation including *all* contributions to the process  $pp \rightarrow e^+e^- \mu^+ \nu_\mu \mu^- \bar{\nu}_\mu$  is definitely possible within AMC@NLO5. For the present work, a total of one million events has been generated at both LO and NLO, necessitating only 2.5 and 15 hours of running time respectively and on a cluster with more nodes than the 104 integration channels. The slowest channels are those of the virtual contribution, whose evaluation time for a single phase-space point is  $t_{ML} = \mathcal{O}(40\text{ms})$ . The runtime speed of MADLOOP5 is therefore the limiting factor in this case, on which the total running time depends linearly<sup>10</sup>. The function 'check timing' of MADLOOP5 standalone (see sect. 3.4.1) indicates that  $t_{ML}$  increases<sup>11</sup> to  $\mathcal{O}(210\text{ms})$  ( $\mathcal{O}(53\text{ms})$ ) for the process  $pp \rightarrow e^+e^- \mu^+ \nu_\mu \mu^- \bar{\nu}_\mu$  ( $pp \rightarrow \tau^+ \tau^- \mu^+ \nu_\mu e^- \bar{\nu}_e$ ). One can therefore expect a million events to be generated in about three (less than one) days in this case.

<sup>10</sup>This is of course true only when comparing processes of similar convergence rate upon integration, otherwise the total number of phase-space point evaluations necessary to achieve a given numerical accuracy can vary significantly.

<sup>11</sup>This is a very moderate increase in evaluation time, given the growth of the number of loop diagrams from 55 for  $pp \rightarrow ZW^+W^-$  to 987 (381) for the decayed case to three (two) different fermion families. This partly results from the optimizations described in sect. 3.4.3 and also from the fact that the number of contributing helicity configurations drops from 54 to 8 when considering the decays to massless leptons.





# 5 Conclusion

## 5.1 Prospects

What was presented so far shows that the MADLOOP5 project within AMC@NLO lived up to its expectations. There are however still limitations to be lifted and several interesting optimizations to consider. We list here the main directions in which the work of this thesis will be pursued.

### 5.1.1 Computation of electro-weak corrections

The expansion parameter  $\alpha/2\pi$  in Quantum Electro Dynamics (QED) is roughly<sup>1</sup> hundred times smaller than the QCD one,  $\alpha_S/2\pi$ . QED corrections are therefore generally smaller than QCD ones but have nonetheless been shown to significantly affect and differential distributions of some processes (see the work of ref. [79, 72] for example). Moreover, what really matters is their size relative to the experimental precision which we know is going to increase to unprecedented levels thanks to the LHC. Also, ref. [32] shows an example of a process for which the contribution of the photon component of the proton<sup>2</sup> is very relevant. In what follows, we employ QED to refer to the complete electroweak SU(2)xU(1) sector, hence considering the effect of loops involving all four bosons  $W^\pm$ ,  $Z$  and  $\gamma$ .

Computations of higher orders in QCD should naturally be accompanied by the corresponding lower order correction in QED. For example, hadroproduction of dijet has already been partially computed at NNLO accuracy in QCD [147] because it features a very large total rate with a characteristic signature and it is therefore experimentally well measured, so that a precise theoretical prediction is necessary. At this order in QCD, NLO QED corrections are naively expected to contribute equally as much and they were shown to significantly contribute at large jet transverse energies [79, 134].

On a longer term perspective, lepton linear colliders like proposed in the CLIC [125] or ILC [39] projects aim at doing precision measurements for which theoretical predictions including QED corrections will be crucial.

---

<sup>1</sup>The exact ratio depends on the renormalization scale used for the running of these coupling constants.

<sup>2</sup>Which *must* be considered in the context of computations of QED corrections.

For these reasons, QED computations with MADLOOP5 within AMC@NLO5 have a wide range of applications but also imply heavy modifications in all steps of the calculation. There are mainly three technical difficulties to overcome:

- The MADLOOP5 algorithm can already generate electroweak loops in Feynman gauge and write out the corresponding numerical code for their computation. We are however still lacking a validated UFO model file containing the necessary information for treating such loops, typically their UV and  $R_2$  counterterms. The elaboration of such a model is already underway and the first results are promising with already many  $2 \rightarrow 2$  processes cross-checked against dedicated codes.
- The infrared divergences due to the photon<sup>3</sup> and color-charged parton emissions factorize different underlying born contributions with different QCD and QED coupling factors. The Monte-Carlo integration in MADFKS must be reorganized so as to correctly handle these contributions of different mixed coupling structures. In turn, this also means that MADLOOP5 output must be restructured in order to be able to provide one-loop matrix element evaluations factorizing definite QCD and QED couplings. This implies that loop amplitudes are no longer necessarily multiplied by all born contributions. For example, in the process  $d\bar{d} \rightarrow u\bar{u}$  discussed in sect. 3.4.1, the loop of fig. 3.4.1b should not be multiplied by the photon s-channel Born (but only the gluon s-channel one) in order to get the leading QED correction and only this one.
- Also, when considering the matching of NLO QED parton level predictions to a PSMC, the corresponding shower-dependent MC counterterms must be properly derived. These are not trivial tasks as PSMC electroweak showers are not well established yet.

This non-exhaustive list shows that this pioneer project involves the whole AMC@NLO collaboration. Upon completion of these tasks, we should be able to use our framework to systematically quantify the impact of QED corrections which were very often overlooked so far solely because of their computational complexity.

### 5.1.2 BSM model support

Non trivial extensions of the Standard Model are very complicated because of their large number of fields and couplings, or the complexity of the color, Lorentz and other group structures they may involve. The MADGRAPH5 framework has always put special emphasis on its flexibility and the UFO format (see sect. 3.4.2) it uses to input the model information is general enough to deal with almost any BSM model.

---

<sup>3</sup>Their corresponding subtraction counterterm are trivial to derive from the existing ones for QCD; essentially only color factors differ.

Even then, the implementation by hand of these UFO model file (see sect. 3.4.2) is very long and error prone, especially when also including the necessary information for loop computations. Fortunately, the MATHEMATICA package FEYNRULES, already mentioned in the introduction, solves this by automatically computing the Feynman rules as well as the  $R_2$  and UV counterterms directly from the Lagrangian given in input and then outputting those to a UFO module. For LO computations, this tool is now mature, extensively used and well tested. For the computation of loop contributions, FEYNRULES authors recently managed to upgrade the code so as to produce UFO models including the extra information described in appendix A.2 and the significant work of validating FEYNRULES output for loop models is in progress. The prospects are great as ultimately all already existing LO model files generated by FEYNRULES will be in principle available for one-loop computations as well. In certain cases however (typically effective theories) it might be necessary that the user provides, along with the Lagrangian, the UV renormalization conditions. Of course, when taking these new UFO loop models in input, MADLOOP5 must still be able to process their elementary objects and treat them correctly in the context of a NLO computation. In many cases, this is beyond MADLOOP5 capabilities which is for now tailored to the Standard Model event though its structure was conceived from the beginning to be general enough so as to eventually handle all BSM novelties.

Within a theory beyond the standard model, it is possible to distinguish three kinds of loop corrections: those of pure QCD origin with only QCD states running in the loop<sup>4</sup>, the pure BSM ones and finally the most general mixed case. We shall first focus on the computation of the pure QCD corrections, which are most relevant, and move on with the general case depending on its importance and the technical difficulties encountered. The interest of being able to tackle loops for any BSM model greatly depends on potential new discoveries at particle colliders, but it is worth mentioning here three direct applications and, for each, what are the necessary modifications in MADLOOP5.

- **Supersymmetric models**

This popular extension of the SM features an additional symmetry linking each fermion of the theory with a bosonic partner and vice-versa. It is appealing because it addresses the so-called hierarchy problem, features gauge coupling unification and provides a natural Dark Matter (DM) candidate as the Lightest Supersymmetric Particle (LSP). The phenomenology of this class of models has been thoroughly studied in the last thirty years and there exist some basic  $2 \rightarrow 2$  computations at NLO in QCD hardcoded in the program PROSPINO [143, 17].

Latest LHC data further excluded the phase-space of parameters available for the simplest incarnation of supersymmetric theories [14] but precise theoretical prediction for inclusive quantities might become relevant in direct discovery scenarios.

In the context of indirect detection/exclusion with future precision measurement,

---

<sup>4</sup>Notice however that the loop can still include BSM vertices if the QCD states interact with the BSM ones.

it is important to assess the impact on SM observables of supersymmetric states running in the loop.

As far as MADLOOP5 is concerned, the presence of Majorana particles is the greatest difficulty. Even if the present version of MADGRAPH5 handles them at LO, their proper treatment in the context of loop computations is still not properly addressed, as it has never been tested.

- **Extra-dimensional models**

This class of models considers the four space-time dimensions as embedded in a larger structure with  $N$  additional dimensions called the bulk. The compactification of the bulk dimensions and the dynamic of the particles in these characterize the model and provide a natural explanation for the hierarchy of particle masses in the SM. The Randall-Sundrum [145] model is arguably the most famous realization of such models, with only one additional dimension and the corresponding metric wrapped by an exponential factor. In such a theory, gravity naturally appears weaker on the four-dimensional brane as its bosonic force carrier, the graviton, is the only mode propagating in the bulk hence diluting its coupling strength.

The treatment of the gravitons necessitates MADLOOP5 to support spin 2 (and spin 3/2 for supersymmetric model) particles. This is achieved by MADGRAPH5 at LO but the generalization at NLO is not automatic.

- **Effective theories**

A well-known class of effective theories come from extensions of the SM with a strongly coupled hidden sector which is integrated out. Depending on the details of the hidden sector, the resulting models differ, but most go by the name of *Composite Higgs* [59] or *Technicolor* [100] theories. Perturbative expansion in effective theories is not straightforward as they are generally not renormalizable. It is however still possible to make sense of the corrections by adding, order by order in the expansion, sets of higher dimensional counter-terms which are set either empirically or by matching them to the underlying theory (when known).

One-loop computations in the Higgs effective theory<sup>5</sup> could give predictions for Higgs production with partial two-loop (which is NLO in this case) contributions.

The challenge for MADLOOP5 with these models is to handle operators of dimension higher than four. The loops in which these are present can have an integrand numerator of rank higher than the one of the denominator. The OPP procedure is more involved in these cases and as for the TIR techniques, they quickly reach their rank limitation and their numerical stability is unknown in this regime. Finally, multifermion interactions can also potentially be problematic.

---

<sup>5</sup>Where the Higgs production through gluon fusion via fermion loops is integrated out and yields the effective 3- and 4-point interaction  $ggH$  and  $ggHH$ .

### 5.1.3 Interface to tensor integral reduction codes

One of the major optimization brought to MADLOOP5 is the *open-loop* technique discussed in sect. 3.4.3, and which was shown in sect. 3.4.5 to significantly decrease the running time of the code generated. We recall here that the core idea of the method is to cast the numerator  $\mathcal{N}(\ell^\mu)$  into a polynomial in the loop momentum, as presented in eq. (3.4.4). As a byproduct of the method, the basis of this decomposition turns out to be well suited for the use of algebraic reduction techniques specific to tensor integrals, defined precisely as any loop integral with a numerator  $q^{\mu_0} q^{\mu_1} \cdots q^{\mu_r}$ . In a preliminary study, the computer code PJFRY++ has been successfully linked against MADLOOP5 for the trivial process  $e^+e^- \rightarrow d\bar{d}$ .

These Tensor Integral Reduction (TIR) techniques are complementary to the OPP one because for loop numerators of sufficiently small rank in  $l^\mu$  (typically  $\leq 6$ ), they are faster and more stable<sup>6</sup>. TIR techniques applicability for higher ranks is at present limited by the occurrence of very large algebraic expressions and OPP reduction is therefore preferred in this case.

Being able to exploit both of the two reduction methods allows for more reliable consistency and stability checks. In particular, TIR may solve certain of the instability issues mentioned in sect. 3.4.4 and hopefully avoid the inefficient use of quadruple precision.

Finally, by slightly modifying the architecture of the output code, it is possible to independently decide which reduction method to use for each loop, hence maximizing the efficiency of each method by limiting it to its range of best applicability. Such improvements would be of great help to study processes of similar complexity as  $pp \rightarrow t\bar{t}jj$  for which we showed in table 3.4.3 that the channel  $gg > t\bar{t}gg$  presents already more than a percent of unstable PS points (when requiring an accuracy of at least three digits) when solely relying on the OPP reduction method.

### 5.1.4 Further code optimizations

The different optimizations presented in sect. 3.4.3 significantly improved MADLOOP5 output runtime speed, but the integration time of the virtual contribution remains the limiting factor for almost all processes in AMC@NLO5, thanks to the very efficient FKS formalism adopted for the real subtractions terms (see sect. 1.2.3). It therefore remains essential to further optimize the code output by MADLOOP5. We shall then list here a couple of pending improvements, although none of them is expected to be very significant.

- The open loop coefficients of identical loops such as the pure massless quark ones in multi-gluon amplitudes are computed individually instead of being grouped together.

<sup>6</sup>This is true in TIR only when properly identifying the instability sources, which are vanishing Gram determinants, and modifying the reduction procedure around these points (as discussed in sect. 3.4.4).

This simple optimization will be implemented at some point, but preliminary studies<sup>7</sup> showed that its impact is moderate.

- The recycling of already computed wavefunctions across different diagrams plays a big role in the success of the MADGRAPH approach to tree diagrams computations. This is now also very efficient in the open-loop paradigm since loop wavefunctions can be recycled as well. It is then possible to implement this recycling also across helicity configurations, when the external particles of given subtrees share the same helicity configuration. This necessitates a consequent change in the structure of the output code and the gain is unclear and very process-dependent.
- Table 3.4.4b shows that the largest fraction of the computation time is spent in the determination of the open-loop coefficients<sup>8</sup>. To improve on this, one could have ALOHA generating optimized subroutines (similar to the HELAS ones) to obtain these coefficients at once (i.e. not in the progressive way described in sect. 3.4.3). Alternatively, the analytic dependence on the wavefunctions attached to the loop could be retained, similarly to what is done for the loop momentum. Unfortunately, both these alternatives become inefficient or inapplicable for large  $n$ -point loops (typically, with  $n \geq 3$ ) which are precisely the most time consuming ones.

In addition to these propositions, a popular technique for going around the slowness of one-loop computations is to first generate events according to the Born distribution and then reweight them with the virtual matrix-element. Also, it is possible to organize the NLO computation within MADFKS as an expansion in the inverse of the number of  $SU(3)_c$  colors  $N_c$  [109] so as to retain only the leading and possibly subleading terms. These very often constitute the largest fraction of the virtual contribution (much larger than naively expected from the fact that  $N_c = 3$ ) as shown in ref. [21, 85] for specific complicated processes. These alternative solutions to a direct speed-up of full-fledged loop computations are currently investigated by the AMC@NLO collaboration as they could allow us to reach a whole new class of process complexity.

---

<sup>7</sup>This optimization can be *emulated* simply by timing the evaluation of given processes while allowing for only one massless quark flavor to contribute.

<sup>8</sup>At least for the case of unpolarized phase-space points.

## 5.2 Closing remarks

The discovery at the LHC of the Higgs boson, or what looks very much like it, is a turning point in high energy physics. Not only is it the last missing piece of the Standard Model puzzle, but also the most speculative one as no scalar fundamental particle had ever been observed before. This confirms the impressive undisputed ability of the Standard Model at describing the microscopic structure of matter. This also comes with some sort of disappointment, in the sense that this finding does not provide any lead toward answers to the remaining open questions in particle physics, in particular a more natural explanation for the origin of electroweak symmetry breaking. It now becomes clear that the LHC will not provide sudden new unambiguous evidence for any beyond the Standard Model theory, at least with the current beam energy of 4 TeV. The quest to the observation of new physics then relies on *precise* measurements of Standard Model observables and their comparison with at least *equally precise* theoretical predictions. We presented in this thesis the details of the computer code MADLOOP that we elaborated, along with AMC@NLO, specifically for answering this need of precision. When developing this framework, special emphasis was put on being easy to use, automatic, reliable and flexible with respect to the observables, processes and physics models considered. These are key requirements to satisfy in order to have experimental collaborations include AMC@NLO in their analysis tools and thereby benefit from accurate NLO predictions.

We first summarized the various ingredients contributing to the computation of theoretical predictions, from the Lagrangian of a theory down to fully simulated events. We gave a brief outline of the FKS formalism, employed to isolate the soft and collinear divergences appearing in the real emission matrix element, and showed how the resulting poles cancel against those of the virtual contribution. The original Passarino-Veltman technique for one-loop computations is then illustrated, followed by the description of the more modern OPP loop reduction numerical technique which is used by MADLOOP via its implementation in CUTTOOLS. The strength of the OPP reduction algorithm is its agnosticism of the analytic details of the loop integrand numerator, making it well suited for fully automatic and flexible loop computations. One drawback of the method is the necessity of implementing extra Feynman rules and tree-diagram contributions for the computation of a rational term  $R_2$  missing in the finite part of the loops as computed by CUTTOOLS. We showed that by extending the existing UFO format for loop models, we could specify these  $R_2$  counterterms along with the UV ones and without harming the flexibility and automatism offered by the OPP approach.

In the second part, we presented the details of MADLOOP5, completely embedded in the PYTHON program MADGRAPH5. In particular, a novel algorithm was proposed for the efficient generation of loop diagrams from their tree equivalent obtained by a single cut. These L-cut diagrams and their computation can be generated using MADGRAPH5 tree-level capabilities, hence recycling the well-rounded MADGRAPH tree-level technology for the computation of loop integrand numerators. This technique proved to be extremely

efficient and achieved unprecedented process generation and output speed, given the flexibility of the tool. An introduction to the usage of MADLOOP5 and AMC@NLO5 follows and, although being far from exhaustive, it should efficiently guide the user through his first steps in the framework. Many optimizations were considered to speed the code output by MADLOOP5 but, despite bringing significant improvement, the integration of the virtual contribution remains the limiting factor in AMC@NLO5. The most important improvement brought to MADLOOP5 is the implementation of the recently proposed open loop technique in which loop integrand numerators are parametrized so as to keep the loop momentum dependence explicit. The many evaluations of this numerator required by the OPP reduction procedure are then practically at zero cost timewise. As a byproduct of the method, the possibility is given of linking MADLOOP5 with tensor integral reduction algorithms to be used in conjunction with CUTTOOLS for a maximal speed and numerical stability.

Numerical stability is known to often be problematic in loop computations and we presented the MADLOOP5 strategy to handle them. The detection of numerically unstable phase-space points is performed by making use of Lorentz and loop flow reversal invariance; it was shown to be a method sufficiently sensitive. The cure to these instabilities is a complete re-computation using quadruple precision arithmetics which, despite being a factor hundred slower, proved to always be stable so far. The capabilities of MADLOOP5 are concisely summarized in the two tables 3.4.4b and 3.4.3 revealing the performances of the code in terms of speed and stability. These numbers can be used as a reference to compare MADLOOP5 against other one-loop matrix element generators. The conclusion drawn from these timings is that the phenomenology of all  $2 \rightarrow 3$  SM processes are accessible as well as most  $2 \rightarrow 4$  ones, depending on the number of external color-charged states. The list of results for the processes of table 3.2, obtained with the older version MADLOOP4, exemplifies the variety of processes at reach.

We finished by showing an example of the study including NLO QCD correction of the phenomenology of two processes at the LHC. The first one is  $pp \rightarrow (H/A)t\bar{t}$  whose experimental study at the LHC could possibly help measuring the parity of the Higgs boson. The second one is  $pp \rightarrow ZW^+W^- \rightarrow e^+e^-\mu^+\nu_\mu\mu^-\bar{\nu}_\mu$  which draws interest in part because of its sensitivity to the SM quartic gauge couplings. Its NLO QCD computation and analysis was entirely performed within AMC@NLO5 and in a fully automatic way. The very recent tool MADSPIN was used for the decay of the vector bosons and we showed how it efficiently reconstructed offshell and spin-correlation effects.

We are looking forward to seeing the now public AMC@NLO enterprise help both theoretical and experimental physicists to access NLO predictions whenever needed.



# A MadLoop technical details

## A.1 MADGRAPH5 testing suite

To insure the stability of the development of the code and to guarantee the reliability of the published versions, MADGRAPH5 features a powerful and well organized testing suite. This is especially more necessary as PYTHON is an interpreted language, so that even syntax error can in principle slip through. Many tests specific to MADLOOP5 and AMC@NLO5 in general have been included and we outline here how they are organized, classified and executed.

All the source codes related to the tests are placed in the directory '`MG_root/tests`' and they can be run via the executable '`test_manager.py -p X`' where '`X`' is one of the three following capital letters designating a certain class of tests:

- '*U*' for *Unit tests* — These are simple and fast self-consistency tests which aim at executing all constituting functions or groups of functions of MADGRAPH5 and make sure that their output is consistent with what is expected from the predefined input coded in the test. These are the quickest tests to run and should assess that the basic mechanics of MADGRAPH5 are not corrupted.
- '*A*' for *Acceptance tests* — These are more high level tests which probe the behavior of MADGRAPH5 as a whole, by comparing the output of some predefined user input (typically a command in the MADGRAPH5 user interface) and make sure that the code does not crash and that the output is characteristic of what is expected by the user. These tests are typically longer to run and therefore considered only in case of potentially dangerous modifications to the code.
- '*P*' for *Parallel tests* — These are the checks of the highest level and they do not test directly MADGRAPH5 but rather its output, the numerical code for matrix element computations. It verifies that it successfully compiles and returns the correct numbers upon execution for predefined kinematic configurations. This is of vital importance for the stability of the MADLOOP5 code and such parallel tests are implemented for more than thirty loop processes. The reference numbers are taken either from MADLOOP4 or previous versions of MADLOOP5 which themselves were validated by comparisons such as presented in appendix B. These kind of tests are the longest to run and we have divided them into two groups, those whose name start with '`short_`' can be run altogether in about an hour while executing the whole set takes a day or so.

### A.2 UFO format for loop models

In this section, more detailed information is given on the new features to the UFO format providing the necessary additional information for loop computations. For each of the objects defined by the UFO format, we will discuss the meaning and values of the new attributes.

#### A.2.1 CouplingOrder

- **expansion\_order** : This attribute gives a constraint on the maximum value that can be taken by this coupling order for the squared matrix element. By default, this attribute is set to '-1', meaning that no constraint is applied.

*Example:* In the Higgs effective theory, one does not want to have a HIG-type coupling appearing more than once in a squared matrix element. This corresponds to setting `expansion_order=1`.

- **perturbative\_expansion** : This limits how many loops containing this coupling order can be present in a diagram generated from this UFO model. This attribute is '0' for coupling orders whose corresponding<sup>1</sup> loops are forbidden and '1' for those for which at most one loop of that kind is allowed. The default value is '0', suited for all tree-level models.

*Example:* Typically for the `loop_sm` UFO model, supporting only 1-loop QCD corrections, this parameter has this attribute set to 1 for QCD and 0 for QED.

- **hierarchy** : This information is necessary in order to set which are the numerically leading contributing diagrams when the user does not specify any coupling order. Each coupling defined in the model is assigned an approximative numerical *strength* represented by an integer. The strongest coupling is by default assigned the integer 1 and every other coupling is given an integer corresponding to how many orders of the strongest coupling are required to match the strength of this one. In principle, this is equivalent to  $\lfloor \log_{10}(\frac{g_{coup}}{g_{strongest}}) \rfloor$ , but this ratio can take different values at different energies and coupling orders are not necessarily in one-to-one correspondence with a given parameter. It is then very convenient to have an arbitrary numerical hierarchy among the coupling orders to let the model builder guide the selection rules at the diagram generation stage when no user-constraint is enforced. By default, the hierarchy of all coupling orders is set to '1'.

*Example:* In the SM, the UFO model would naturally set the hierarchy of the coupling order QCD to 1 and QED to 2.

---

<sup>1</sup>See the description of `{Process}` in sect. 3.4.1 to understand how a coupling order is associated to a kind of loops.

### A.2.2 Particle

- **loop\_particles** : This attribute defines the particle running in the loops sourcing the UV wavefunction renormalization. For a given loop, its particle content is described by an unordered list with each particle contributing appearing only once and with particle and anti-particles undifferentiated<sup>2</sup>. If several loops give the same contribution, their respective particle content can be put together in one list. All these particle content definitions are listed in this attribute.

*Example:* In the SM, the **loop\_particles** defined for the  $R_2$  vertex of the gluon bubble counterterm is `[[[u], [d], [s]], [c], [b], [t], [G]]`, meaning that massless fermion loops each give the same contribution, while the one from the massive quarks and gluon are different. Notice that the ghost does not appear here because its contribution is included in the value of the coupling associated to the `[[G]]` counterterm. It is possible to specify a triply nested empty list for the **loop\_particles** to include the full counterterm (i.e. summing together all loops contributing to it) in one single coupling. However, this simplification prevents the loop matrix element generator loading this model to select out particles as their appearance in counterterm contributions can no longer be disentangled.

- **counterterm** : This attribute sets this particle wavefunction renormalization counterterm  $\delta Z$  whose contributions are assumed to be of the form  $Z(\epsilon) = \prod_{i=1}^{N_{order}} \alpha_i^{n_i}$ , with  $N_{order}$  the number of coupling orders defined in the model. It is represented by a dictionary with an entry for each such a contribution. Entries keys are tuples of the form `'(ni, ..., nNorder, m)'` with  $m$  indicating that this contribution originates from the loop with particle content `loop_particles[m]`. The values mapped to these keys are the Laurent expansion of  $Z(\epsilon)$  given as a dictionary.

*Example:* In the SM, the 'counterterm' attribute to the gluon particle is `{(1,0,0):CTParam.GWcft_UV_c.value,(1,0,2):CTParam.G_UVb.value,(1,0,3):CTParam.G_UVt.value}`

### A.2.3 CTVertex

This class has the same information as the 'Vertex' class except for the following differences:

- **loop\_particles**: Exactly as for the **Particle** class.
- **couplings**: Same as for the original **Vertex** class except that here the keys of the dictionary have an additional entry to specify which loop content this counterterm coupling corresponds to.
- **type**: Strings such as 'UV' and 'R2' identifying the theoretical origin of the counterterm.

---

<sup>2</sup>By convention, the particle is put in the list.

## Appendix A. MadLoop technical details

---

As an example, we present below the gluon-gluon-Z-photon  $R_2$  counterterm from the SM UFO model supporting QCD-type loops.

```
V_GGZA = CTVertex(name = 'V_GGZA',
                  particles = [P.G, P.G, P.Z, P.A],
                  color = ['Tr(1, 2)'],
                  lorentz = [L.R2_GGVV],
                  loop_particles = [[[P.u], [P.c], [P.t]], [[P.d], [P.s], [P.b]]],
                  couplings = {(0, 0, 0) : C.R2_GGZAup, (0, 0, 1) : C.R2_GGZAdown},
                  type = 'R2')
```

### A.3 UV renormalization counterterms

In MADLOOP, UV renormalization is for now performed using a scheme which subtracts the massless modes according to  $\overline{\text{MS}}$ , and the massive ones at zero momentum (see *e.g.* ref. [16]). For QCD corrections, all UV counterterms except that relevant to mass renormalization give a contribution to eq. (3.1.8) which is proportional to the Born amplitude squared.  $C_A$ ,  $C_F$  and  $T_F$  denote the usual color factors.  $N_c$  is the number of colors, and  $n_{lf}$  and  $n_{hf}$  are the numbers of light and heavy flavors respectively that circulate in the loops (a quark is by definition heavy if it has a non-zero mass). The common prefactor  $N_\epsilon$  is defined as follows:

$$N_\epsilon = \frac{1}{16\pi^2} (4\pi)^\epsilon \Gamma(1 + \epsilon). \quad (\text{A.3.1})$$

If the Born cross section is of order  $\alpha_s^b$ , the contribution to eq. (3.1.8) due to strong-coupling renormalization reads:

$$V_{\alpha_s}^{\text{UV}} = b \left| \mathcal{A}^{(n,0)} \right|^2 g_S^2 N_\epsilon \left[ \frac{4}{3\epsilon} T_F n_{lf} - \frac{11}{3\epsilon} C_A + \frac{4}{3\epsilon} T_F \sum_{\{n_{hf}\}} \left( \frac{\mu_R^2}{m_{hf}^2} \right)^\epsilon \right], \quad (\text{A.3.2})$$

where the sum in the third term on the r.h.s. runs over all heavy flavors that circulate in the loops. The contribution due to the renormalization of the Yukawa couplings reads:

$$V_{\text{yuk}}^{\text{UV}} = - \left| \mathcal{A}^{(n,0)} \right|^2 g_S^2 N_\epsilon 2C_F \left[ \frac{3}{\epsilon} n_{\text{yuk},l} + \left( 4 + \frac{3}{\epsilon} \right) \sum_{\{n_{\text{yuk},h}\}} \left( \frac{\mu_R^2}{m_{\text{yuk},h}^2} \right)^\epsilon \right], \quad (\text{A.3.3})$$

with  $n_{\text{yuk},l}$  and  $n_{\text{yuk},h}$  the number of Yukawa vertices with massless and massive particles respectively. Color singlets and massless color triplets do not require any wave-function renormalization. The gluon wave function is renormalized only if there are massive color

#### A.4. Restoring precision on input kinematic configurations

triplets fermions running in the loop. Denoting by  $n_g$  the number of external gluons at Born level, the contribution to eq. (3.1.8) due to gluon wave-function renormalization reads:

$$V_{g_{\text{wf}}}^{\text{UV}} = -n_g \left| \mathcal{A}^{(n,0)} \right|^2 g_S^2 N_\epsilon T_F \frac{4}{3\epsilon} \sum_{\{n_{hf}\}} \left( \frac{\mu_R^2}{m_{hf}^2} \right)^\epsilon. \quad (\text{A.3.4})$$

The wave-function renormalization of the external massive quarks (denoted  $\text{ext}_{hf}$ ) gives the following contribution:

$$V_{\text{ext}_{hf}}^{\text{UV}} = - \left| \mathcal{A}^{(n,0)} \right|^2 g_S^2 N_\epsilon C_F \left( 4 + \frac{3}{\epsilon} \right) \sum_{\{\text{ext}_{hf}\}} \left( \frac{\mu_R^2}{m_{\text{ext}_{hf}}^2} \right)^\epsilon. \quad (\text{A.3.5})$$

Finally, for carrying out mass renormalization for a quark line with momentum  $k$ , mass  $m$ , and colour indices  $i$  and  $j$ , one uses the mass insertion given by the following equation:

$$\mathcal{G}_{ij}^{\text{UV}\delta m}(k) = \frac{i\delta_{ik}}{\not{k} - m} (-i\delta m) \frac{i\delta_{kj}}{\not{k} - m}, \quad (\text{A.3.6})$$

with

$$\delta m = g_S^2 C_F N_\epsilon \left( \frac{\mu_R^2}{m^2} \right)^\epsilon \left( 4 + \frac{3}{\epsilon} \right) m. \quad (\text{A.3.7})$$

## A.4 Restoring precision on input kinematic configurations

Most Monte-Carlo phase-space generators employ techniques involving many successive Lorentz boosts. The precision of the kinematic configurations obtained this way is sometimes deteriorated so that energy-momentum conservation as well as onshell relations are poorly satisfied. Also, when MADLOOP5 switches to quadruple precision arithmetics, the precision of the phase-space point given in input must be upgraded.

To remedy to these situations, the following transformation is considered:

$$\left| \begin{array}{l} p_1 = (E_1, 0, 0, p_{1z}) \\ p_2 = (E_2, 0, 0, p_{2z}) \\ p_{i>2} = (E_i, p_{ix}, p_{iy}, p_{iz}) \end{array} \right. \longrightarrow \left| \begin{array}{l} p_1 = (E_1 + S_E, 0, 0, p_{1z} + S_z) \\ p_2 = -p_1 + \sum_{i=2}^{n_{\text{ext}}} p_i \\ p_{i>2} = (E_i, p_{ix}, p_{iy}, p_{iz} + S_i) \end{array} \right. \quad (\text{A.4.1})$$

where it is assumed that the masses  $m_1$  and  $m_2$  of the two initial states are zero while the masses  $m_{i>2}$  of the final states are left arbitrary. The shifts  $S_i$ ,  $S_E$  and  $S_z$  restoring  $p_i^2 = m_i^2$  should be such that they are zero if the original kinematic configuration already satisfied energy-momentum conservation and onshell constraints. This guarantees that the phase space point deformation introduced is minimal.

## Appendix A. MadLoop technical details

---

The analytical expressions of these shifts are given in terms of  $E_t = \sum_{i=2}^{n_{ext}} E_i$ ,  $p_{t(x,y)} = \sum_{i=2}^{n_{ext}} p_{i(x,y)}$ ,  $p_{tz} = \sum_{i=2}^{n_{ext}} (p_{iz} + S_i)$  and  $p_t^2 = E_t^2 - p_{tx}^2 - p_{ty}^2 - p_{tz}^2$

$$\begin{aligned}
 S_i &= \frac{p_{iz}}{|p_{iz}|} \sqrt{m_i^2 - E_i^2 + p_x^2 + p_y^2} - p_{iz} \\
 S_E &= -\frac{p_{tz}|p_t^2| - E_t p_t^2}{2(E_t^2 - p_{tz}^2)} - E_1 \\
 S_z &= -\frac{E_t|p_t^2| - p_{tz} p_t^2}{2(E_t^2 - p_{tz}^2)} - p_{1z}
 \end{aligned} \tag{A.4.2}$$

A more general solution for decay kinematic configurations and massive initial states can in principle also be obtained, but one must be careful to make sure that the solutions for the shifts are always real and minimize the deformation on the original phase-space point. Notice that this transformation is performed on the input kinematic configuration in double precision only if the option 'ImprovePSPoint' is turned on in the MADLOOP parameter card.

### A.5 MADLOOP runtime parameters

The file '*<ProcFolder>/Cards/MadLoopParams.dat*' contains the runtime parameters dictating MADLOOP5 behavior. We describe here the most important ones.

- *CTModeRun* – It is the most important parameters and controls what is MADLOOP5 strategy for detecting and curing numerical instabilities. Sect. 3.4.4 explains the various strategies at play and the trade-off between runtime speed and numerical stability. The default '-1' mode is the safe behavior while '1' provides the fastest possible evaluation speed without any intrinsic control over numerical stability. The latter can be justified if a stability analysis has been performed beforehand (see the 'check stability' command).
- *MLStabThres* – It is only relevant with 'CTModeRun=-1' and sets the target numerical accuracy via the parameter  $\epsilon$  of eq. (3.4.14). It translates into  $-\lfloor \log_{10}(\text{MLStabThres}) \rfloor$  correct digits. The default value insures 3 correct digits which is enough for practical Monte-Carlo applications, but it can be increased for checks and comparisons on specific kinematic configurations.
- *ImprovePSPoint* – By default, MADLOOP5 performs a minimal transformation on the kinematic configuration given in input to insure exact<sup>3</sup> energy-momentum conservation and onshellness of external four-momenta. This transformation leaves the original configuration unmodified if it already satisfies these constraints.

---

<sup>3</sup>Exact up to double precision (17 digits) for standard computations and up to quadruple precision (34 digits) when a stability recovery is necessary.

- *DoubleCheckHelicityFilter* – For the first few times MADLOOP5 is called, it detects what are the helicity configurations whose contributions are identically vanishing by evaluating them all and comparing their contributions relative to their sum. This is referred to as the initialization stage and upon its successful completion, MADLOOP5 creates a filter file 'HelFilter.dat' in the running directory to store the result of this initialization so that it can be skipped in future runs. The shortcomings of this method is that the helicity filter might depend on some model parameters (a fermion mass changed from zero to a finite value for example) and the use of the outdated filter would yield the wrong result. To this effect, this option allows MADLOOP to double check the helicity filter consistency upon its first call and to update it if found inconsistent.

## A.6 Example of filtering of loop diagrams

This appendix illustrates a simple example of the procedure implemented in MADLOOP for the generation of one-loop diagrams through L-cut diagrams. Let us consider QCD with one light flavor, identified with the  $u$  quark to be definite, and consider the process

$$e^+e^- \longrightarrow u\bar{u}. \quad (\text{A.6.1})$$

As discussed in sect. 3.1.1, the associated L-cut processes are (ghost do not contribute):

$$e^+e^- \longrightarrow g^*g^*u\bar{u}, \quad (\text{A.6.2})$$

$$e^+e^- \longrightarrow u^*\bar{u}^*u\bar{u}, \quad (\text{A.6.3})$$

The L-cut diagrams are shown in fig. A.6.1, and the corresponding diagram identities are reported in tables A.1 and A.2. These diagram identities are constructed in the following way. Firstly, the L-cut particles  $q^*$  and  $\bar{q}^*$  (with  $(q^*, \bar{q}^*) = (g^*, g^*)$  and  $(q^*, \bar{q}^*) = (u^*, \bar{u}^*)$  for eqs. (A.6.2) and (A.6.3) respectively) are assigned momenta equal to  $\ell$  and  $-\ell$  respectively. This implies that the loop momentum flows from particles  $\bar{q}^*$  to particle  $q^*$ . Secondly, for any given L-cut diagram, one starts from particle  $q^*$  and, by following the loop flow backwards, writes down either the identity of a loop particle, or a symbol  $T$  associated unambiguously with a tree structure attached to the loop. The diagram identity is completed when particle  $\bar{q}^*$  is encountered. Finally, as described in sect. 3.1.1, diagrams are filtered out according to the properties of their identities under cyclic permutation and mirror symmetry. It is not difficult to see that this procedure allows one to associate symmetry factors with loop diagrams as customary in QCD – they are all equal to one, except for the case of a gluon bubble, where such factor is equal to one-half. This renders it trivial to take them into account in MADLOOP.

## Appendix A. MadLoop technical details

Diagram #	ID	Topology	Action
g.1	$g^*T_1u^*T_2u^*T_3g^*$	triangle	keep
g.2	$g^*T_1u^*T_4g^*$	bubble	discard
g.3	$g^*T_3u^*T_2u^*T_1g^*$	triangle	discard ( $\equiv g.1$ )
g.4	$g^*T_4u^*T_1g^*$	bubble	discard
g.5	$g^*T_3u^*T_5g^*$	bubble	discard
g.6	$g^*T_5u^*T_3g^*$	bubble	discard
g.7	$g^*T_6g^*$	tadpole	discard
g.8	$g^*T_7g^*$	tadpole	discard

Table A.1: Identities of L-cut diagrams for the process in eq. (A.6.2).

Diagram #	ID	Topology	Action
q.1	$u^*T_3g^*T_1u^*T_2u^*$	triangle	discard ( $\equiv g.1$ )
q.2	$u^*T_4g^*T_1u^*$	bubble	discard
q.3	$u^*T_2u^*T_3g^*T_1u^*$	triangle	discard ( $\equiv g.1$ )
q.4	$u^*T_3g^*T_5u^*$	bubble	discard
q.5	$u^*T_8u^*T_2u^*$	bubble	keep
q.6	$u^*T_2u^*T_8u^*$	bubble	discard ( $\equiv q.5$ )
q.7	$u^*T_6u^*$	tadpole	discard
q.8	$u^*T_7u^*$	tadpole	discard

Table A.2: Identities of L-cut diagrams for the process in eq. (A.6.3).

Tree	Particle content
$T_1$	$u$
$T_2$	$\gamma e^+ e^-$
$T_3$	$\bar{u}$
$T_4$	$u(\gamma e^+ e^-)\bar{u}$
$T_5$	$\bar{u}(\gamma e^+ e^-)u$
$T_6$	$gu[u(\gamma e^+ e^-)\bar{u}]$
$T_7$	$g\bar{u}[\bar{u}(\gamma e^+ e^-)u]$
$T_8$	$gu\bar{u}$

Table A.3: Tree structures used in tables A.1 and A.2. The brackets indicate sub-trees, and are inserted here for the sole purpose of simplifying the reading of the diagrams.



## A.6. Example of filtering of loop diagrams

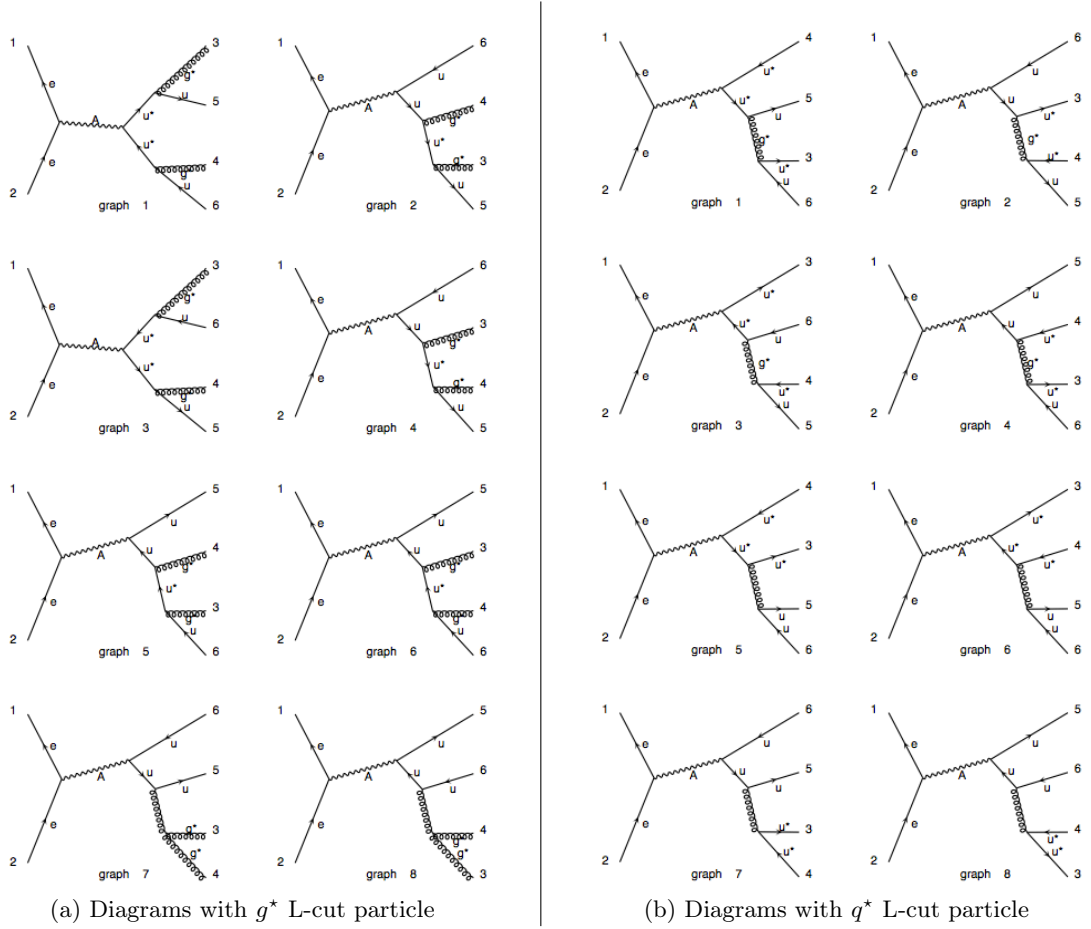


Figure A.6.1: L-cut diagrams of the processes in eqs. (A.6.2) and (A.6.3).

By following the general rules outlined above, the reader can work out the diagram identities reported in table A.1 (table A.2) using the diagrams depicted in the left (right) panel of fig. A.6.1. By doing so, one is naturally led to introduce the tree structures reported in table A.3. When filtering, MADLOOP begins from diagram #1 of the process in eq. (A.6.2), moving on eventually to diagrams associated with the process in eq. (A.6.3). Notice that the choice of a specific L-cut diagram, among those equivalent, to be used for the actual computation is irrelevant. However, as discussed in sect. 3.4.3, in the context of the open loop computational technique there is an optimal choice because of the possibility of recycling loop wavefunctions. A diagram is kept or filtered out as indicated in the last columns of tables A.1 and A.2. All bubbles on external lines and tadpoles<sup>4</sup> are discarded by definition. Diagram g.3 is identical to diagram g.1 up to mirror symmetry, while diagrams q.1 and q.3 are identical to diagram g.1 up to cyclic permutations. Diagram q.6 is identical to diagram q.5 up to a cyclic permutation. Diagram q.5 represents a closed fermion bubble on an internal line; it must be taken into account, but its contribution is

<sup>4</sup>When considering QED corrections, this will be relaxed as there is a contribution such as for example a Z-boson tadpole attached to a W-boson line.

## Appendix A. MadLoop technical details

equal to zero, being proportional to the trace of a single Gell-Mann matrix. We are thus left out with one triangle loop diagram (arising from sewing diagram g.1) that contributes to the one-loop corrections to eq. (A.6.1). This is of course the well-known result.

Details of the MADLOOP5 loop diagram tagging algorithm are better illustrated when considering more complicated L-cut diagrams such as the two below.

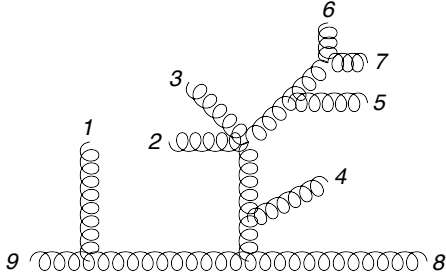


Figure A.6.2: Tagging involving a complicated tree structure attached to a gluon bubble cut at the level of particles 8 and 9.

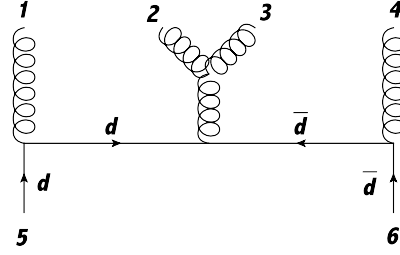


Figure A.6.3: Tagging of a quark triangle loop, cut at the level of the quarks 5 and 6, with an amplitude-type vertex opposite to the L-cut location.

When tagging the L-cut diagram of fig. A.6.2, MADLOOP starts with gluon number 8 and finds the first loop vertex. It identifies the next loop line and all the other legs of this vertex are considered to be *bridge legs* leading to a tree structure attached to the loop. In this case, there is only one such structure and MADLOOP launches an iterative function to characterize it. This function will call itself successively on each of the vertices of the structure, starting from the one closest to the loop and walking up the tree until it reaches the external legs. In doing so, it builds a *unique unambiguous* tag, referred to as *canonical*, which can be used to compare structures among each others throughout the different L-cut diagrams. This canonical tag is the analogue of each of the  $T_i$ 's definitions of table A.3. In the case of this first complicated structure, the canonical tag constructed is:

$$(((2,3,4,5,6,7),33),((2,3,5,6,7),44),((5,6,7),33),((6,7),33))$$

with 33 the three-gluon vertex ID and 44 the four-gluon vertex one. As one sees, the structures shows the parent legs and the vertices ID starting from bridge leg and going outwards. The order for vertices of the same depth level is fixed by the reconstruction procedure. This structure identification is iterated with the next loop vertex<sup>5</sup> until the second L-cut leg (number 9) is reached. This procedure builds the loop *ID*, identifying its topology, like those shown on tables A.2 and A.1. The final ID of the L-cut diagram

<sup>5</sup>in the case of fig. A.6.2, that would be the vertex with the trivial structure made of the lone external leg number 1.

of fig. A.6.2 is then

$$[[21, [111, ], 33], [21, [222, ], 33]]$$

with 21 the PDG of the gluon, 111 the ID of the first complicated structure and 222 the one of the lone leg number 1. Notice that the structure ID is in a list since there are several structures attached to the same loop vertex if it connects more than three legs.

The second example of L-cut diagram of fig. A.6.2 shows the importance of the vertices reconstruction. MADLOOP5 tree diagram generator does not build them in an order suited for loop computations. In this example, the diagram construction is as follows:

- The polarization vectors of legs 4 and 6 are merged into the  $\bar{d}$  wavefunction.
- The polarization vectors of legs 1 and 5 are merged into the  $d$  wavefunction.
- Wavefunctions  $d$  and  $\bar{d}$  are merged into the intermediate gluon wavefunction.
- The intermediate gluon wavefunction forms the c-number amplitude with the polarization vectors of legs 2 and 3.

The order of this diagram construction is not optimal for loop computations because one would like to first compute all external tree-structures (which are independent of the loop momentum) and then only progressively compute all loop wavefunctions from leg 5 to 6. The reconstruction of the L-cut diagram vertices in this optimal order is performed automatically during the tagging procedure. Assuming 111, 222 and 333 are the ID's of the structures with the group of leg numbers (1), (2,3) and (4) respectively, then one would naively expect the loop ID to be (1 is the PDG of the down-type quark, -1 the one of the anti-down and 2 is the ID of the  $d\bar{d}g$  vertex)

$$[[1, [111, ], 2], [1, [222, ], 2], [-1, [333, ], 2]]$$

But thanks to vertices reconstruction, what is obtained instead is

$$[[1, [111, ], 2], [1, [222, ], 2], [1, [333, ], 2]]$$

This guarantees the unicity of the loop ID (up to cyclic/mirror permutations) for this triangle fermion loop while still keeping track of the fermion flow. For example, the ID of the same loop as above but with opposite fermion flow would read

$$[[-1, [111, ], 2], [-1, [222, ], 2], [-1, [333, ], 2]]$$

which is different and therefore both fermion flows are kept for this loop, as it should be. In the case of bubbles, one of them would be discarded because the mirror operation on loop ID's flips the fermion flow.



# B Comparisons with existing results

In this appendix, we present the comparisons between MADLOOP results, and those obtained either with public computer codes, or by implementing ourselves analytical results published in the literature. As discussed in sect. 3.1.4, these comparisons are an essential part of the validation of MADLOOP, and allow us to check all the building blocks used by the code to construct the one-loop amplitudes relevant to arbitrary processes.

We compute the quantity<sup>1</sup> defined in eq. (3.1.2), which can be re-expressed as follows:

$$V(r) = \frac{(4\pi)^\epsilon}{\Gamma(1-\epsilon)} \left( \frac{\mu_F^2}{Q^2} \right)^\epsilon F \left( \frac{c_{-2}}{\epsilon^2} + \frac{c_{-1}}{\epsilon} + c_0 \right). \quad (\text{B.0.1})$$

We shall also denote by

$$a_0 = \overline{\sum_{\substack{\text{colour} \\ \text{spin}}} \left| \mathcal{A}^{(n,0)} \right|^2} \quad (\text{B.0.2})$$

the Born matrix element squared, summed/averaged over spin and color degrees of freedom. The constant  $F$  in eq. (B.0.1) may clearly be absorbed into the coefficients  $c_i$ ; we have introduced it in order to facilitate the comparison between MADLOOP results and those of other codes. In the following, and where not explicitly indicated otherwise, its value has been set equal to one. The expression in eq. (B.0.1) understands that we may treat as independent the Ellis-Sexton scale  $Q$ , the factorization scale  $\mu_F$ , and the renormalization scale  $\mu_R$  (which is the argument of  $\alpha_S$ , contained implicitly in  $c_i$ ). As explained in ref. [105] (see in particular appendices B and C there), this is most conveniently done by computing the one-loop contribution by setting all scales equal to the Ellis-Sexton scale there, and by introducing in the short-distance cross section a compensating contribution, proportional to the Born amplitude squared and depending linearly on  $\log \mu_F/Q$  and on  $\log \mu_F/\mu_R$ . This contribution is included in MADFKS (i.e. integrated along with the Born matrix element) and consistently with this choice only the Ellis-Sexton scale  $Q$  enters the computations performed by MADLOOP. It should be remarked that most of the codes used in this appendix as benchmarks for the validation

---

<sup>1</sup>Except in one case, when we shall consider the square of a non-divergent one-loop amplitude – see sect. B.2.7.

## Appendix B. Comparisons with existing results

---

of MADLOOP are forced in any case to set

$$\mu \equiv Q = \mu_F = \mu_R, \quad (\text{B.0.3})$$

and hence the compensating factor in MADFKS is equal to zero. In a few cases, the condition of eq. (B.0.3) could be relaxed and thus allowed to test the full scale dependence of the virtual computations.

All the comparisons presented here are local, i.e. performed at fixed  $2 \rightarrow n$  kinematic configurations. I typically show the results for one such configuration, although as a safety measure a few more of them have been checked. No attempt was made to choose the same set of input parameters for different processes, since priority was given to using the reference codes with their defaults, in order to limit as much as possible external operations on them. This consideration is particularly important when it comes to choosing the kinematic configuration(s) used for the comparisons. When using a public code which embeds the one-loop amplitudes in a cross-section integrator, the code is run and minimally modified so as to record the kinematic configurations considered and their corresponding one-loop results. A few of them are then picked at random, and given as input to MADLOOP. This procedure guarantees that the public code is not modified except for a few trivial output statements.

As discussed in sect. 3.1.4, it is not always possible to compare the results for  $c_{-2}$  and  $c_{-1}$  with some public codes. However, these coefficients are always compared to their known analytic forms<sup>2</sup>, and in doing so the agreement found is at the level of the 12<sup>th</sup> digit or better for all processes. The corresponding comparisons with public codes are often worse than this, being at the level of single-precision computations of real-number algebra. The reason for this is indeed a single-precision to double-precision conversion done by the computer, since some of the parameters in the input cards of MADLOOP are in single precision (whereas all computations are performed in double precision). These differences are obviously completely irrelevant in cross section calculations, and are mentioned here for the sake of completeness.

In the context of the computation of a cross section, the infrared divergences of  $V(r)$  cancel those present in the subtracted real-emission contribution. Since the latter is computed using Conventional Dimensional Regularization (CDR), this is the scheme of choice for  $V(r)$  as well. On the other hand, other schemes are more suitable to one-loop computations. The 't Hooft-Veltman scheme is used by CUTTOOLS: the finite part  $c_0$  computed in such a scheme is identical to that computed in CDR. The residues  $c_{-2}$  and  $c_{-1}$  in the 't Hooft-Veltman scheme can be obtained from those in CDR by setting the number of space-time dimensions equal to four there (in CDR one has  $d = 4 - 2\epsilon$ ).

---

<sup>2</sup>This is done when single poles do not contain UV contributions, namely if UV renormalization is performed. Although this is done by default, there are cases in which the reference computations do not include UV renormalization – see sects. B.1.5, B.1.6, and B.3.2. In these situations, the comparisons with analytical results for pole residues are not carried out.

Another popular infrared scheme is Dimensional Reduction (DR). The difference between the finite parts  $c_0$  computed in CDR and DR is proportional to the Born, and can thus be easily accounted for. The relevant formulae can be found in eqs. (B.3) and (B.4) of ref. [105]. For more detailed discussions on infrared schemes, see e.g. ref. [124]. In this appendix, either the 't Hooft-Veltman or the DR scheme is used for the finite parts, while pole residues are always given in the 't Hooft-Veltman scheme.

When considering closed fermion loops with one EW vector boson leg there is possibly an anomalous contribution. By default, the complete quark families are included in the loops, thereby avoiding this problem. This appendix presents cases in which the anomaly cancellation may not be immediately evident (this occurs in connection with the decoupling limit – see sect. 3.1.4). The relevant processes are discussed in some details.

Unless otherwise indicated, all dimensionful quantities appearing in this appendix are given in GeV.

Finally, most of these checks were originally performed with MADLOOP4 but can be reproduced easily with the public version of MADLOOP5 by simply following the sequence of three commands shown on the listing 3.2. The testing suite of MADGRAPH5 involves parallel tests (see appendix A.1) automatically verifying the consistency of MADLOOP5 results with those of MADLOOP4 for all the type of processes presented in this chapter as well as more complicated ones. These automated tests insure that the checks made here with MADLOOP4 also hold for MADLOOP5 and will remain so upon further development of the code.

## B.1 QCD processes

All processes considered in this section are pure-QCD ones, i.e. EW-boson exchanges are excluded from computations.

### B.1.1 The process $u\bar{u} \rightarrow d\bar{d}$

The following set of parameters is used:

Parameter	value	Parameter	value
$\alpha_S$	0.13	$n_{lf}$	2
$\mu$	91.188		

Notice that  $n_{lf} = 2$  implies that massive quark are excluded and only two generations of massless fermions run in the loop.

## Appendix B. Comparisons with existing results

---

The kinematic configuration considered is:

$$\begin{aligned}
 p_u &= ( 102.6289752320661 , 0 , 0 , 102.6289752320661 ) \\
 p_{\bar{u}} &= ( 102.6289752320661 , 0 , 0 , -102.6289752320661 ) \\
 p_d &= ( 102.6289752320661 , -85.98802977488269 , -12.11018104528534 , 54.70017191625945 ) \\
 p_{\bar{d}} &= ( 102.6289752320661 , 85.98802977488269 , 12.11018104528534 , -54.70017191625945 )
 \end{aligned}$$

The finite part is given in the 't Hooft-Veltman scheme. MADLOOP results are compared with those of the code of ref. [107], which implements the formulae given in ref. [93]. We obtain what follows:

$u\bar{u} \rightarrow d\bar{d}$	MADLOOP	Ref. [107]
$a_0$	0.76152708418254678E+000	0.76152695293848227E+000
$c_{-2}$	-0.08403255449056724E+000	-0.08403254000812221E+000
$c_{-1}$	-0.10222774402685941E+000	-0.10222772640859645E+000
$c_0$	-0.44023547006851060E-001	-0.44023539433227843E-001

Since the code of ref. [107] allows one to set the mass scales entering the process independently from each other, we have also found excellent agreement with MADLOOP plus the compensating contribution computed by MADFKS for  $\mu_R \neq \mu_F \neq Q$ ; we refrain from reporting the results of these tests here.

### B.1.2 The process $dg \rightarrow dg$

The same parameters as in sect. B.1.1 are chosen. The kinematic configuration considered is:

$$\begin{aligned}
 p_d &= ( 220.9501779577791 , 0 , 0 , 220.9501779577791 ) \\
 p_g &= ( 220.9501779577791 , 0 , 0 , -220.9501779577791 ) \\
 p_d &= ( 220.9501779577791 , 119.9098300357375 , 183.0492135511419 , -30.55485589367430 ) \\
 p_g &= ( 220.9501779577791 , -119.9098300357375 , -183.0492135511419 , 30.55485589367430 )
 \end{aligned}$$

The comparison between MADLOOP and the code of ref. [107] reads as follows:

$dg \rightarrow dg$	MADLOOP	Ref. [107]
$a_0$	13.032125409659082E+000	13.032125409659088E+000
$c_{-2}$	-2.3368499538132292E+000	-2.3368499538132284E+000
$c_{-1}$	2.1147910298734116E+000	2.1147910298729693E+000
$c_0$	-1.8580245435782883E+000	-1.8580245414019134E+000



For the present process, the crossing checks as discussed in sect. 3.1.4 were performed, by comparing it to the  $gg \rightarrow d\bar{d}$  and  $d\bar{d} \rightarrow gg$  processes, and perfect agreement was found.

### B.1.3 The processes $d\bar{d} \rightarrow t\bar{t}$ and $gg \rightarrow t\bar{t}$

We compare the MADLOOP results for top-pair production with those of MCFM [46]. The following input parameters are used:

Parameter	value	Parameter	value
$\alpha_s$	0.13	$n_{lf}$	5
$m_{top}$	172.5	$\mu$	91.188

Note that the top quark is considered a stable particle, and hence its width is set to zero. The phase-space point used for this check is:

$$\begin{aligned}
 p_1 &= ( 63.71791270829688, 0, 0, 63.717912708296879 ) \\
 p_2 &= ( 814.2396220727112, 0, 0, -814.2396220727112 ) \\
 p_t &= ( 663.0455079348429, -54.65940267927511, 25.31239299113409, -637.3733035297141 ) \\
 p_{\bar{t}} &= ( 214.9120268461650, 54.65940267927511, -25.31239299113409, -113.14840583470011 )
 \end{aligned}$$

with  $p_1$  and  $p_2$  the momenta of the initial-state partons coming from the left ( $g$  or  $d$ ) and from the right ( $g$  or  $\bar{d}$ ) respectively. The finite part is given in the DR scheme. We obtain what follows:

$d\bar{d} \rightarrow t\bar{t}$	MADLOOP	MCFM
$a_0$	1.1446316446116180E+000	1.1446316446116067E+000
$c_{-2}$	-6.3153578543239441E-002	-
$c_{-1}$	9.4367389242209110E-002	-
$c_0$	-0.3252731490962368E+000	-0.3252731490962548E+000
$gg \rightarrow t\bar{t}$		
$a_0$	1.3065171790431791E+000	1.3065171790431644E+000
$c_{-2}$	-0.1621921604777766E+000	-
$c_{-1}$	0.1441104689442122E+000	-
$c_0$	-2.1116148093780568E-002	-2.1116148095016787E-002

The residues of the double and single poles have been checked against those returned by MADFKS, and perfect agreement was found. This is not entirely trivial, because of the role played by UV renormalization, and in particular by the insertion of the UV mass counterterm on the virtual top-quark line that appears in the  $gg$  channel. This term in particular was not probed in the case of dijet production.

## Appendix B. Comparisons with existing results

---

### B.1.4 The process $ug \rightarrow t\bar{t}u$

The process  $pp \rightarrow t\bar{t}+1j$  has been first computed by Dittmaier, Uwer and Weinzierl [82, 83]. Recently the results of this calculation have been verified by HELAC-1Loop [30] and by Melnikov and Schultze [132]. Here the  $ug \rightarrow t\bar{t}u$  channel is considered, and MADLOOP results compared with those of ref. [83]. The parameters employed are:

Parameter	value	Parameter	value
$\alpha_S$	0.1075205492734706	$n_{lf}$	5
$m_{top}$	174.0	$\mu$	174.0
$F$	$\Gamma(1 - \epsilon) \Gamma(1 + \epsilon) g_S^6 a_0$		

where the value of  $F$  has been chosen in order to follow the conventions of the appendix of ref. [83]. The kinematic configuration adopted is:

$$\begin{aligned}
 p_u &= ( 500 & , 0 & , 0 & , 500 & ) \\
 p_g &= ( 500 & , 0 & , 0 & , -500 & ) \\
 p_t &= ( 458.5331753852783 & , 207.0255169909440 & , 0 & , 370.2932732896167 & ) \\
 p_{\bar{t}} &= ( 206.6000026080000 & , -10.65693677252589 & , 42.52372780926147 & , -102.3998210421085 & ) \\
 p_u &= ( 334.8668220067217 & , -196.3685802184181 & , -42.52372780926147 & , -267.8934522475083 & )
 \end{aligned}$$

We obtain:

$ug \rightarrow t\bar{t}u$	MADLOOP	Ref. [83]
$a_0$	1.607845322071586E-005	1.607845322071585E-005
$c_{-2}$	-9.697041910469525E-002	-9.69704191047088E-002
$c_{-1}$	-5.643095699401332E-003	-5.6430956994203E-003
$c_0$	4.003849386476366E-001	4.003849386477017E-001

### B.1.5 The process $u\bar{u} \rightarrow b\bar{b}b\bar{b}$ with massless $b$

This six-quark amplitude is one of the results presented in ref. [155] by A. van Hameren *et al.*<sup>3</sup>. The results by MADLOOP are thus a check of the implementation of the CUT-TOOLS software in a framework different from that of HELAC-1Loop [30]. The following parameters are used:

---

<sup>3</sup>The authors of ref. [155] have compared their results against those obtained by T. Binoth *et al.* in ref. [34].

Parameter	value	Parameter	value
$g_s$	1	$n_f$	5
$m_{top}$	174.0	$m_b$	0
$\mu$	500.0	$F$	$1/(64\pi^2)$

where the value of  $m_{top}$  reminds one that massive top quarks enter the loops. The kinematic configuration considered is:

$$\begin{aligned}
 p_u &= ( 250 & , 0 & , 0 & , 250 & ) \\
 p_{\bar{u}} &= ( 250 & , 0 & , 0 & , -250 & ) \\
 p_b &= ( 147.5321146846735 & , 24.97040523056789 & , -18.43157602837212 & , 144.2306511496888 & ) \\
 p_{\bar{b}} &= ( 108.7035966213640 & , 103.2557390255471 & , -0.5484684659584054 & , 33.97680766420219 & ) \\
 p_b &= ( 194.0630765341365 & , -79.89596300367462 & , 7.485866671764871 & , -176.6948628845280 & ) \\
 p_{\bar{b}} &= ( 49.70121215982584 & , -48.33018125244035 & , 11.49417782256567 & , -1.512595929362970 & )
 \end{aligned}$$

The finite part is given in the 't Hooft-Veltman scheme (with  $d = 4$  here, so that it is formally equivalent to CDR). For consistency with ref. [155], no UV counterterms are included<sup>4</sup>, both for their contribution to the finite part and the single pole residue.

$u\bar{u} \rightarrow b\bar{b}b\bar{b}$	MADLOOP	Ref. [155]
$a_0$	5.75329342809431E-009	5.753293428094391E-009
$c_{-2}$	-9.205269484950836E-008	-9.205269484951069E-008
$c_{-1}$	-2.404679886707934E-007	-2.404679886692200E-007
$c_0$	-2.553568662825831E-007	-2.553568662778129E-007

Different crossings of this process have been considered, moving either a  $b$  or a  $\bar{b}$  quark to the initial state, and MADLOOP's evaluations were fully consistent.

### B.1.6 The process $u\bar{u} \rightarrow t\bar{t}b\bar{b}$ with massless $b$

This process has been first computed by Bredenstein *et al.* in ref. [40]. Here, we compare MADLOOP with the result of A. van Hameren *et al.* [155], similarly to what was done in sect. B.1.5. The following set of parameters is used:

Parameter	value	Parameter	value
$g_s$	1	$n_f$	5
$m_{top}$	174.0	$m_b$	0
$F$	$1/(16\pi^2)$	$\mu$	500.0

<sup>4</sup>I thus set  $\epsilon_{IR} = \epsilon_{UV}$ , and shall do the same in sects. B.1.6 and B.3.2.

## Appendix B. Comparisons with existing results

The top width and the mass of the  $b$  quark are set equal to zero. The kinematic configuration considered is:

$$\begin{aligned}
 p_u &= ( 250 & , 0 & , 0 & , 250 & ) \\
 p_{\bar{u}} &= ( 250 & , 0 & , 0 & , -250 & ) \\
 p_t &= ( 190.1845561691092 & , 12.99421901255723 & , -9.591511769543683 & , 75.05543670827210 & ) \\
 p_{\bar{t}} &= ( 182.9642163285034 & , 53.73271578143694 & , -0.2854146459513714 & , 17.68101382654795 & ) \\
 p_b &= ( 100.9874727883170 & , -41.57664370692741 & , 3.895531135098977 & , -91.94931862397770 & ) \\
 p_{\bar{b}} &= ( 25.86375471407044 & , -25.15029108706678 & , 5.981395280396083 & , -0.7871319108423604 & )
 \end{aligned}$$

The finite part is given in the 't Hooft-Veltman scheme. For consistency with ref. [155], no UV counterterms are included except the one relevant to top-mass renormalization. The comparison yields:

$u\bar{u} \rightarrow t\bar{t}b\bar{b}$	MADLOOP	Ref. [155]
$a_0$	2.201164677187738E-008	2.201164677187727E-008
$c_{-2}$	-2.347908989000171E-007	-2.347908989000179E-007
$c_{-1}$	-2.082520105664531E-007	-2.082520105681483E-007
$c_0$	3.909384299566400E-007	3.909384299635230E-007

## B.2 Processes with a single vector boson

### B.2.1 The process $u\bar{d} \rightarrow e^- \bar{\nu}_e$

It is a matter of trivial algebra to show that for this process one has:

$$c_0 = \frac{\alpha_S}{2\pi} C_F ( -\log^2(\mu^2/s) - 3\log(\mu^2/s) + \pi^2 - 8 ) a_0, \quad (\text{B.2.1})$$

where  $s$  is the parton center-of-mass energy squared. For this simple case, it suffices thus to compute the ratio  $c_0/a_0$ , which only depends on  $s$ ,  $\mu$  and  $\alpha_S$ . These parameters are chosen as follows:

Parameter	value	Parameter	value
$\alpha_S$	0.118	$\mu$	91.1876
$\sqrt{s}$	200		

Giving:

$u\bar{d} \rightarrow e^- \bar{\nu}_e$	MADLOOP	Analytic result
$c_0/a_0$	0.10303097397333823	0.10303099058268723

## B.2. Processes with a single vector boson

### B.2.2 The processes $u\bar{d} \rightarrow \nu_e e^+ g$ and $ug \rightarrow \nu_e e^+ d$

These two processes contribute to the NLO corrections to  $W + 1$  jet. MADLOOP results are compared with those from the implementation of the process in MCFM [46]. The following input parameters are used:

Parameter	value	Parameter	value
$\alpha_S$	0.118	$n_{lf}$	5
$m_Z$	91.1876	$\mu$	91.1876
$m_W$	80.44	$\alpha^{-1}$	132.6844139
$\sin^2 \theta_W$	$1 - m_W^2/m_Z^2$	$\Gamma_W$	2.1054

The kinematic configuration is:

$$\begin{aligned}
 p_u &= ( 214.56992446426548 \quad , \quad 0 \quad , \quad 0 \quad , \quad 214.56992446426548 \quad ) \\
 p_{\bar{d},g} &= ( 76.595570417607490 \quad , \quad 0 \quad , \quad 0 \quad , \quad -76.595570417607490 \quad ) \\
 p_{\nu_e} &= ( 186.05703769425895 \quad , \quad -25.245095379680929 \quad , \quad 11.566386894022147 \quad , \quad 183.97316415458937 \quad ) \\
 p_{\bar{t}} &= ( 34.360975783073229 \quad , \quad 23.891509313117499 \quad , \quad 15.166967889135465 \quad , \quad 19.489369526901015 \quad ) \\
 p_{g,d} &= ( 70.747481404540792 \quad , \quad 1.3535860665634296 \quad , \quad -26.733354783157612 \quad , \quad -65.488179634832392 \quad )
 \end{aligned}$$

The finite part is given in the DR scheme.

$u\bar{d} \rightarrow \nu_e e^+ g$	MADLOOP	MCFM
$a_0$	0.93604465169278606	0.93604465172998652
$c_{-2}$	-9.96153744476348524E-002	-
$c_{-1}$	-0.17006206699872445	-
$c_0$	0.18788412330548998	0.18788412331301654
$ug \rightarrow \nu_e e^+ d$		
$a_0$	0.25449996399907276	0.25449996400918706
$c_{-2}$	-2.70842947126827029E-002	-
$c_{-1}$	-4.43691342449630960E-002	-
$c_0$	4.58106840475423702E-002	4.58106840493787554E-002

The residues of the double and single poles have been checked against those returned by MADFKS, and perfect agreement has been found.

## Appendix B. Comparisons with existing results

---

### B.2.3 The processes $d\bar{d}(\rightarrow \gamma^*/Z) \rightarrow e^-e^+g$ and $dg(\rightarrow \gamma^*/Z) \rightarrow e^-e^+d$

These two processes contribute to the NLO corrections to  $Z + 1$  jet. We compare the MADLOOP results with the implementation of MCFM [46]. The amplitudes in MCFM do not include closed fermion loops attached to the vector boson, which simplifies the calculation slightly. This means that in MADLOOP these contributions have been removed as well. Editing the `UserFilter` function in the `loop_diagram_generation.py` file of MADLOOP5 (or in the `Diagram.cpp` file of MADLOOP4) makes it straightforward to remove the triangle loop diagrams attached to the EW vector boson. There is, however, one subtlety: in MADLOOP4, the `UserFilter` does not affect the  $R_2$  contributions which is non zero when considering five massless quark flavors. It must therefore be removed by hand in MADLOOP4 while this is automatically taken care of in MADLOOP5. The following input parameters are used:

Parameter	value	Parameter	value
$\alpha_s$	0.118	$n_{lf}$	5
$m_Z$	91.1876	$\mu$	91.1876
$m_W$	80.44	$\alpha^{-1}$	132.6844139
$\sin^2 \theta_W$	$1 - m_W^2/m_Z^2$	$\Gamma_Z$	2.4952

The kinematic configuration is:

$$\begin{aligned}
 p_d &= ( 219.81636757818666 \quad , \quad 0 \quad , \quad 0 \quad , \quad 219.81636757818666 \quad ) \\
 p_{\bar{d},g} &= ( 78.514049708950481 \quad , \quad 0 \quad , \quad 0 \quad , \quad -78.514049708950481 \quad ) \\
 p_{e^-} &= ( 190.91987238779512 \quad , \quad -28.468337054964493 \quad , \quad 10.154026810698143 \quad , \quad 188.51219376322723 \quad ) \\
 p_{e^+} &= ( 36.663063494801236 \quad , \quad 27.114750988401063 \quad , \quad 16.579327972459467 \quad , \quad 18.278303740841352 \quad ) \\
 p_{g,d} &= ( 70.747481404540792 \quad , \quad 1.3535860665634296 \quad , \quad -26.733354783157612 \quad , \quad -65.488179634832392 \quad )
 \end{aligned}$$

## B.2. Processes with a single vector boson

The finite part is given in the DR scheme.

$d\bar{d}(\rightarrow \gamma^*/Z) \rightarrow e^-e^+g$	MADLOOP	MCFM
$a_0$	6.76069763764682863E-002	6.76069763035082871E-002
$c_{-2}$	-7.19484295416346949E-003	-
$c_{-1}$	-1.21173922992901528E-002	-
$c_0$	1.40892172309674130E-002	1.40892172165083020E-002
$dg(\rightarrow \gamma^*/Z) \rightarrow e^-e^+d$		
$a_0$	1.71059868986021858E-002	1.71059868803008740E-002
$c_{-2}$	-1.82044658566124528E-003	-
$c_{-1}$	-2.91385295414951957E-003	-
$c_0$	3.17029216184223396E-003	3.17029215866125201E-003

In order to further test the internal consistency of MADLOOP, the calculation has been redone while including the contributions of the closed fermion loops, that had been neglected in the comparison with MCFM. In doing so,  $m_{top}$ -dependence studies introduced in sect. 3.1.4 could be performed. To be definite, let us consider only the process  $d\bar{d}(\rightarrow \gamma^*/Z) \rightarrow e^-e^+g$ . In fig. B.2.1, the results for the finite part  $c_0$  as a function of  $m_{top}$  are presented, for the kinematic configuration given above. The five-flavor calculation (which is independent of  $m_{top}$ , and from which the contribution of closed fermion loops was removed) is compared with the six-flavor calculation that retains the full  $m_{top}$  dependence (and where closed fermion loops are included). In the decoupling limit ( $m_{top} \rightarrow \infty$ ) the six-flavor result does not agree with the five-flavour one. This difference is due to the non-anomalous part of the  $b$ -quark triangle diagrams, which contributes only to the six-flavor result, having been excluded by hand from the five-flavor one. Indeed in the decoupling limit the third fermion family effectively includes only the non-anomalous contributions of the  $b$  quark, the anomalous part being cancelled by the top quark ones also in this decoupling limit, because it is mass independent.

The opposite limit for  $m_{top} \rightarrow 0$  is equal to the five-flavor result even though we are using a renormalization scheme in which we subtract the top quark loop at zero momentum. This means that the heavy-flavor contributions to the UV counterterms relevant to strong coupling and gluon wave function renormalization diverge, but for this particular process there are an equal number of powers of  $\alpha_s$  as of external gluons, so that these divergences cancel (see eqs. (A.3.2) and (A.3.4)). Furthermore, due to the fact that the mass difference between the top quark and the bottom quark goes to zero, the contribution of triangle diagrams is exactly zero at  $m_{top} = 0$ , and hence the six-flavor result coincides with the five-flavor one.

## Appendix B. Comparisons with existing results

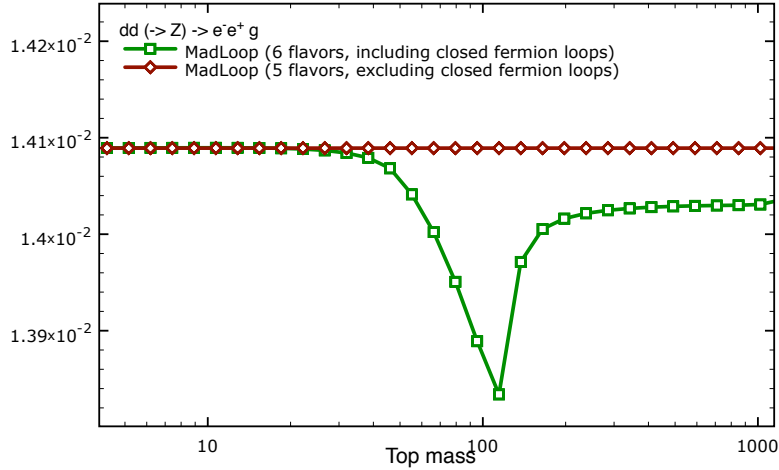


Figure B.2.1: The finite part  $c_0$  for  $d\bar{d}(\rightarrow \gamma^*/Z) \rightarrow e^-e^+g$  and the kinematic configuration reported in the text, as a function of  $m_{top}$ , with five and six flavors circulating in the loop. In the five-flavor case all contributions due to closed fermion loops have been excluded. See the text for details.

### B.2.4 The processes $dc(\rightarrow W^-) \rightarrow e^-\bar{\nu}_e uc$ and $dg(\rightarrow W^-) \rightarrow e^-\bar{\nu}_e ug$

The virtual corrections to these processes can be inferred from those relevant to  $e^+e^- \rightarrow 4$  partons that have been first calculated by Bern, Dixon and Kosower (BDK) [27]. Here we compare the MADLOOP results against the implementation of the crossings of the BDK amplitudes in MCFM [46]. The BDK amplitudes and their implementations in MCFM assume five massless quark flavors, plus the top quark which is taken to be massive. However, only terms up to  $1/m_{top}^2$  have been kept, with higher inverse powers of  $m_{top}$  being neglected. The MADLOOP implementation also features five massless quarks plus a massive top quark, but the dependence on  $m_{top}$  is retained in full. Therefore, we only expect agreement with MCFM for large top-quark masses. The following input parameters are used:

Parameter	value	Parameter	value
$\alpha_s$	0.118	$n_{lf}$	5
$m_Z$	91.1876	$\mu$	91.1876
$m_W$	80.44	$\alpha^{-1}$	132.6844139
$\sin^2 \theta_W$	$1 - m_W^2/m_Z^2$	$\Gamma_W$	2.1054

and a diagonal CKM matrix.



## B.2. Processes with a single vector boson

The kinematic configuration is:

$$\begin{aligned}
 p_d &= ( 77.882588584131682 , 0 , 0 , 77.882588584131682 ) \\
 p_{c,g} &= ( 324.00529231091792 , 0 , 0 , -324.00529231091792 ) \\
 p_{e^-} &= ( 41.228205880918381 , -10.045117616293838 , 17.003544184693592 , -36.190330993144983 ) \\
 p_{\bar{\nu}_e} &= ( 169.31980614449293 , -82.680596722191993 , -81.515421497409065 , -123.24103105934591 ) \\
 p_u &= ( 142.62173792637984 , 51.789721902948564 , 71.086870231086095 , -112.27395831226823 ) \\
 p_{c,g} &= ( 48.718130943258451 , 40.935992435537273 , -6.5749929183706302 , 25.582616637972905 )
 \end{aligned}$$

The results are presented here in the form of two plots where the finite part  $c_0$  (in the

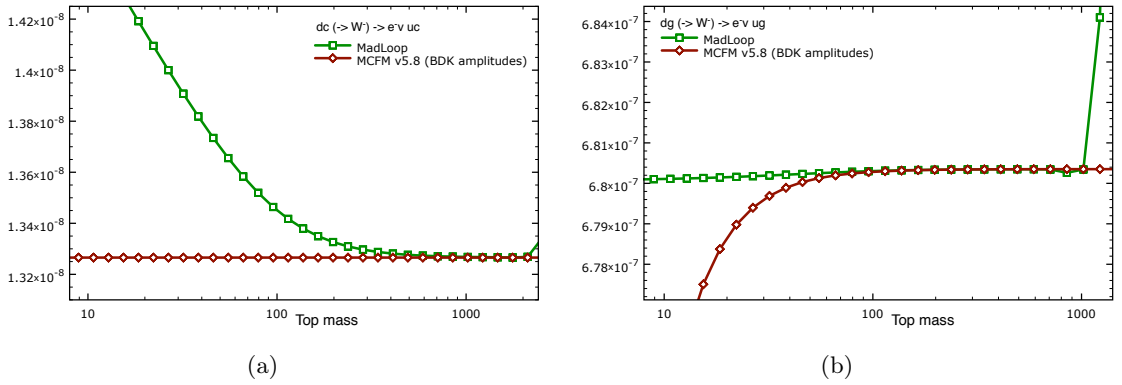


Figure B.2.2: The finite part  $c_0$  for (a)  $dc(\rightarrow W^-) \rightarrow e^- \bar{\nu}_e uc$  and (b)  $dg(\rightarrow W^-) \rightarrow e^- \bar{\nu}_e ug$ , as a function of  $m_{top}$ . MADLOOP (boxes) and MCFM (diamonds) results are shown.

DR scheme) is shown as a function of  $m_{top}$ .

For the process  $uc(\rightarrow W^-) \rightarrow e^- \bar{\nu}_e uc$ , fig. B.2.2(a), we find a relatively large dependence on the top quark mass in MADLOOP, while the MCFM result is a constant (as explained in ref. [27]). However, from the plot it is clear that the two results converge to the same number in the limit  $m_{top} \rightarrow \infty$ . For  $m_{top} \approx 1.7$  TeV, the relative difference between MADLOOP and MCFM is smaller than  $10^{-5}$ . For yet larger top masses numerical instabilities in MADLOOP4 render it impossible to reach such level of precision. These instabilities are due to large cancellations between the  $R_2$  and the cut-constructible-plus- $R_1$  contributions. Performing this analysis again with MADLOOP5 would solve this problem by using quadruple precision numerics (see sect. 3.4.4).

For the process  $dg(\rightarrow W^-) \rightarrow e^- \bar{\nu}_e ug$ , fig. B.2.2(b), the situation is similar. At  $m_{top} = 600$  GeV, the relative difference between MADLOOP and MCFM is of the order of  $10^{-7}$ . For larger masses, MADLOOP4 displays the same numerical instabilities as those mentioned above.

## Appendix B. Comparisons with existing results

---

I conclude this section by pointing out that the results presented here do not allow one to assess the impact of terms of order  $1/m_{top}^4$  and higher on observable cross sections. In fact, although for the physical value of the top mass these terms seem generally to have a small effect ( $\mathcal{O}(1\%)$ ), they do depend on the partonic channel and the kinematic configuration chosen. A firm conclusion can thus be reached only through a comparison at the level of integrated cross sections.

### B.2.5 The process $ug(\rightarrow Z/\gamma^*) \rightarrow e^-e^+ug$

The virtual corrections to this process can be inferred from those relevant to  $e^+e^- \rightarrow 4$  partons that have been first calculated by Bern, Dixon and Kosower (BDK) [27]. Here the MADLOOP results are compared against the implementation of the crossings of the BDK amplitudes in MCFM [48], where they contribute to the  $pp \rightarrow Z/\gamma^* + 2j$  cross section. We start by restricting ourselves to testing the pure vector coupling, and hence the  $Z$ -boson exchange contributions is switched off in both MADLOOP and MCFM. The same remark on the  $m_{top}$ -dependence of the BDK amplitudes presented in in sect. B.2.4 applies here as well.

For the present comparison we use the same input parameters as in sects. B.2.3 and B.2.4, and choose the following kinematic configuration:

$$\begin{aligned}
 p_u &= ( 79.343740010234328 \quad , \quad 0 \quad , \quad 0 \quad , \quad 79.343740010234328 \quad ) \\
 p_g &= ( 330.04970916921303 \quad , \quad 0 \quad , \quad 0 \quad , \quad -330.04970916921303 \quad ) \\
 p_{e^-} &= ( 44.502332440251230 \quad , \quad -9.0128674723142481 \quad , \quad 20.893959782906148 \quad , \quad -38.244846151337029 \quad ) \\
 p_{e^+} &= ( 173.55124786955787 \quad , \quad -83.712846866171589 \quad , \quad -85.405837095621621 \quad , \quad -125.76978133334636 \quad ) \\
 p_u &= ( 142.62173792637984 \quad , \quad 51.789721902948564 \quad , \quad 71.086870231086095 \quad , \quad -112.27395831226823 \quad ) \\
 p_g &= ( 48.718130943258451 \quad , \quad 40.935992435537273 \quad , \quad -6.5749929183706302 \quad , \quad 25.582616637972905 \quad )
 \end{aligned}$$

The results are presented in fig. B.2.3 as a function of  $m_{top}$ .

## B.2. Processes with a single vector boson

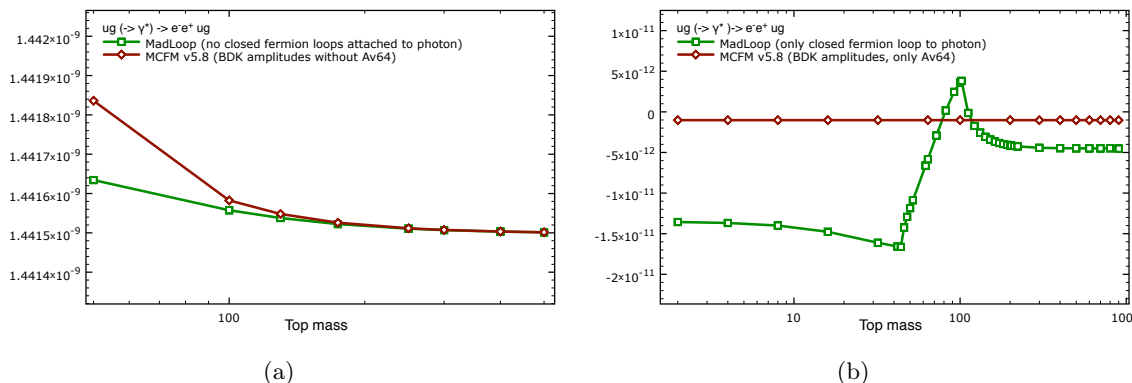


Figure B.2.3: Contributions to the finite part  $c_0$  for  $ug(\rightarrow \gamma^*) \rightarrow e^-e^+ug$ , as a function of  $m_{top}$ ; MADLOOP (boxes) and MCFM (diamonds) results are shown. Panel (a) is the contribution without closed fermion loops attached to the photon, and panel (b) shows only the contribution from those loops. The sum of the two is equal to  $c_0$ .

Figure B.2.3(b) shows the contribution to the finite part  $c_0$  due *only* to the closed fermion loops attached to the photon (up to the interference with the Born, this contribution is called  $A_{6,4}^v$  in ref. [27]). Figure B.2.3(a) shows all the other contributions to  $c_0$ . The MADLOOP and MCFM results in fig. B.2.3(a) are seen to be in excellent agreement for large top quark masses (at  $m_{top} = 500$  GeV there is a relative difference of order  $10^{-7}$ ).

The situation of fig. B.2.3(b) is different, since the MADLOOP and MCFM results are in clear disagreement. The contribution to  $c_0$  considered here is due to six box diagrams, whose sum is gauge invariant. Moreover, it is a finite contribution, so it does not require UV counterterms (nor terms to switch from the 't Hooft-Veltman scheme to the DR scheme). For  $m_{top} \rightarrow \infty$ , the ratio between MADLOOP and MCFM is not an overall constant, but depends on the kinematic configuration chosen. Also, in such a decoupling limit, MADLOOP result agrees with the one obtained by running MADLOOP with five massless flavors only. Furthermore, in the limit  $m_{top} \rightarrow 0$ , MADLOOP result coincides with that obtained by running MADLOOP with six massless flavours. These tests clearly suggested that the box contribution was wrongly implemented in MCFM.

The analogue of the comparison shown in fig. B.2.3(b) was also carried out by considering the axial (for a  $Z$  exchange) rather than the vector coupling. The same pattern as for the vector coupling was observed, namely a disagreement with MCFM<sup>5</sup>. In order to confirm that there is no problem with the computation of these box diagrams in MADLOOP, they have checked them against a different implementation of the BDK amplitudes – see sect. B.2.6.

<sup>5</sup>Triggered by the present results, John Campbell has reconsidered the implementation of BDK amplitudes in MCFM, and found a mistake in the vector part. To the best of my knowledge, the disagreement on the axial part persists to this day.

## Appendix B. Comparisons with existing results

---

### B.2.6 Closed fermion loops contributing to $e^+e^- \rightarrow d\bar{d}g\bar{g}$

As anticipated in sect. B.2.5, MADLOOP results for the BDK box and triangle diagrams [27] (with the latter contributing only to the axial part) are compared with that of their implementation in the program MENLO PARC [148, 85]. This is done so by considering the process  $e^+e^- \rightarrow d\bar{d}g\bar{g}$ . I remind the reader that the BDK amplitudes retain the top-mass dependence in the loops only up to terms of order  $1/m_{top}^2$ .

The same input parameters as in sect. B.2.3 are used, to the exception of  $\mu = m_Z = 91.187$  and  $\alpha_S = 0.118$ . Furthermore, we the coupling constants of the photon to the fermions (both quarks and leptons) is set equal to one. The  $Z$  boson couplings to fermions is purely axial, with magnitude 1 for leptons and up-type quarks, and  $-1$  for down-type quarks. The result are presented in the 't Hooft-Veltman scheme and the chosen kinematic configuration is:

$$\begin{aligned}
 p_{e^+} &= ( 45.5935 & , 0 & , 0 & , 45.5935 & ) \\
 p_{e^-} &= ( 45.5935 & , 0 & , 0 & , -45.5935 & ) \\
 p_{\bar{d}} &= ( 30.844322198071779 & , -19.016873847975504 & , 2.6503380947327226 & , 24.139312933309792 & ) \\
 p_d &= ( 11.409429861138499 & , -1.5750381678441148 & , -9.8113210223060605 & , 5.6064538099701196 & ) \\
 p_g &= ( 21.321201379655506 & , 12.486676226087143 & , -12.407109827066350 & , -12.030800922457644 & ) \\
 p_{\bar{g}} &= ( 27.612046561134214 & , 8.1052357897324754 & , 19.568092754639686 & , -17.714965820822268 & )
 \end{aligned}$$

The intermediate (off-shell) photon case is considered first. In such a way only the vectorial couplings are tested and six boxes are relevant in MADLOOP, which correspond to the  $A_{6;4}^v$  term of ref. [27]. In the program MENLO PARC,  $A_{6;4}^v$  can be easily computed by setting the `color part` parameter equal to `vect`. As can be seen from fig. B.2.3(b), this term is independent of the top mass. Thus, the comparison with MADLOOP prediction can be performed by either considering the decoupling limit or directly excluding the top-quark contribution to the loops; the latter option is adopted here<sup>6</sup>. An excellent agreement was found.

---

$e^+e^- \rightarrow \gamma^* \rightarrow \bar{q}qg\bar{g}$ (closed fermion loops)	MADLOOP	Refs. [148, 85]
$c_0$	-4.50041164255807986E-007	-4.5004116164533885E-007

---

We next consider the case of a purely-axial intermediate  $Z$  boson. This corresponds to the  $A_{6;4}^{ax}$  and  $A_{6;5}^{ax}$  terms of ref. [27], which can be obtained from MENLO PARC by setting the parameter `color part` equal to `axal`. The results are presented in fig. B.2.4 as a function of the top mass, for the same kinematic configuration as was used above.

---

<sup>6</sup>The decoupling limit was also computed and found consistent with the results presented here.

## B.2. Processes with a single vector boson

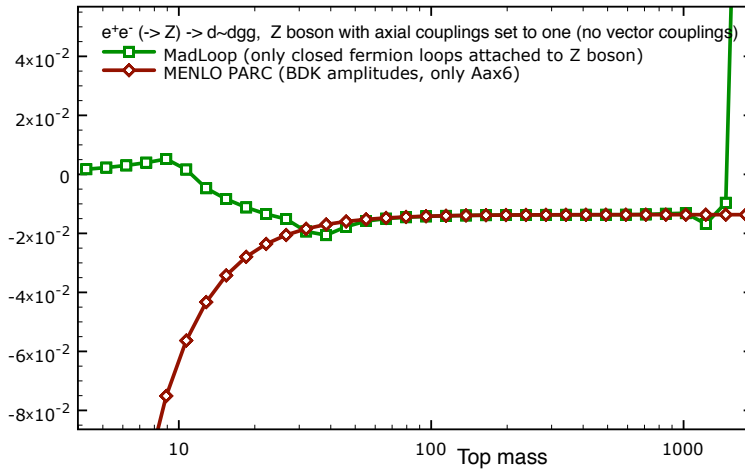


Figure B.2.4: Pure-axial contributions to the finite part  $c_0$  for  $e^+e^- \rightarrow d\bar{d}gg$ , as a function of  $m_{top}$ ; MADLOOP (boxes) and MENLO PARK (diamonds) results are shown.

As in the case of the purely vector couplings, we find excellent agreement between the two results. In particular, for large  $m_{top}$  the relative difference between MADLOOP and MENLO PARK is of the order of  $10^{-4}$ . When  $m_{top} = \mathcal{O}(1 \text{ TeV})$ , numerical instabilities in MADLOOP4 spoil the accuracy of the comparison; as in previous cases, these instabilities are due to large cancellations between the cut-constructible-plus- $R_1$  and  $R_2$  contributions. It would be interesting redo the same analysis using quadruple precision within MADLOOP5 to see how close one can get to MENLO PARK result and up to which top mass scale the result is numerically stable in this case.

For  $m_{top} \rightarrow 0$ , the BDK amplitudes diverge (due to the fact that terms are kept only up to  $1/m_{top}^2$ ), while MADLOOP reproduces the correct result. This is equal to zero, since in this limit the bottom and top quark loop contributions exactly cancel each other.

It was checked explicitly that MADLOOP is self-consistent (and consistent with the results given in sect. B.2.5) by crossing the antiquark and one of the gluons to the initial state, and the  $e^+e^-$  pair to the final state.

### B.2.7 The $gg \rightarrow Zg$ one-loop amplitude squared

As a final check on the computations of closed fermion loop diagrams with one external EW boson leg, we consider the process  $gg \rightarrow Zg$ , whose amplitude was first computed by Van der Bij and Glover in ref. [115]<sup>7</sup>. At variance with the cases discussed in sect. B.2.5 and B.2.6, this process does not have a Born-level contribution. So we shall not compute here the quantity  $V$  defined in eq. (3.1.2), but rather the one-loop amplitude squared

<sup>7</sup>The results also agree with an independent calculation by F. Tramontano.

## Appendix B. Comparisons with existing results

---

( $|\mathcal{A}^{(n,1)}|^2$ ), summed/averaged over spins and colors<sup>8</sup>. This implies that for the present case we had to hack the MADLOOP4 code, in order for it to compute the square of an amplitude rather than the interference of two amplitudes. In MADLOOP5, this is done automatically at the 'generate' stage. If MADLOOP5 is unable to generate any Born level contribution, it assumes this process is purely loop-induced and that the user wants as an output a code for a matrix element given as the square of the loop amplitudes<sup>9</sup>.

As far as the computation of ref. [115] is concerned, the helicity amplitudes presented in appendix B of that paper are typed<sup>10</sup> in `Mathematica`, which is then used to perform all subsequent analytical and numerical manipulations, and to obtain the results denoted by "Ref. [115]" in what follows. I stress that the results of ref. [115] are given for only one quark flavor circulating in the loop. The following input parameters are used:

Parameter	value	Parameter	value
$\alpha_s$	0.1176	$\alpha^{-1}$	128.0
$M_Z$	91.188	$m_{top}$	80.0
$\sin^2 \theta_W$	0.23122	$\mu$	91.188

The width of the top mass is set to zero, because MADLOOP4 did not support the complex mass scheme. The same study with MADLOOP5 would allow to assess the impact of off-shell effects of loop fermions, at least locally here. The chosen kinematic configuration is such that the Mandelstam variables are  $t = u = -\frac{3}{2}M_Z^2$ , as defined in ref. [115]. This can be obtained using e.g. the following four-momenta:

$$\begin{aligned}
 p_1 &= ( 91.188 & , 0 & , 0 & , 91.188 & ) \\
 p_2 &= ( 91.188 & , 0 & , 0 & , -91.188 & ) \\
 p_Z &= ( 113.985 & , -48.35973987212917 & , -48.35973987212917 & , 0 & ) \\
 p_{g_f} &= ( 68.391 & , 48.35973987212917 & , 48.35973987212917 & , 0 & )
 \end{aligned}$$

Note that  $\sqrt{s} = 2M_Z$ , and hence we have adopted a value of  $m_{top}$  that is not effectively close to the decoupling limit – this is useful lest we have to deal with very small amplitude values. In any case, the dependence on  $m_{top}$  has been studied as well, as can be seen in fig. B.2.5. The axial and the vector coupling lead to amplitudes separately gauge independent, which do not interfere (simply because of the symmetry and antisymmetry of their respective color factors); they can thus be studied independently. The vector

---

<sup>8</sup>We also point out that in the present case the  $Z$  is on-shell, while the intermediate vector bosons were off-shell in the cases discussed in sect. B.2.5 and B.2.6.

<sup>9</sup>It is necessary for these loop amplitudes to be finite, otherwise their single poles can have a finite contribution when crossed with their terms of order  $\epsilon$  (not computable within the MADLOOP framework). In this case, MADLOOP5 checks that this holds and warns the user if not so.

<sup>10</sup>This pain-stacking work was realized by myself during the four months of my master project at the Université Catholique de Louvain. MADLOOP need for a cross-check of these kind of loops provided a good occasion to recycle this work and put it to use. My master thesis can therefore provide more information on this MATHEMATICA implementation if needed.

## B.2. Processes with a single vector boson

coupling is considered first, for which only the top quark is kept running in the loop, since the corresponding amplitude is not anomalous. The resulting Feynman diagrams are then six (finite) massive fermion-loop boxes. The comparison of this implementation with MADLOOP4 yields:

$gg \rightarrow Zg$ vector	MADLOOP	Ref. [115]
$c_0$	1.41346852305044352E-006	1.4134685231123695E-006

The  $m_{top}$  dependence of this result is also studied, and the resulting comparison between MADLOOP and ref. [115] is presented in fig. B.2.5. The thresholds at  $m_{top}/m_Z = 0.5$  and  $m_{top}/m_Z = 1$  can be easily understood in terms of the optical theorem.

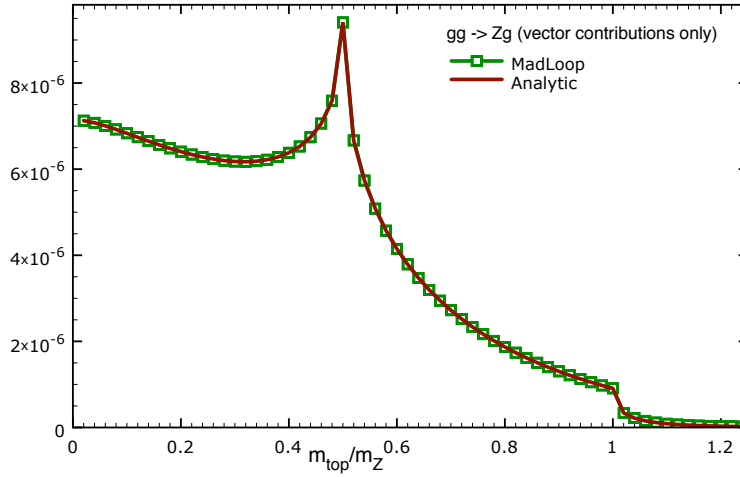


Figure B.2.5: Square of the one-loop amplitude for  $gg \rightarrow Zg$  (vectorial coupling only), as a function of  $m_{top}/m_Z$ , with only the top quark circulating in the loop.

When one considers the axial couplings of the  $Z$  boson, there is an anomalous contribution independent of the mass of the fermion that circulates in the loop. The most straightforward way to circumvent the problem of the anomaly is that of considering both the top and the bottom quarks as loop particles. The computation of ref. [115] is performed assuming non-zero quark masses, so that the  $m_b$  must be finite and in this case kept fixed and equal to 20 GeV. On the MADLOOP side, the bottom-mass dependence was studied, and no peculiar numerical behaviors was found. The specific value  $m_b = 20$  GeV was chosen for these results in order to be able to probe both regions  $m_{top} \gg m_b$  and  $m_{top} \ll m_b$  (see fig. B.2.6). Specifically setting  $m_{top} = 80$  GeV yields:

$gg \rightarrow Zg$ axial	MADLOOP	Ref. [115]
$c_0$	1.17192023257760489E-004	1.1719202325756625E-004

## Appendix B. Comparisons with existing results

Analogously to what was done in fig. B.2.5, the fig. B.2.6 presents the results for the axial part as a function of  $m_{top}$ . In the decoupling limit  $m_{top} \rightarrow \infty$ , only the non-anomalous<sup>11</sup> part of the contribution due to the bottom quark is left. As is expected, the contributions due to top and bottom quarks exactly cancel each other when  $m_{top} = m_b$ . We have also checked that this is the case for various value of  $m_b$  (including the large-mass limit).

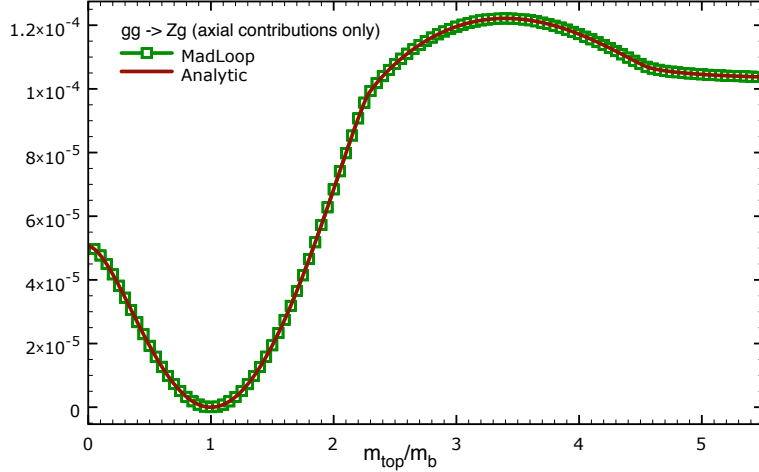


Figure B.2.6: Square of the one-loop amplitude for  $gg \rightarrow Zg$  (axial coupling only), as a function of  $m_{top}/m_b$ , with the top and bottom quarks circulating in the loop.

I conclude this section by mentioning that all possible gluon crossings of the process considered in this section were checked. As for all other cases in which gluons appear, gauge independence (eq. (3.1.13)) is verified to hold.

### B.2.8 The process $ug \rightarrow t\bar{b}d$ (four-flavor $t$ -chan. single-top production)

The  $t$ -channel single-top process in the four-flavor scheme is an interesting case from the point of view of NLO computations [50, 51]. Even though it is a  $2 \rightarrow 3$  process at the Born level, the color-singlet exchange of the  $W$ -boson in the  $t$  channel “disconnects” NLO corrections to the light and heavy quark lines, essentially removing all pentagon diagrams. The complexity here arises then from the fact that both the top and the bottom quarks have to be treated as massive.

In order to generate this process with MADLOOP, a minimal amount of manual work is required. This is due to the fact that selecting such a topology is in general not a gauge invariant procedure and it is therefore not desirable to let the user specify one. Therefore, when entering  $ug \rightarrow t\bar{b}d$  as an input to MADLOOP also the  $s$ -channel contributions are obtained, and in this case they are eventually set equal to zero by hand ( with the `UserFilter` function).

<sup>11</sup>Once again, we remind the reader that the anomalous part is mass-independent.



## B.2. Processes with a single vector boson

The following input parameters are used, with a diagonal CKM matrix:

Parameter	value	Parameter	value
$\alpha_s$	0.118	$n_f$	4
$m_Z$	91.188	$\mu$	91.188
$m_W$	80.419	$\alpha^{-1}$	132.506980
$m_{top}$	174.3	$m_b$	4.5
$\sin^2 \theta_W$	$1 - m_W^2/m_Z^2$	$\Gamma_W$	2.0476

Once again, due to the lack of support for the complex mass scheme in MADLOOP4, the top width is set to zero. A complete analysis of this process with MADLOOP5, including all contributions and off-shell top quark effects is undergoing. The kinematic configuration is:

$$\begin{aligned}
 p_u &= ( 250 & , 0 & , 0 & , 250 & ) \\
 p_g &= ( 250 & , 0 & , 0 & , -250 & ) \\
 p_t &= ( 458.5331753852783 & , 29.17335589243201 & , 159.7715722928748 & , -91.96084974966891 & ) \\
 p_{\bar{b}} &= ( 177.5248259329844 & , -66.11648748945143 & , -111.8173550700313 & , 120.9144450003231 & ) \\
 p_d &= ( 67.10225480257022 & , 36.94313159701945 & , -47.95421722284348 & , -28.95359525065417 & )
 \end{aligned}$$

and the results are presented in the 't Hooft-Veltman scheme. The results obtained by MADLOOP with the virtual corrections computed in ref. [50] and implemented in MCFM. Excellent agreement was found:

$ug \rightarrow t\bar{b}d$ ( $t$ -channel)	MADLOOP	Ref. [50]
$a_0$	7.79629086614075984E-007	7.79629086614075031E-007
$c_{-2}$	-8.29693789210587181E-008	-8.29693789210586651E-008
$c_{-1}$	2.15034348206562335E-007	2.15034348206885610E-007
$c_0$	2.31517097632403642E-007	2.31517097628348630E-007

## Appendix B. Comparisons with existing results

### B.2.9 The process $u\bar{d}(\rightarrow W^+) \rightarrow \nu_e e^+ b\bar{b}$ with massive $b$

This process has been computed very recently<sup>12</sup> by Badger, Campbell and Ellis and implemented in MCFM [12]. The following input parameters:

Parameter	value	Parameter	value
$\alpha_S$	0.118298	$n_{lf}$	4
$\sin^2 \theta_W$	0.223	$\mu$	$m_W + 2m_b$
$m_W$	80.44	$G_F$	$1.16639 \cdot 10^{-5} \text{ GeV}^{-2}$
$m_{top}$	172.6	$m_b$	4.62
$V_{ud} = V_{cs}$	0.974	$V_{us} = V_{cd}$	0.227

and the kinematic configuration:

$$\begin{aligned}
 p_u &= ( 105.1910162427912, 0, 0, 105.1910162427912 ) \\
 p_{\bar{d}} &= ( 1315.106152715695, 0, 0, -1315.106152715695 ) \\
 p_{\nu_e} &= ( 552.4486825382789, 159.0272780479767, 133.6457759793429, -511.9069038778545 ) \\
 p_{e^+} &= ( 148.3926012456811, 43.98296570595704, -5.568920346765623, -141.6151473478021 ) \\
 p_b &= ( 348.0072091647683, 68.78221202106434, 5.036723885587666, -341.0737632135319 ) \\
 p_{\bar{b}} &= ( 371.4486760097574, -271.7924557749981, -133.1135795181650, -215.3193220337149 )
 \end{aligned}$$

The finite part is given in the DR scheme. The  $b$  quark mass is set equal to zero in closed fermion loops as well as for  $\alpha_S$  renormalization (while the exact top-quark-mass dependence is kept everywhere). The results are:

$u\bar{d}(\rightarrow W^+) \rightarrow \nu_e e^+ b\bar{b}$	MADLOOP	MCFM [12]
$a_0$	1.79478780194792655E-007	1.794787732024681E-007
$c_{-2}$	-9.01109441027896061E-009	-
$c_{-1}$	8.46671286067843610E-008	-
$c_0$	1.54008876289213431E-007	1.540098268053898E-007

The residues of the double and single poles have been checked against those returned by MADFKS, and perfect agreement has been found.

<sup>12</sup>The older computation by Cordero, Reina and Wackerroth in ref. [97] does not include spin correlations, i.e. the  $W$  is produced unpolarized and on-shell.

## B.3 Processes with two vector bosons

### B.3.1 The process $d\bar{d} \rightarrow W^+W^- \rightarrow \nu_e e^+ e^- \bar{\nu}_e$

This process, that contributes to the NLO corrections to fully-decayed  $W^+W^-$  production (i.e, all spin correlations are included), has been implemented in MCFM [47], using the virtual amplitudes calculated in ref. [84]. The computation of ref. [84] includes the singly-resonant contributions where an off-shell photon or  $Z$  boson “decays” into a pair of  $W$  bosons. However, it does not include diagrams in which the off-shell photon or  $Z$  boson “decays” to leptons and one of the leptons radiates a  $W$  boson. This latter contribution is however kinematically highly suppressed w.r.t. the others, and its neglect is a very good approximation for most physics applications. Such a contribution is included in the MADLOOP result, but in order not to consider it and be consistent with ref. [84], the couplings of photons and  $Z$  bosons to leptons are simply set equal to zero. The following input parameters are used:

Parameter	value	Parameter	value
$\alpha_s$	0.118	$n_{lf}$	5
$m_Z$	91.1876	$\mu$	91.1876
$m_W$	80.44	$\alpha^{-1}$	132.6844139
$\sin^2 \theta_W$	$1 - m_W^2/m_Z^2$	$\Gamma_W$	2.1054

and kinematic configuration:

$$\begin{aligned}
 p_d &= ( 39.534683750772302, 0, 0, 39.534683750772302 ) \\
 p_{\bar{d}} &= ( 546.24075297747743, 0, 0, -546.24075297747743 ) \\
 p_{\nu_e} &= ( 188.27600670927578, 3.8276243346653374, -38.361733789650529, -184.28668257634874 ) \\
 p_{e^+} &= ( 295.10612392593191, 49.617890129404948, 30.642119343108476, -289.28662236587513 ) \\
 p_{e^-} &= ( 41.828055877825669, -7.1022701637404531, -30.841911801229820, -27.348135100677510 ) \\
 p_{\bar{\nu}_e} &= ( 60.565250215216373, -46.343244300329829, 38.561526247771873, -5.7846291838037445 )
 \end{aligned}$$

The finite part is given in the DR scheme:

$d\bar{d} \rightarrow \nu_e e^+ e^- \bar{\nu}_e$	MADLOOP	MCFM [84, 47]
$a_0$	1.11000204402873114E-004	1.11000204410578607E-004
$c_{-2}$	-5.55897408896383675E-006	-
$c_{-1}$	-4.67335122692354957E-006	-
$c_0$	2.24254527912372296E-005	2.24254527928672022E-005

The residues of the double and single poles have been checked against those returned by MADFKS, and perfect agreement has been found.

## Appendix B. Comparisons with existing results

### B.3.2 The processes $u\bar{u} \rightarrow W^+W^-b\bar{b}$ and $gg \rightarrow W^+W^-b\bar{b}$ with massless $b$

$W$ -boson pair plus  $b$ -quark pair production is among the different result presented in ref. [155] by A. van Hameren *et al.*. The comparisons performed in this section constitute therefore a check of the implementation of the CUTTOOLS software in a framework different from that of HELAC-1Loop [30] (see sect. B.1.5 and B.1.6 for a similar comparison). The following set of input parameters is used:

Parameter	value	Parameter	value
$g_S$	1	$n_f$	5
$m_{top}$	174.0	$m_W$	80.419
$\Gamma_{top}$	0	$m_b$	0
$m_Z$	91.188	$\Gamma_Z$	2.44140351
$G_F$	1.1663910e-05	$\sin^2 \theta_W$	$1 - \frac{m_W^2}{m_Z^2}$
$\alpha$	$\sqrt{2}G_F m_W^2 \sin^2 \theta_W / \pi$	$\mu$	500.0

The CKM matrix is diagonal and the Higgs channel (i.e., diagrams that contain the “decay”  $H \rightarrow W^+W^-$ ) is not included<sup>13</sup>. The chosen kinematic configuration is:

$$\begin{aligned}
 p_1 &= ( 250 & , 0 & , 0 & , 250 & ) \\
 p_2 &= ( 250 & , 0 & , 0 & , -250 & ) \\
 p_{W^+} &= ( 154.8819879118765 & , 22.40377113462118 & , -16.53704884550758 & , 129.4056091248114 & ) \\
 p_{W^-} &= ( 126.4095336206695 & , 92.64238702192333 & , -0.4920930146078141 & , 30.48443210132545 & ) \\
 p_b &= ( 174.1159068988160 & , -71.68369328357026 & , 6.716416578342183 & , -158.5329205583824 & ) \\
 p_{\bar{b}} &= ( 44.59257156863792 & , -43.36246487297426 & , 10.31272528177322 & , -1.357120667754454 & )
 \end{aligned}$$

with  $p_1$  and  $p_2$  the momenta of the initial-state partons coming from the left ( $u$  or  $g$ ) and from the right ( $\bar{u}$  or  $g$ ) respectively. The finite part is given in the 't Hooft-Veltman scheme. For consistency with ref. [155], no UV counterterms are included except the one relevant to top-mass renormalization.

<sup>13</sup>MADLOOP can easily compute this contribution, but it is very small and anyhow not included in the computation performed by Van Hameren *et al.*.

### B.3. Processes with two vector bosons

The results are:

$u\bar{u} \rightarrow W^+W^-b\bar{b}$	MADLOOP	Ref. [155]
$a_0$	2.338047209268890E-008	2.338047130649064E-008
$c_{-2}$	-2.493920703542680E-007	-2.493916939359002E-007
$c_{-1}$	-4.885901939046758E-007	-4.885901774740355E-007
$c_0$	-2.775800623041098E-007	-2.775787767591390E-007
$gg \rightarrow W^+W^-b\bar{b}$		
$a_0$	1.549795815702494E-008	1.549794572435312E-008
$c_{-2}$	-2.686312747217639E-007	-2.686310592221201E-007
$c_{-1}$	-6.078687041491385E-007	-6.078682316434646E-007
$c_0$	-5.519004042667462E-007	-5.519004727276688E-007

The  $Z$ -boson decay width is not specified in ref. [155], and this is most likely the reason for which we find a relative difference of  $\mathcal{O}(10^{-6})$  between MADLOOP and ref. [155]<sup>14</sup>. Since the agreement is however already quite satisfactory, we have refrained from investigating this point further.

As a final remark it should be noted that due to possible intermediate top quarks, which can go on-shell, the top width should be taken into account. To do this in a gauge-independent and consistent way, one must work within a scheme such as e.g. the complex-mass one to carry a *full* phase-space integration of the process. This option is available in MADLOOP5 so that phenomenology associated to this process can be studied in the most recent framework<sup>15</sup>.

<sup>14</sup>We point out, in fact, that the two results for the residue of the double pole can be made to coincide by multiplying the MADLOOP results by  $\sigma_{\text{BornAVH}}/\sigma_{\text{BornMadLoop}}$ .

<sup>15</sup>Using the complex-mass scheme, the phase-space integration for the process  $pp \rightarrow W^+W^-b\bar{b}$  at the NLO has already been performed by two groups [73, 31].

## B.4 Processes with a single Higgs boson

### B.4.1 The process $bg \rightarrow Hb$

The process of SM Higgs boson production in association with a bottom quark was computed by Campbell *et al.* in ref. [49]. The corresponding computer code is publicly available in the MCFM package. In our comparison, the following input parameters are used:

Parameter	value	Parameter	value
$\alpha_s$	0.118	$m_H$	120
$v$	246.2185 GeV	$\mu$	91.188
$m_b$	0	$\overline{m}_b(\mu)$	2.937956

with  $\overline{m}_b(\mu)$  being used for the calculation of the Yukawa coupling only. The chosen kinematic configuration is:

$$\begin{aligned}
 p_b &= ( 250 & , & 0 & , & 0 & , & 250 & ) \\
 p_g &= ( 250 & , & 0 & , & 0 & , & -250 & ) \\
 p_H &= ( 264.4 & , & -83.84841332241601 & , & -86.85350630148753 & , & -202.3197272300720 & ) \\
 p_b &= ( 235.6 & , & 83.84841332241599 & , & 86.85350630148751 & , & 202.3197272300720 & )
 \end{aligned}$$

The finite part is given in the 't Hooft-Veltman scheme:

$bg \rightarrow Hb$	MADLOOP	Ref. [49]
$a_0$	3.11285493284766746E-007	3.112854933728111162E-007
$c_{-2}$	-3.31275018959845830E-008	-3.31275018959846227E-008
$c_{-1}$	6.99063829676915201E-008	6.99063829676930686E-008
$c_0$	-1.41076086675311370E-007	-1.4107608671538634E-007

**B.4.2 The process  $gb \rightarrow H^-t$**

Charged-Higgs boson production in association with a top quark was first calculated in ref. [158]. Recently, the computation has been redone in two independent ways in the context of the implementation of this process in the MC@NLO framework [112, 156] for a generic 2HDM model. The latter result is used for the comparisons and the following input parameters are adopted:

Parameter	value	Parameter	value
$\alpha_S$	0.10751760258646566	$m_b$	0
$m_{top}$	174.3	$\mu$	174.3
$m_H$	120	$a$	-0.0170580225049951247
$b$	0		

with  $a$  and  $b$  the coefficients entering the  $Htb$  vertex, according to the conventions of ref. [156]:

$$G_{H^-tb} = iV_{tb}(a - b\gamma_5), \quad (\text{B.4.1})$$

with a diagonal CKM matrix. The  $R_2$  SM vertices are sufficient for the computation of this process. The following kinematic configuration is chosen:

$$\begin{aligned}
 p_g &= ( 200 & , & 0 & , & 0 & , & 200 & ) \\
 p_b &= ( 200 & , & 0 & , & 0 & , & -200 & ) \\
 p_{H^-} &= ( 180.0243875 & , & -120.4281794945461 & , & -1.755237425897029 & , & 59.18405883308687 & ) \\
 p_t &= ( 219.9756125 & , & 120.4281794945461 & , & 1.755237425897029 & , & -59.18405883308687 & )
 \end{aligned}$$

The finite part is given in the 't Hooft-Veltman scheme:

$gb \rightarrow H^-t$	MADLOOP	Ref. [156]
$a_0$	1.10048820395828282E-005	1.10048820395828078E-005
$c_{-2}$	-8.16032006344512711E-007	-
$c_{-1}$	2.77298585886145253E-007	-
$c_0$	5.32062254695102591E-007	5.32062219706480764E-007

The residues of the double and single poles have been checked against those returned by MADFKS, and perfect agreement has been found.

## Appendix B. Comparisons with existing results

### B.4.3 The processes $u\bar{u} \rightarrow t\bar{t}H$ and $gg \rightarrow t\bar{t}H$

Two groups have calculated these two subprocesses that contribute to  $t\bar{t}H$  hadroproduction at the NLO in QCD – see refs. [146, 63] and refs. [15, 16]. However, their codes are not publicly available. MADLOOP results are therefore compared with those obtained with the HELAC-1Loop code [155]. The following input parameters are used:

Parameter	value	Parameter	value
$\alpha_s$	0.1076395107858145	$m_H$	130
$m_{top}$	172.6	$\mu$	172.6
$v$	246.21835258713082		

with the running mass of the top entering the Yukawa coupling set equal to the pole mass. The chosen kinematic configuration is:

$$\begin{aligned}
 p_{u,g} &= ( 250 & , 0 & , 0 & , 250 & ) \\
 p_{\bar{u},g} &= ( 250 & , 0 & , 0 & , -250 & ) \\
 p_t &= ( 181.47665951104506 & , 20.889486679044587 & , -50.105625289561424 & , 14.002628607367491 & ) \\
 p_{\bar{t}} &= ( 182.16751255202476 & , -36.023358488530903 & , 22.118891298530357 & , -40.091332234320859 & ) \\
 p_H &= ( 136.35582793693018 & , 15.133871809486299 & , 27.986733991031045 & , 26.088703626953386 & )
 \end{aligned}$$

The finite part is given in the 't Hooft-Veltman scheme:

$u\bar{u} \rightarrow t\bar{t}H$	MADLOOP	Ref. [155]
$a_0$	4.07927424576157583E-005	4.07927080724888850E-005
$c_{-2}$	-1.86356048126662262E-006	-1.86355892362235005E-006
$c_{-1}$	-1.14634232495081623E-006	-1.14634136678800731E-006
$c_0$	-1.06894889909139909E-005	-1.06894800561762434E-005
$gg \rightarrow t\bar{t}H$		
$a_0$	1.13589882608476193E-005	1.13589786860990613E-005
$c_{-2}$	-1.16756954296913433E-006	-1.16756856706412638E-006
$c_{-1}$	5.81128096324302437E-007	5.81127610592268124E-007
$c_0$	1.75265433284702459E-006	1.75265286791477312E-006

It is likely that the agreement between the two codes could be further improved, since they are known differences beyond single-precision accuracy between the input parameters used in the two codes.



## B.5 Checks of MADLOOP5

### B.5.1 The process $gg \rightarrow ng$ , $n=2,3,4$

Because of the absence of the 4-gluon  $R_2$  counterterm in MADLOOP4 (see sect. 3.2), this class of processes can only be generated by MADLOOP5. Even with the help of the UFO formalism (see sect. 3.4.2), the implementation of the complicated Feynman rules of this counterterm is cumbersome and necessitates a careful crosscheck. The literature on loop corrections to pure gluon scattering amplitudes is abundant, but only a few present numerical results for the quantity  $V(r)$  of eq. (B.0.1), with massless quarks in the loop, full color and summed over all helicity configurations. The public code NGLUON [11] computes exactly this quantity, and is used here to cross-check MADLOOP5 amplitudes up to six-gluons. The complexity of this process is at the edge of what can be handled by the current version of the code. NGLUON does not include the contributions of the massive quarks running in the loop and these were correspondingly removed from MADLOOP5 output. Such topologies were already verified when comparing the processes of sect. B.2 and they do not yield  $R_2$  contributions, so that their MADLOOP computation can be trusted.

The kinematic configurations considered are given here for the each of the  $n = 2, 3, 4$  case.

$p_{g_1}$ and $p_{g_1}$ for all $n$			
$p_{g_1} = ( 50$	, 0	, 0	, 50 )
$p_{g_2} = ( 50$	, 0	, 0	, -50 )
$p_{g_{i>2}}$ for $n = 2$			
$p_{g_3} = ( 50$	, 43.328718243523372	, 12.317414119409190	, 21.700310707092285 )
$p_{g_4} = ( 50$	, -43.328718243523372	, -12.317414119409190	, -21.700310707092285 )
$p_{g_{i>2}}$ for $n = 3$			
$p_{g_3} = ( 49.359470019669386$	, 22.397003141303164	, 10.521565504548473	, -42.708643039138961 )
$p_{g_4} = ( 49.601785815191898$	, -21.610638977601023	, -10.830210473092767	, 43.313092479577988 )
$p_{g_5} = ( 1.0387441651387164$	, -0.78636416370214065	, 0.30864496854429404	, -0.60444944043902757 )
$p_{g_{i>2}}$ for $n = 4$			
$p_{g_3} = ( 48.160156867258136$	, 21.980718944580564	, -42.444508313840180	, 5.8917245484340103 )
$p_{g_4} = ( 37.372855246144170$	, -11.415344131821260	, 35.339097064523461	, -41.914730424433162 )
$p_{g_5} = ( 3.3911791874168823$	, -2.4299107687218199	, 0.71451072871390430	, 2.2550175954461832 )
$p_{g_6} = ( 11.075808699180811$	, -8.1354640440374835	, 6.3909005206028147	, -3.9552691014368773 )

Notice that that the 4-momenta of the first and second initial state gluon are identical for the three cases and take an overall minus sign when taken as an input of NGLUON because it considers the  $0 \rightarrow (n + 2) g$  kinematical topology and not  $2 \rightarrow n g$ .

## Appendix B. Comparisons with existing results

---

The input parameters employed are:

Parameter	value	Parameter	value
$\alpha_S$	0.118	$n_f$	2
$\mu$	700.0		

NGLUON numerical results were translated into the CDR scheme to match those directly output by MADLOOP5 and presented below. An agreement better than 10 digits was found when running MADLOOP5 in double precision for all processes below. In order to show the highest degree of agreement achieved, we choose to provide here the result of computations obtained with quadruple precision numerics<sup>16</sup>, except for the Born.

$gg \rightarrow gg$	MADLOOP5	NGLUON
$a_0$	60.85321142865562	60.85321142865557
$c_{-2}$	-13.71408659307165	-13.71408659307164
$c_{-1}$	-85.23414764837082	-85.23414764837081
$c_0$	-193.7284710880142	-193.7284710880142
$gg \rightarrow ggg$	MADLOOP5	NGLUON
$a_0$	8.450374528544618e+03	8.450374528544615e+03
$c_{-2}$	-2.380506412636426e+03	-2.380506412636425e+03
$c_{-1}$	-2.013780422559013e+04	-2.013780422559014e+04
$c_0$	-7.316183959337519e+04	-7.316183959337522e+04
$gg \rightarrow gggg$	MADLOOP5	NGLUON
$a_0$	5.990436333957672	5.990436333957688
$c_{-2}$	-2.025037644327821	-2.025037644327822
$c_{-1}$	-16.14156372683876	-16.14156372683874
$c_0$	-50.64655894143655	-50.64655894143647

---

<sup>16</sup>This also implies that at least 15 digits of the MADLOOP results presented in this section are numerically stable.

### B.5.2 The channels of the process $pp \rightarrow 4j$

The BLACKHAT [19] collaboration presented in ref. [24] their computation of the NLO QCD correction to four jets productions at hadron colliders. They also provide benchmark results for the four contributing channels with 0, 1 and 2 and 3 massless quark pairs respectively. I report these results here with their MADLOOP5 counterpart. The input parameters are:

Parameter	value	Parameter	value
$\alpha_S$	0.118	$n_{lf}$	5
$\mu$	600.0		

In the context of the computation of ref. [24],  $n_{lf} = 5$  means that the top contribution (via a closed quark loop) is not considered and the b-quark is treated massless. To mimic this in MADLOOP5, the massless b-quark variant (or *restriction*) of the UFO 'loop\_sm' model was loaded and the top-quark forbidden in the process definition with the '/'  $\tau$ ' syntax. The kinematic configuration is chosen according to eq.(9.1)-(9.2) of ref. [23] but with  $\mu = 600$  GeV and it remains the same for all four channels:

$$\begin{aligned}
 p_{g,d} &= ( 300 & , -212.13203435596426 & , -106.06601717798213 & , -183.71173070873836 & ) \\
 p_{g,\bar{d}} &= ( 300 & , 212.13203435596426 & , 106.06601717798213 & , 183.71173070873836 & ) \\
 p_{g,u} &= ( 200.00000000000000 & , 200.00000000000000 & , 0 & , 0 & ) \\
 p_{g,\bar{u}} &= ( 85.714285714285714 & , -31.578947368421053 & , 79.685060448070799 & , 0 & ) \\
 p_{g,s} &= ( 100.00000000000000 & , -18.421052631578947 & , 46.482951928041299 & , 86.602540378443865 & ) \\
 p_{g,\bar{s}} &= ( 214.28571428571429 & , -150.00000000000000 & , -126.16801237611210 & , -86.602540378443865 & )
 \end{aligned}$$

The results are given in MADLOOP5 default regularization scheme, namely the t'Hoft Veltman scheme whose finite part is identical to CDR in exactly four-dimensional space-time. This also the scheme of choice for the BLACKHAT benchmark results. The BLACKHAT results displayed here are identical to the ones presented in ref. [24]<sup>17</sup>, up to a normalization factor ( $10^8 \sigma_{Born} \frac{\alpha_S}{2\pi} C$ ), with  $10^8$  correcting for the scale-up of  $\mu$  and the integer  $C$  accounting for the factor averaging over initial state colors and helicities as well as the final state symmetry factor, both included in MADLOOP<sup>18</sup>.

Ref. [24] only specifies 10 digits and even though MADLOOP5 double precision evaluations already matches them (bar the 6g channel for which only 6 digits are correct in double precision), the results below were obtained using quadruple precision, except for the Born.

<sup>17</sup>Available at <http://arxiv.org/src/1112.3940v2/anc/sample-point.pdf> as a supplementary file of publication [24].

<sup>18</sup>More specifically,  $C = 8^2 \cdot 2^2 \cdot 4!$  for  $gg \rightarrow gggg$ ,  $C = 3^2 \cdot 2^2 \cdot 4!$  for  $d\bar{d} \rightarrow gggg$ ,  $C = 3^2 \cdot 2^2 \cdot 2!$  for  $d\bar{d} \rightarrow u\bar{u}gg$  and  $C = 3^2 \cdot 2^2 \cdot 1$  for  $d\bar{d} \rightarrow u\bar{u}s\bar{s}$ .

## Appendix B. Comparisons with existing results

$gg \rightarrow gggg$	MADLOOP5	Ref. [24]
$a_0$	8.100481343065544e-04	8.100481342e-04
$c_{-2}$	-2.738328018594504e-04	-2.738328018e-04
$c_{-1}$	-9.910444501919850e-04	-9.910444501e-04
$c_0$	-4.887971230607458e-04	-4.887971230e-04
$d\bar{d} \rightarrow gggg$	MADLOOP5	Ref. [24]
$a_0$	2.502547591440412e-06	2.502547591e-06
$c_{-2}$	-6.893121062821290e-07	-6.893121064e-07
$c_{-1}$	-2.738345818034983e-06	-2.738345818e-06
$c_0$	-2.065956953556197e-06	-2.065956954e-06
$d\bar{d} \rightarrow u\bar{u}gg$	MADLOOP5	Ref. [24]
$a_0$	1.909142107951222e-06	1.909142108e-06
$c_{-2}$	-4.063479356746059e-07	-4.063479356e-07
$c_{-1}$	-1.721706412156829e-06	-1.721706412e-06
$c_0$	-1.339089403523334e-06	-1.339089403e-06
$d\bar{d} \rightarrow u\bar{u}s\bar{s}$	MADLOOP5	Ref. [24]
$a_0$	1.021144983744993e-08	1.021144984e-08
$c_{-2}$	-1.534191365570245e-09	-1.534191366e-09
$c_{-1}$	-5.050905851972616e-09	-5.050905853e-09
$c_0$	-1.289542438842943e-10	-1.289542439e-10

Finally, all the self-consistency checks implemented via the 'check' command of MADLOOP5 (see sect. 3.4.1) were ran on these processes. This concludes the comparisons aiming at assessing the correctness of the implementation of the complicated 4-gluon R2 vertex Feynman rule.

### B.5.3 Pushing MADLOOP to the edge: a result for $d\bar{d} \rightarrow t\bar{t}t\bar{t}b\bar{b}$

This process has no phenomenological relevance to this day but it shows that MADLOOP can be pushed to very complicated cases. This process has two mass scales, the top and bottom quark masses, more than 14'000 loop diagrams, 128 contributing helicity configurations and up to 8-points loops<sup>19</sup>. There is no corresponding computation in the literature to validate this process but the result presented here is reliable thanks to the

<sup>19</sup>Notice that the 8-points loops have numerators of rank 4 in  $\ell^\mu$  at most, so that the numerical stability featured by this process is not so surprising.

independent checks of the elementary bricks building it (see sect. 3.1.4). The runtime speed of the numerical code output by MADLOOP5 for this process is too slow for direct integration (36s per computation, summed over helicity and color configurations) but it exemplifies the usage of MADLOOP5 as a tool to validate other numerical codes, faster but produced via semi-automated method and therefore less reliable. In this perspective, the great speed of MADLOOP5 process generation (about one hour for this process) is of remarkable importance.

The input parameters used for this evaluation are

Parameter	value	Parameter	value
$\alpha_s$	0.118	$n_{lf}$	4
$\mu$	1000.0	$m_b$	4.7
$m_t$	173.0	$\Gamma_t$	0

The chosen kinematic configuration is

$$\begin{aligned}
 p_d &= ( 500 & , 0 & , 0 & , 500 & ) \\
 p_{\bar{d}} &= ( 500 & , 0 & , 0 & , -500 & ) \\
 p_t &= ( 179.99988408336151 & , -4.7783934612000483 & , 21.017539776621486 & , -44.792725388076938 & ) \\
 p_{\bar{t}} &= ( 202.60071046988355 & , -33.626859979113320 & , -99.883156322279248 & , -3.2614803304350191 & ) \\
 p_t &= ( 179.57569046075946 & , -38.305077469683603 & , -28.997924768382379 & , 3.2046846377240308 & ) \\
 p_{\bar{t}} &= ( 281.21273582865592 & , 110.53120577118455 & , 169.72848217342479 & , -90.148198440739293 & ) \\
 p_b &= ( 31.866524753009699 & , -18.093776102514568 & , -4.6075475331015605 & , 25.392344750267995 & ) \\
 p_{\bar{b}} &= ( 124.74445440432983 & , -15.727098758673009 & , -57.257393326283115 & , 109.60537477125921 & )
 \end{aligned}$$

MADLOOP5 evaluation was checked to be numerically stable. However, the results below were those obtained by using quadruple precision algebra so as to maximize the number of correct digits.

$d\bar{d} \rightarrow t\bar{t}t\bar{b}b$	MADLOOP5
$a_0$	1.4590401276370345E-015
$c_{-2}$	-7.3069831789274155E-017
$c_{-1}$	1.0212112329618302E-016
$c_0$	6.8060995481163271E-015



# Bibliography

- [1] AAD, G., ET AL. Combined search for the Standard Model Higgs boson using up to  $4.9 \text{ fb}^{-1}$  of  $pp$  collision data at  $\sqrt{s} = 7 \text{ TeV}$  with the ATLAS detector at the LHC. *Phys.Lett. B710* (2012), 49–66, 1202.1408.
- [2] AAD, G., ET AL. Observation of a new particle in the search for the Standard Model Higgs boson with the ATLAS detector at the LHC. *Phys.Lett. B716* (2012), 1–29, 1207.7214.
- [3] AALTONEN, T., ET AL. Invariant Mass Distribution of Jet Pairs Produced in Association with a W boson in  $p\bar{p}$  Collisions at  $\sqrt{s} = 1.96 \text{ TeV}$ . 1104.0699.
- [4] AALTONEN, T., ET AL. Evidence for a particle produced in association with weak bosons and decaying to a bottom-antibottom quark pair in Higgs boson searches at the Tevatron. *Phys.Rev.Lett. 109* (2012), 071804, 1207.6436.
- [5] ALCARAZ, J., ET AL. A Combination of preliminary electroweak measurements and constraints on the standard model. hep-ex/0612034.
- [6] ALWALL, J., DEMIN, P., DE VISSCHER, S., FREDERIX, R., HERQUET, M., ET AL. MadGraph/MadEvent v4: The New Web Generation. *JHEP 0709* (2007), 028, 0706.2334.
- [7] ALWALL, J., HERQUET, M., MALTONI, F., MATTELAER, O., AND STELZER, T. MadGraph 5 : Going Beyond. 1106.0522.
- [8] ANDERSEN, J., ET AL. The SM and NLO Multileg Working Group: Summary report. 21–189, 1003.1241.
- [9] ARNOLD, K., BAHR, M., BOZZI, G., CAMPANARIO, F., ENGLERT, C., ET AL. VBFNLO: A Parton level Monte Carlo for processes with electroweak bosons. *Comput.Phys.Commun. 180* (2009), 1661–1670, 0811.4559.
- [10] ARTOISENET, P., FREDERIX, R., MATTELAER, O., AND RIETKERK, R. Automatic spin-entangled decays of heavy resonances in Monte Carlo simulations. 1212.3460.
- [11] BADGER, S., BIEDERMANN, B., AND UWER, P. NGLuon: A Package to Calculate One-loop Multi-gluon Amplitudes. *Comput.Phys.Commun. 182* (2011), 1674–1692, 1011.2900.

## Bibliography

---

- [12] BADGER, S., CAMPBELL, J. M., AND ELLIS, R. QCD corrections to the hadronic production of a heavy quark pair and a W-boson including decay correlations. *JHEP* 1103 (2011), 027, 1011.6647.
- [13] BAHR, M., GIESEKE, S., GIGG, M., GRELLSCHEID, D., HAMILTON, K., ET AL. Herwig++ Physics and Manual. *Eur.Phys.J. C58* (2008), 639–707, 0803.0883.
- [14] BECHTLE, P., BRINGMANN, T., DESCH, K., DREINER, H., HAMER, M., ET AL. Constrained Supersymmetry after two years of LHC data: a global view with Fittino. *JHEP* 1206 (2012), 098, 1204.4199.
- [15] BEENAKKER, W., DITTMAYER, S., KRAMER, M., PLUMPER, B., SPIRA, M., ET AL. Higgs radiation off top quarks at the Tevatron and the LHC. *Phys.Rev.Lett.* 87 (2001), 201805, hep-ph/0107081.
- [16] BEENAKKER, W., DITTMAYER, S., KRAMER, M., PLUMPER, B., SPIRA, M., ET AL. NLO QCD corrections to t anti-t H production in hadron collisions. *Nucl.Phys. B653* (2003), 151–203, hep-ph/0211352.
- [17] BEENAKKER, W., HOPKER, R., AND SPIRA, M. PROSPINO: A Program for the production of supersymmetric particles in next-to-leading order QCD. hep-ph/9611232.
- [18] BELYAEV, A., AND REINA, L.  $pp \rightarrow gt$ ; t anti-t H,  $H \rightarrow gt$ ; tau+ tau-: Toward a model independent determination of the Higgs boson couplings at the LHC. *JHEP* 0208 (2002), 041, hep-ph/0205270.
- [19] BERGER, C., BERN, Z., DIXON, L., FEBRES CORDERO, F., FORDE, D., ET AL. An Automated Implementation of On-Shell Methods for One-Loop Amplitudes. *Phys.Rev. D78* (2008), 036003, 0803.4180.
- [20] BERGER, C., BERN, Z., DIXON, L. J., FEBRES CORDERO, F., FORDE, D., ET AL. One-Loop Calculations with BlackHat. *Nucl.Phys.Proc.Suppl. 183* (2008), 313–319, 0807.3705.
- [21] BERGER, C., BERN, Z., DIXON, L. J., FEBRES CORDERO, F., FORDE, D., ET AL. Precise Predictions for  $W + 3$  Jet Production at Hadron Colliders. *Phys.Rev.Lett.* 102 (2009), 222001, 0902.2760.
- [22] BERGER, C., BERN, Z., DIXON, L. J., FEBRES CORDERO, F., FORDE, D., ET AL. Precise Predictions for  $W + 4$  Jet Production at the Large Hadron Collider. *Phys.Rev.Lett.* 106 (2011), 092001, 1009.2338.
- [23] BERGER, C. F., BERN, Z., DIXON, L. J., FORDE, D., AND KOSOWER, D. A. Bootstrapping One-Loop QCD Amplitudes with General Helicities. *Phys.Rev. D74* (2006), 036009, hep-ph/0604195.



- 
- [24] BERN, Z., DIANA, G., DIXON, L., FEBRES CORDERO, F., HOECHE, S., ET AL. Four-Jet Production at the Large Hadron Collider at Next-to-Leading Order in QCD. *Phys.Rev.Lett.* 109 (2012), 042001, 1112.3940.
- [25] BERN, Z., DIXON, L. J., DUNBAR, D. C., AND KOSOWER, D. A. One loop n point gauge theory amplitudes, unitarity and collinear limits. *Nucl.Phys. B425* (1994), 217–260, hep-ph/9403226.
- [26] BERN, Z., DIXON, L. J., AND KOSOWER, D. A. Dimensionally regulated one loop integrals. *Phys.Lett. B302* (1993), 299–308, hep-ph/9212308.
- [27] BERN, Z., DIXON, L. J., AND KOSOWER, D. A. One loop amplitudes for  $e^+ e^-$  to four partons. *Nucl.Phys. B513* (1998), 3–86, hep-ph/9708239.
- [28] BEVILACQUA, G., CZAKON, M., GARZELLI, M., VAN HAMEREN, A., KARDOS, A., ET AL. HELAC-NLO. 1110.1499.
- [29] BEVILACQUA, G., CZAKON, M., PAPADOPOULOS, C., PITTAU, R., AND WOREK, M. Assault on the NLO Wishlist:  $pp$  to  $t$  anti- $t$   $b$  anti- $b$ . *JHEP 0909* (2009), 109, 0907.4723.
- [30] BEVILACQUA, G., CZAKON, M., PAPADOPOULOS, C., AND WOREK, M. Dominant QCD Backgrounds in Higgs Boson Analyses at the LHC: A Study of  $pp \rightarrow t$  anti- $t$  + 2 jets at Next-To-Leading Order. *Phys.Rev.Lett.* 104 (2010), 162002, 1002.4009.
- [31] BEVILACQUA, G., CZAKON, M., VAN HAMEREN, A., PAPADOPOULOS, C. G., AND WOREK, M. Complete off-shell effects in top quark pair hadroproduction with leptonic decay at next-to-leading order. *JHEP 1102* (2011), 083, 1012.4230.
- [32] BIERWEILER, A., KASPRZIK, T., KUHN, H., AND UCCIRATI, S. Electroweak corrections to  $W$ -boson pair production at the LHC. 1208.3147.
- [33] BINOTH, T., BOUDJEMA, F., DISSERTORI, G., LAZOPOULOS, A., DENNER, A., ET AL. A Proposal for a standard interface between Monte Carlo tools and one-loop programs. *Comput.Phys.Commun.* 181 (2010), 1612–1622, 1001.1307.
- [34] BINOTH, T., GREINER, N., GUFFANTI, A., REUTER, J., GUILLET, J.-P., ET AL. Next-to-leading order QCD corrections to  $pp$  to  $b$  anti- $b$   $b$  anti- $b$  +  $X$  at the LHC: the quark induced case. *Phys.Lett. B685* (2010), 293–296, 0910.4379.
- [35] BINOTH, T., GUFFANTI, A., GUILLET, J.-P., HEINRICH, G., KARG, S., ET AL. Precise predictions for LHC using a GOLEM. *Nucl.Phys.Proc.Suppl.* 183 (2008), 91–96, 0807.0605.
- [36] BINOTH, T., GUILLET, J., AND HEINRICH, G. Algebraic evaluation of rational polynomials in one-loop amplitudes. *JHEP 0702* (2007), 013, hep-ph/0609054.

## Bibliography

---

- [37] BINOTH, T., GUILLET, J.-P., HEINRICH, G., PILON, E., AND REITER, T. Golem95: A Numerical program to calculate one-loop tensor integrals with up to six external legs. *Comput.Phys.Commun.* 180 (2009), 2317–2330, 0810.0992.
- [38] BINOTH, T., OSSOLA, G., PAPADOPOULOS, C., AND PITTAU, R. NLO QCD corrections to tri-boson production. *JHEP* 0806 (2008), 082, 0804.0350.
- [39] BRAU, JAMES, E., ET AL. ILC Reference Design Report: ILC Global Design Effort and World Wide Study. 0712.1950.
- [40] BREDENSTEIN, A., DENNER, A., DITTMAIER, S., AND POZZORINI, S. NLO QCD corrections to  $t$  anti- $t$   $b$  anti- $b$  production at the LHC: 1. Quark-antiquark annihilation. *JHEP* 0808 (2008), 108, 0807.1248.
- [41] BREDENSTEIN, A., DENNER, A., DITTMAIER, S., AND POZZORINI, S. NLO QCD corrections to  $pp \rightarrow g\bar{t}; t$  anti- $t$   $b$  anti- $b$  + X at the LHC. *Phys.Rev.Lett.* 103 (2009), 012002, 0905.0110.
- [42] BUTTAR, C., DITTMAIER, S., DROLLINGER, V., FRIXIONE, S., NIKITENKO, A., ET AL. Les houches physics at TeV colliders 2005, standard model and Higgs working group: Summary report. hep-ph/0604120.
- [43] BUTTERWORTH, J. M., DAVISON, A. R., RUBIN, M., AND SALAM, G. P. Jet substructure as a new Higgs search channel at the LHC. *Phys.Rev.Lett.* 100 (2008), 242001, 0802.2470.
- [44] CACCIARI, M., SALAM, G. P., AND SOYEZ, G. FastJet User Manual. *Eur.Phys.J.* C72 (2012), 1896, 1111.6097.
- [45] CAMPANARIO, F., HANKELE, V., OLEARI, C., PRESTEL, S., AND ZEPPENFELD, D. QCD corrections to charged triple vector boson production with leptonic decay. *Phys.Rev.* D78 (2008), 094012, 0809.0790.
- [46] CAMPBELL, J. M., AND ELLIS, R. MCFM for the Tevatron and the LHC. *Nucl.Phys.Proc.Suppl.* 205-206 (2010), 10–15, 1007.3492.
- [47] CAMPBELL, J. M., AND ELLIS, R. K. An Update on vector boson pair production at hadron colliders. *Phys.Rev.* D60 (1999), 113006, hep-ph/9905386.
- [48] CAMPBELL, J. M., AND ELLIS, R. K. Next-to-leading order corrections to  $W^+$  2 jet and  $Z^+$  2 jet production at hadron colliders. *Phys.Rev.* D65 (2002), 113007, hep-ph/0202176.
- [49] CAMPBELL, J. M., ELLIS, R. K., MALTONI, F., AND WILLENBROCK, S. Higgs-Boson production in association with a single bottom quark. *Phys.Rev.* D67 (2003), 095002, hep-ph/0204093.

- 
- [50] CAMPBELL, J. M., FREDERIX, R., MALTONI, F., AND TRAMONTANO, F. Next-to-Leading-Order Predictions for t-Channel Single-Top Production at Hadron Colliders. *Phys.Rev.Lett.* 102 (2009), 182003, 0903.0005.
- [51] CAMPBELL, J. M., FREDERIX, R., MALTONI, F., AND TRAMONTANO, F. NLO predictions for t-channel production of single top and fourth generation quarks at hadron colliders. *JHEP* 0910 (2009), 042, 0907.3933.
- [52] CASCIOLI, F., MAIERHOFER, P., AND POZZORINI, S. Scattering Amplitudes with Open Loops. *Phys.Rev.Lett.* 108 (2012), 111601, 1111.5206.
- [53] CATANI, S., DOKSHITZER, Y. L., SEYMOUR, M., AND WEBBER, B. Longitudinally invariant  $K_t$  clustering algorithms for hadron hadron collisions. *Nucl.Phys. B406* (1993), 187–224.
- [54] CHATRCHYAN, S., ET AL. Combined results of searches for the standard model Higgs boson in  $pp$  collisions at  $\sqrt{s} = 7$  TeV. *Phys.Lett. B710* (2012), 26–48, 1202.1488.
- [55] CHATRCHYAN, S., ET AL. Observation of a new boson at a mass of 125 GeV with the CMS experiment at the LHC. *Phys.Lett. B716* (2012), 30–61, 1207.7235.
- [56] CHRISTENSEN, N. D., AND DUHR, C. FeynRules - Feynman rules made easy. *Comput.Phys.Commun.* 180 (2009), 1614–1641, 0806.4194.
- [57] COLLINS, J. C., SOPER, D. E., AND STERMAN, G. F. Factorization of Hard Processes in QCD. *Adv.Ser.Direct.High Energy Phys.* 5 (1988), 1–91, hep-ph/0409313.
- [58] CONTE, E., FUKS, B., AND SERRET, G. MadAnalysis 5, A User-Friendly Framework for Collider Phenomenology. 1206.1599.
- [59] CONTINO, R. The Higgs as a Composite Nambu-Goldstone Boson. 1005.4269.
- [60] CORCELLA, G., KNOWLES, I., MARCHESINI, G., MORETTI, S., ODAGIRI, K., ET AL. HERWIG 6.5 release note. hep-ph/0210213.
- [61] CULLEN, G., ET AL. Automated One-Loop Calculations with GoSam. 1111.2034.
- [62] DAWSON, S., JACKSON, C., ORR, L., REINA, L., AND WACKEROTH, D. Associated Higgs production with top quarks at the large hadron collider: NLO QCD corrections. *Phys.Rev. D68* (2003), 034022, hep-ph/0305087.
- [63] DAWSON, S., ORR, L., REINA, L., AND WACKEROTH, D. Associated top quark Higgs boson production at the LHC. *Phys.Rev. D67* (2003), 071503, hep-ph/0211438.
- [64] DAWSON, S., AND REINA, L. QCD corrections to associated Higgs boson production. *Phys.Rev. D57* (1998), 5851–5859, hep-ph/9712400.

## Bibliography

---

- [65] DE AQUINO, P., LINK, W., MALTONI, F., MATTELAER, O., AND STELZER, T. ALOHA: Automatic Libraries Of Helicity Amplitudes for Feynman Diagram Computations. *Comput.Phys.Commun.* 183 (2012), 2254–2263, 1108.2041.
- [66] DE VISSCHER, S., GERARD, J.-M., HERQUET, M., LEMAITRE, V., AND MALTONI, F. Unconventional phenomenology of a minimal two-Higgs-doublet model. *JHEP* 0908 (2009), 042, 0904.0705.
- [67] DEGRANDE, C., DUHR, C., FUKS, B., GRELLSCHEID, D., MATTELAER, O., ET AL. UFO - The Universal FeynRules Output. 1108.2040.
- [68] DEL AGUILA, F., AND PITTAU, R. Recursive numerical calculus of one-loop tensor integrals. *JHEP* 0407 (2004), 017, hep-ph/0404120.
- [69] DENNER, A., AND DITTMAIER, S. Reduction of one loop tensor five point integrals. *Nucl.Phys. B*658 (2003), 175–202, hep-ph/0212259.
- [70] DENNER, A., AND DITTMAIER, S. Reduction schemes for one-loop tensor integrals. *Nucl.Phys. B*734 (2006), 62–115, hep-ph/0509141.
- [71] DENNER, A., AND DITTMAIER, S. The Complex-mass scheme for perturbative calculations with unstable particles. *Nucl.Phys.Proc.Suppl.* 160 (2006), 22–26, hep-ph/0605312.
- [72] DENNER, A., DITTMAIER, S., KALLWEIT, S., AND MUCK, A. Electroweak corrections to Higgs-strahlung off W/Z bosons at the Tevatron and the LHC with HAWK. *JHEP* 1203 (2012), 075, 1112.5142.
- [73] DENNER, A., DITTMAIER, S., KALLWEIT, S., AND POZZORINI, S. NLO QCD corrections to WWbb production at hadron colliders. *Phys.Rev.Lett.* 106 (2011), 052001, 1012.3975.
- [74] DENNER, A., DITTMAIER, S., KALLWEIT, S., AND POZZORINI, S. NLO QCD corrections to off-shell top-antitop production with leptonic decays at hadron colliders. *JHEP* 1210 (2012), 110, 1207.5018.
- [75] DENNER, A., DITTMAIER, S., ROTH, M., AND WIEDERS, L. H. Electroweak corrections to charged-current  $e^+ e^- \rightarrow 4$  fermion processes: Technical details and further results. *Nucl. Phys. B*724 (2005), 247–294, hep-ph/0505042.
- [76] DERMISEK, R., AND GUNION, J. F. Many Light Higgs Bosons in the NMSSM. *Phys.Rev. D*79 (2009), 055014, 0811.3537.
- [77] DITTMAIER, S., DITTMAIER, S., MARIOTTI, C., PASSARINO, G., TANAKA, R., ET AL. Handbook of LHC Higgs Cross Sections: 2. Differential Distributions. 1201.3084.

- 
- [78] DITTMAIER, S., ET AL. Handbook of LHC Higgs Cross Sections: 1. Inclusive Observables. 1101.0593.
- [79] DITTMAIER, S., HUSS, A., AND SPECKNER, C. Weak radiative corrections to dijet production at hadron colliders. *JHEP* 1211 (2012), 095, 1210.0438.
- [80] DITTMAIER, S., KRAMER, MICHAEL, ., AND SPIRA, M. Higgs radiation off bottom quarks at the Tevatron and the CERN LHC. *Phys.Rev. D70* (2004), 074010, hep-ph/0309204.
- [81] DITTMAIER, S., KRAMER, M., LIAO, Y., SPIRA, M., AND ZERWAS, P. Higgs radiation off quarks in supersymmetric theories at  $e^+e^-$  colliders. *Phys.Lett. B478* (2000), 247–254, hep-ph/0002035.
- [82] DITTMAIER, S., UWER, P., AND WEINZIERL, S. NLO QCD corrections to  $t$  anti- $t$  + jet production at hadron colliders. *Phys.Rev.Lett.* 98 (2007), 262002, hep-ph/0703120.
- [83] DITTMAIER, S., UWER, P., AND WEINZIERL, S. Hadronic top-quark pair production in association with a hard jet at next-to-leading order QCD: Phenomenological studies for the Tevatron and the LHC. *Eur.Phys.J. C59* (2009), 625–646, 0810.0452.
- [84] DIXON, L. J., KUNSZT, Z., AND SIGNER, A. Helicity amplitudes for  $O(\alpha_s)$  production of  $W^+W^-$ ,  $W^\pm Z$ ,  $ZZ$ ,  $W^\pm\gamma$ , or  $Z\gamma$  pairs at hadron colliders. *Nucl.Phys. B531* (1998), 3–23, hep-ph/9803250.
- [85] DIXON, L. J., AND SIGNER, A. Complete  $O(\alpha_s^3)$  results for  $e^+e^- \rightarrow (\gamma, Z) \rightarrow$  four jets. *Phys.Rev. D56* (1997), 4031–4038, hep-ph/9706285.
- [86] DOBBS, M., FRIXIONE, S., LAENEN, E., TOLLEFSON, K., BAER, H., ET AL. Les Houches guidebook to Monte Carlo generators for hadron collider physics. 411–459, hep-ph/0403045.
- [87] DRAGGIOTIS, P., GARZELLI, M. V., PAPADOPOULOS, C. G., AND PITTAU, R. Feynman rules for the rational part of the qcd 1-loop amplitudes. *JHEP* 0904 (2009), 072.
- [88] DRAGGIOTIS, P., GARZELLI, M. V., PAPADOPOULOS, C. G., AND PITTAU, R. Feynman Rules for the Rational Part of the QCD 1-loop amplitudes. *JHEP* 04 (2009), 072, 0903.0356.
- [89] EBOLI, O. J., GONZALEZ-GARCIA, M., LIETTI, S., AND NOVAES, S. Anomalous quartic gauge boson couplings at hadron colliders. *Phys.Rev. D63* (2001), 075008, hep-ph/0009262.
- [90] ELLIS, R., KUNSZT, Z., MELNIKOV, K., AND ZANDERIGHI, G. One-loop calculations in quantum field theory: from Feynman diagrams to unitarity cuts. 1105.4319.

## Bibliography

---

- [91] ELLIS, R. K., GIELE, W., AND KUNSZT, Z. A Numerical Unitarity Formalism for Evaluating One-Loop Amplitudes. *JHEP 0803* (2008), 003, 0708.2398.
- [92] ELLIS, R. K., GIELE, W. T., KUNSZT, Z., AND MELNIKOV, K. Masses, fermions and generalized  $D$ -dimensional unitarity. *Nucl.Phys. B822* (2009), 270–282, 0806.3467.
- [93] ELLIS, R. K., AND SEXTON, J. QCD Radiative Corrections to Parton Parton Scattering. *Nucl.Phys. B269* (1986), 445.
- [94] ELLIS, R. K., AND ZANDERIGHI, G. Scalar one-loop integrals for QCD. *JHEP 0802* (2008), 002, 0712.1851.
- [95] ELLWANGER, U., HUGONIE, C., AND TEIXEIRA, A. M. The Next-to-Minimal Supersymmetric Standard Model. *Phys.Rept. 496* (2010), 1–77, 0910.1785.
- [96] ENGLERT, F., AND BROUT, R. Broken Symmetry and the Mass of Gauge Vector Mesons. *Phys.Rev.Lett. 13* (1964), 321–323.
- [97] FEBRES CORDERO, F., REINA, L., AND WACKEROTH, D. NLO QCD corrections to  $W$  boson production with a massive  $b$ -quark jet pair at the Tevatron  $p$  anti- $p$  collider. *Phys.Rev. D74* (2006), 034007, hep-ph/0606102.
- [98] FLEISCHER, J., RIEMANN, T., AND YUNDIN, V. One-Loop Tensor Feynman Integral Reduction with Signed Minors. 1112.0500.
- [99] FLEISCHER, J., RIEMANN, T., AND YUNDIN, V. New Results for Algebraic Tensor Reduction of Feynman Integrals. 1202.0730.
- [100] FOADI, R., FRANDBSEN, M. T., RYTTOV, T. A., AND SANNINO, F. Minimal Walking Technicolor: Set Up for Collider Physics. *Phys.Rev. D76* (2007), 055005, 0706.1696.
- [101] FREDERIX, R., FRIXIONE, S., HIRSCHI, V., MALTONI, F., PITTAU, R., AND TORIELLI, P. aMC@NLO predictions for  $Wjj$  production at the Tevatron. 1110.5502.
- [102] FREDERIX, R., FRIXIONE, S., HIRSCHI, V., MALTONI, F., PITTAU, R., AND TORIELLI, P. Four-lepton production at hadron colliders: aMC@NLO predictions with theoretical uncertainties. 1110.4738.
- [103] FREDERIX, R., FRIXIONE, S., HIRSCHI, V., MALTONI, F., PITTAU, R., AND TORIELLI, P. Scalar and pseudoscalar Higgs production in association with a top-antitop pair. *Phys.Lett. B701* (2011), 427–433, 1104.5613.
- [104] FREDERIX, R., FRIXIONE, S., HIRSCHI, V., MALTONI, F., PITTAU, R., AND TORIELLI, P.  $W$  and  $Z/\gamma^*$  boson production in association with a bottom-antibottom pair. *JHEP 1109* (2011), 061, 1106.6019.

- 
- [105] FREDERIX, R., FRIXIONE, S., MALTONI, F., AND STELZER, T. Automation of next-to-leading order computations in QCD: The FKS subtraction. *JHEP* 0910 (2009), 003, 0908.4272.
- [106] FREDERIX, R., FRIXIONE, S., MELNIKOV, K., AND ZANDERIGHI, G. NLO QCD corrections to five-jet production at LEP and the extraction of  $\alpha_s(M_Z)$ . *JHEP* 1011 (2010), 050, 1008.5313.
- [107] FRIXIONE, S. A General approach to jet cross-sections in QCD. *Nucl.Phys. B*507 (1997), 295–314, hep-ph/9706545.
- [108] FRIXIONE, S. Isolated photons in perturbative QCD. *Phys.Lett. B*429 (1998), 369–374, hep-ph/9801442.
- [109] FRIXIONE, S. Colourful FKS subtraction. *JHEP* 1109 (2011), 091, 1106.0155.
- [110] FRIXIONE, S., KUNSZT, Z., AND SIGNER, A. Three jet cross-sections to next-to-leading order. *Nucl.Phys. B*467 (1996), 399–442, hep-ph/9512328.
- [111] FRIXIONE, S., LAENEN, E., MOTYLINSKI, P., AND WEBBER, B. R. Angular correlations of lepton pairs from vector boson and top quark decays in Monte Carlo simulations. *JHEP* 0704 (2007), 081, hep-ph/0702198.
- [112] FRIXIONE, S., AND WEBBER, B. R. Matching nlo qcd computations and parton shower simulations. *JHEP* 0206 (2002), 029.
- [113] GIELE, W., AND GLOVER, E. N. A Computational formalism for one loop integrals. *JHEP* 0404 (2004), 029, hep-ph/0402152.
- [114] GLEISBERG, T., HOECHE, S., KRAUSS, F., SCHONHERR, M., SCHUMANN, S., ET AL. Event generation with SHERPA 1.1. *JHEP* 0902 (2009), 007, 0811.4622.
- [115] GLOVER. Z boson production and decay via gluons. *Nuclear Physics B*, 313 (1989), 237–257.
- [116] GREEN, D. Triple vector boson production at the LHC. hep-ex/0310004.
- [117] HAHN, T. Generating Feynman diagrams and amplitudes with FeynArts 3. *Comput.Phys.Commun.* 140 (2001), 418–431, hep-ph/0012260.
- [118] HAN, T., AND SOBEY, R. Triple electroweak gauge boson productions at Fermilab Tevatron energies. *Phys.Rev. D*52 (1995), 6302–6308, hep-ph/9507409.
- [119] HANKELE, V., AND ZEPPENFELD, D. QCD corrections to hadronic WWZ production with leptonic decays. *Phys.Lett. B*661 (2008), 103–108, 0712.3544.
- [120] HIGGS, P. W. Broken Symmetries and the Masses of Gauge Bosons. *Phys.Rev.Lett.* 13 (1964), 508–509.

## Bibliography

---

- [121] HIGGS, P. W. Broken symmetries, massless particles and gauge fields. *Phys.Lett.* *12* (1964), 132–133.
- [122] HIRSCHI, V. New developments in MadLoop. *PoS for RADCOR2011* (2011), 1111.2708.
- [123] HIRSCHI, V., ET AL. Automation of one-loop QCD corrections. *JHEP* *05* (2011), 044, 1103.0621.
- [124] KUNSZT, Z., SIGNER, A., AND TROCSANYI, Z. One loop helicity amplitudes for all  $2 \rightarrow 2$  processes in QCD and  $N=1$  supersymmetric Yang-Mills theory. *Nucl. Phys. B* *411* (1994), 397–442, hep-ph/9305239.
- [125] L. LINSSEN, A. MIYAMOTO, M. S., AND WEERTS, H. Physics and Detectors at CLIC: CLIC Conceptual Design Report. *CERN Yellow Report CERN-2012-003* (2012), 1202.5940.
- [126] LANDAU, L. On the angular momentum of a two-photon system. *Dokl.Akad.Nauk Ser.Fiz.* *60* (1948), 207–209.
- [127] LAZOPOULOS, A., MELNIKOV, K., AND PETRIELLO, F. QCD corrections to tri-boson production. *Phys.Rev.* *D76* (2007), 014001, hep-ph/0703273.
- [128] MALTONI, F., RAINWATER, D. L., AND WILLENBROCK, S. Measuring the top quark Yukawa coupling at hadron colliders via  $t\bar{t}H, H \rightarrow W^+W^-$ . *Phys.Rev.* *D66* (2002), 034022, hep-ph/0202205.
- [129] MALTONI, F., AND STELZER, T. MadEvent: Automatic event generation with MadGraph. *JHEP* *0302* (2003), 027, hep-ph/0208156.
- [130] MARTIN, A., STIRLING, W., THORNE, R., AND WATT, G. Parton distributions for the LHC. *Eur.Phys.J.* *C63* (2009), 189–285, 0901.0002.
- [131] MASTROLIA, P., OSSOLA, G., REITER, T., AND TRAMONTANO, F. Scattering AMplitudes from Unitarity-based Reduction Algorithm at the Integrand-level. *JHEP* *1008* (2010), 080, 1006.0710.
- [132] MELNIKOV, K., AND SCHULZE, M. NLO QCD corrections to top quark pair production in association with one hard jet at hadron colliders. *Nucl.Phys.* *B840* (2010), 129–159, 1004.3284.
- [133] MODAK, T., SAHOO, D., SINHA, R., AND CHENG, H.-Y. Inferring the nature of the boson at 125-126 GeV. 1301.5404.
- [134] MORETTI, S., NOLTEN, M., AND ROSS, D. Weak corrections to four-parton processes. *Nucl.Phys.* *B759* (2006), 50–82, hep-ph/0606201.



- 
- [135] OHNEMUS, J. Hadronic  $ZZ$ ,  $W^-W^+$ , and  $W^\pm Z$  production with QCD corrections and leptonic decays. *Phys.Rev. D50* (1994), 1931–1945, hep-ph/9403331.
- [136] OSSOLA, G., PAPADOPOULOS, C. G., AND PITTAU, R. Reducing full one-loop amplitudes to scalar integrals at the integrand level. *Nuclear Physics B 763* (2007), 147.
- [137] OSSOLA, G., PAPADOPOULOS, C. G., AND PITTAU, R. Reducing full one-loop amplitudes to scalar integrals at the integrand level. *Nucl.Phys. B763* (2007), 147–169, hep-ph/0609007.
- [138] OSSOLA, G., PAPADOPOULOS, C. G., AND PITTAU, R. CutTools: A Program implementing the OPP reduction method to compute one-loop amplitudes. *JHEP 0803* (2008), 042, 0711.3596.
- [139] OSSOLA, G., PAPADOPOULOS, C. G., AND PITTAU, R. NLO corrections with the OPP method. *Nucl.Phys.Proc.Suppl. 183* (2008), 42–47.
- [140] OSSOLA, G., PAPADOPOULOS, C. G., AND PITTAU, R. On the Rational Terms of the one-loop amplitudes. *JHEP 0805* (2008), 004, 0802.1876.
- [141] PASSARINO, G., AND VELTMAN, M. One Loop Corrections for  $e^+ e^-$  Annihilation Into  $\mu^+ \mu^-$  in the Weinberg Model. *Nucl.Phys. B160* (1979), 151.
- [142] PESKIN, M. E., AND SCHROEDER, D. V. An Introduction to quantum field theory.
- [143] PLEHN, T. Measuring the MSSM Lagrangean. *Czech.J.Phys. 55* (2005), B213–B220, hep-ph/0410063.
- [144] PLEHN, T., SALAM, G. P., AND SPANNOVSKY, M. Fat Jets for a Light Higgs. *Phys.Rev.Lett. 104* (2010), 111801, 0910.5472.
- [145] RANDALL, L., AND SUNDRUM, R. Out of this world supersymmetry breaking. *Nucl.Phys. B557* (1999), 79–118, hep-th/9810155.
- [146] REINA, L., DAWSON, S., AND WACKEROTH, D. QCD corrections to associated  $t$  anti- $t$   $h$  production at the Tevatron. *Phys.Rev. D65* (2002), 053017, hep-ph/0109066.
- [147] RIDDER, A. G.-D., GEHRMANN, T., GLOVER, E., AND PIRES, J. Second order QCD corrections to jet production at hadron colliders: the all-gluon contribution. 1301.7310.
- [148] SIGNER, A., AND DIXON, L. J. Electron - positron annihilation into four jets at next-to-leading order in  $\alpha$ -s. *Phys.Rev.Lett. 78* (1997), 811–814, hep-ph/9609460.
- [149] SIGNER, A., AND STOCKINGER, D. Using Dimensional Reduction for Hadronic Collisions. *Nucl. Phys. B808* (2009), 88–120, 0807.4424.

## Bibliography

---

- [150] SJOSTRAND, T., MRENNNA, S., AND SKANDS, P. Z. PYTHIA 6.4 Physics and Manual. *JHEP 0605* (2006), 026, hep-ph/0603175.
- [151] SJOSTRAND, T., MRENNNA, S., AND SKANDS, P. Z. A Brief Introduction to PYTHIA 8.1. *Comput.Phys.Commun. 178* (2008), 852–867, 0710.3820.
- [152] STELZER, T., AND LONG, W. F. Automatic generation of tree level helicity amplitudes. *Computer Physics Communications 81* (1994), 357.
- [153] 'T HOOFT, G., AND VELTMAN, M. Scalar One Loop Integrals. *Nucl.Phys. B153* (1979), 365–401.
- [154] VAN HAMEREN, A. OneLOop: For the evaluation of one-loop scalar functions. *Comput.Phys.Commun. 182* (2011), 2427–2438, 1007.4716.
- [155] VAN HAMEREN, A., PAPADOPOULOS, C. G., AND PITTAU, R. Automated one-loop calculations: a proof of concept. *JHEP 09* (2009), 106, 0903.4665.
- [156] WEYDERT, C., FRIXIONE, S., HERQUET, M., KLASSEN, M., LAENEN, E., ET AL. Charged Higgs boson production in association with a top quark in MC@NLO. *Eur.Phys.J. C67* (2010), 617–636, 0912.3430.
- [157] YANG, C.-N. Selection Rules for the Dematerialization of a Particle Into Two Photons. *Phys.Rev. 77* (1950), 242–245.
- [158] ZHU, S.-H. Complete next-to-leading order QCD corrections to charged Higgs boson associated production with top quark at the CERN large hadron collider. *Phys.Rev. D67* (2003), 075006, hep-ph/0112109.

# Valentin Hirschi

# Curriculum vitae

DATE OF BIRTH 3 March 1986

NATIONALITY Swiss

MARITAL STATUS Single

## PERSONAL STATEMENT

Ph.D. student with strong analytical mind and computer skills gained in developing a theoretical physics tool within an internationally broad collaboration.

## EDUCATION AND TRAINING

- 04.2009 to now** ITP, EPFL, Lausanne, Switzerland.  
Ph.D. on the automation of NLO computations in particle physics.
- 09.2008-02.2009** UCL, Louvain-La-Neuve, Belgium.  
Master thesis on Z' phenomenology.
- 09.2007-07.2008** EPFL, Lausanne, Switzerland.  
Master cycle, specialization in theoretical particle physics.
- 09.2006-07.2007** Exchange year at Iowa State University, Ames, Iowa, USA.  
Third and last bachelor year.
- 09.2004-07.2006** EPFL, Lausanne, Switzerland.  
Bachelor cycle. General physics, real and complex analysis, quantum physics, statistics. Complete list on the grade transcript.
- 08.2001-07.2004** High school at GAP, Lausanne, Switzerland.  
"Maturité Fédérale" in Physics.  
Awarded with the mathematics prize and the physics prize.

## PROFESSIONAL AND TEACHING EXPERIENCE

- 04.2009-07.2012** As a Ph.D. student at EPFL I was assistant for several physics master courses such as *Relativity and Cosmology* and *Classical Electrodynamics* by Pr. M. Shaposhnikov and Pr. R. Rattazzi.
- 07.2008-09.2008** Took part of the CERN *Summer Student Program* at LHCb on cross-talk corrections for the VELO readout electronics. Ref: K. Rinnert
- 10.2007-07.2008** Assistant of Pr. M. Grioni for his general physics course.
- 07.2007-09.2007** Research assistant at the LPM laboratory, EPFL. I studied the electric properties of epoxy matrixes doped with graphite.
- 06.2007-07.2008** Assistant of Pr. J.C. Chappelier for his C++ course.  
I supervised exercises sessions and the semester projects of the students.
- 03.2006-06.2006** Assistant of Pr. J.P. Ansermet for his general physics course.
- 2002 - 2006** Student jobs at McDonald's, Coop.

## MAIN TALKS AND CONFERENCES PARTICIPATION

---

18-20.04.2013	Talk given at MC4BSM, DESY, Hambourg
01-08.10.2012	Lecturer at the MadGraph School on LHC Pheno, Natal, Brazil
04.09.2012	Talk given at "Hard Precision for Hard Processes", HP2, München
23.07-03.08.2012	Attended SSI 2012, SLAC Summer School, Stanford
17.06.2012	Talk given at TOOLS 2012, Stockholm
27.03.2012	Talk given at FeynRules 2012 Workshop, St-Odile, France
28.09.2011	Talk given at RADCOR 2011, Mamallapuram, India
22.09.2011	Talk given at the MadGraph 2011 Workshop, Rome
21.04.2011	Invited speaker for a seminar on MadLoop at DESY, Berlin
20.03-01.04.2011	Visiting FermiLab for collaborative work with J.Alwall, Illinois, USA

## LANGUAGES

---

<b>French</b>	Mother tongue.
<b>English</b>	One year spent studying in Iowa, USA. Level C1.
<b>German</b>	High school basics. Level A2.

## ADDITIONAL INFORMATION

---

<b>Computer</b>	Proficiency in python and expertise of C++ and FORTRAN. Good knowledge of UNIX-based OS, Mathematica and LaTeX. Know-how in common MS Office programs.
<b>Publications</b>	Details of my seven publications available upon request.
<b>Miscellaneous</b>	Finished second at CodeCup 2012, a competition of artificial intelligence programming. <a href="http://archive.codecup.nl/2012">http://archive.codecup.nl/2012</a>
<b>Other Interests</b>	badminton, table tennis, board games, fishing